Comparison study of computational modeling approaches for calcium silicate elements masonry structures

by

Audy Maulizar

4745019

To obtain the degree of Master of Science at Delft University of Technology

Comparison study of computational modeling approaches for calcium silicate elements masonry structures

by

Audy Maulizar

4745019

to obtain the degree of Master of Science at Delft University of Technology

to be defended publicly on Thursday March 19, 2020 at 16:00 PM

Prof. dr. ir. J.G. Rots,	Structural Mechanics (chairman)
Dr. ir. F. Messali,	Structural Mechanics (daily supervisor)
Dr. ir. G.J.P. Ravenshorst,	Biobased Structures and Materials

Summary

The exploitation of natural gas in the Groningen region has become an important economic activity in the region. But, on the other hand, it has introduced induced seismicity in the region. This puts many residential buildings in the region at risk of suffering from seismic induced damage since a substantial portion of residential buildings in the region consists of unreinforced masonry (URM) structures, that are particularly weak to seismic loads. The increased seismic activity can, therefore, cause severe damages to the structure, with consequent economic losses and possible human casualties.

A number of experimental and numerical studies on the seismic response of URM structures have been carried out. Two full-scale URM building specimens had been tested with cyclic pushover loading. One of them was a specimen built from CS element masonry units, which was built to simulate post-1980 masonry residential buildings in Groningen (Esposito et al. 2018). Apart from physical testing, several numerical studies have also been conducted on the structure. A blind prediction contest was held in 2017 involving nine consultants, who each used various modeling methods (Messali et al. 2018). This blind prediction contest yields results with varying degrees of success in predicting the seismic performance of the structure.

In this thesis, several different modeling approaches are considered for modeling the tested specimen. These numerical analyses are conducted to assess how different methods affect the outcome of the simulation of the structure. These results are then compared to the experimental results to assess the viability of each modeling approach for practical use. Sensitivity studies are also carried out to study the effects of changes in the material parameters on the numerical results. The effect of the inclusion of interface elements in the wall-pier connections is also be analyzed in this thesis.

The analyses are carried out by performing nonlinear pushover analyses of numerical models with different parameters. The structural analysis software package DIANA 10.3 is used for the numerical analyses. Two categories of modeling approaches are analyzed in this thesis: the continuum element-based macro-modeling approach and the block-based micro-modeling approach. The analysis results of each model are compared to the results of the other models in the same category and the experimental results. Based on these comparisons, a conclusion on the viability of the modeling approaches to be used for practical use can be derived.

The numerical analyses for macro-models are carried out on three macro-model variations. One model variation with the Total Strain Rotating Crack Model (Macro-TSRCM) and the other two using the Engineering Masonry Model with different values of staircase crack angle (Macro-EMM(1) & Macro-EMM(2)). A comparison between the results of the three macro-models shows that the Macro-TSRCM model provides the most accurate approximation of the structural behavior out of the three macro-models. The

behavior of the capacity curve from the numerical model closely resembles the behavior of the backbone curve with the reduction of stiffness and the sudden decrease in base shear force. The Macro-EMM models, on the other hand, show an excessively ductile behavior. Despite the promising results, the Macro-TSRCM model considered in this study still has some limitations. The model cannot accurately simulate the out-of-plane behavior of the structure, due to the limitation of the constitutive model. The model also seems to greatly overestimate the structural capacity of the specimen. All of these limitations and issues mean that this particular model is not suitable for practical use. Prior research on a similar model showed that the overestimation issue with the model might be rectified with the calibration of material parameters (Pari et al. 2017).

Sensitivity studies are conducted on the macro-models to assess the effect of various material parameters on the analysis results, such as tensile and compressive strength and fracture energy in tension and compression. From the sensitivity study performed on the Macro-TSRCM model, it appears that most changes in the value of material parameters affect the post-peak behavior of the structure. The pre-peak behavior is not significantly affected by the changes of any parameter. This is an unexpected result since changes in the parameters that govern tensile cracking in the pre-peak region are expected to cause significant changes to the pre-peak behavior. This unusual behavior suggests that there is another factor that influences the pre-peak behavior of the model. However, this study was unable to identify that factor. A sensitivity study is also performed on the Macro-EMM models. The results show that the Macro-EMM models are more sensitive to the parameters related to the compressive behavior than the tensile behavior. Additional sensitivity studies are also performed by varying Young’s modulus of the concrete floors. The change in concrete Young’s modulus seems to affect the pre-peak behavior of both model variations significantly. A significant increase in initial stiffness can be observed on both models due to the change and in the case of the Macro-TSRCM model, a significant change to the initiation of the rocking mechanism.

The effect of the inclusion of interface elements on the macro-models is also investigated in this thesis. In the case of the Macro-TSRCM model, the inclusion of the interface elements to the wall-pier connections significantly changes the diagonal cracking failure formation in the piers. In the case of the Macro-EMM models, the change is minuscule with the failure of the vertical joints being the only noticeable change. The introduction of nonlinear behavior at the vertical interfaces on all macro-models, however, leads to instability of the analysis. Several analyses suffer from non-convergence at an early stage of the analysis after cracks open in the vertical interfaces. Due to this reason, it is not possible to properly evaluate the consequence of the introduction of the nonlinear behavior to the vertical interface on the post-peak behavior.

Micro-models are also constructed for numerical analyses with continuum elements simulating the CS elements and the interface elements simulating the mortar and element-mortar bond. The nonlinear pushover analyses on the models yield results with varying degrees of success in approximating the behavior of the structure. Three different interface element constitutive models are used for the micro-models: Coulomb friction, discrete cracking and nonlinear elasticity. The results show that most of the micro-models suffer from instability issues. This instability issue occurs especially in the Coulomb friction models and the nonlinear elasticity models with non-convergence occurring at the early stage of the analyses. Out of all micro-models, the discrete cracking models show the most stable behavior and offer the most accurate approximation of the backbone curve. However, the discrete cracking models are not able to represent adequately the frictional behavior along the corners of the building and they lead to a large overestimation of the structural capacity. For this reason, this type of modeling is not recommended for practical use. Considering all of these issues related to the micro-models, no micro-model considered in this thesis can be recommended for engineering purposes.

Based on the analyses carried out on both macro-models, one of the main issues from the models is the gross overestimation of the structural capacity. It is recommended to carry out further sensitivity studies on other material parameters. It is also possible that the modeling strategy taken in modeling the structure has an influence on the overestimation of the structural capacity. It is, therefore, advised to run another numerical study on the physical structure with another modeling strategy. In regards to the micro-models, it is advisable to analyze each model variation with a simpler model to investigate the cause of the instability issue in each model variation. It is also recommended to consider analyses with more detailed modeling approaches (e.g. 3D brick elements with combined cracking-shear-crushing constitutive model), as both the macro- and micro-models have shown some significant limitations, especially regarding the modeling of out-of-plane behavior.

Acknowledgements

I would like to express my gratitude to everyone who has given me their support throughout my thesis work:

My daily supervisor, Dr. ir. Francesco Messali, for his guidance during the entire process of my thesis work. Thank you for your patience in guiding me and providing helpful suggestions on my thesis work.

Prof.dr.ir. J.G. Rots and Dr.ir. G.J.P. Ravenshorst for their helpful feedbacks and constructive criticisms on my thesis work during the committee meetings. Thank you for helping me improve my thesis work and encouraging me to be more critical on my work.

My parents for their continuous and tireless support. Thank you for giving me much needed encouragement and reassurance when I really need it.

All of my friends, just for being there to share a laugh and providing me with a much needed break in between my work on my thesis.

Audy Maulizar

Delft, March 2020

Table of Contents

List of Figures

List of Tables

Chapter 1
Introduction

The exploitation of natural gas in the Groningen region has become an integral part of the Dutch economy for years. However, the extraction of natural gas also introduces some risks with it. The extraction operation in the region for many years has caused stresses to build up in the ground leading to induced seismicity in the region. This induced seismicity causes damage to the structures in the surrounding area, which leads to economic losses and brings unacceptable risks to human lives.

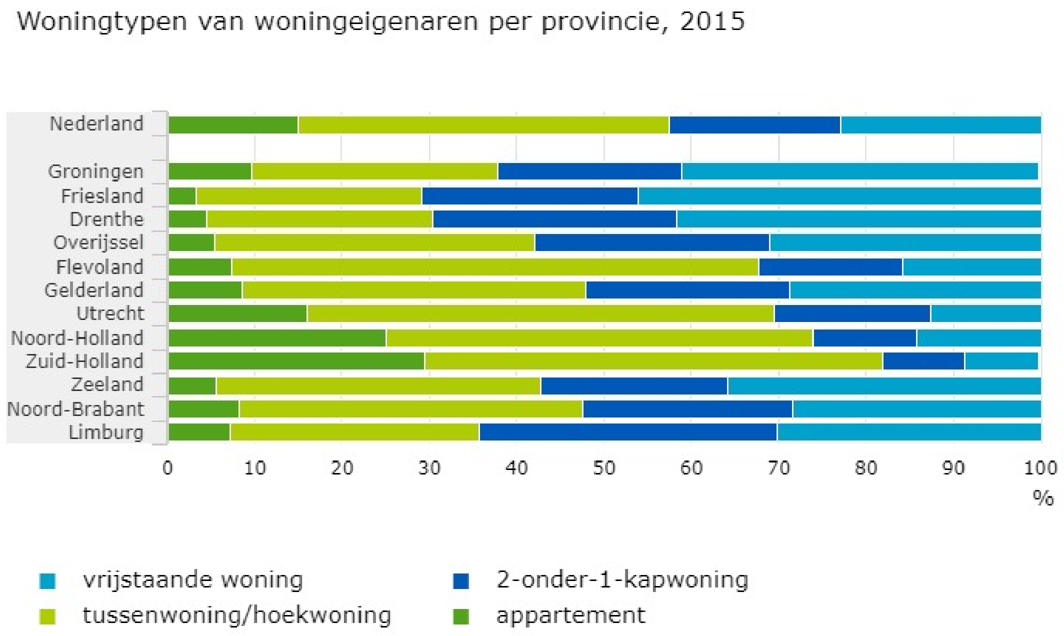

Figure 1.1 Types of residential buildings in Netherlands and the 12 provinces as of year 2015 showing statistics for the housing categories; (1) free-standing (*vrijstaande woning*); (2) semi-detached (*2-onder-1-kapwoning*); (3) terraced houses (*tussenwoning/hoekwoning*); (4) apartment (*appartement*) (CBS 2016)

Residential buildings are among the structures affected by the earthquake in the region. One type of residential buildings that are commonly found in Groningen is the terraced houses. A report on the state of the accommodation situation in the Netherlands by the Dutch bureau of statistics, CBS (*Centraal Bureau voor de Statistiek*), in 2015 showed that a substantial portion of residential buildings in the province of Groningen is comprised of terraced houses (*tussenwoning/hoekwoning*) (CBS 2016). About 28% of the residential buildings in Groningen belong to this category as shown in Figure 1.1. These terraced houses are typically made from unreinforced masonry (URM) in which calcium-silicate (CS) masonry material is prevalently used. These structures are typically not designed to withstand seismic loadings. Furthermore, other particular characteristics of the structure such as the presence of large daylight openings (commonly found on Dutch houses), slender load-bearing piers and limited connections between walls and floors further weaken the structure resistance to seismic loading (Esposito et al. 2018). This causes substantial damages to the buildings in the form of cracking as shown in Figure 1.2.

Figure 1.2 Damages on a masonry building (RTV Noord 2019)

This has led to a number of numerical and experimental studies on the behavior of URM structure subjected to lateral seismic loads. At TU Delft, a full-scale URM two-story building physical specimen made from CS element, simulating a housing unit in a row of terraced houses, had been tested through the application of cyclic pushover loading. CS element was chosen as the building material to represent residential buildings built after 1980 (Esposito et al. 2018).

Apart from experimental studies, numerical studies have also been carried out on CS element structure. A numerical study of the structure has been carried out using a continuum macro-modeling approach (Pari et al. 2017). The results of the analysis initially showed an overestimation of the structural capacity, which was resolved by calibrating the material parameters. The crack pattern of the structure was, however, not modeled accurately, since the discontinuities between the masonry units were not modeled.

A blind prediction contest involving nine consultants was also held in 2017 (Messali et al. 2018). The contest was held as a means to improve the understanding of the structural behavior of the structure by cross-validating the models and validating them against lab results. The participating consultants use various assessment methods, including continuum element macro-models, block-based micro-models, equivalent frame method and analytical approach. The results have varying degrees of success in predicting the failure modes and the structural capacity (Messali and Pari 2017).

1.1 Objective and Scope

Given the uncertainty involved in the structural modeling of CS element masonry structures, this thesis project will be aimed toward investigating the behavior of numerical models with different modeling approaches in relation to the experimental results.

Therefore, the purpose of this thesis project is to answer the following research question:

“To what extent does the use of different modeling approaches and/or different constitutive models affect the results of the numerical analyses on a CS Element masonry structure when compared to the experimental results?”

The main objective of this research is to assess how different modeling methods affect the results of the structural analysis. Factors influencing the results will be investigated, including the use of different modeling approaches (e.g. continuum- or block-based-models) and different constitutive models (e.g. Engineering Masonry Model or Total Strain Based Rotating Crack). The results of this assessment will then be used to form a conclusion on the viability of each modeling approach to modeling the physical specimen and provide recommendations on possible improvements for each numerical model.

A number of numerical model variations are constructed and analyzed using nonlinear static pushover analysis. These nonlinear pushover analyses are performed using the structural analysis software package DIANA 10.3. Each model variation is subjected to monotonic lateral loading. The results of the analysis of each model variation in terms of capacity curves, cracking pattern and failure mechanisms are then analyzed and compared with the other methods and the experimental results.

The scope of this research will be limited to the use of monotonic nonlinear pushover analysis. The choice of constitutive models and finite elements to be used is limited to the ones available in the structural analysis software package DIANA 10.3.

1.2 Synopsis

This research thesis is started with a literature review presented in Chapter 2. This chapter provides background information on the properties of masonry materials, the structural behavior of masonry structures and the numerical modeling methods.

The details of the finite element models used in this thesis are discussed in Chapter 3. These include the model geometry, the types of finite elements used and the constitutive models used in the models.

Chapter 4 discusses the analysis of the masonry structure by analytical method. The result of the analytical method is then used for comparison with the numerical analysis result.

The numerical analyses of the finite element models are discussed in Chapter 5, Chapter 6 and Chapter 7. Chapter 5 is dedicated to the discussion on the numerical analysis and the comparison of macro-models without any interface element. The effects of the interface elements on the macro-models are discussed in Chapter 6. Apart from the macro-models, the viability of the micro-models as alternative modeling approaches to modeling the masonry structures is also analyzed in this thesis. The discussion of the numerical analysis results of the micro-models is presented in Chapter 7.

Based on the results and analyses of the prior chapters, conclusions are then derived and recommendations for future research are outlined in Chapter 8.

Chapter 2
Literature Review

In this chapter, the background information on masonry structure and its analysis will be discussed. Section 2.1 will discuss the behavior of masonry as a material, while the structural behavior of masonry structures will be discussed in section 2.2. The available numerical modeling approaches will be discussed in section 2.3. Constitutive models and finite element types used in the analyses of the numerical models in later chapters are discussed in section 2.4 and section 2.5 respectively. Section 2.6 will provide a brief description of the procedure of the quasi-static pushover analysis.

2.1 Masonry Material

2.1.1 Properties of Masonry Unit and Mortar

The constituents of masonry are masonry units and mortar that joins the masonry units together. The material properties of the masonry unit and mortar influence the strength properties of the masonry structure. Therefore, the strength of the masonry unit and mortar in the material level is of interest to the analysis and design of masonry structures.

Compressive strength has been used as the main strength parameter for the masonry unit since it is relatively simple to perform a compressive test on a masonry unit specimen. Eurocode 6 uses compressive strength as the strength parameter used in the design masonry structures. Unfortunately, determining the true value of the compressive strength is not a simple task. The standard compression test of a masonry unit specimen using solid platens does not yield the true value of the compressive strength due to the restraining effect from the platens (Lourenço 1996). Eurocode 6 mitigates that problem by using the normalized compressive strength f_b, which is the compressive strength from the test multiplied by shape/size factor . The normalized compressive strength f_b refers to the strength of a masonry unit specimen with a size of 100x100x100 mm^3. Another parameter related to the masonry unit is the compression fracture energy G_c. This parameter is not easy to determine, as it requires the examination of the post-peak behavior of the masonry unit

The tensile strength of a masonry unit is difficult to be determined. Finding the correlation between the tensile strength and the compressive strength is difficult due to the difference in shapes, materials, manufacturing process and the volume of perforations. Extensive testing performed on clay, calcium-silicate and concrete units in the longitudinal direction resulted in the tensile strength to compressive strength ratio between 0.03 to 0.10 (Schubert 1988). For the tensile fracture energy G_{ft}^{I}, values ranging from 0.06 to 0.13 N/mm are found for tensile strength of 1.5 to 3.5 N/mm^2 (van der Pluijm 1992).

Similar to the masonry unit, compressive strength is also used to characterize the strength of mortar. The compressive strength of mortar f_{m0} is obtained from the compressive test of the two halves of a mortar specimen sized 40x40x160 mm^3 after the flexural test has been conducted (Lourenço 1996). This test does not, however, account for water absorption of the masonry units and thus is not representative of the mortar condition inside the masonry assemblage.

2.1.2 Properties of Masonry Unit-Mortar Joint Interface

The bond between masonry unit and mortar joint is in many cases the weakest link in a masonry structure. Therefore, it is of interest to ascertain the behavior of this masonry unit-mortar joint bond. This bond behaves nonlinearly and exhibits softening behavior due to cracking. There are two failure modes in the unit-mortar interface; the mode-I tensile failure and the mode-II shear failure.

Mode-I Tensile Failure

The mode-I failure mode corresponds to the tensile failure of the unit-mortar interface. The unit-mortar interface behaves as a quasi-brittle material that undergoes softening after cracks in the interface open up.

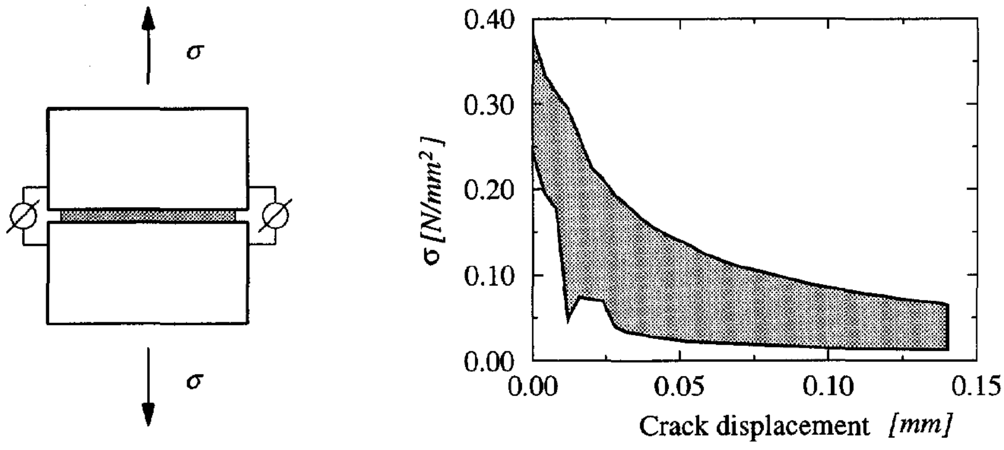

(a) (b)

Figure 2.1 The tensile behavior of the unit-mortar interface from a test (a) the test set up and (b) the resulting stress-displacement diagram (van der Pluijm 1992)

Figure 2.1 shows the deformation tests conducted on small masonry specimens (van der Pluijm 1992). These tests result in exponential tensile softening curves as shown in the figure. This softening behavior is governed by the tensile fracture energy G_{ft}^{I}, which is defined as the amount of energy needed to create a unitary area crack in the unit-mortar interface (Lourenço 1996). In the stress-displacement diagram, G_{ft}^{I} is the area below the tension softening curve.

Mode-II Shear Failure

Apart from the tensile failure, the unit-masonry interface can also undergo shear failure. The shear behavior of the unit-masonry interface was investigated by (van der Pluijm 1993) by conducting a deformation test on several different masonry specimens. Figure 2.2 shows the test set up used in the experiment. The testing apparatus applied a uniform confining pressure on the unit-mortar interface before applying shear forces on the specimen.

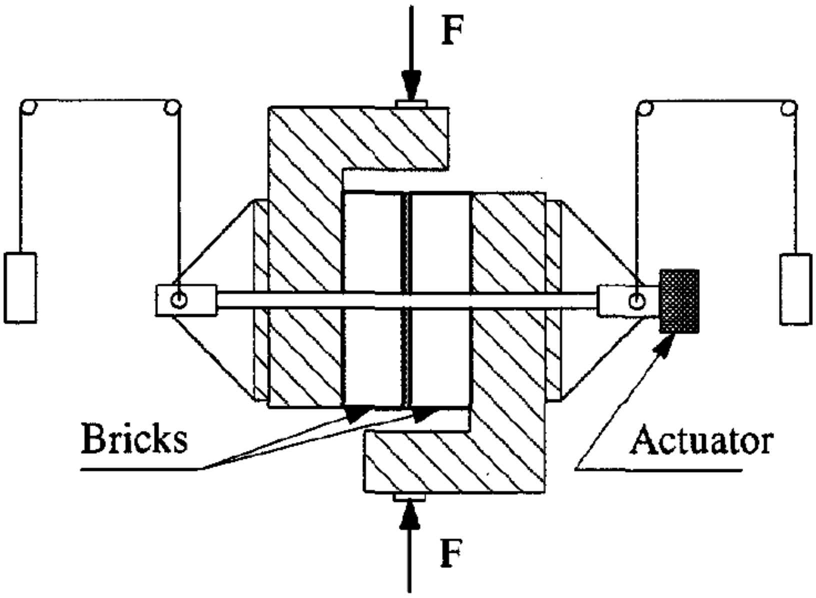

Figure 2.2 The test set up of shear deformation tests on the joints between two masonry units (van der Pluijm 1993)

The test resulted in exponential shear softening diagrams with residual dry friction as can be seen from Figure 2.3. From the same figure, it can also be observed that the confining pressures applied to the interface also influence the shear behavior. The shear behavior is influenced by the shear fracture energy G_{ft}^{II}, which is defined by the area underneath the stress-displacement diagram and the residual dry shear friction. Figure 2.3 shows the value of G_{ft}^{II} increasing with the increasing confining stress.

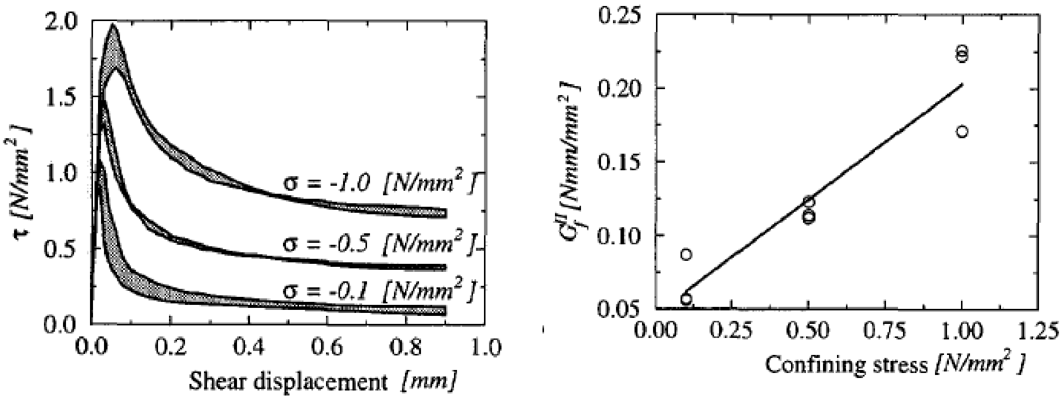

(a) (b)

Figure 2.3 The resulting shear behavior of the unit-masonry interface from tests conducted on joints between solid clay units showing; (a) the resulting shear stress-displacement curves and (b) the relationship between G_{ft}^{II} and confining stress (van der Pluijm 1993)

2.1.3 The Behavior of Masonry Assemblage

Uniaxial Compression

The compressive strength of masonry normal to the bed joints was traditionally regarded as the single relevant structural parameter of masonry. The actual uniaxial compressive strength of masonry can be assessed by performing the RILEM test (Lourenço 1996). The RILEM test is done by loading a masonry specimen of a certain dimension in the direction normal to the bed joints. The RILEM specimen is, however, large and expensive to execute. Therefore, the simpler stacked bond prism specimen is commonly used for obtaining the compressive strength.

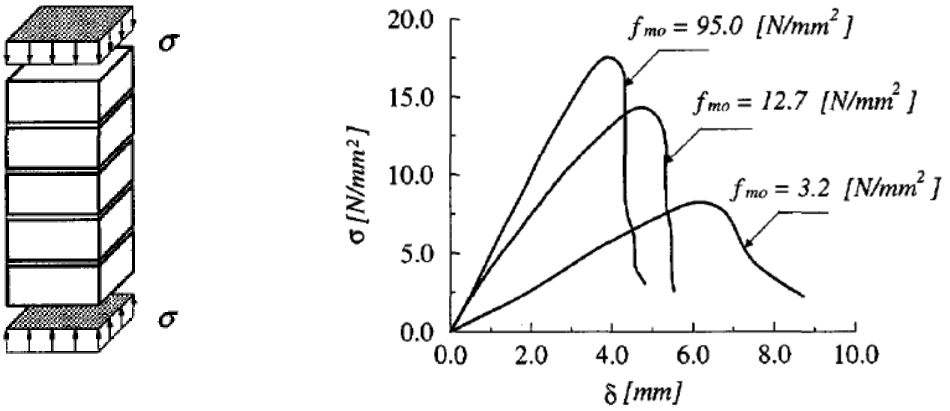

Figure 2.4 The stacked bond prism specimen and the typical stress-displacement diagrams obtained from the experiment on 500x250x600 mm^3 prisms of soft mud brick. The variable f_{m0} is the compressive strength of the mortar (Binda, Fontana, and Frigerio 1988)

Uniaxial compression of masonry causes the mortar to undergo triaxial compression and the masonry units to undergo compression accompanied by biaxial tension (Lourenço 1996). Vertical cracks appear from the loading procedure in the masonry units along the middle line of the specimen. As the load increases, additional cracks start appearing on other parts of the specimen. Vertical cracks appear at the small side of the specimen and the specimen fails from splitting.

Due to the anisotropic nature of masonry, the uniaxial compression in the direction parallel to the bed joints is noticeably different from that in the normal direction of the bed joints. In the case of high or unfavorable perforations in the masonry units, the masonry units can exhibit low longitudinal compressive strength. In this case, compressive loads parallel to the bed joints can govern the load-bearing capacity (Lourenço 1996). A study on masonry samples made from clay units, calcium-silicate units, lightweight concrete units and aerated concrete unit showed the ratio of uniaxial compressive strength in the direction parallel and normal to the bed joints ranging from 0.2 to 0.8 (Schubert and Hoffmann 1994).

Uniaxial Tension

In the case of the uniaxial tension in the direction perpendicular to the bed joints, failure is caused by the low tensile bond strength between the mortar joints and the units. The tensile strength of the masonry can be approximated with the tensile bond strength between the mortar joints and the units.

Failure due to the stresses exceeding the masonry unit tensile strength can also occur if the masonry units have low strength and the tensile bond strength between the mortar joints and the masonry units is greater (Lourenço 1996). In this case, the masonry tensile strength can be approximated with the tensile strength of the unit.

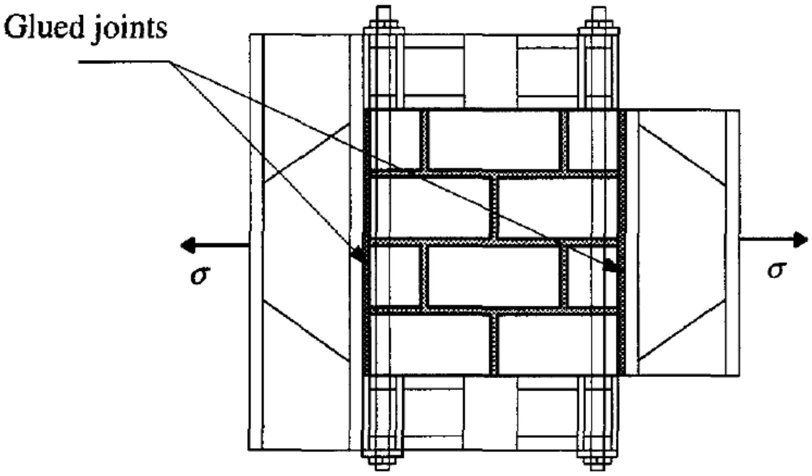

Figure 2.5 Test set-up for tensile strength parallel to the bed joints (Backes 1985)

A complete test program to study the tensile behavior of masonry in the direction parallel to the bed joints (Backes 1985). The test was performed on a specimen consisting of four courses. Lateral loads are then applied to the specimen in the direction parallel to the bed joints through steel plates glued to the specimen as shown in Figure 2.5.

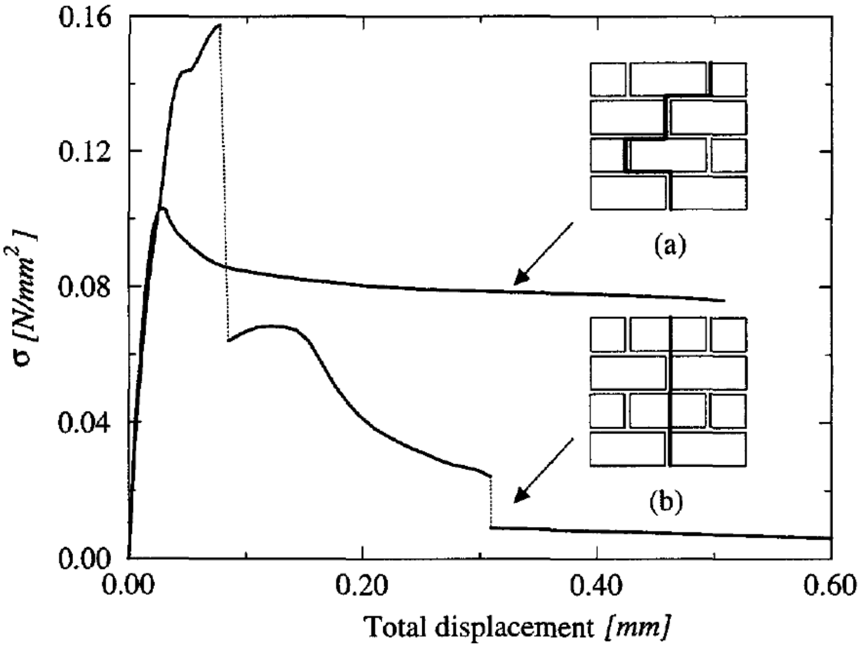

Figure 2.6 Typical stress-displacement obtained from the test on the masonry tension strength parallel to the bed joints showing two failure modes for the specimen: (a) a stepped crack through head and bed joints; (b) failure through head joints and units (Backes 1985)

The experimental results showed two possible failure modes, which depend on the relative strength of the mortar joints and the units (Lourenço 1996). The first failure mode is the stepped crack through head and bed joints. In this type of failure, the post-peak behavior of the masonry specimen shows residual plateau with increasing deformation. This type of failure is governed by fracture energy of the head joints and the mode-II post-peak behavior of the bed joints. Another failure mode is the failure caused by vertical cracks that run through the head joints and the masonry units. The stress-displacement of this failure type shows abrupt drops in stresses and progressive softening until zero in the post-peak region. This failure mode is governed by the fracture energy of the head joints and the units.

Biaxial Behavior

The behavior of masonry in the biaxial states of stresses cannot be completely described based on the behavior under uniaxial loading (Lourenço 1996). Investigation on the influence of the biaxial stress states on masonry has been conducted, resulting in a biaxial strength envelope. Due to the anisotropic nature of masonry, the biaxial strength envelope cannot be described only with principal stresses. The biaxial strength envelope must, thus, either be described in terms of full stress vector with fixed material axes or in terms of principal stresses and the rotation angle θ between the principal stresses and the material axes. The different failure modes for masonry under the biaxial stress states are presented as follows.

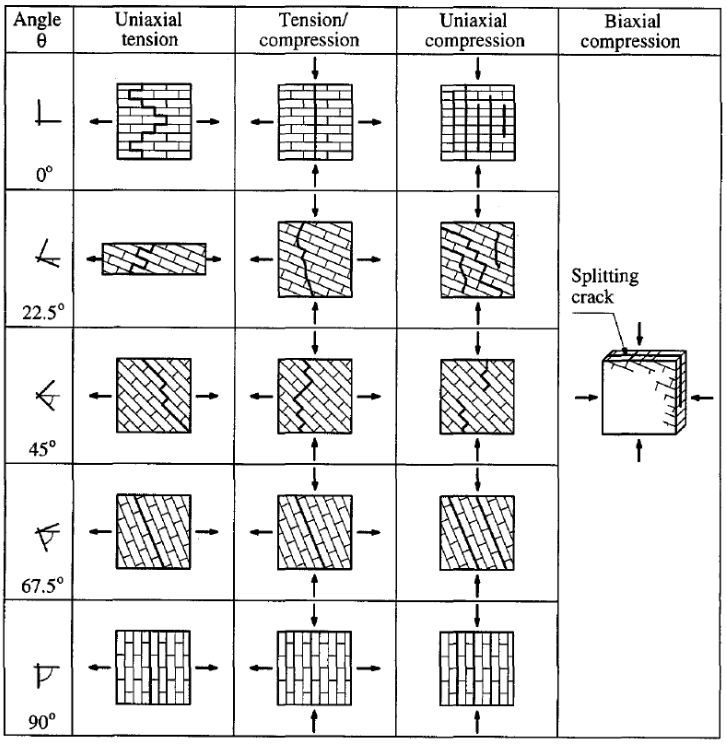

Figure 2.7 Failure modes of solid clay masonry units under biaxial loading (Dhanasekar and Page 1985)

2.2 Structural Behavior of Masonry Elements

The structural behavior of masonry structures can be divided into in-plane and out-of-plane behavior.

2.2.1 In-plane Behavior

Under the axial and lateral loads, the failure modes of the masonry in the in-plane direction can be attributed to the flexural and shear behaviors (Calderini, Cattari, and Lagomarsino 2009).

The failure mechanism of the flexural behavior depends on the axial loads (Calderini, Cattari, and Lagomarsino 2009). When subjected to low axial loads, lateral forces on the structure produce tensile flexural cracks at the corners. As these cracks grow, the masonry piers start to undergo rigid body motion in the form of rocking around the toe. In the case of high axial loads, the formation of flexural cracks will be reduced and there will be a widespread damage pattern on the piers with the cracks concentrated on the more compressed side. The ultimate limit state is reached when the corner of the piers fails due to crushing.

Other failure modes are governed by shear behavior. Masonry piers can fail from two shear failure modes, *sliding* and *diagonal shear cracking* (Magenes and Calvi 1997). Sliding failure occurs when the piers slide along the bed joints due to the reduction of the resisting components from the formation of tensile horizontal cracks in the bed joints (Calderini, Cattari, and Lagomarsino 2009). This failure mode could occur when the axial loads and/or the friction coefficient are relatively low. Diagonal shear cracking failure occurs when diagonal cracks are formed on the piers. These cracks are usually formed from the center of the piers and propagate towards the corner. Depending on the strength of the mortar joints, brick-mortar interfaces and masonry units, the cracks can assume the typical staircase shape by going through the bed- and head-joints or go through the units.

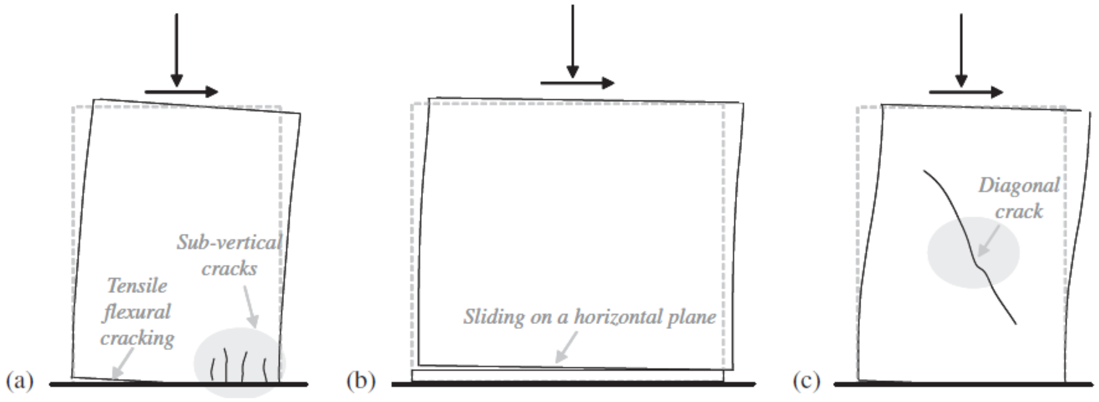

Figure 2.8 Typical failure modes on the masonry piers subjected to in-plane loadings (a) flexural failure, (b) sliding shear failure and (c) diagonal shear cracking (Calderini, Cattari, and Lagomarsino 2009)

The type of failure modes that occur in the masonry piers depends on several parameters such as the geometry of the structure, the boundary conditions, the axial loads, the mechanical properties of the masonry components and the geometrical characteristics of the masonry (Calderini, Cattari, and Lagomarsino 2009). In reality, several failure modes may occur simultaneously and interact with each other making it difficult to discern a specific mechanism.

2.2.2 Out-of-plane Behavior

The out-of-plane behavior of masonry piers is related to the flexural behavior of the masonry assemblage. A study on the post-earthquake damages of masonry buildings in Christchurch, New Zealand, indicates at least three out-of-plane failure modes: (a) overturning mechanism; (b) one-way bending failure; (c) two-way bending failure (Giaretton et al. 2016). The type of failure modes occurring on a structure is influenced heavily by the effectiveness of the wall-floor and/or wall-transversal walls connections.

Damages to the structural elements connected to the wall in question could also alter the boundary conditions changing the type of failure modes (Abrams et al. 2017).

Overturning mechanism occurs when the masonry walls behave like a cantilever beam. This mechanism mainly occurs in structures with poor top boundary conditions and limited connections effectivity with orthogonal structural components (Giaretton et al. 2016). Two classes of overturning mechanism are proposed in a study: (a) overturning collapse of the walls due to vertical cracks at the connections to the transversal walls; (b) overturning collapse due to diagonal cracks on the connected transversal walls (de Felice and Giannini 2001). Observations of the recurring post-earthquake damage patterns on masonry structures indicate consistency with the proposed mechanisms.

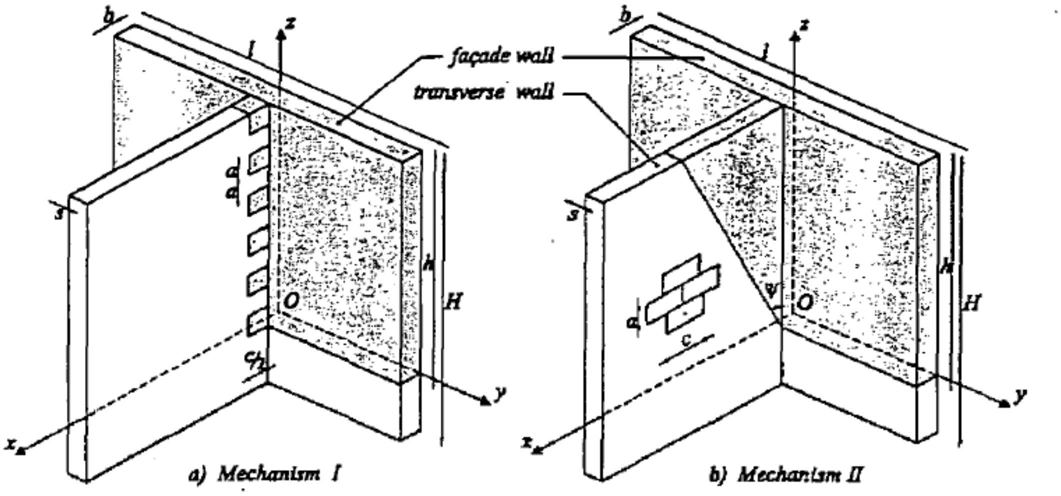

Figure 2.9 Out-of-plane overturning mechanism: (a) wall detachment from transversal walls due to vertical cracks on the connection; (b) wall detachment due to diagonal cracks on the transversal walls (de Felice and Giannini 2001)

One-way bending failure occurs when the side supports have limited flexural and shear resistance (Abrams et al. 2017). This type of failure can occur provided that the floor-wall connections are adequate and the floor diaphragms are relatively rigid to walls. The failure is typically indicated by horizontal cracks on the wall extremities (top and bottom) and at the mid-height of the wall (Giaretton et al. 2016). A portion of the wall located between two openings, where there is often no boundary restraint, can exhibit this behavior.

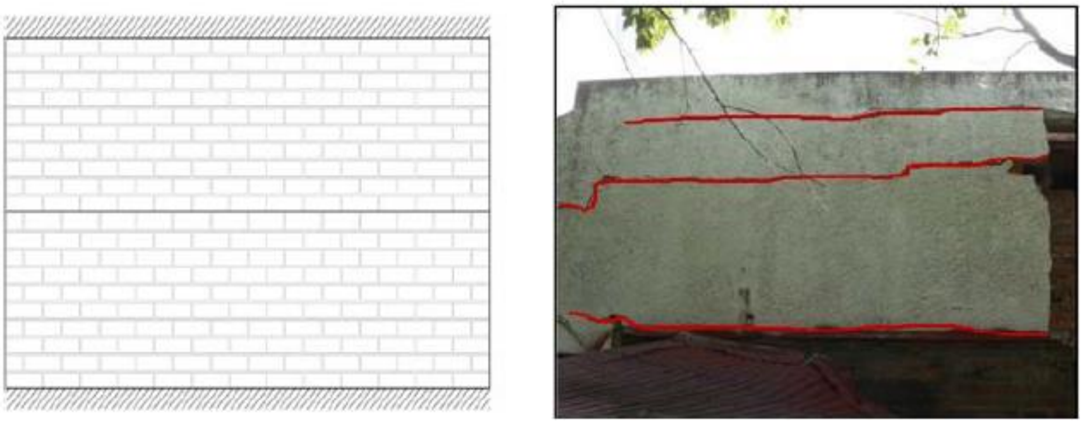

(a) (b)

Figure 2.10 One-way bending failure mechanism showing: (a) the failure schematic and (b) a one-way bending failure on a brick wall (Giaretton et al. 2016).

Two-way bending failure occurs especially on walls that span both vertically and horizontally (Abrams et al. 2017). The failure mode follows the failure-line mechanism which is similar to the yield-line mechanism of a two-way concrete slab. Considering that a URM wall does not have any reinforcement, there is no ductile element that yields to contribute to the mechanism. However, the vertical axial compression on the wall can help develop flexural strength after cracking and forms the failure-lines. Axial compression has also been shown to have positive effects on the flexural strength of the wall (Griffith and Vaculik 2007). Depending on the span length, the cracking patterns can be U-shaped or V-shaped (Giaretton et al. 2016).

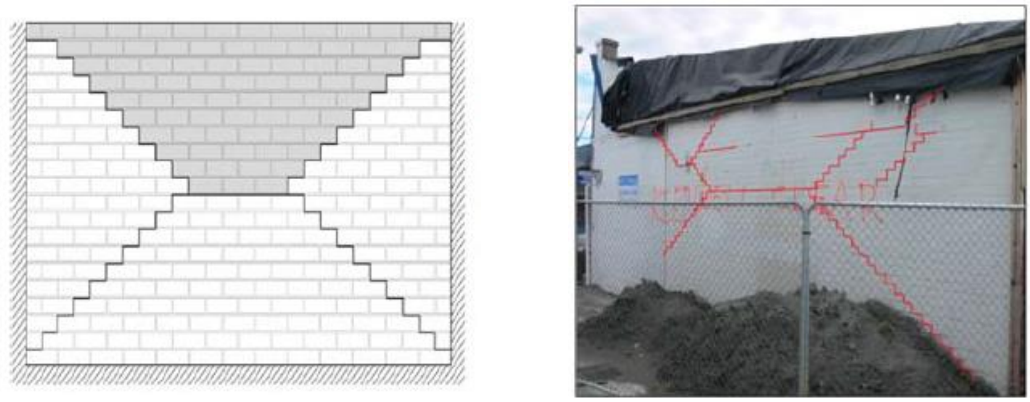

(a) (b)

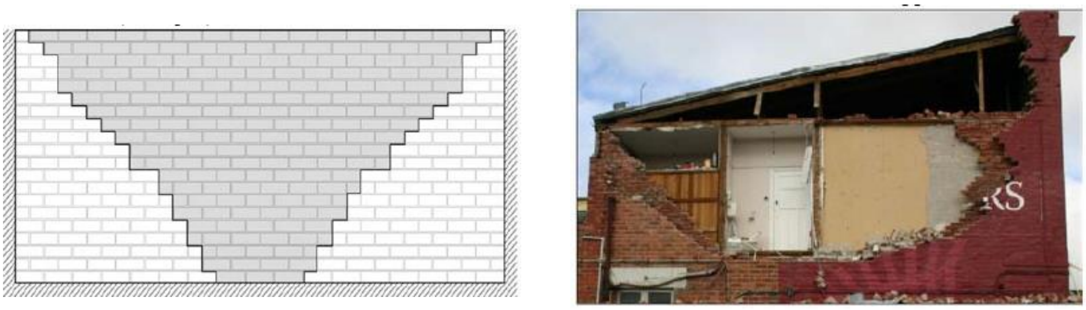

(c) (d)

Figure 2.11 Two-way bending failure mechanisms: (a) U-shaped failure pattern; (b) U-shaped cracking patterns on a façade wall; (c) V-shaped failure pattern; (d) V-shaped collapse of a cavity wall (Giaretton et al. 2016).

2.2.3 The Behavior of Wall-Pier Connection

Aside from the in-plane and out-of-plane failure of the masonry structural elements, the wall-pier connection can also undergo failure. Experimental research on the behavior of the connection had been performed on masonry specimens by Raijmakers and Van der Pluijm (Rots 1997). The specimens in question are U-shaped masonry structures consisting of a transversal wall and two piers. The specimens are constructed differently from each other with a variety of unit sizes and connection types. A preloading compressive force was applied on top of the transversal wall and a horizontal force was then applied to the structure. The test set-up for experimental research is illustrated below.

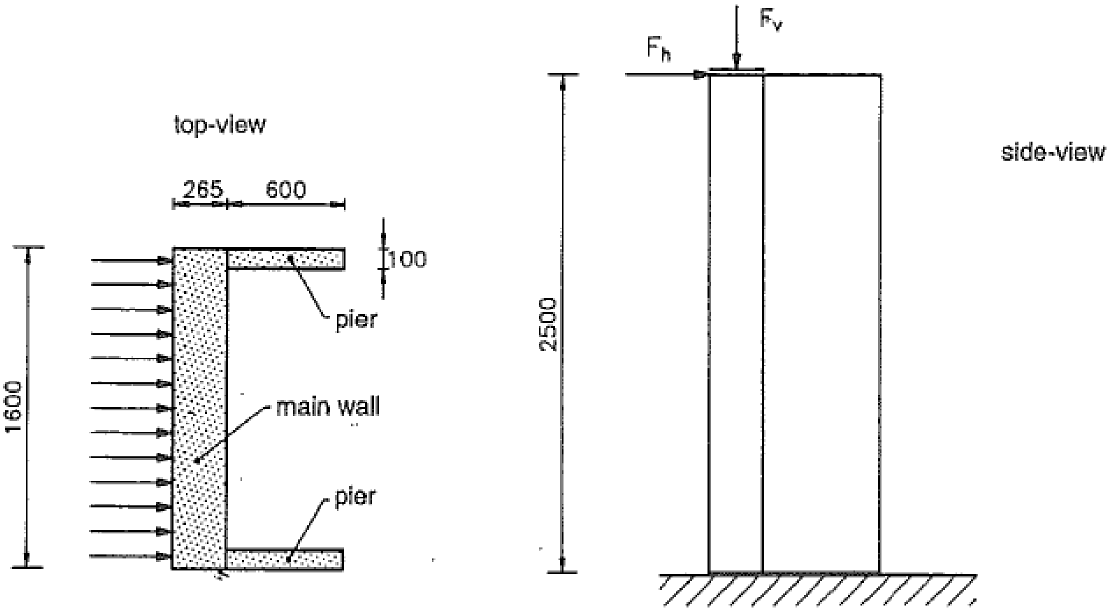

Figure 2.12 Test set-up of the experimental research on wall-pier connection by Raijmakers and Van der Pluijm (Rots 1997)

From the experimental test, three failure modes can be identified:

a) Tilting of the whole construction around the toe of the pier.

b) Failure of the pier due to compression with splitting cracks in the compression diagonal.

c) Failure of the connection joint.

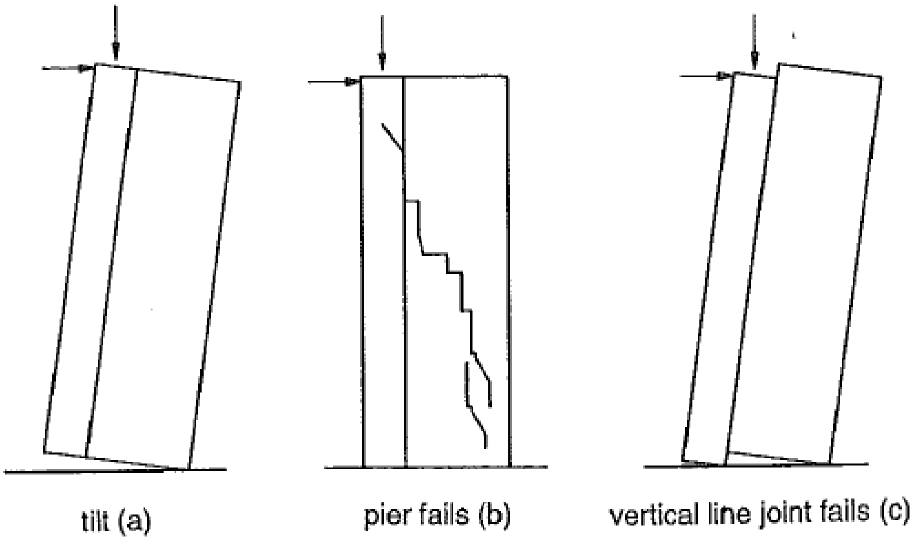

Figure 2.13 Failure modes of masonry wall-pier connections; (a) tilting of the entire structure; (b) failure of the piers; (c) failure of the vertical line joint (Rots 1997)

The type of failure modes that occurs on the connections depends on the top load and the strength of the connections (Rots et al. 1997). Mechanism(a) can occur when the top load is relatively low or the vertical connections are very strong. The structure tilts as a whole without suffering from any damage and undergoes tilting equilibrium. In another case, cracks start to appear along the diagonal compression strut resulting in Mechanism(b). This can occur with toothed connections. The last failure mechanism, Mechanism(c), occurs when the vertical connection fails due to shearing, which leads to a sudden reduction of structural capacity.

2.3 Numerical Modeling Strategies

Numerical modeling of the masonry structures can be approached using several different modeling strategies. This section will give a brief description of the two modeling strategies that are of interest to this thesis project. For a more comprehensive discussion on various modeling strategies, including the ones not mentioned in this section, the readers are referred to the paper by (D’Altri et al. 2019).

2.3.1 Block-based Models

Block-based models model the masonry structure as an assemblage of blocks that are joined together by mortar joints (D'Altri et al. 2019). This approach takes into account the heterogeneity of the masonry materials and the actual masonry textures that govern the anisotropy and the failure mechanisms of the material.

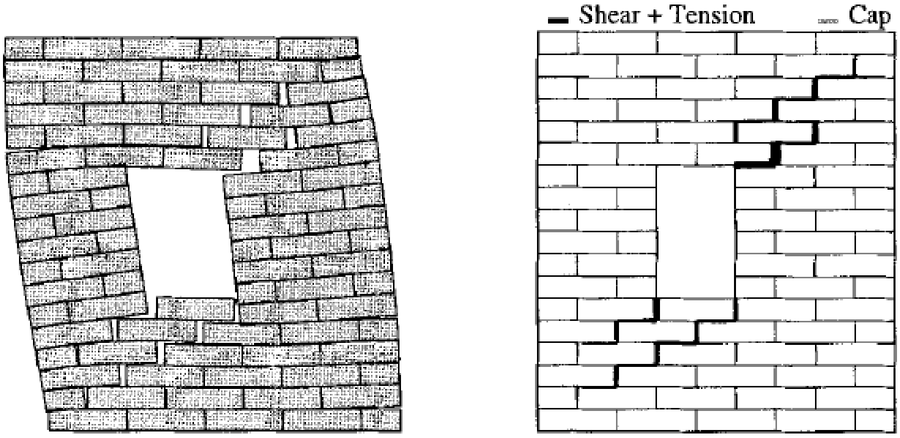

Figure 2.14 Example of the application of block-based models (Lourenço and Rots 1997)

Block-based models can further be categorized into the following sub-categories:

1) Interface element-based approaches
2) Contact-based approaches
3) Textured continuum-based approaches
4) Block-based limit analysis approaches
5) Extended finite element analysis approaches

One particular approach to block-based models that is of interest for this thesis project is the interface element-based approaches. These approaches use the interface elements to model the discontinuities present in the structural elements. In a thesis on the subject of computational modeling of the masonry structure (Lourenço 1996), two kinds of block-based models, which utilize this approach, are discussed. The first model is called the detailed micro modeling, in which both the masonry units and the mortar joints are modeled as continuum elements, while the bonds between the masonry units and the mortar joints are modeled as interface elements. The second model is called the simplified micro modeling, where the masonry units are modeled as expanded continuum elements and the mortar joints are modeled as interface elements.

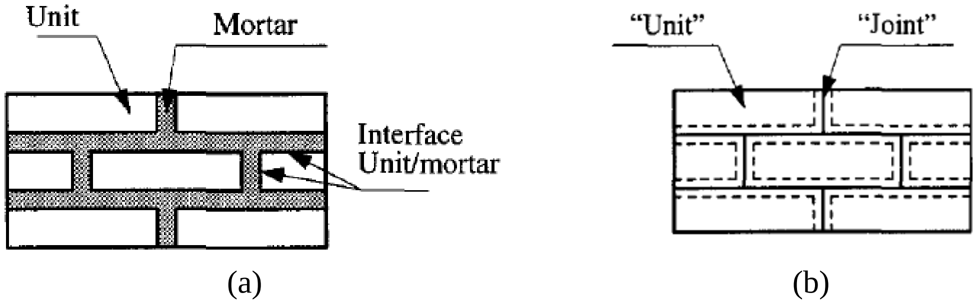

(a) (b)

Figure 2.15 Two approaches in modeling interface element block-based model; (a) Detailed micro-modeling; (b) Simplified micro-modeling (Lourenço 1996)

Block-based models have several advantages. They can represent the masonry bonds and many structural details. The models are also able to present clear representations of failure mechanisms that do not require demanding interpretations. In the case of the models built using 3-D solid or 2-D shell elements, the in-plane and out-of-plane structural responses of masonry walls can be accounted for.

While there are a lot of merits in using the block-based models, the usage of these models also has its disadvantages. The main issue with the block-based models is the large computational demand the analysis requires (D'Altri et al. 2019). This problem causes its usage to often be limited to the modeling of panel-sized structural elements. The process of assembling the model is also time-consuming and complex, which limits the model application to academic studies and a few high-level consultant groups.

2.3.2 Continuum Models

In the case of continuum models, the masonry material is modeled as a continuum deformable body (D'Altri et al. 2019). The masonry material is modeled as homogeneous material and any distinction between the masonry units and the mortar joints is neglected. Given the heterogeneous nature of masonry, however, defining a suitable homogeneous constitutive law for the material is proving to be a difficult task. This can be achieved through various approaches as follows:

1) *Direct approaches*. With these approaches, the constitutive models of the material that can approximate the mechanical responses of the masonry material are used. The material parameters used can be calibrated using experimental data or data from other sources to better approximate the structural responses.

2) *Homogenization procedures and multi-scale approaches.* In these approaches, the constitutive model of the material is derived using homogenization processes that relate the material-scale model to the structural-scale model. The homogenization processes are typically based on RVEs (Representative Volume Element). RVE represents the material-scale heterogeneity of the masonry material and the definition of a proper RVE is of importance to the homogenization process.

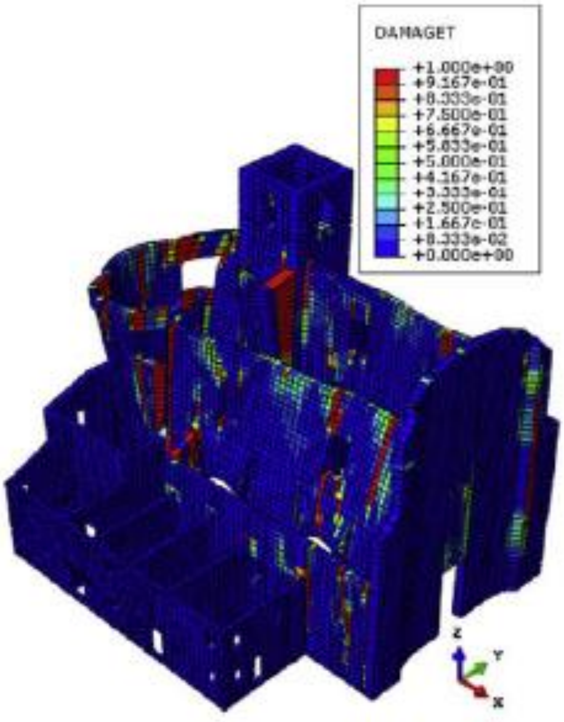

Figure 2.16 Example of continuum model applied to historic building (D’Altri et al. 2019)

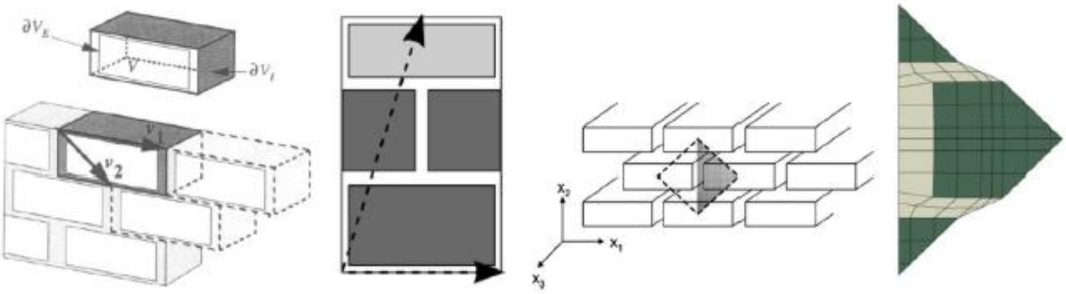

Figure 2.17 Some example of RVEs that have been used for homogenization processes (D’Altri et al. 2019)

Continuum models have advantages over block-based models in that the mesh size can be larger since the mesh discretization does not need to consider the heterogeneities of the material (D’Altri et al. 2019). Due to this, the computational demand for the analysis of these models is generally lower than the block-based models. This makes these models suitable for the application in the engineering practice.

2.4 Constitutive Models

2.4.1 Cracking Behavior of Continuum Elements

Cracking in continuum elements is modeled by smearing the potential of cracks across the elements. This approach allows cracks to occur anywhere on the elements. DIANA provides several constitutive models for application on the finite elements. For this project, the Total Strain Crack Model and the Engineering Masonry Model will be used.

Total Strain Crack Model

Total Strain Crack Model is one of the constitutive models used for modeling cracks on continuum elements. Total Strain Crack Model offers three different ways of modeling the crack orientation; fixed, rotating and the combined rotating to fixed (DIANA FEA 10.3 User Manual 2019). The difference between the three variants is on the way the stress-strain relations are evaluated. In the case of the fixed crack orientation, the stress-strain relations are evaluated in a fixed coordinate system. For the rotating crack orientation, the stress-strain relations are evaluated in the principal directions of the strain vector. In the case of rotating to fixed behavior, a total strain threshold value that governs the change of the crack behavior from rotating to fixed is applied.

The material parameters inputted for the Total Strain Crack Model are the linear elastic material properties and the parameters for the tensile and compressive behavior of the structure. The linear elastic material properties include Young's modulus of the material and the Poisson ratio. The tensile behavior can be modeled using one of the tensile curves provided in DIANA. The parameters specified for tensile curves are the tensile strength (f_t) and the tensile fracture energy (G_{ft}^{I}). Likewise, the compressive behavior of the structure can be modeled using one of the compressive curves available in DIANA. The parameters for the compressive curves are the compressive strength (f_c) and the compressive fracture energy (G_{fc}). The shear behavior is modeled differently depending on the chosen crack model (DIANA FEA 10.3 User Manual 2019). The shear behavior parameters are specified only for the fixed and the combined rotating-to-fixed crack model. For these models, shear retention functions are specified to reduce the shear stiffness after cracking. For the rotating model, shear behavior does not need to be specified since the cracks are oriented according to the principal directions.

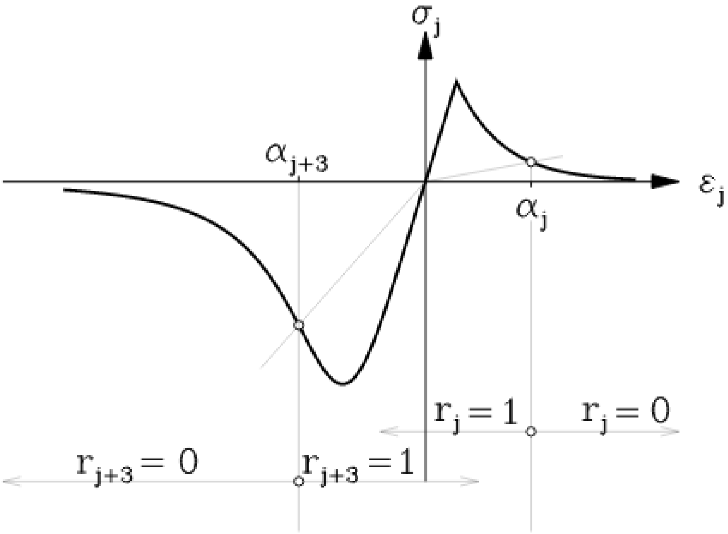

Figure 2.18 The stress-strain diagram of Total Strain Crack Model showing the tensile cracking curve and the compression crushing curve (DIANA FEA 10.3 User Manual 2019)

DIANA offers various types of stress-strain curves to model the tensile and the compressive behavior of the continuum elements. For this particular project, a linear tensile softening curve based on tensile fracture energy and a parabolic curve will be used to model tensile behavior and compressive behavior respectively.

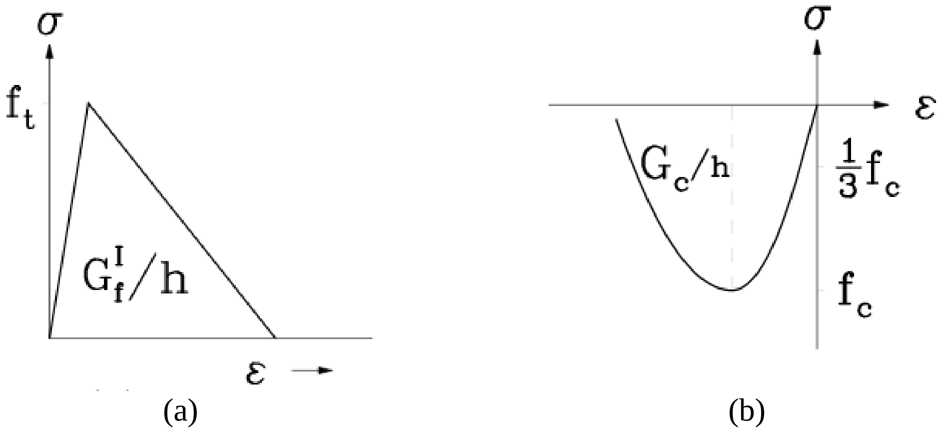

(a) (b)

Figure 2.19 The stress-strain curves used for the structural analysis of the models; (a) Linear fracture energy-based; (b) Parabolic (DIANA FEA 10.3 User Manual 2019)

Engineering Masonry Model

The structural analysis software package DIANA provides a specialized constitutive model for analyzing masonry structures called EMM (Engineering Masonry Model). The constitutive model provides a complete description of the masonry behavior including cracking, crushing and shearing. EMM is also able to take into account the cracking failure in the direction of bed-joint, head-joint and diagonal staircase crack with a predefined cracking angle.

Cracking

The EMM provides the possibility of taking into account cracking in the element x- and y-directions. The stress-strain curve for tensile cracking is defined by a linear increase of stress to the value of tensile strength followed by a softening curve which is assumed to be linear. The definition of the curve is provided by the value of Young's modulus E, tensile strength f_t and tensile fracture energy G_{ft}. The curve is given by the figure below.

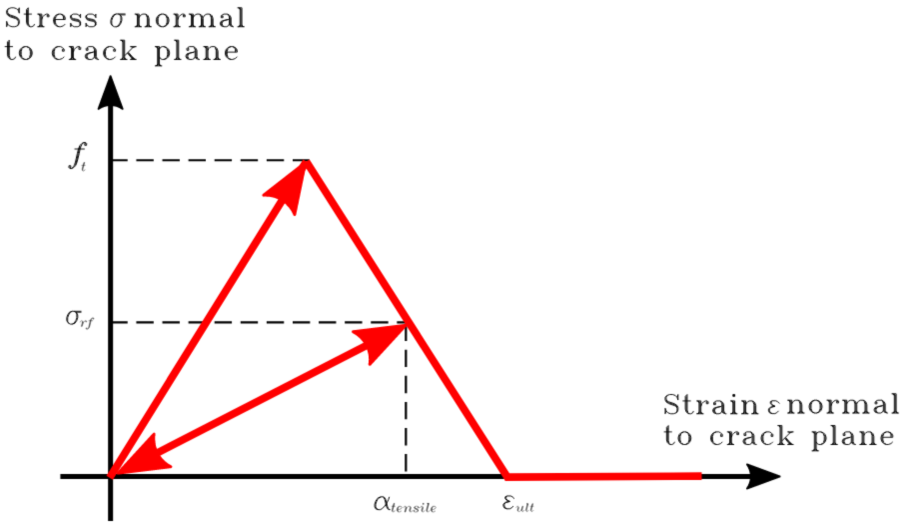

Figure 2.20 The uniaxial tensile cracking behavior of the Engineering Masonry Model (DIANA FEA 10.3 User Manual 2019)

The ultimate tensile strain ε_{ult} is defined as the point in which the crack is fully open and no tensile stress can be transferred. The value of ε_{ult} is defined mathematically as:

$$\varepsilon_{ult} = \frac{2G_{ft}}{hf_t}$$

The variable h is the element crack bandwidth. The unloading and reloading paths are assumed to follow the secant unloading/reloading.

Crushing

The stress-strain curve for compressive loading is defined by Young's modulus E, compressive strength f_c, compressive fracture energy G_c and factor n. Factor n determines the strain ε_{peak} where the peak value of compressive strength is reached. It is defined as

$$n = \frac{E\varepsilon_{peak}}{f_c}$$

The compression curve is defined with the assumption that it comprises of a third-order curve followed by a parabolic curve until the compressive strength f_c and a linear softening curve until residual stress of 0.1 f_c is reached. The ultimate compressive strain ε_{ult} is defined as the strain value reached if the linear softening curve would have reached zero-stress state. The ultimate strain is defined as:

$$\varepsilon_{ult} = \varepsilon_{peak} + \max\left[0, \frac{2G}{hf_c} - \frac{f_c}{A^2 E} - \frac{A+1}{A}\left(\varepsilon_{peak} - \frac{f_c}{E}\right)\right]$$

h is the crack bandwidth of the element and A is defined as:

$$A = \left(\frac{E\varepsilon_{peak}}{f_c}\right)^{\frac{1}{3}}$$

The compression curve is given by the figure below.

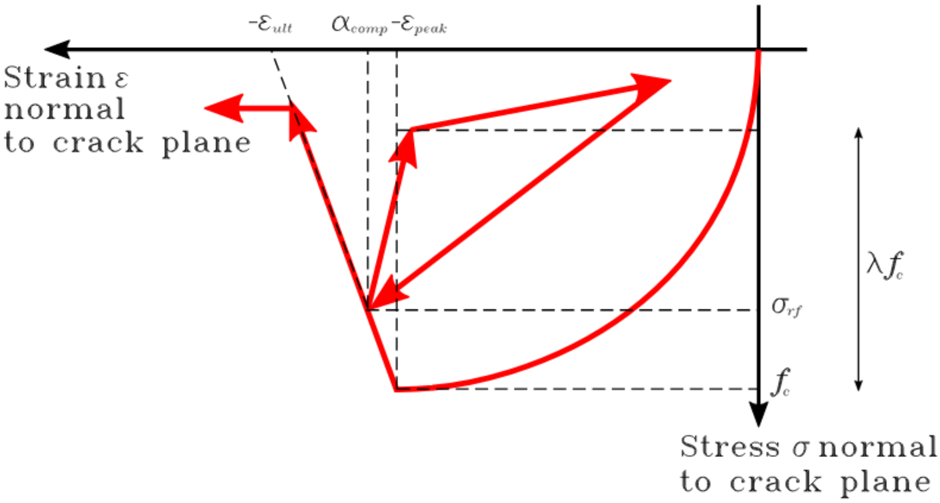

Figure 2.21 The compressive behavior of the Engineering Masonry Model (DIANA FEA 10.3 User Manual 2019)

The stress-strain diagram illustrates the load paths for loading, unloading and reloading scenarios. From the diagram, it can be seen that the unloading path follows the path of initial stiffness until the compressive stress level $\lambda\sigma_{rf,compressive}$ is reached then follows the secant stiffness to the origin. The reloading path follows the secant stiffness to the last extreme point reached. The secant stiffness E_{sec} is defined as:

$$E_{sec} = \frac{\lambda\sigma_{rf}}{\alpha_{comp} - \lambda\frac{\sigma_{rf}}{E}}$$

Shearing

Other than the tensile cracking and crushing behavior, the in-plane shear stress is also included in the constitutive behavior definition of EMM. The limit of shear stress is defined by the maximum stresses called τ_{max}, which is defined according to Coulomb friction as:

$$\tau_{max} = \max\left[0, c - \sigma_{yy} \tan(\varphi)\right]$$

Where c is the cohesion, φ the friction angle and σ_{yy} the vertical axial stresses.

The shear fracture energy G_{fs} determines the total fracture energy released in shear cracking. If defined, the cohesion c then reduces linearly to zero at $\gamma = \gamma_{ult}$. γ_{ult} is defined as:

$$\gamma_{ult} = \frac{2G_{fs}}{h\,.\,c} - \frac{c}{G}$$

Where h is the crack bandwidth of the element and G is the initial shear modulus. The in-plane shear stress-strain diagram as a function of the in-plane shear strain γ is illustrated with the figure below.

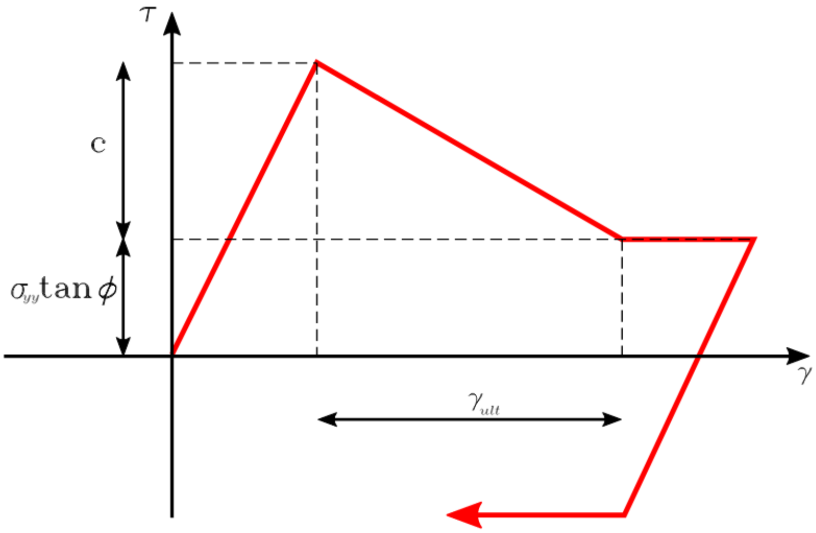

Figure 2.22 The shear behavior of the Engineering Masonry Model (DIANA FEA 10.3 User Manual 2019)

2.4.2 Cracking Behavior of Interface Elements

The cracking behavior of interface elements is modeled as a discontinuity between two elements. Cracks are lumped in the interface elements in the form of relative displacements. On masonry structural elements, cracks usually form in the mortar joints. For this reason, interface elements are usually applied to the location of the mortar joints.

Additional interface elements can also be added in masonry units to simulate cracking inside the units. Several constitutive models are implemented in DIANA to model cracking with interface elements ranging from models that consider only the uniaxial tension stress to models that simulate crushing, tensile cracking and shear.

Discrete Cracking

Discrete cracking is used to model the uniaxial tensile behavior of the connections. The traction-displacement curves involve the initial increase of traction linearly until the ultimate tensile strength is reached, at which point the interface elements open and they undergo softening.

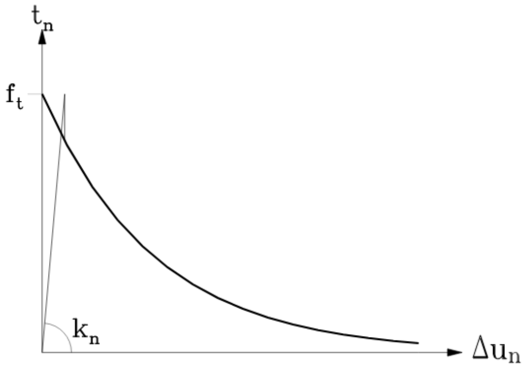

Figure 2.23 The tensile cracking softening curve for the discrete cracking model (DIANA FEA 10.3 User Manual 2019)

The initial linear stiffness of the interface element is chosen as such that the relative displacement of the interface during the linear phase can be considered negligible. For this reason, a very high value of dummy stiffness is usually used.

DIANA provides several softening curves for discrete cracking. For this thesis project, the linear softening curve will be used.

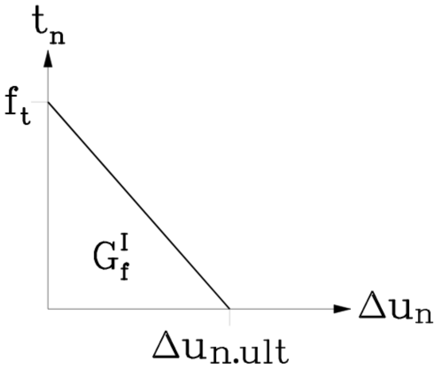

Figure 2.24 Linear softening curve for the discrete cracking model (DIANA FEA 10.3 User Manual 2019)

Coulomb Friction

Coulomb friction is used to model the sliding behavior of the interfaces. In DIANA 10.3, the Coulomb friction criterion is expressed in the following equations:

$$\begin{cases} f = \sqrt{t_t^2} + t_n \tan\phi(\kappa) - \bar{c}(\kappa) = 0 \\ g = \sqrt{t_t^2} + t_n \tan\psi \end{cases}$$

With t_n as stresses in the direction normal to the interface elements, t_t as stresses parallel to the interface elements, ψ as dilatancy angle, $\bar{c}$ as cohesion and $\tan\phi$ as the friction coefficient. Cohesion and friction coefficient are defined as the functions of internal parameter κ.

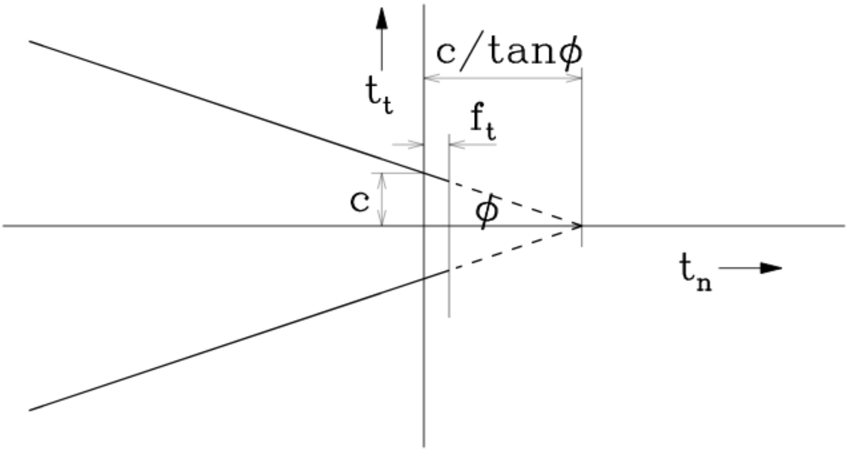

Figure 2.25 Coulomb friction criterion model in DIANA 10.3 with tension cut-off (DIANA FEA 10.3 User Manual 2019)

Combined Cracking-Shearing-Crushing

Another alternative in modeling the material is the Cracking-Shearing-Crushing model that incorporates cracking, shearing and crushing behavior. This material model is based on the interface model developed by Lourenço and Rots (Lourenço and Rots 1997). A detailed explanation of the derivation of the material model can be found in the aforementioned research paper.

The paper by Lourenco and Rots described the 2D plane stress interface model. The model is based on the multi-surface plasticity theory (Lourenço and Rots 1997). In this model, a composite yield surface composed that includes tension, shear and compressive failure with softening bounds the elastic domain.

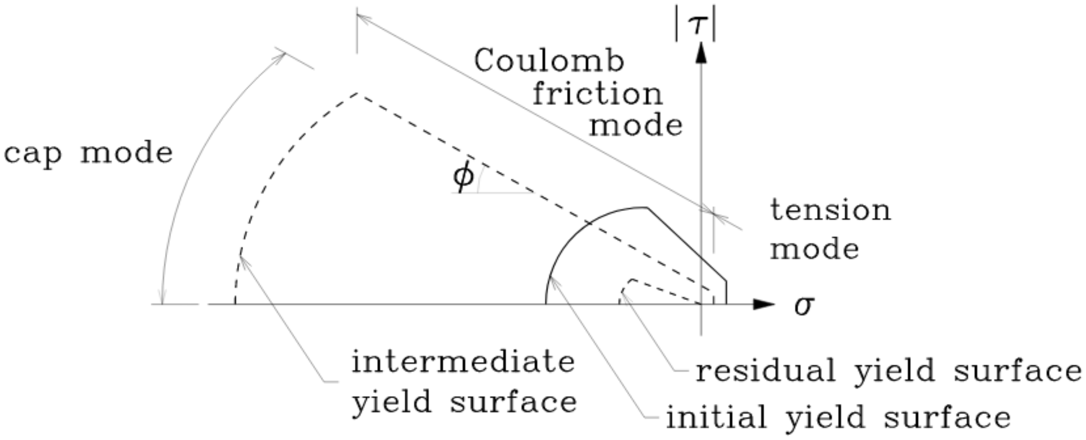

Figure 2.26 The composite yield surface of the interface model (DIANA FEA 10.3 User Manual 2019)

The interface model implemented in DIANA includes three yield functions (referred to as criterion):

1. Criterion 1 (Shear Slipping)
2. Criterion 2 (Tension Cutoff)
3. Criterion 3 (Compression Cap)

The shear slipping behavior is defined by the Coulomb friction yield/crack initiation function. This is defined in the equation below.

$$f = |\tau| + \sigma\,\Phi - c$$

Φ is the friction coefficient that is equal to $\tan\phi$ and c is the adhesion. Both the friction coefficient and adhesion undergo softening behavior. The adhesion is assumed to undergo exponential softening as described in the following equation.

$$c(\sigma,\kappa) = c_0\, e^{-\frac{c_0}{G_f^{II}}\kappa}$$

With c_0 as the initial adhesion and G_f^{II} as the mode-II fracture energy.

The softening behavior of the friction coefficient is coupled with the softening behavior of the adhesion and defined as follows.

$$\Phi(\sigma,\kappa) = \Phi_0 + (\Phi_r - \Phi_0)\frac{c_0 - c}{c_0}$$

With Φ_0 as the initial friction coefficient and Φ_r as the residual friction coefficient.

The yield function for the tension cutoff is defined by the following equation:

$$f_2 = \sigma - \sigma_t$$

σ_t is the bond strength of the masonry unit-mortar joint. The bond strength is assumed to soften exponentially as defined in the following equation.

$$\sigma_t = f_t\, e^{-\frac{f_t}{G_f^I}\kappa_2}$$

The compression cap function is defined by the following equation:

$$f_3 = \sigma^2 + C_s\tau^2 - \sigma_c^2$$

With C_s as the parameter governing the shear stress contribution to failure and σ_c as the compressive strength. As shown in Figure 2.26, the yield surface of the compression cap exhibits both hardening and softening behavior. The yield surface will undergo parabolic hardening and then parabolic/exponential softening that is governed by G_{fc} as shown in the figure below.

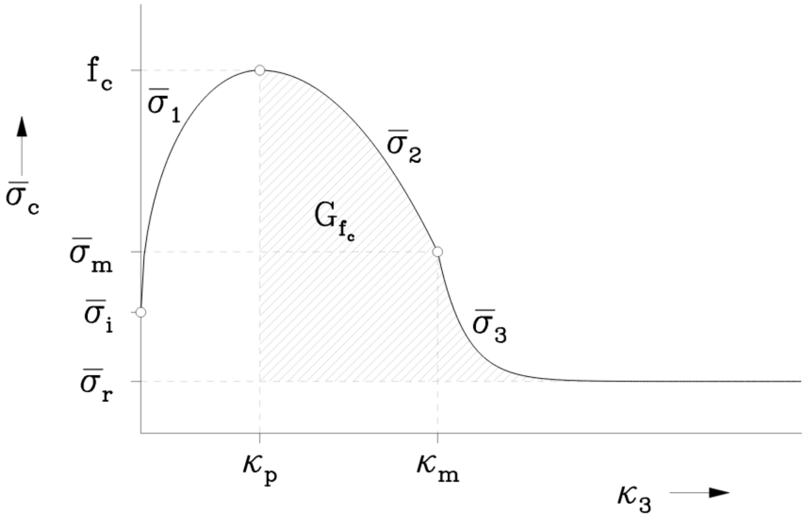

Figure 2.27 The hardening and softening behavior of the compression cap yield surface (DIANA FEA 10.3 User Manual 2019)

The three regions of the curve in Figure 2.27 are governed by the following equations:

$$\overline{\sigma_1} = \overline{\sigma_i} + (f_c - \overline{\sigma_i})\sqrt{\frac{2\kappa_3}{\kappa_p} - \frac{\kappa_3^2}{\kappa_p^2}}$$

$$\overline{\sigma_2} = f_c + (\overline{\sigma_m} - f_c)\left(\frac{\kappa_3 - \kappa_p}{\kappa_m - \kappa_p}\right)^2$$

$$\overline{\sigma_3} = \overline{\sigma_r} + (\overline{\sigma_m} - \overline{\sigma_r}) \exp\left(2\left(\frac{\overline{\sigma_m} - f_c}{\kappa_m - \kappa_p}\right)\left(\frac{\kappa_3 - \kappa_m}{\overline{\sigma_m} - \overline{\sigma_r}}\right)\right)$$

The two-dimensional interface model can be expanded into three-dimension. In this case, shear strain and shear stress in the transversal direction are added and the failure surface turns into the shape of a truncated cone.

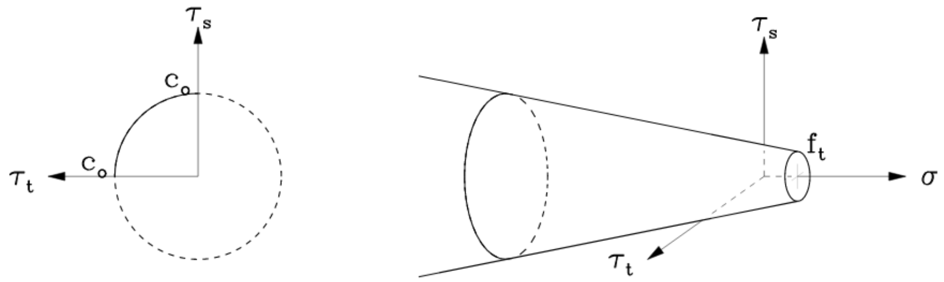

Figure 2.28 The failure surface of the three-dimensional interface model (DIANA FEA 10.3 User Manual 2019)

2.5 Finite Element Types

Several types of finite elements are used in the analyses of the models. For this research project, a shell continuum macro-model and a shell block-based micro-model are analyzed. For the two models, shell elements and interface elements are used. Shell elements are used to model the structural walls in the macro-model and the masonry units in the micro-model. Interface elements are used in the micro-model to model the mortar joints including the connections between the transversal walls and the piers. The aforementioned elements used are explained in the section below.

Regular Curved Shell Elements

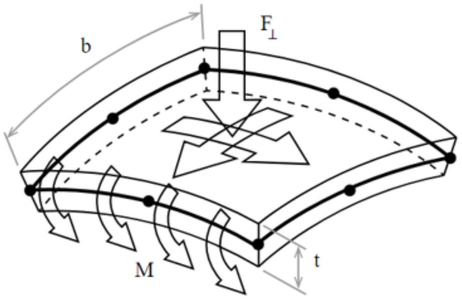

$$\hat{\varepsilon} = \begin{Bmatrix} \varepsilon_{xx} \\ \varepsilon_{yy} \\ \varepsilon_{zz} \\ \gamma_{xy} \\ \gamma_{yz} \\ \gamma_{zx} \end{Bmatrix} \qquad \sigma = \begin{Bmatrix} \sigma_{xx} \\ \sigma_{yy} \\ \sigma_{zz} = 0 \\ \sigma_{xy} = \sigma_{yx} \\ \sigma_{yz} = \sigma_{zy} \\ \sigma_{zx} = \sigma_{xz} \end{Bmatrix}$$

Figure 2.29 Regular Curved Elements (DIANA FEA 10.3 User Manual 2019)

The curved shell elements can sustain in-plane membrane forces and out-of-plane forces. Shear deformations are included in the elements following the Mindlin-Reissner theory (DIANA FEA 10.3 User Manual 2019). Axial stresses normal to the plane of the element is assumed to be negligible.

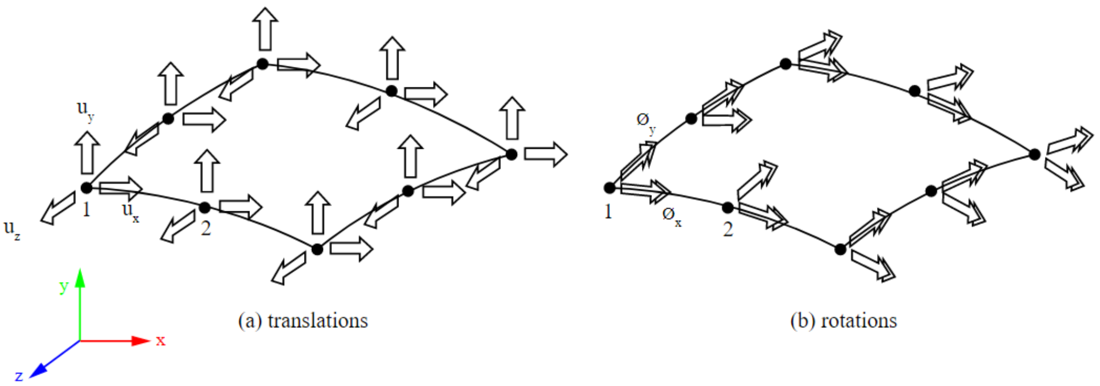

Figure 2.30 Degree of Freedoms of the curved shell elements (DIANA FEA 10.3 User Manual 2019)

Each node in the elements has five degrees of freedoms; three translations and two rotations. The elements have six strain variables as can be seen from Figure 2.29 with the shear deformations γ_{yz} and γ_{xz} assumed to be constant over the element thickness. This is done to prevent shear locking. Six stresses variables are present in the elements that are reduced to only five since the stresses normal to the element plane σ_{zz} is assumed to be zero.

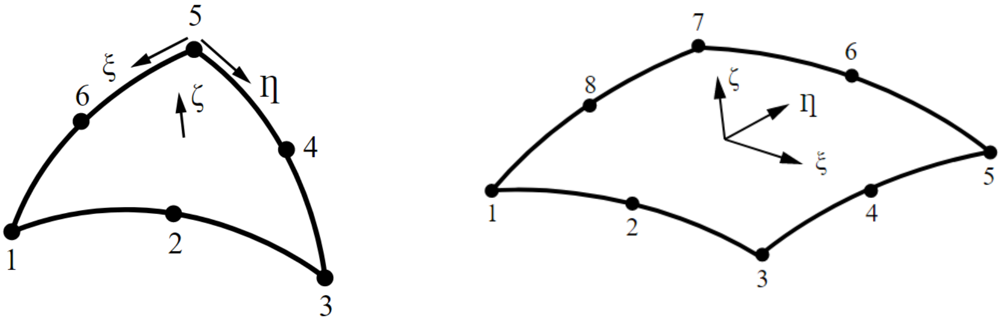

(a) (b)

Figure 2.31 The triangular and quadrilateral shell elements; (a) CT30S and (b) CQ40S (DIANA FEA 10.3 User Manual 2019)

Two types of shell elements are used in the models. The triangular shell elements CT30S with 6 nodes and the quadrilateral shell elements CQ40S with 8 nodes. CT30S uses 3 integration points across the element area, while CQ40S uses 2x2 integration points across the element area. For the integration over the element thickness, both elements use 3 integration points by default. This can be increased to 5, 7 or more to achieve a smoother interpolation, especially for nonlinear analysis.

It is of note that triangular elements might have a shear locking problem and the analysis of such elements might yield an inaccurate result on the shear forces. Therefore, it is recommended to use the quadrilateral elements as much as possible for the structural analysis.

Line Interface Elements

For this project, line interface elements are used for the structural models. Line interface elements can be placed between one-dimensional elements or the edges of two-dimensional elements. The surface and directions of the interfaces are determined automatically from the element geometry.

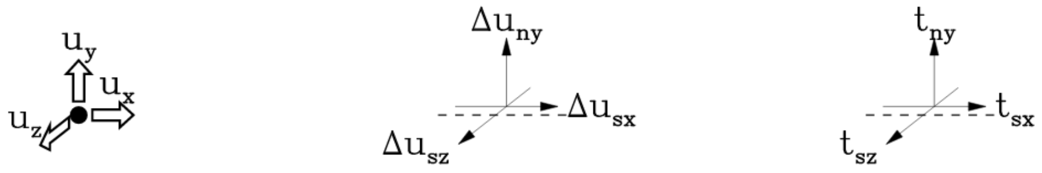

(a) displacements (b) relative displacements (c) tractions

Figure 2.32 Variables of three-dimensional line interface elements (DIANA FEA 10.3 User Manual 2019)

The basic 3D line interface element formulation in DIANA has three translational degrees of freedom. Three relative displacements are present in the elements with Δu_{ny} in the direction perpendicular to the interfaces and the other two (Δu_{sx} and Δu_{tz}) in the direction tangential to the interfaces. Consequently, three traction variables exist corresponding to the relative displacements.

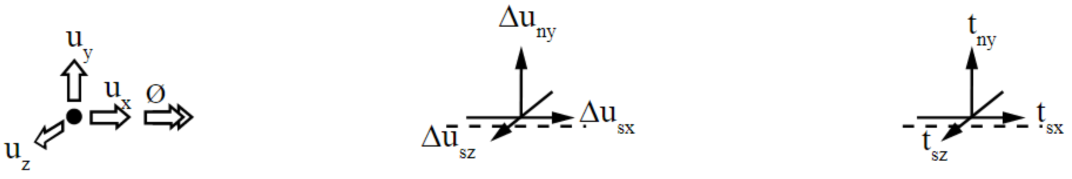

(a) displacements (b) relative displacements (c) tractions

Figure 2.33 Variables of three-dimensional line interface to shells (DIANA FEA 10.3 User Manual 2019)

The other alternative to the 3D line interface element is the 3D line interface element to shells. The formulation of this interface element is almost identical to the aforementioned 3D line interface element with one difference. For this element, an additional rotational degree of freedom around the local x-axis is added. This is done to give the element compatibility to curved shell elements.

For this research project, the 3D line interface to shells will be used to give the interface elements better compatibility with the existing curved shell elements.

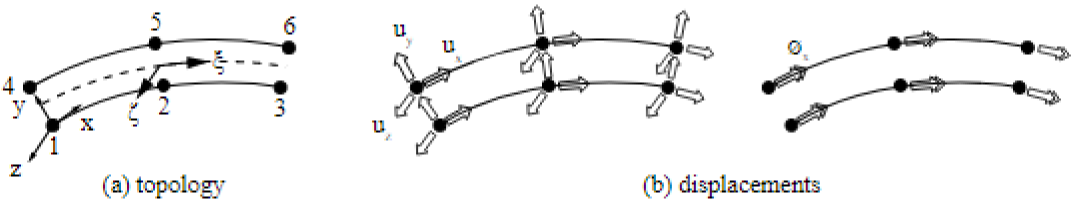

(a) topology

(b) displacements

Figure 2.34 The configuration of a CL24I interface element (DIANA FEA 10.3 User Manual 2019)

Several types of interface elements to shells are implemented in DIANA. One of them that is of note is CL24I. CL24I is 3+3 nodes line to shell interface elements. The 3+3 nodes configuration makes this element a good choice for the CQ40S and CT30S shell elements mentioned previously. The 3-point Newton-Cotes integration scheme is implemented for the integration along the longitudinal axis, while the 3-point Simpson integration scheme is implemented for the integration over the thickness.

2.6 Analysis Method: Nonlinear Quasi-Static Pushover Loading

To predict the response of a structure to the seismic loads, it becomes necessary to conduct inelastic analyses. This is due to the fact that elastic analysis is insufficient in predicting the force and deformations distribution realistically especially when damages from cracking or yielding start to appear on the structure.

There are a number of analysis options available for assessing the seismic performance of a structure. One of the most realistic ones is the inelastic time history analysis. This analysis method uses a collection of ground motion data that are deemed representative to ascertain the seismic performance of the structure. Despite offering the most accurate and realistic description of the structural seismic performance, this analysis method is very complex and requires a considerable amount of time and computation demand. To bridge the gap between the need to obtain accurate results and the need for a time-efficient method of analysis, the nonlinear quasi-static pushover analysis was developed.

The nonlinear quasi-static pushover analysis involves determining two basic variables: seismic capacity and seismic demand. Seismic capacity is the ability of a structure to resist the seismic loads, while seismic demand is the description of the effects that the ground motions have on a structure.

The seismic capacity is assessed by conducting a series of inelastic analyses on the structure. This is done by subjecting the structure in question to monotonically increasing lateral loads. The lateral loads “push” the structure, hence the term pushover analysis. The lateral loads are applied until a predetermined limit is reached or until the structure becomes unstable and collapses. The limit, in this case, can be a deformation limit or a ductility limit.

Various data on structural performance can be obtained from the analysis. One of the most important products of the analysis is the relationship between base shear force and horizontal displacement (Tso and Moghadam 1998). The aforementioned curve is commonly referred to as the capacity curve. Various information on the seismic performance of the structure can be inferred from the curve such as the initial elastic stiffness, the initiation of first yielding, the rapid stiffness deterioration and the ultimate strength. Other products from the analysis are the interstory drift, hinge locations and the member ductility, which can be used to infer the damage pattern. Undesirable characteristics such as a soft-story mechanism can be inferred from the damage pattern. The determination of seismic capacity is often the only step taken in a pushover analysis.

Estimation of the seismic demand is undertaken to determine a target displacement. A target displacement is the ultimate displacement of the structure when subjected to seismic loading. The target displacement is determined through dynamic analysis. This is required to determine the structural damage when subjected to a specified level of ground motions.

The pushover analysis method mentioned above is the monotonic pushover analysis. It assumes that the seismic response of a structure can be sufficiently represented by a capacity curve that envelops the cyclic hysteretic behavior of the structure. The monotonic nature of the loading, however, rarely applies to earthquake loading (Barbagallo et al. 2019). Most of the seismic loading involves repetitive lateral loads that have a changing direction. Furthermore, the structural damage from the seismic loading comes from damages accumulated during the duration of the earthquake. Neglecting the cyclic nature of the seismic loads can result in the overestimation of the structural capacity and the underestimation of the structural demand. Therefore, it is important to consider the cyclic behavior of the seismic loads in the analysis.

The procedure of a cyclic pushover analysis is similar to the monotonic one. The main difference is on the loading protocol that is used. In a cyclic pushover analysis, the structure is initially loaded in one direction until it reaches a predetermined value of lateral deformation and then the load is reversed in the other direction until it reaches the second value of lateral deformation. This loading is then repeated in cycles according to the selected loading protocol to simulate the loading and deformation histories incurred by the structure from the earthquake.

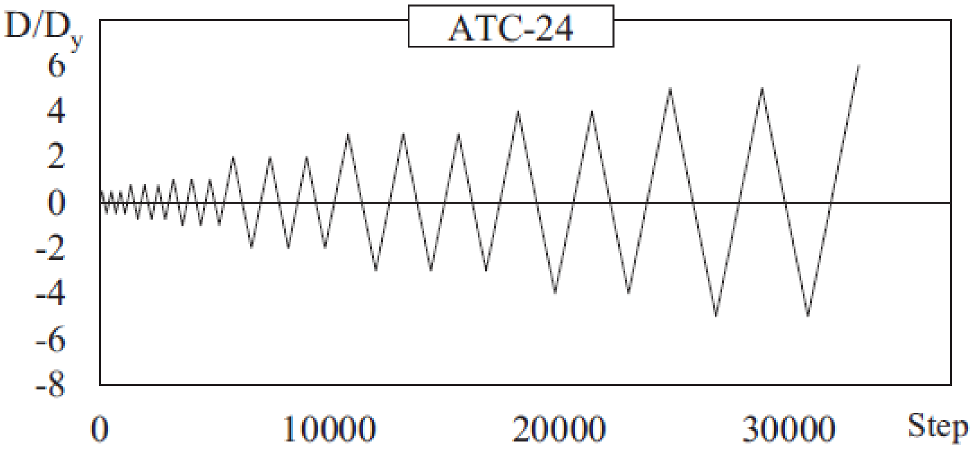

Figure 2.35 Example of a cyclic loading protocol from the ATC-24 code (Barbagallo et al. 2019)

The choice of a loading protocol for the analysis is important. It must be able to simulate the loading and deformation histories of a structure when said structure is subjected to seismic loading. Unfortunately, no loading protocol can perfectly simulate the hysteretic behavior of a structure when subjected to seismic loading due to the influence of various factors on the actual cumulative damages sustained by the structure.

Chapter 3
Finite Element Models Of The Masonry Structure

The structure considered for the analysis is the full-scale model of typical two-story masonry residential buildings in the Netherlands. Two full-scale models were built in the Stevinlab TU Delft with different building materials, one with small-sized calcium-silicate bricks and the other one with larger sized calcium-silicate elements. Both specimens were subjected to cyclical quasi-static pushover loading. The model with CS elements will be the focus of study in this project. The following chapter will discuss the finite element models considered in the study. A brief description of the physical model and the experiment performed will also be discussed to provide some background information. Two main finite element models will be analyzed in this research project; shell elements macro-model and shell elements micro-model. Each modeling approach has its own variations, which will be described in Chapter 5 and Chapter 7.

3.1 Overview of the Experiment and the Results

The structure considered in this study is the full-scale model of a two-story residential building built with CS elements. CS element is chosen as the building material to simulate the residential buildings in the Netherlands built during the period of 1980 – 2000 which saw the rise of CS element use, due to its larger size which allows for simplification in construction. The residential buildings in the Netherlands are often not designed to withstand seismic loading. The buildings are built using unreinforced masonry (URM) and have peculiar characteristics such as slender piers and limited connectivity between walls and floors. The full-scale specimen had been built to reflect those characteristics.

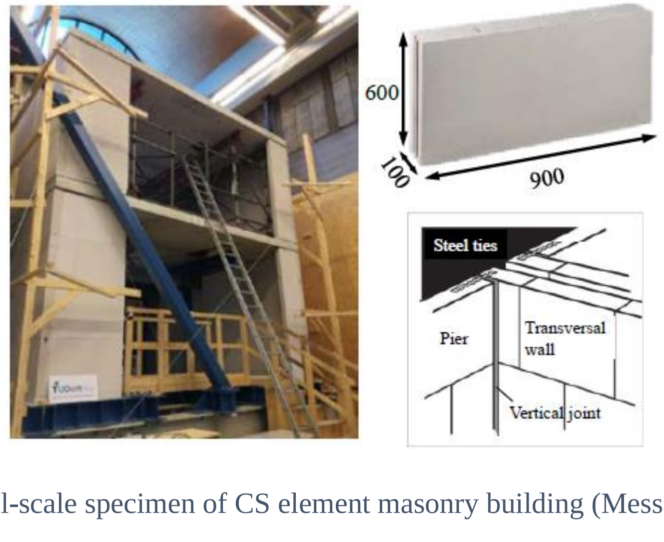

Figure 3.1 The full-scale specimen of CS element masonry building (Messali and Pari 2017)

The picture above shows the experimental setup for the CS element structure. As can be seen from the picture, the structure is comprised of four piers with different width at the westside and eastside façade. These were connected to the transversal walls with concrete slabs placed on top of each floor. The connections between transversal walls and piers were done by putting a thin layer of kimmortar across the height of the connection with steel anchors put in bed joints.

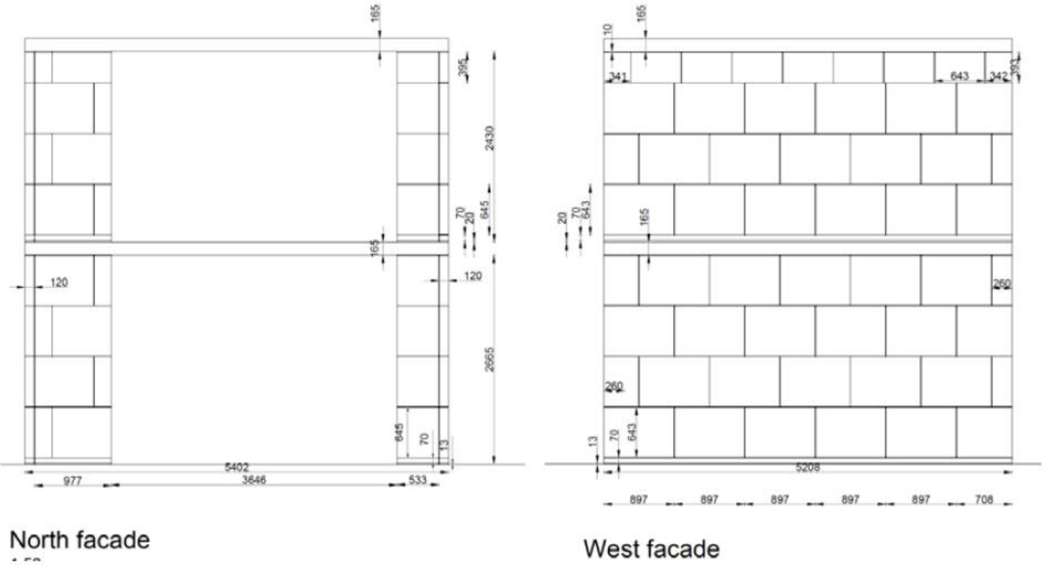

Figure 3.2 The geometry of the full-scale model (Schipper, Ravenshorst, and Ham 2017)

The figure above illustrates the dimension of the structure. The north and south façade consisted of two differently sized piers with the long pier having a width of 977 mm and the smaller pier having a width of 533 mm. The west and east façade consisted of long transversal walls with a length of 5208 mm. CS elements with the dimension of 897x643x120 mm^3 were used for the transversal walls, while CS elements with the dimension of 897x643x100 mm^3 were used for the piers. On top of each floor, concrete slabs with a thickness of 165 mm were placed. Thin layers of kicker joint used in the construction to smoothen small level differences called kim-layer were also applied below the transversal walls and piers on each floor. The thickness of the kim-layer is 70 mm. The kim-layer at the ground floor was glued to the steel frame.

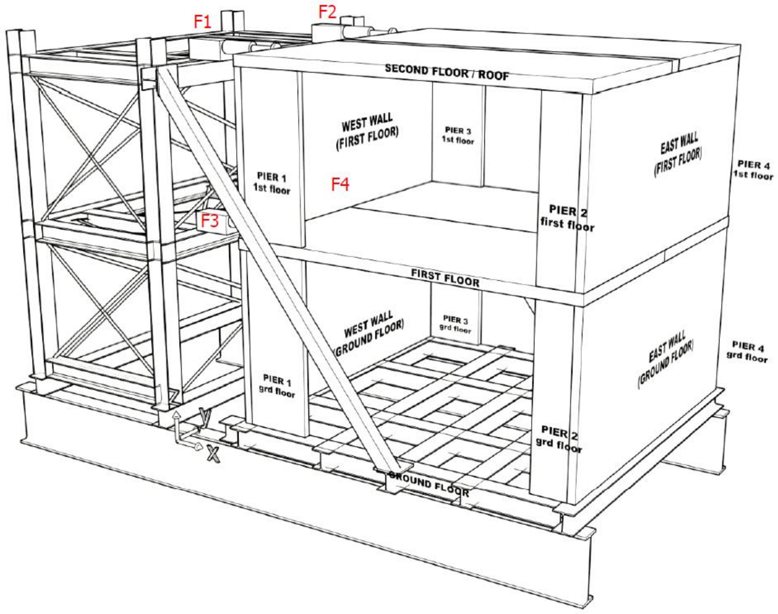

Figure 3.3 The test set-up of the full-scale model (Schipper, Ravenshorst, and Ham 2017)

The structure is laterally loaded through the use of four horizontal actuators with two actuators on each floor. The actuators were placed inward at about 1 meter from the facades with piers. For the purpose of the experiment, a uniform loading profile (F1 = F3, F2 = F4 and F1+F2 = F3+F4) was used. The actuators on the first floor introduced the quasi-static displacements on the structure. To maintain the uniform loading profile, the actuators on the second floor were mechanically coupled with the ones on the first floor.

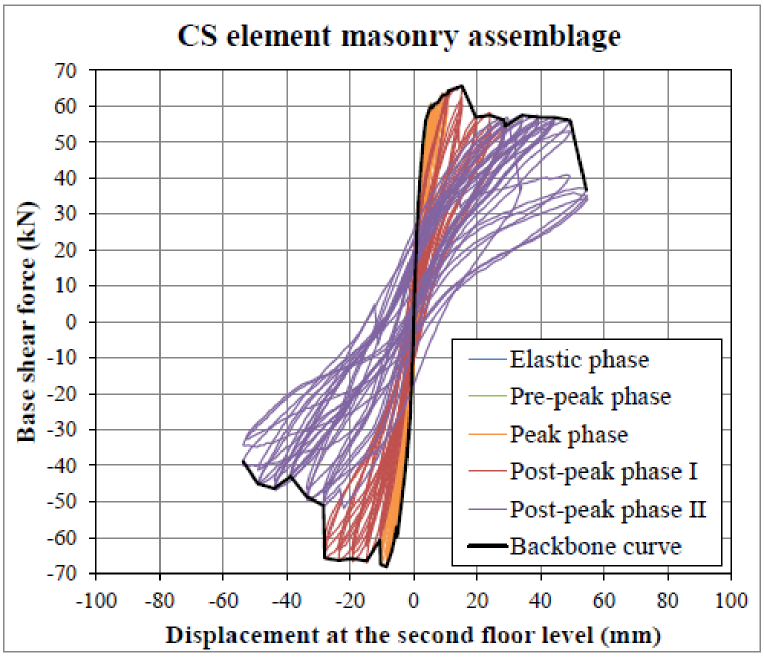

Figure 3.4 The capacity curve of the CS Element building model obtained from the physical experiment (Esposito et al. 2018)

The physical experiment on the full-scale model results in The capacity curve shown in Figure 3.4. The CS Element structure reached a peak base shear value of +65 kN and -69 kN. A 20% reduction of base shear force was achieved at the first floor displacement d_2 of +50 mm and -28 mm (Esposito et al. 2018).

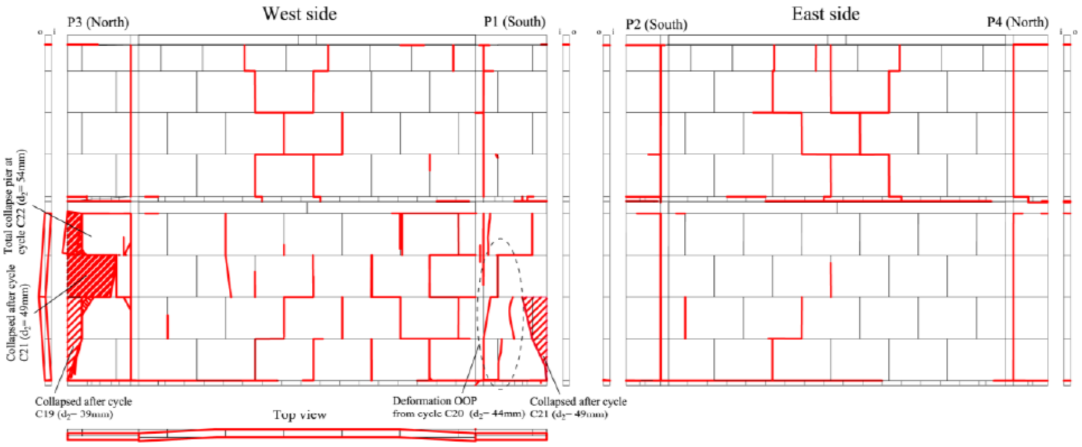

Figure 3.5 The crack pattern of the CS Element building model obtained from the physical experiment (Esposito et al. 2018)

Observation of the failure of the CS Element structure found that the failure of the structure was governed by in-plane damages of the long piers at the ground floor. The failure of the structure started with the appearance of cracks at the joint between the concrete floor and the transversal walls, which was then followed by the diagonal/vertical cracks in the long piers at the ground floor. It is of note that large out-of-plane deformations were also observed on the CS Element structure due to the large size of the masonry element (Esposito et al. 2018).

3.2 Shell Elements Macro-Model

Shell elements macro-model is the finite element model constructed using the macro-modeling approach. The joints between mortar and masonry units are not taken into account and the failure of the structure in the form of cracking is distributed across the continuum elements. For this model, shell elements are used as continuum elements to model the structural elements.

3.2.1 The Geometry of Shell Elements Macro-Model

The model is constructed as a 3D model. Since the physical model is symmetric, only half of the structure needs to be modeled. This approach allows for a faster computation process and more efficient use of computation resources. In this thesis, the southside half of the structure is considered for the analysis.

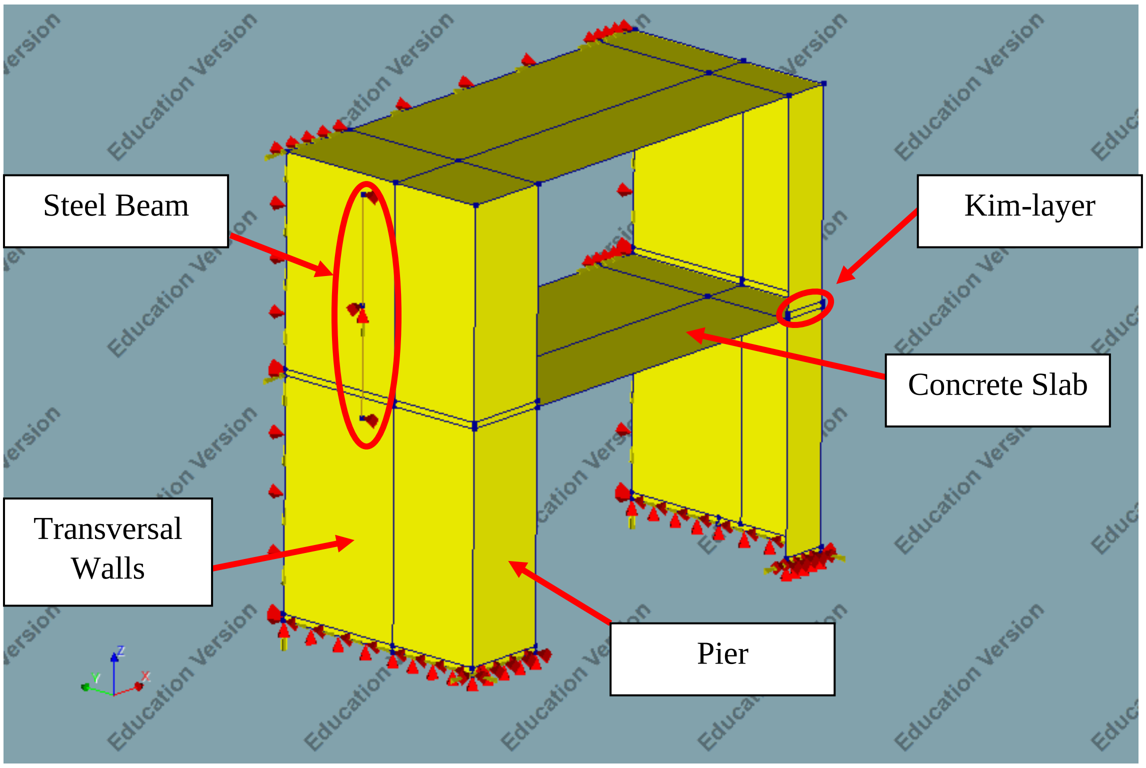

Figure 3.6 The geometry of the shell elements macro-model

The model is constructed following the geometry of the physical model outlined in the experiment proposal (Schipper, Ravenshorst, and Ham 2017). The length of the structure along the global X-axis is 5402 mm, while the length along the global Y-axis until the plane of symmetry is 2604 mm. The model is comprised of two floors with the ground floor having a height of 2665 mm and the first floor having a height of 2430 mm. There are two piers with the wider one having a width of 977 mm and the narrower one having a width of 533 mm.

Shell elements with a thickness of 120 mm are used for the transversal walls, while elements with a thickness of 100 mm are used for the piers. Concrete slabs of the thickness 165 mm are placed on top of each floor. A 70 mm thick kim-layer layer is placed beneath the transversal walls and the piers on each floor. An extremely stiff dummy beam is added to the model to introduce the lateral loads to the model.

Since the kim-layer on the ground floor is glued to the steel frame, the base of the structure can be assumed to be clamped. At the plane of symmetry, the concrete slabs are supported in the global Y-direction and restrained rotationally around the global X-axis. The transversal walls at the symmetry plane are also supported in the global Y-direction and restrained rotationally around the global Z-axis. A point support is added to the middle of the dummy beam to allow the structure to be loaded with a prescribed displacement. Two lateral tyings between the end nodes of the beam and the nodes of the concrete slabs are applied to transfer the lateral load from the beam to the structure. The complete description of the supports applied to the model is illustrated in the figures below.

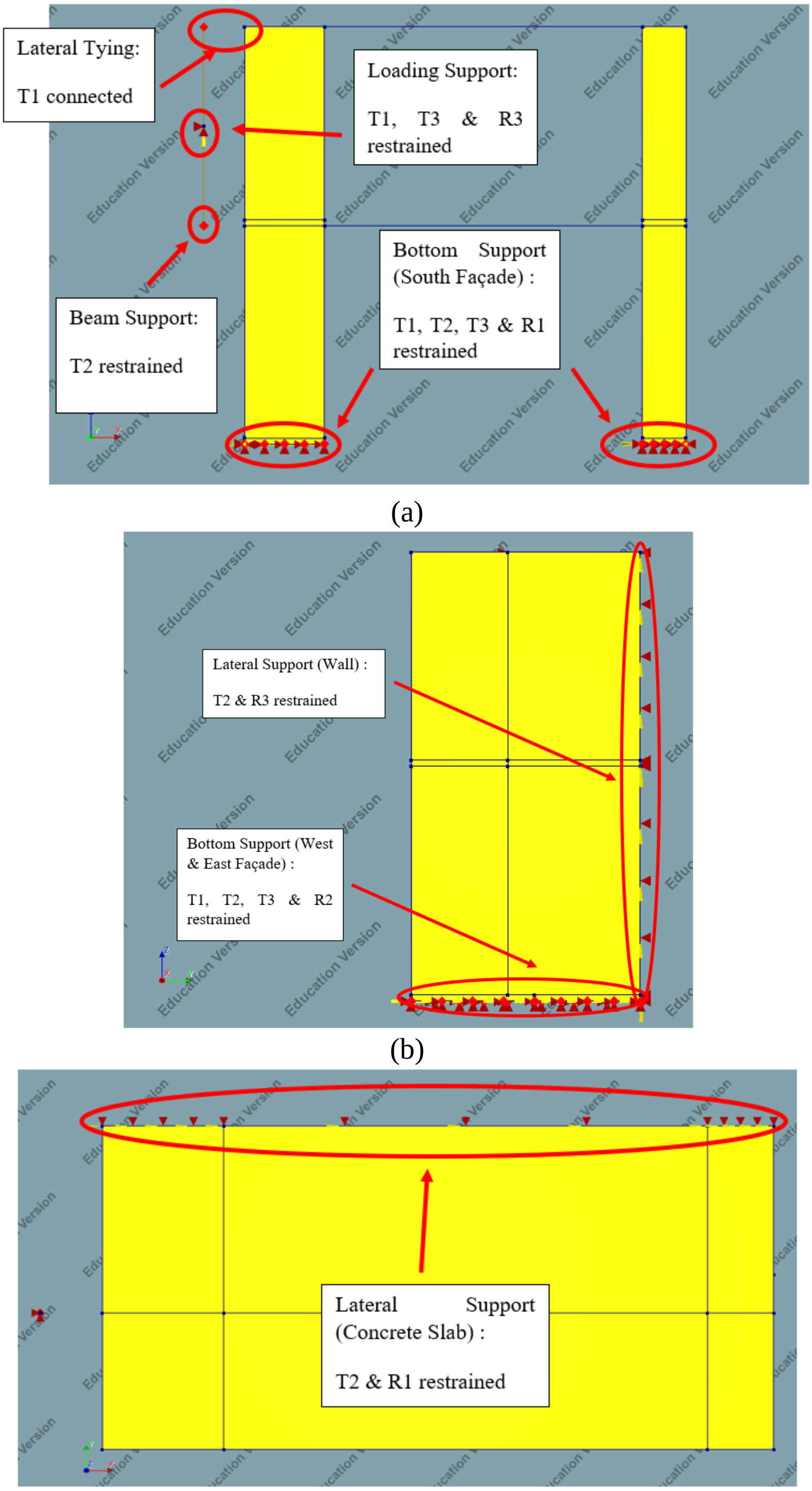

(a)

(b)

(c)

Figure 3.7 The support conditions of Shell elements macro-model from several viewpoints; (a) southern side façade, (b) eastern side façade and (c) top view

3.2.2 Finite Element Mesh of Shell Elements Macro-Model

Regular curved shell elements as discussed in section 2.5 are used for the continuum elements. Curved shell elements are used to accurately simulate the in-plane and out-of-plane behavior of the masonry structure.

Quadrilateral shell elements CQ40S with 8-nodes are used for the model. The integration scheme used is 2x2 Gauss integration for the in-plane integration, while 3-point Simpson integration is used for the integration over the element thickness.

A mesh size of 100 mm is applied for the masonry walls, masonry piers and concrete floors. The generated mesh for the model is shown in the figure below. A summary of the properties of the finite elements used is given in the table below.

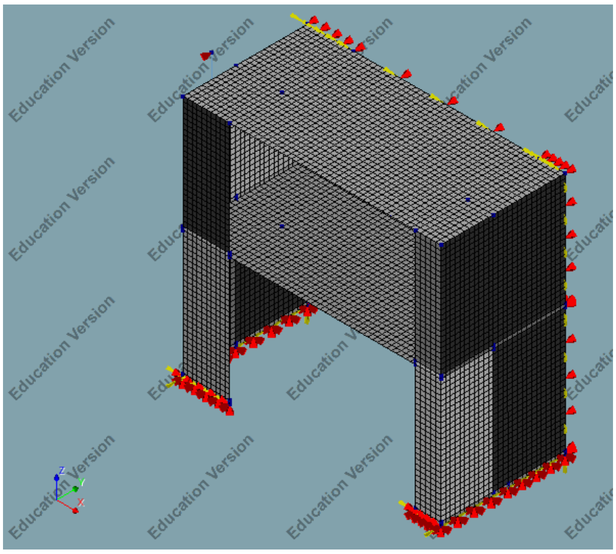

Figure 3.8 The generated finite element mesh of Shell elements macro-model

Table 3.1 Summary of finite elements of Shell elements macro-model

	Masonry Walls	**Masonry Piers**	**Kim-layer**	**Concrete Floors**
Element Type	CQ40S	CQ40S	CQ40S	CQ40S
Integration Schemes	2x2x3	2x2x3	2x2x3	2x2x3
Thickness	120 mm	100 mm	120 mm (Wall) 100 mm (Pier)	165 mm
Element Sizes	100 mm	100 mm	100 mm	100 mm
Number of Elements	2600	750	134	2808
Total Number of Nodes	19270			

3.2.3 Constitutive Models of Shell Elements Macro-Model

Two types of constitutive models are used in the analysis of shell elements macro-model. They are the Total Strain Rotating Crack Model (TSRCM) and the Engineering Masonry Model (EMM). The average values of the material parameters are used as a reference for further analyses.

Several material parameters are determined based on assumptions. The tensile strength of the masonry (f_t) is taken as 2/3 of the out-of-plane flexural strength parallel to the bed joint ($f_{x,1}$). The tensile fracture energy is determined according to the equation: $G_{ft}^{I} = 0.025(2\,f_t)^{0.7}$ and the compressive fracture energy is determined by using the equation: $G_{fc} = 15 + 0.43 f_c - 0.0036 f_c^2$ (Schreppers et al. 2017). The rest of the material parameters is taken from the experimental report of the physical experiment.

Table 3.2 Structural parameters of masonry walls and piers for Shell elements macro-model (TSRCM variation)

Masonry Walls & Piers (TSRCM)		
$\boldsymbol{E}$	8001	N/mm^2
$\boldsymbol{\nu}$	0.16	
$\boldsymbol{\rho}$	1805	kg/m^3
Tensile Behavior	Linear-Crack Energy	
$\boldsymbol{f_t}$	0.39	N/mm^2
$\boldsymbol{G_{ft}^{I}}$	0.021	N/mm
Crushing Curve	Parabola	
$\boldsymbol{f_c}$	13.93	N/mm^2
$\boldsymbol{G_{fc}}$	20.29	N/mm
Crack Bandwidth	Rots	

Table 3.3 Structural parameters of masonry walls and piers for Shell elements macro-model (EMM variation)

Masonry Walls & Piers (EMM)		
$\boldsymbol{E_x}$	7400	N/mm^2
$\boldsymbol{E_y}$	8001	N/mm^2
$\boldsymbol{G_{xy}}$	3200.4	N/mm^2
$\boldsymbol{\nu}$	0.16	
$\boldsymbol{\rho}$	1805	kg/m^3
Head-joint failure type	Diagonal staircase crack	
$\boldsymbol{f_t}$	0.39	N/mm^2
$\boldsymbol{G_{ft}^{I}}$	0.021	N/mm
Angle between diagonal crack-bed	69.37; 78.39	degrees

f_c	13.93	N/mm^2
G_{fc}	20.29	N/mm
Factor to strain at the compressive strength	2	
c	0.83	N/mm^2
ϕ	55.92	degrees
Crack bandwidth	Rots	

The damage and structural failure are assumed to be concentrated on the masonry walls and piers. Both the concrete floors and the kim-layers are assumed to be linear elastic. The properties of the concrete floors and the kim-layers are summarized in the tables below.

Table 3.4 Structural parameters of concrete floors for shell elements macro-model

Concrete Floors		
E	35500	N/mm^2
ν	0.2	
ρ	2400	kg/m^3

Table 3.5 Structural parameters of kim-layer for shell elements macro-model

Kim-layer		
E	8001	N/mm^2
ν	0.16	
ρ	1805	kg/m^3

3.3 Shell Elements Micro-Model

The second model is a micro-model constructed using shell elements. The micro-modeling approach chosen is the simplified approach as explained in section 2.3. With this approach, the expanded masonry units are modeled using continuum elements and the mortar joints between the units are modeled using interface elements.

3.3.1 The Geometry of Shell Elements Micro-Model

The geometry and the support conditions are identical to the macro-model as explained in section 3.2.1. The main difference is that the transversal walls and the piers are modeled as assemblages of individual masonry units which are joined with each other by mortar joints. The geometry of the model is constructed according to the physical geometry of the structure described in the experiment proposal (Schipper, Ravenshorst, and Ham 2017).

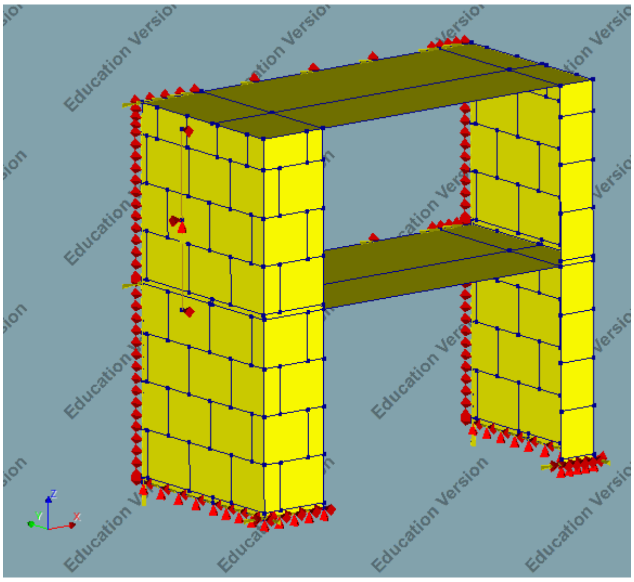

Figure 3.9 The geometry of shell elements micro-model

For the sake of simplicity, the simplified micro-modeling approach is used for the analysis. As has been explained in section 2.3, this approach involves modeling the mortar joints with interface elements instead of continuum elements. The masonry units are then expanded to account for the gap left by not modeling the mortar joints as continuum elements. The interface elements on the model are shown in the figure below.

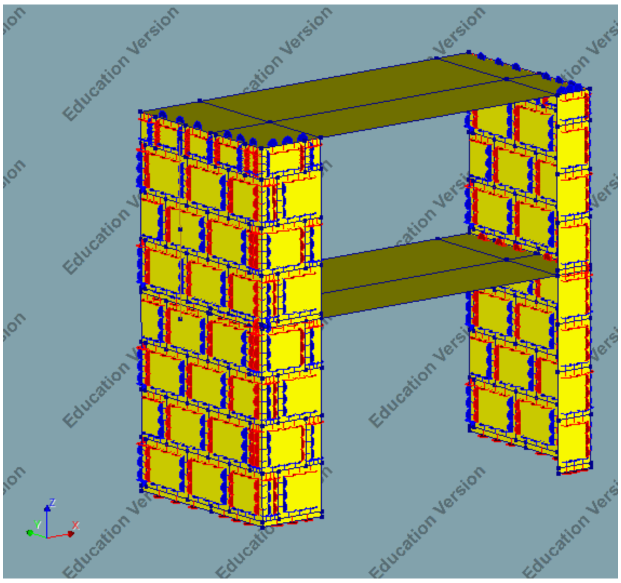

Figure 3.10 The interface elements on shell elements micro-model

Wall-pier connections in the model are modeled with interface elements instead of shared nodes. The interface elements span across the height of the wall-pier connections from the top of the kim-layer on the ground floor.

3.3.2 Finite Element Mesh of Shell Elements Micro-Model

As with the previous model, regular curved shell elements are used to model the masonry structural elements and the concrete slab. Quadrilateral shell elements CQ40S are used for the transversal walls and the piers to give better results and minimize the risk of shear locking. A small number of triangular shell elements CT30S are present in the model to adapt to the geometry of the model. A mesh size of 100 mm is applied to all structural elements. The generated finite element mesh for the model is displayed below.

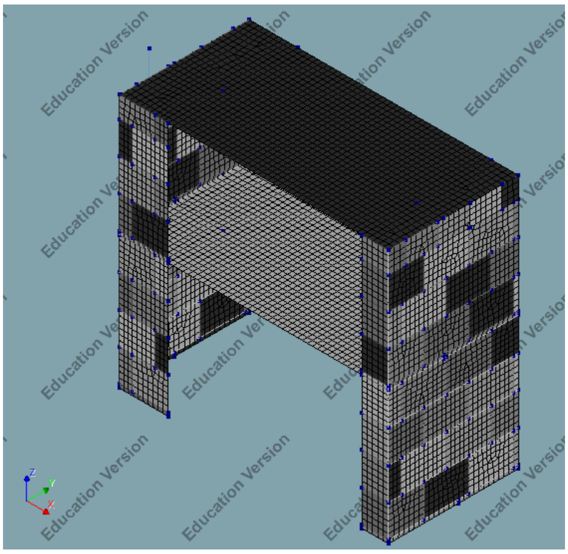

Figure 3.11 Shell elements micro-model finite element mesh

Interface elements used on the model are the 3D line to shell interface elements since they give good compatibility with the shell elements. The 3+3 nodes interface to shell elements CL24I are used in the model for better compatibility with the 8 nodes CQ40S elements and 6 nodes CT30S elements. The local axes of the interface elements are displayed in the figure below.

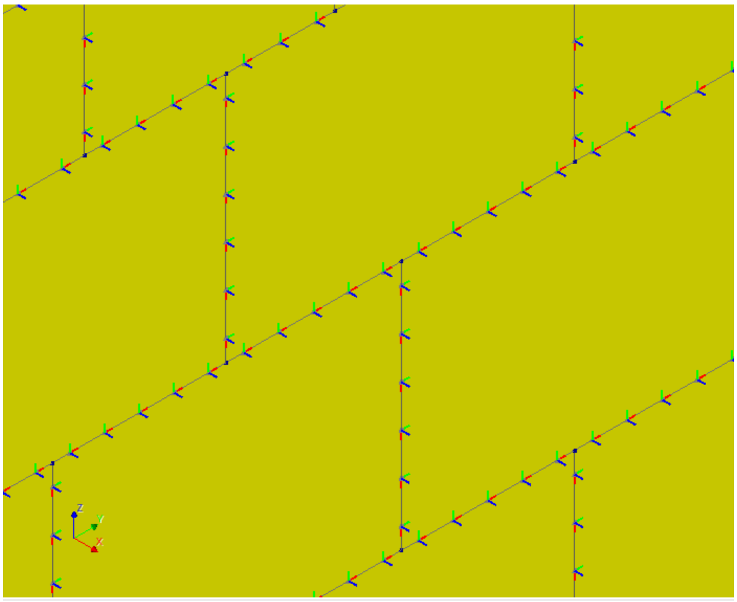

Figure 3.12 The local axes of interface elements (mortar joints)

The integration schemes used on the shell elements for integration over the element area are 3 point integration for CT30S elements and 2x2 point Gauss integration for CQ40S elements. For integration over the thickness, 3 point Simpson integration is applied to all shell elements.

For interface elements, the integration scheme used for integration along the longitudinal axis is 3-point Newton-Cotes integration. For integration in the thickness direction, a 3-point Simpson is applied.

A summary of the finite elements used in the model and its properties are presented in the table below.

Table 3.6 Summary of finite elements of shell elements micro-model

	Masonry Walls	**Masonry Piers**	**Kim-layer**	**Concrete Floors**	**Mortar Joints**	**Wall-Pier Connection**
Element Type	CQ40S+CT30S	CQ40S+CT30S	CQ40S	CQ40S	CL24I	CL24I
Integration Schemes	2x2x3+3x3	2x2x3+3x3	2x2x3	2x2x3	3x3	3x3
Thickness	120 mm	100 mm	120 mm (Wall) 100 mm (Pier)	165 mm	120 mm (Wall) 100 mm (Pier)	100 mm
Element Sizes	100 mm	100 mm	100 mm	100 mm	100 mm	100 mm

Number of Elements	2633	738	134	2789	1039	96
Total Number of Nodes	21808					

3.3.3 Constitutive Models Of Shell Elements Micro-Model

The structural analyses of shell elements micro-models will be performed using two variations of the constitutive model for shell elements. In the first variation, the masonry walls and piers will be assumed to behave perfectly linear elastic and the failure will be lumped to the interface elements. In the second variation, the masonry transversal walls and piers will be assumed to undergo cracking as well. The masonry transversal walls and piers will be assigned the Total Strain Rotating Crack model to simulate these internal cracks.

Table 3.7 Structural parameters of masonry walls and piers (Linear Elastic case)

Masonry Walls & Piers (Linear Elastic)		
$\boldsymbol{E}$	8001	N/mm^2
$\boldsymbol{\nu}$	0.16	
$\boldsymbol{\rho}$	1805	kg/m^3

Table 3.8 Structural parameters of masonry walls and piers (TSRCM case)

Masonry Walls & Piers (TSRCM)		
$\boldsymbol{E}$	8001	N/mm^2
$\boldsymbol{\nu}$	0.16	
$\boldsymbol{\rho}$	1805	kg/m^3
Tensile Behavior	Linear-Crack Energy	
$\boldsymbol{f_t}$	0.39	N/mm^2
$\boldsymbol{G_{ft}^I}$	0.021	N/mm
Crushing Curve	Parabola	
$\boldsymbol{f_c}$	13.93	N/mm^2
$\boldsymbol{G_{fc}}$	20.29	N/mm
Crack Bandwidth	Rots	

Several constitutive models for the interface elements are analyzed. For shell elements micro-model, the following constitutive models are considered:

1. Coulomb friction
2. Discrete cracking
3. Nonlinear elasticity

Another alternative constitutive model, the combined cracking-shearing-crushing model, is also the prime candidate for the interface elements constitutive model. This constitutive model is unfortunately not supported for use with shell elements by DIANA. Therefore, it will not be considered in this analysis. Structural parameters for Coulomb friction and discrete cracking constitutive models are presented in the tables below.

Table 3.9 Structural parameters for Coulomb friction interface

Coulomb Friction Interface		
$\boldsymbol{k_{ny}}$	2667	N/mm^3
$\boldsymbol{k_{sx}}$	1066.8	N/mm^3
$\boldsymbol{k_{tz}}$	1066.8	N/mm^3
$\boldsymbol{c}$	0.83	N/mm^2
$\boldsymbol{\phi}$	55.92	degree
$\boldsymbol{\psi}$	0	degree
Interface opening model	Gapping Model	
$\boldsymbol{f_t}$	0.39	N/mm^2
Mode-II shear gap appearance model	Brittle	

Table 3.10 Structural parameters for discrete cracking interface

Discrete Cracking Interface		
$\boldsymbol{k_{ny}}$	2667	N/mm^3
$\boldsymbol{k_{sx}}$	1066.8	N/mm^3
$\boldsymbol{k_{tz}}$	1066.8	N/mm^3
$\boldsymbol{f_t}$	0.39	N/mm^2
Mode-I softening criterion	Linear	
$\boldsymbol{G_{ft}^{I}}$	0.021	N/mm
Interface opening model	Gapping Model	
Unloading/reloading model	Secant	
Mode-II shear criterion for crack development	Zero shear traction	

The nonlinear elasticity interface is defined by specifying traction-displacement diagrams for the interface local axes. Axial traction-relative displacement diagram is specified for the local y-axis of the interface, while shear traction-relative displacement diagram is specified for the local x- and z-axis of the interface.

The following table and figure show the axial traction-relative displacement diagram for the local y-axis. It is assumed that the interface will undergo softening behavior in the tensile region after the crack opens, while the compression region behaves linear-elastically.

Table 3.11 Axial traction-relative displacement values for nonlinear elasticity interfaces (mortar joints)

Δu_{ny} (mm)	t_{ny} (N/mm^2)
-100	-266700
0	0
0.000158	0.39
0.11	0.001
100	0.001

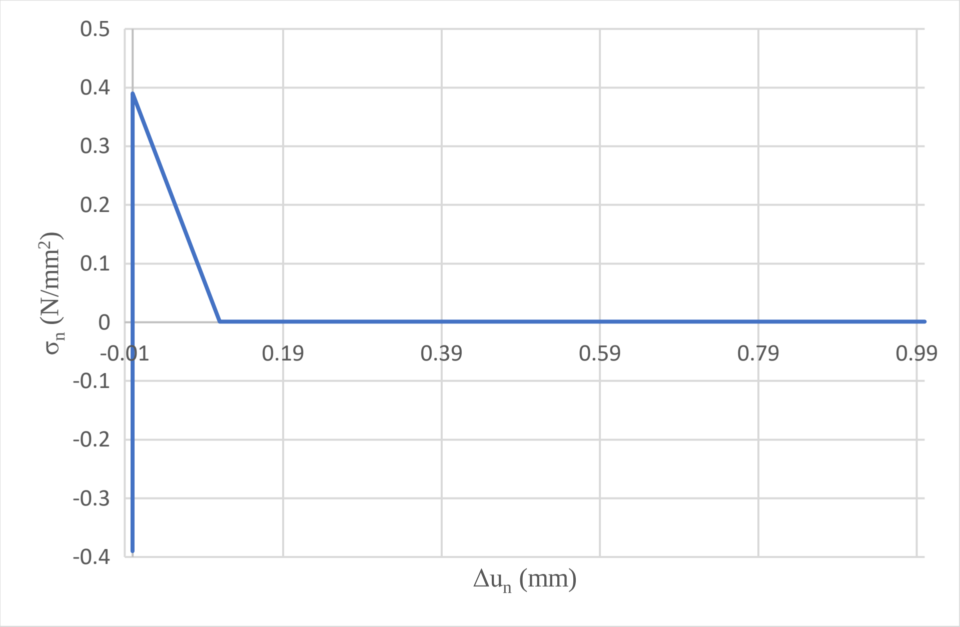

Figure 3.13 Axial traction-relative displacement diagram for nonlinear elasticity constitutive model (mortar joints)

The following table and figure show the shear traction-relative displacement for x- and z-axis. The value of τ_{max} is assumed to be 2 N/mm^2.

Table 3.12 Shear traction-relative displacement values for nonlinear elasticity constitutive model (mortar joints)

τ_{max} = 2 N/mm^2	
Δu_s (mm)	t_s (N/mm^2)
-100	-1.17
-0.25	-1.17
-0.00187	-2
0	0
0.00187	2
0.25	1.17
100	1.17

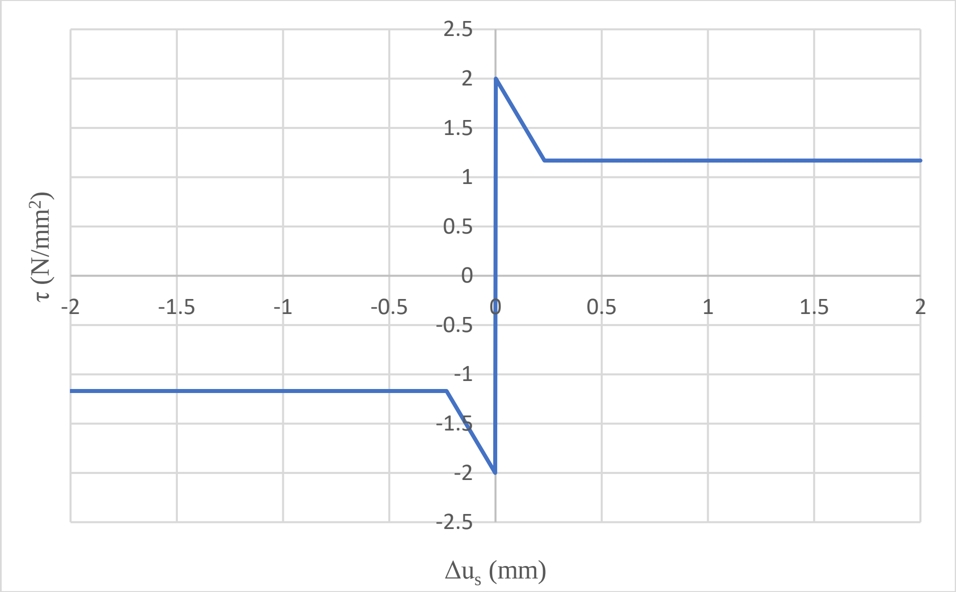

Figure 3.14 Shear traction-relative displacement diagram for nonlinear elasticity constitutive model (mortar joints)

The constitutive model of the interface elements in the wall-pier connections is defined separately from the rest of the interface elements. For these elements, a nonlinear elasticity constitutive model will be used. The diagrams defined for the interface elements are similar to the one for the interface elements between the masonry units as shown in Figure 3.13 and Figure 3.14. The difference is the added contribution from the steel anchors in the wall-pier connection. These steel anchors are assumed to only offer effective resistance in the tensile region. This contribution is added to the axial traction-relative displacement diagram.

Table 3.13 Axial traction-relative displacement values for nonlinear elasticity interfaces (wall-pier connections)

Δu_{ny} (mm)	t_{ny} (N/mm^2)
-100	-266700
0	0
0.000146	0.401
0.11	0.01
100	0.01

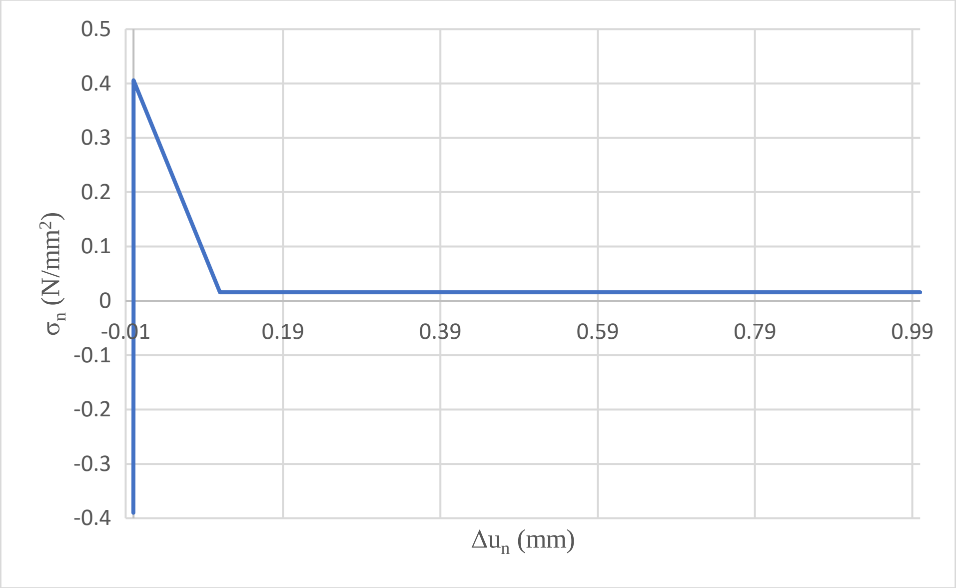

Figure 3.15 Axial traction-relative displacement diagram for nonlinear elasticity constitutive model (wall-pier connection)

For modeling the shear behavior, the shear diagram used for the wall-pier connections identical to the diagram shown in Figure 3.14 will be used.

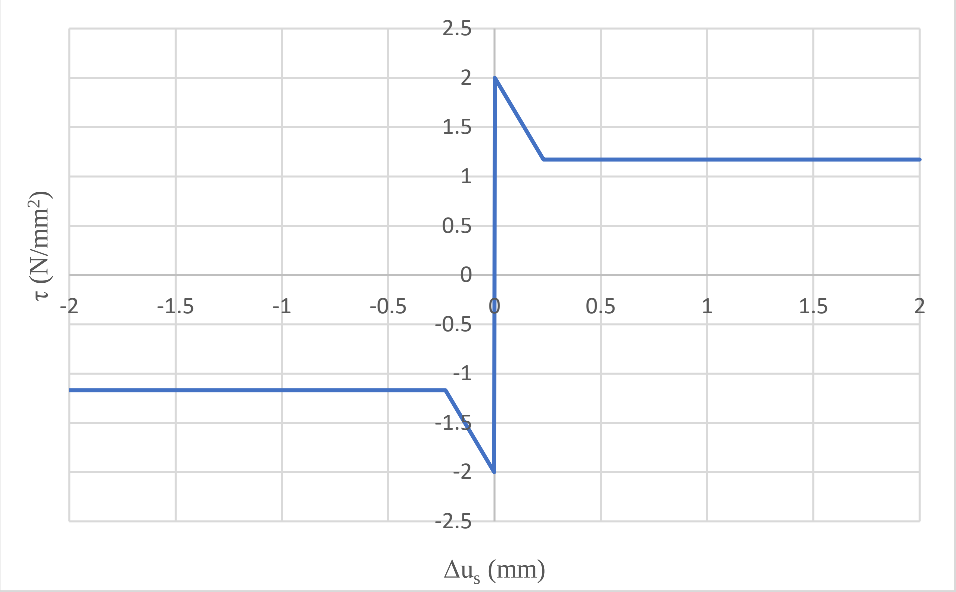

Figure 3.16 Shear traction-relative displacement diagram for nonlinear elasticity constitutive model (wall-pier connections)

Chapter 4
Analytical Method

This chapter will discuss the analysis of the physical specimen through the analytical method. The hand calculation for the analytical method is carried out to provide a comparison to the physical experiment results. A simple limit analysis calculation is used to calculate the upper and lower bound of the structural capacity. This calculation method and its results are discussed in section 4.1. More elaborate and detailed calculation methods are available from a variety of design provisions. However, these alternative analytical methods will not be discussed here.

4.1 Simplified Hand Calculation Method

The hand calculation is performed by considering the force equilibrium at the moment of near-collapse of the piers and treating the masonry structural elements as rigid bodies. Considering the configuration of the structure, the rocking mechanism is assumed to be limited to the ground floor piers and all lateral loads are transferred to the ground floor piers. Due to the position of the first-floor concrete slab, the slab provides a "clamping effect" which allows for redistribution of loads between the piers.

Apart from the piers, some parts of the transversal walls also contribute to the structural capacity through the flange effect. The portion of the walls that can be considered as flanges is unfortunately not easily determined. There is a multitude of ways to determine the area of the flanges. One way is to base the flange area on the cracking pattern in the transversal walls. However, the cracking pattern of a masonry transversal wall is often not clearly defined. Flange contribution to the structural capacity has been discussed in a research paper on the recommendation for the seismic evaluation on URM structures (Moon et al. 2006). In the paper, flanges are classified into three categories as shown in Figure 4.1:

1) Compression flanges: the portion of transversal walls that resists compressive loads

2) Global tension flanges: the portion of transversal walls that is lifted by the global rocking of the structure

3) Component tension flanges: the portion of transversal walls that is lifted by the local rocking of the pier

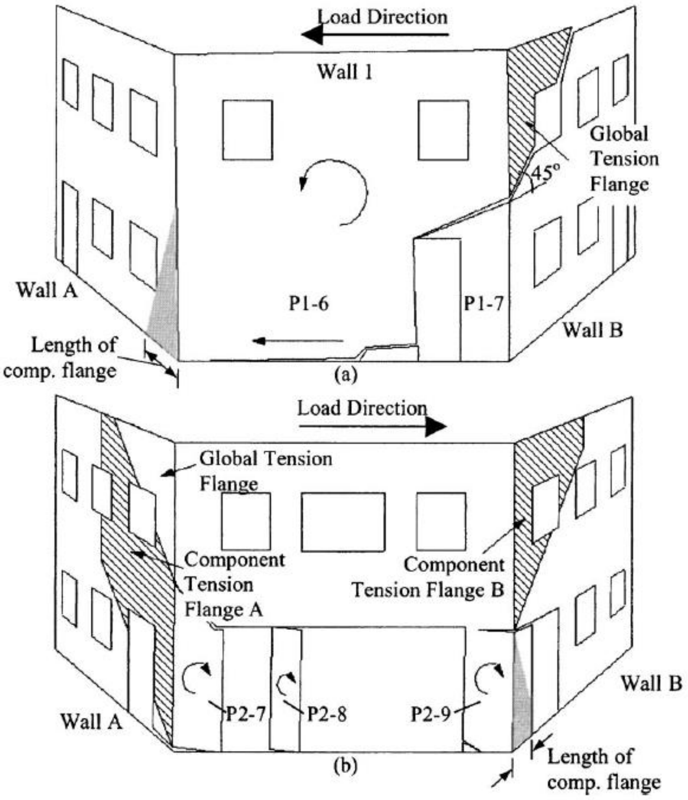

Figure 4.1 Illustration of flanges categories on a structure for two different cases: (a) Scenario 1 with the global rocking of the structure; (b) Scenario 2 involving local pier rocking (Moon et al. 2006)

According to the paper, global tension and component tension flanges can be taken as the portion of walls above a 45^0 crack that extends from the rocking crack to the midpoint of the walls. The definition of compressive flanges length, however, has proved to be more difficult due to large scatter in experimental data (Moon et al. 2006). As a result, the length of compressive flanges has to be taken according to design provisions. In appendix G9.2.6 of the Dutch guideline on the assessment of structural safety (NEN 2017), the length of the compressive flanges can be taken as the lesser of six times the thickness of in-plane walls or the actual length of flanges. Eurocode 6 (CEN 2013) defines the length of the flanges as the lesser of:

1) $h_{tot}/5$, where h_{tot} is the height of the shear walls
2) Half the distance between the shear walls
3) Distance to the end of the wall
4) Half the clear height
5) Six times the length of the intersecting walls

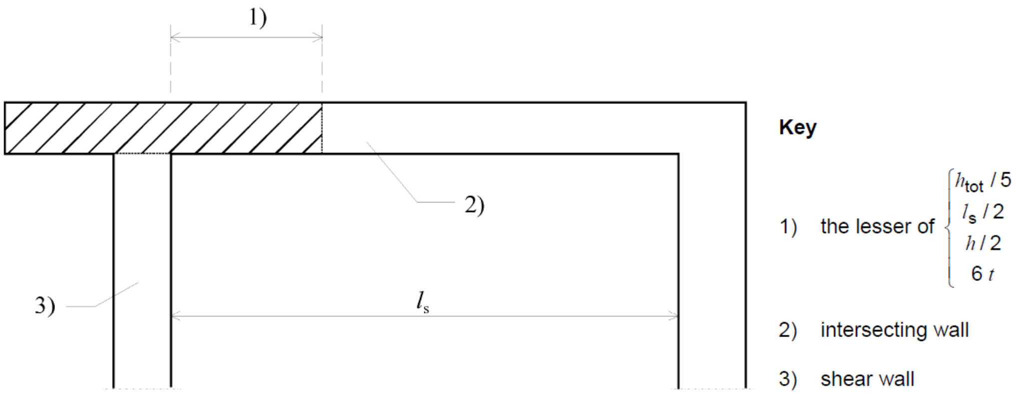

Figure 4.2 Definition of the length of the intersecting wall that can be considered to act as a flange

Based on the approaches discussed above, three assumptions of flange length will be made for the calculation as shown in the figure below. In the case of lower bound calculation, the contribution of these flanges is neglected.

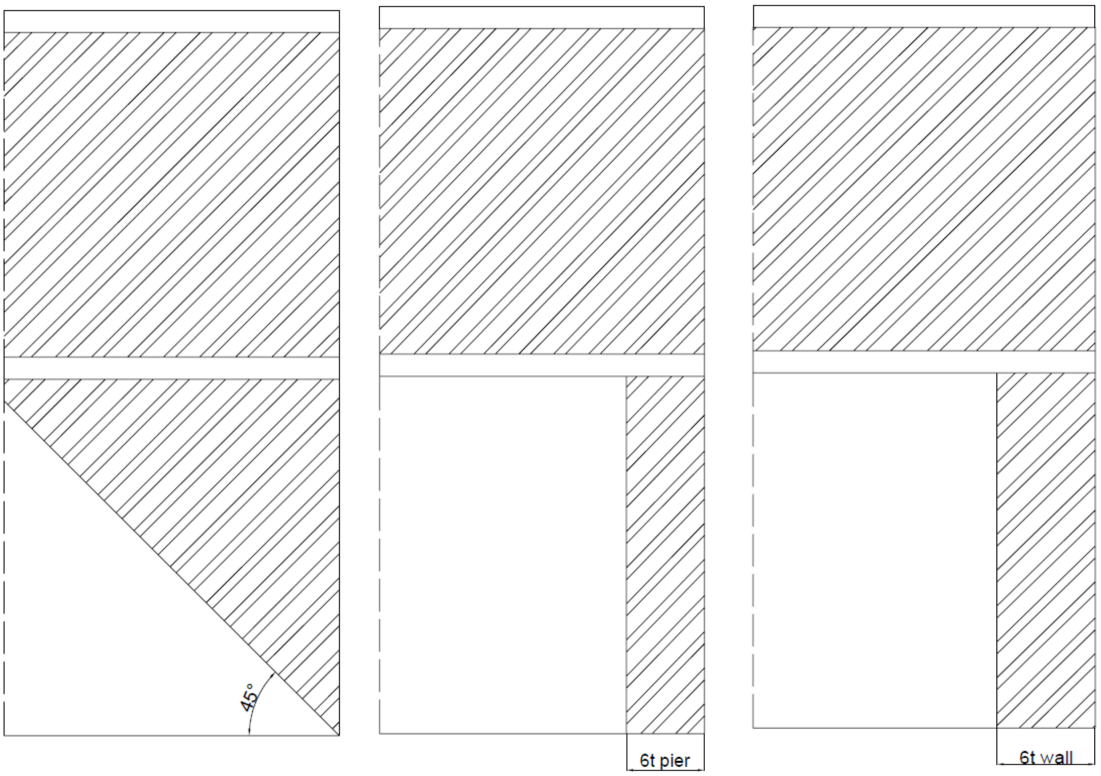

(a) (b) (c)

Figure 4.3 Three alternative assumptions of flange length according to; (a) Cracking pattern (Moon et al. 2006); (b) 6 times pier thickness (NEN 2017); (c) 6 times wall thickness (CEN 2013)

The calculation of the structural capacity is performed by considering the force equilibrium of the global behavior of the façade and the local rocking of the pier as shown by the free body diagrams in Figure 4.4. Since the structure is symmetric, only half of the structure will be considered in the calculation.

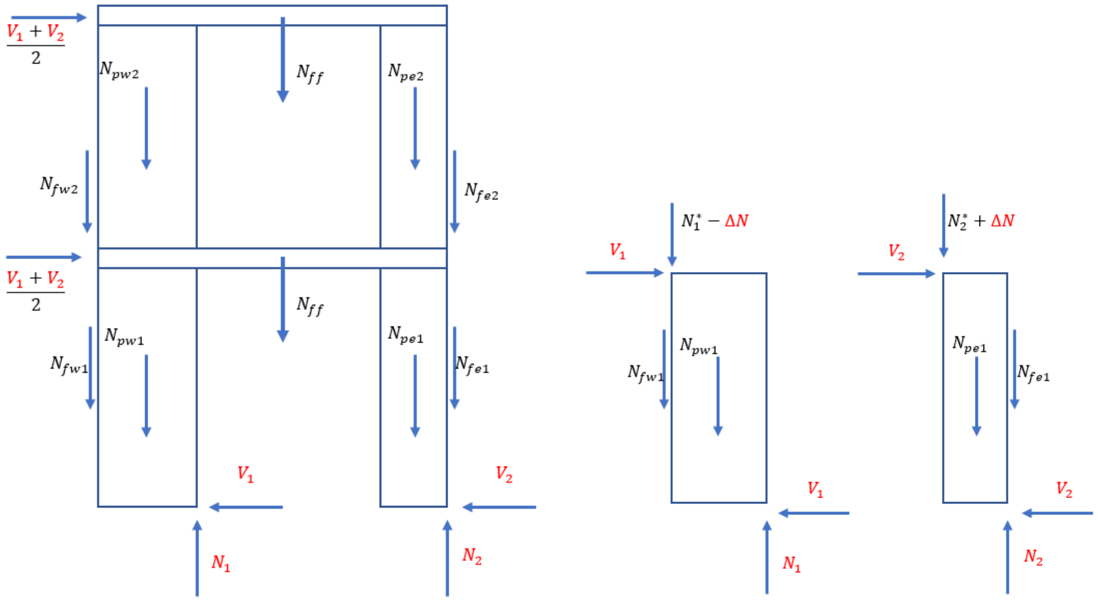

(a) (b)

Figure 4.4 The free body diagrams used for the hand calculation showing; (a) the global behavior of the façade and (b) the local behavior of the piers. The unknown variables are denoted in red.

Figure 4.4 shows the free body diagram for the case of coupled piers indicated by the presence of the variable ΔN, which denotes the redistribution of loads. An upper bound and a lower bound value will be calculated. The calculation of upper bound value assumes the wall-pier connections to be effective and a portion of the walls contributes to the capacity of the structure as flanges. In the case of lower bound calculation, it is assumed that the flanges do not contribute to the structural capacity and the weight of the transversal walls on both floors are neglected. Another calculation assuming the piers to be uncoupled will also be carried out to provide a comparison.

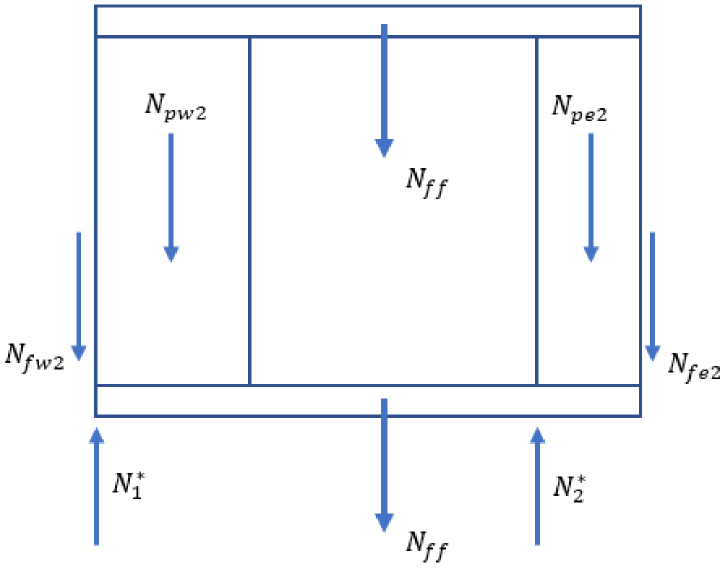

Figure 4.5 The free body diagram of the structural elements

The forces transferred to the ground floor piers from the dead load of the first floor, N_1^* and N_2^*, are not evenly distributed and depend on the lever arm induced by the rocking mechanism. These forces are calculated by considering the force and moment equilibrium of the structural elements resting on top of the ground floor piers as shown in Figure 4.5. The forces acting on the ground floor piers for the case of coupled and uncoupled piers are summarized in Table 4.1.

Table 4.1 Forces acting on the ground floor piers

Force Variable	**Upper Bound**			**Lower Bound**
	Cracking Pattern	**6 t pier**	**6 t wall**	**No Flange**
N_{f1} **(kN)**	7.64	3.45	4.14	0.00
N_{f2} **(kN)**	4.68	4.68	4.68	4.68
N_{pw1} **(kN)**	2.56	2.56	2.56	2.56
N_{pe1} **(kN)**	4.27	4.27	4.27	4.27
N_{pw2} **(kN)**	2.33	2.33	2.33	2.33
N_{pe2} **(kN)**	13.14	13.14	13.14	13.14
N_{ff} **(kN)**	53.57	53.57	53.57	53.57
N_1^* **(kN)**	63.12	63.12	63.12	63.12
N_2^* **(kN)**	76.90	76.90	76.90	76.90

The structural capacity of the structure is simply the sum of the base shear forces V_1 and V_2 multiplied by 2 to account for the use of symmetry. The resulting values for structural capacity V_b and the redistributed axial loads ΔN for all the scenarios considered in the calculation are summarized in the table below.

Table 4.2 Maximum structural capacity and redistributed loads calculated from the analytical method for uncoupled and coupled piers assumption

Case	Flange Effect	V_b (kN)		ΔN (kN)	
		Coupled	Uncoupled	Coupled	Uncoupled
Upper Bound	Cracking Pattern	81.78	84.87	10.30	0.00
	6t pier	78.83	81.80	9.93	0.00
	6t wall	79.32	82.30	9.99	0.00
Lower Bound	No Flange	62.57	64.86	7.90	0.00

The calculation results in higher structural capacity values for the uncoupled case. The assumption of different flange width results in small variations of structural capacity values, which indicates that the contribution of the bottom flange is not very significant to the overall capacity of the structure. The calculations for the coupled case yields quite significant values of redistributed axial load (ΔN), which means that the effect of axial load redistribution cannot be neglected from the analysis. By comparing the structural capacity and the redistributed load, it appears that both variables correlate positively with each other as a higher redistributed load tends to result in a higher maximum structural capacity.

It is important to note that the structural capacity values calculated above are the values for the zero lateral displacement state. As the lateral displacement increases, the second-order effect becomes more dominant and decreases the structural capacity.

4.2 Second-Order Effect

As has been discussed in the previous section, the second-order effect becomes more dominant as the lateral displacement increases. The increase in lateral displacement causes the piers to tilt and changes the length of moment arms in the free body diagram as shown in the figure below.

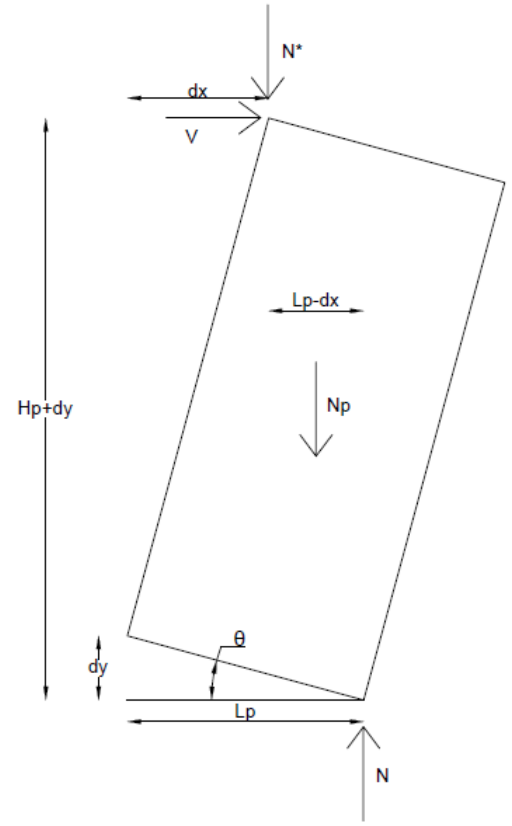

Figure 4.6 Free body diagram of the masonry pier with second-order effect included

The structural capacity calculation with the second-order effect is carried out in a similar fashion as the calculation in the previous section. The only difference is the change in the length of the moment arms, due to the tilting of the pier. The tilting of the pier increases the moment arm of the lateral load that tries to overturn the pier and decreases the moment arms of the axial loads that contribute to the resisting moment of the pier. Consequently, the structural capacity will decrease to compensate for the increased moment arm that results from the tilting. The following variables for the moment arms are defined mathematically as follows.

$$\theta = \frac{dx}{Hp}$$

$$dy = \theta . Lp = dx . \frac{Lp}{Hp}$$

The variables above are then incorporated into the calculation. The results of hand calculations with the second-order effect incorporated are plotted with the backbone curve in Figure 4.7 below. The upper bound values plotted are taken as the minimum structural capacity values from the three possible flange widths.

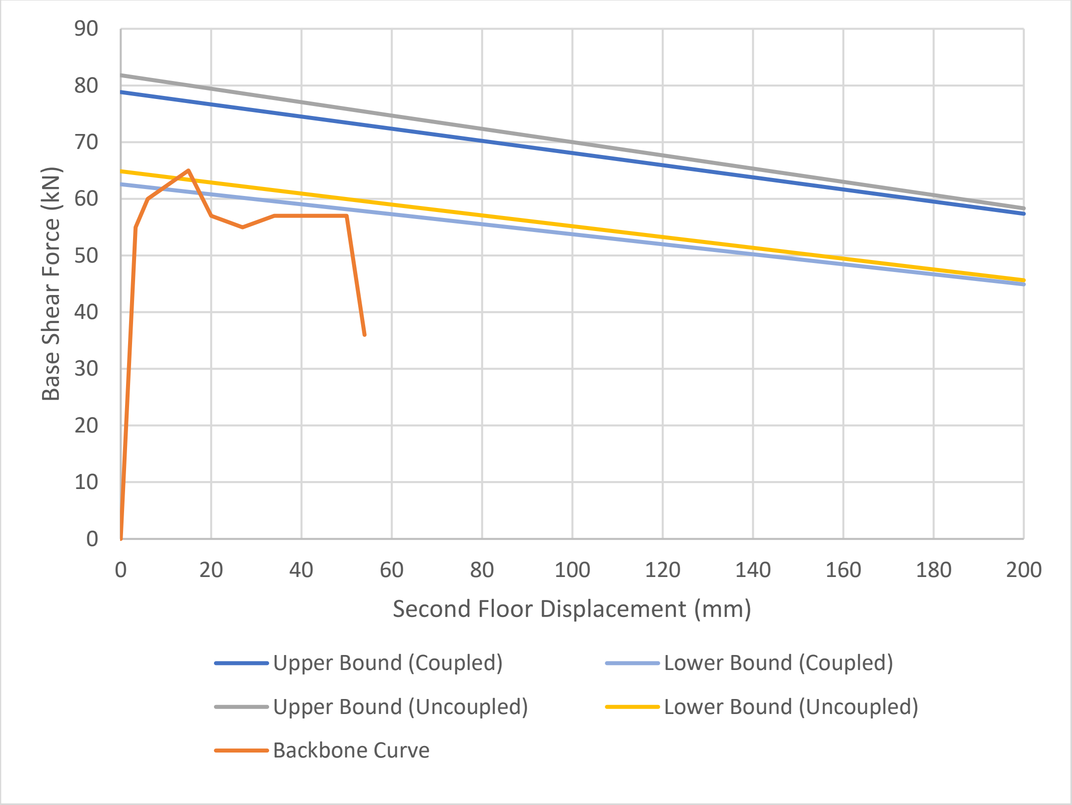

Figure 4.7 The structural capacity of the physical specimen from the hand calculation with the second-order effect

The figure above shows the calculated structural capacity for the physical specimen. The calculated structural capacity curves behave as expected with the structural capacity gradually decreasing as the second-order effect becomes more apparent with increasing horizontal displacement. The backbone curve falls within the boundary of the upper bound values. However, the lower bound values of the structural capacity are somehow higher than the backbone curve. These results are likely influenced by the assumption of how much concrete floor weight contributes to structural capacity.

Chapter 5
Finite Element Analysis Of Shell Elements Macro-Model

Two main variations of shell elements macro-model, each having different constitutive models, are considered for the analysis; Macro-TSRCM (Macro-Model with Total Strain Crack Model) and Macro-EMM (Macro-Model with Engineering Masonry Model). The analysis results of the Macro-TSRCM model will be discussed in section 5.1.1, while the analysis results of the Macro-EMM model will be discussed in section 5.2.1. Considering the uncertainty in the material parameters, the choice of material parameters for the analysis is crucial. A slight change in the value of the material parameters could affect the analysis results significantly. Therefore, sensitivity studies will be performed on both models. Sensitivity studies are conducted on the Macro-TSRCM model and Macro-EMM model in section 5.1.2 and section 5.2.2 respectively. The model variations considered in this project are summarized in the table below.

Table 5.1 Shell macro-model variations considered for the analysis

Modeling Approach	**Numerical Model**	**Constitutive Model (Continuum Element)**
Continuum macro-model (monotonic)	Macro-TSRCM	TSRCM
	Macro-EMM(1)	EMM
	Macro-EMM(2)	EMM

5.1 Macro-TSRCM: Macro-Model with Total Strain Crack Model

5.1.1 Nonlinear Pushover Analysis (Macro-TSRCM)

For the pushover analysis, the model will be subjected to both lateral loads and the self-weight of the structure. The pushover analysis will be performed with the displacement-controlled approach by applying a prescribed displacement on the numerical model. Considering the base shear force result of the physical experiment in Figure 3.4, a lateral displacement of 80 mm in the global X-direction will be applied to the model. The prescribed displacement is applied on the lateral support at the midpoint of the dummy beam to ensure equal distribution of loads on both floors.

The analysis is carried out in two phases. In the first phase, the model is loaded by its self-weight to simulate the static condition. The model is then subjected to the lateral load in the second phase until the prescribed displacement is reached or the analysis is stopped due to divergence. Details of the analysis including the lateral load applied, the nonlinearities considered, the load phases and the iteration schemes considered are presented in the table below.

Table 5.2 The analysis details of the nonlinear analysis of Macro-TSRCM model

Lateral Loads and Nonlinearities Considered		
Prescribed Displacement	80 mm in the global X-direction	
Physical Nonlinearity	Yes	
Geometrical Nonlinearity	No	
Loading Phases and Iteration Schemes		
Self Weight	**Load Steps**	0.1(10)
	Analysis Method	Newton-Raphson (Full)
	Force Norm	0.01
	Displacement Norm	0.01
Lateral Loading	**Load Steps**	0.00625(160)
	Analysis Method	Newton-Raphson (Full)
	Force Norm	0.01
	Displacement Norm	0.01

The results of the nonlinear pushover analysis are presented below.

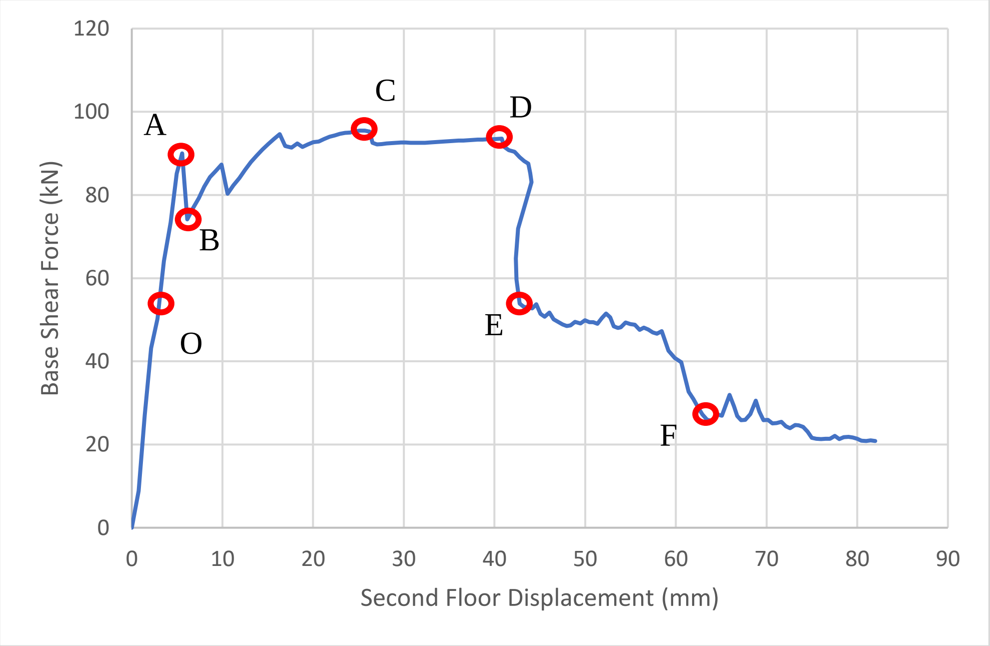

Figure 5.1 Capacity curve of the Macro-TSRCM model

Figure 5.1 shows the capacity curve of the Macro-TSRCM model. It can be seen from the curve that the structural capacity of 95.2 kN and the displacement capacity of 44.08 mm are reached by the numerical model. The numerical model has an initial stiffness value of 16.18 kN/mm. The pre-peak behavior of the numerical model is comprised of the initial linear increase in base shear force followed by the initiation of rocking mechanism and the transition to the plateau of relatively constant base shear force observed on the figure. The post-peak behavior is signified by a sudden drop in structural capacity due to the failure of the long pier at event D as shown in Figure 5.1. Increasing the horizontal displacement after this point results in the development of diagonal cracking failure on the short pier at event E.

The evolution of the cracking pattern of the model is presented in the following figure as follows.

Table 5.3 The evolution of cracking patterns on Macro-TSRCM model corresponding to the events in Figure 5.1

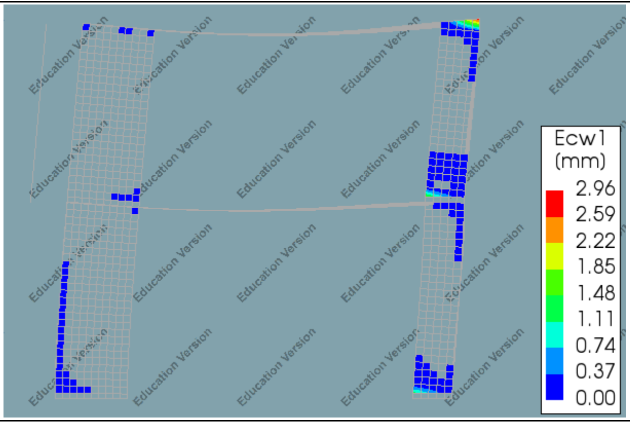	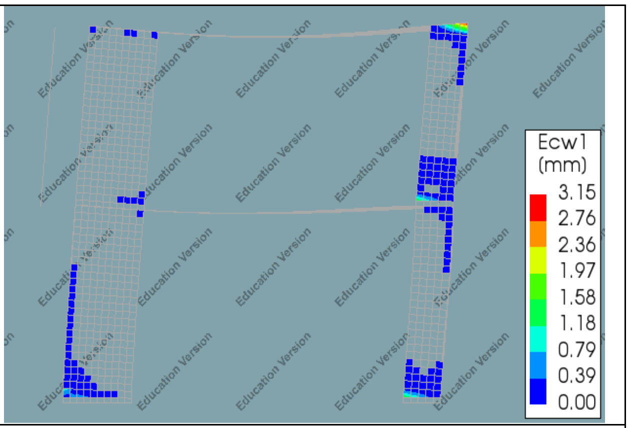
(A) Initiation of rocking mechanism	(B) Loss of structural capacity at the bottom joint of the long pier
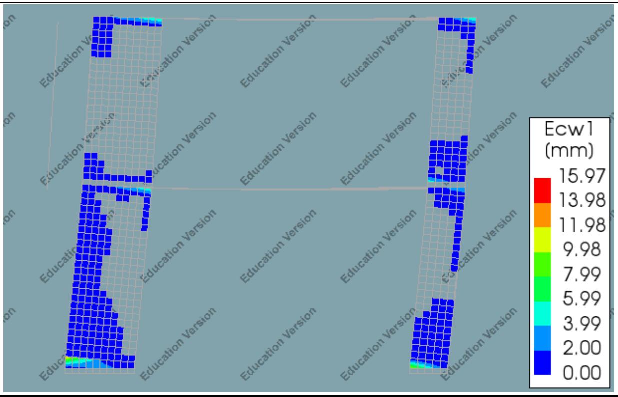	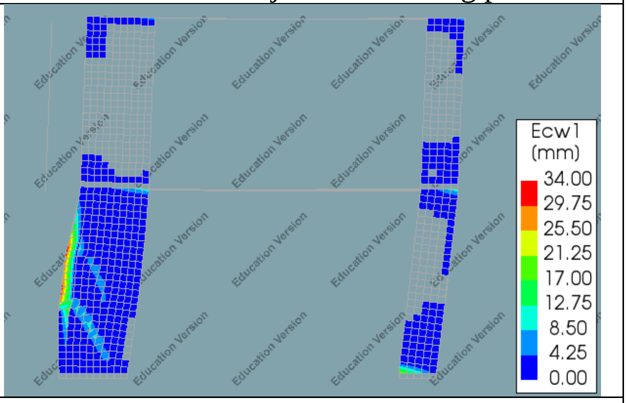
(C) Peak base shear force reached	(D) Near-collapse displacement reached

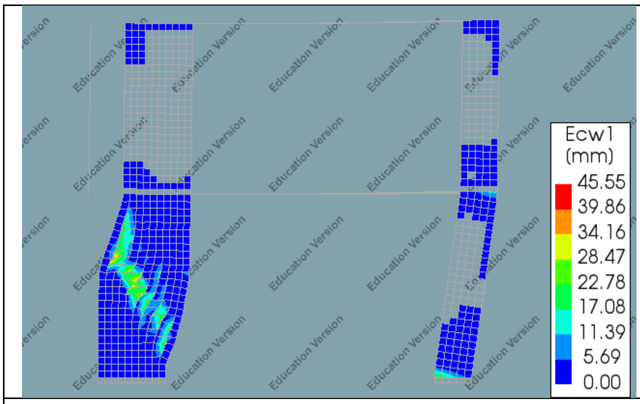	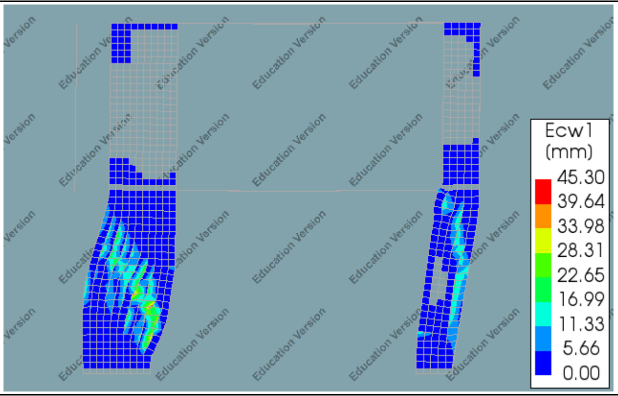
(E) Diagonal cracking failure of the long pier	(F) Diagonal cracking failure of the short pier

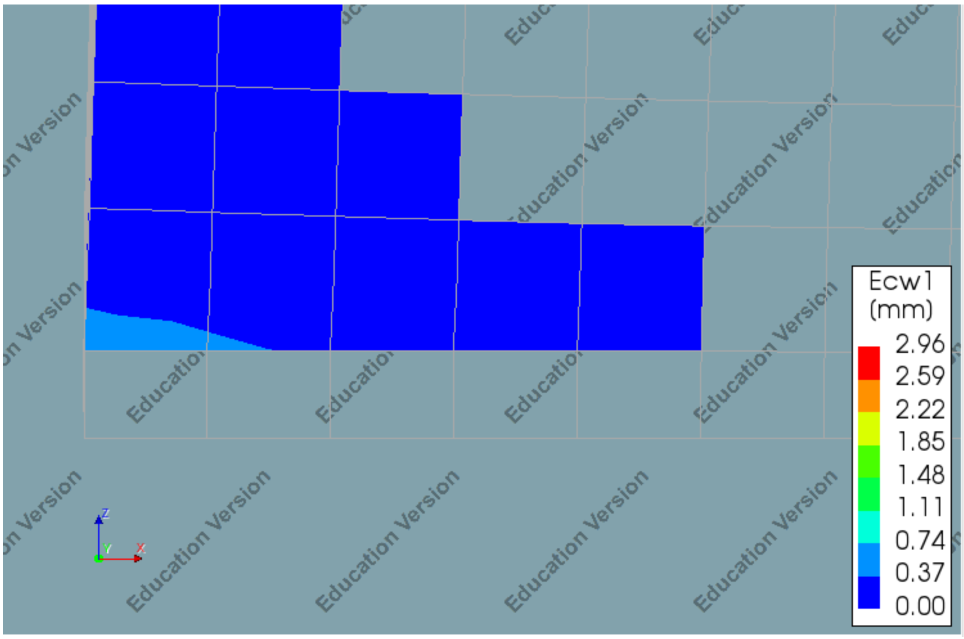

Figure 5.2 Deformed meshes at the bottom joint of the ground floor long pier at event A

The progression of failure mechanisms of the numerical model, represented with the principal crack-width contour plots, are shown in Table 5.3. The figure shows the activation of the rocking mechanism on the numerical model at event A indicated by the opening of the cracks at the extremities of the masonry structural elements. This opening of cracks at the bottom of the long pier is signified by the deformed finite element meshes shown in Figure 5.2. The horizontal loads continue to push the model causing the piers to continue tilting. As the horizontal displacement continues to increase, compression struts start to form in the long pier. The formation of these compression struts causes the opening of cracks in the connection between the long pier and the transversal wall as can be seen at event D. The compression struts then collapse abruptly causing diagonal cracking failure on the model at event E.

From the results presented above, several interesting observations can be made. The first is the fact that the activation of the rocking mechanism at event A results in a quite noticeable decrease in base shear force. Examination of the crack width contour plot of event A and event B indicates that the drop in the base shear force coincides with the opening of large cracks at the bottom of the ground floor long pier. The opening of tensile cracks at the base of the long pier causes the structure to suffer from a slight loss of capacity and a significant reduction in stiffness. After the loss of capacity of the bottom joint, the lateral loads are then transferred to the other joints of the structure, which are still able to sustain load increasing structural capacity. As another crack opens at a joint, the structural capacity drops slightly again and the load is transferred to another joint once more. This phenomenon continues until all cracks induced by the rocking mechanism are opened and the maximum structural capacity is reached. This phenomenon can be seen as the zigzag pattern observed on the capacity curve just after the linear region in Figure 5.1.

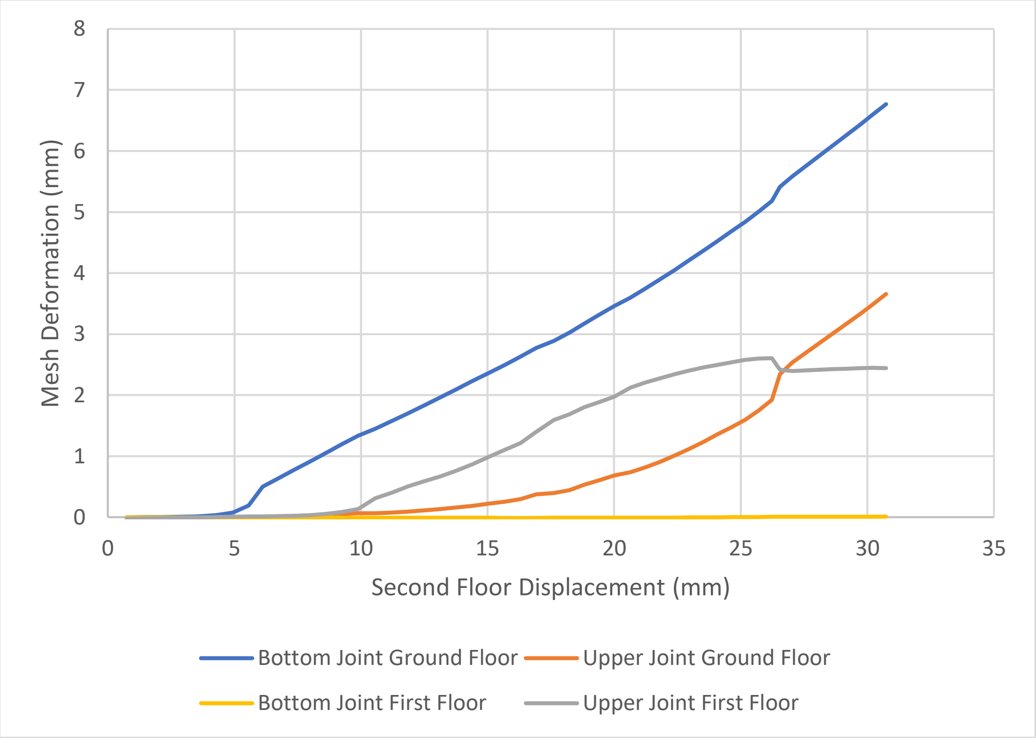

Figure 5.3 The mesh deformation at the joints of the long pier (Macro-TSRCM)

Figure 5.3 shows the plot of the finite element meshes deformation at the long pier joints, where tensile cracks occur on the model. The curve for the mesh deformation at the bottom joint of the ground floor long pier shows an initial zero mesh relative deformation. At a horizontal displacement of 5.56 mm, the mesh suddenly starts to undergo a significant increase in deformation. This coincides with the opening of large tensile cracks at the joint, which activates the rocking mechanism of the structure. The development of the rocking mechanism can be seen on the figure with cracks gradually opening at other joints on the structure as the horizontal displacement continues to increase. The opening of cracks at the upper joint of the first floor long pier can be seen occurring at the horizontal displacement of 9.98 mm, which coincides with the second drop in structural capacity on the capacity curve. This is then followed by another opening of cracks at the upper joints of the ground floor long pier. The opening of cracks at the joints of the ground floor pier indicates the existence of a soft-story mechanism on the ground floor.

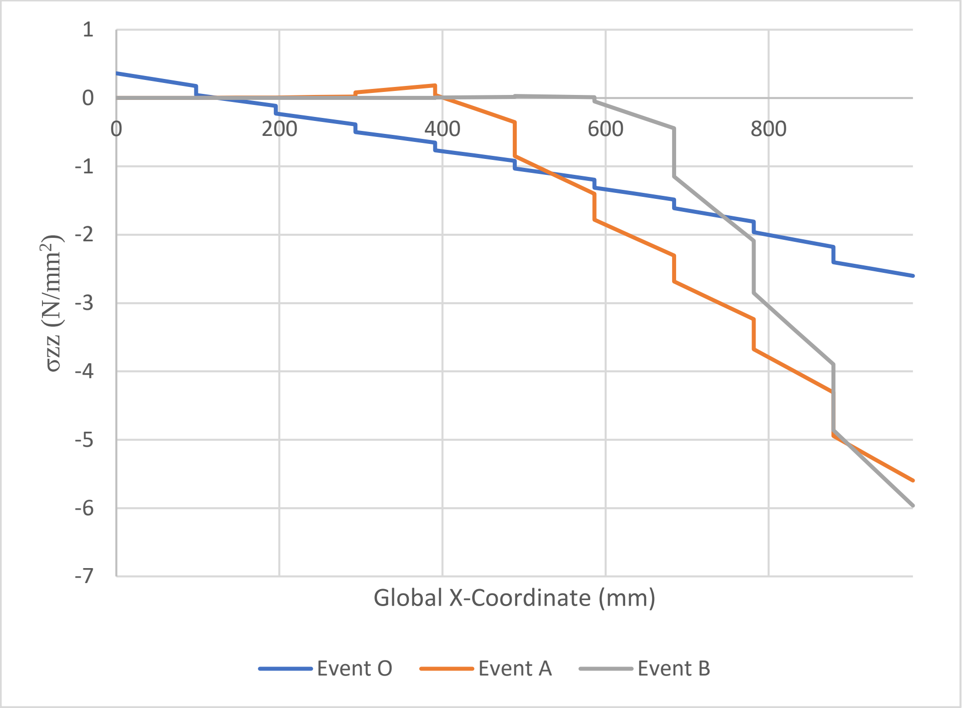

Figure 5.4 Vertical stress distribution in the long pier (Macro-TSRCM)

The vertical stress distributions in the long pier shown in Figure 5.4 provide a closer look at the structural behavior in the pre-peak region. The vertical stress distribution curve at event O shows a linear stress distribution signifying the flexural behavior of the structure. The stress distribution shows the maximum tensile stress value of 0.36 N/mm^2, which is slightly lower than the defined tensile strength of 0.39 N/mm^2. This is consistent with the expectation of the behavior of the shell elements constitutive model. The stress distribution shows that the maximum tensile strength is reached before the activation of the rocking mechanism at event A, which forms micro-cracks at the base of the long pier. As the horizontal displacement of the structure increases, the crack energy is gradually dissipated and a portion of the long pier completely loses its capacity, which is signified by the stress distribution at event A. After event A, the ultimate tensile crack strain (ε_{ult}) is exceeded and the rocking mechanism is activated, which is accompanied by a significant loss of structural capacity and a significant increase in tensile crack width as shown in Figure 5.1 and Figure 5.2.

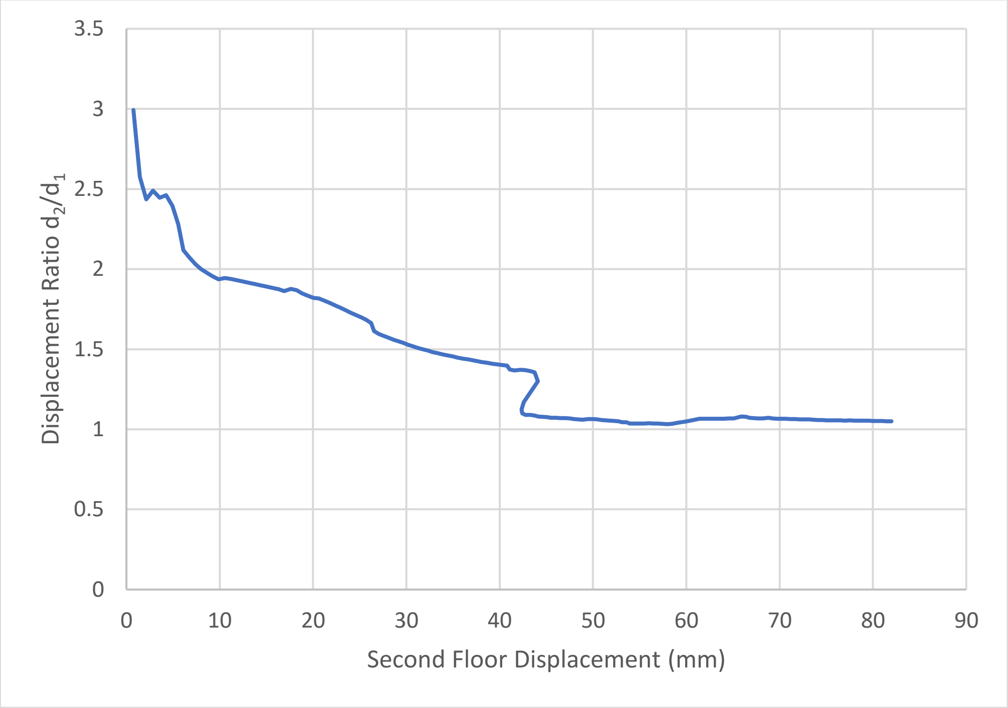

Figure 5.5 Interstory drift curve of the Macro-TSRCM model

The interstory drift of the model is plotted in Figure 5.5 in terms of the displacement ratio between the first floor and the ground floor (d_2/d_1). The interstory drift curve shows a decreasing trend in the displacement ratio. A sharp drop is observed on the curve at the lateral displacement of 44 mm. This corresponds to the diagonal cracking failure of the bottom floor piers. The displacement ratio then remains constant indicating the existence of a soft-story mechanism on the ground floor. This is confirmed by the deformation of the model and the localization of damage on the ground floor of the model shown in Table 5.3.

Table 5.4 The distribution of vertical reaction force in the half of the Macro-TSRCM model

Structural Element	**Vertical Reaction Force (kN)**	
	Static Condition	**Peak Base Shear Force**
Long Pier	20.25	69.98
West Wall	75.08	2.01
Short Pier	12.13	0.43
East Wall	71.84	106.87
Total Reaction Force	179.30	179.30

Table 5.4 shows the distribution of the vertical reaction force at the base of the structure before the structure is loaded with lateral forces and after the maximum structural capacity is achieved. The sum of the reaction forces between the two points shows the same value, which satisfies the vertical force equilibrium. A comparison of the reaction forces at the

two different points in the analysis shows the redistribution of reaction forces between the masonry structural elements. The redistribution of reaction forces causes the reaction forces in the left transversal wall and the long pier to decrease, while the reaction forces in the right transversal wall and the short pier increase. This is consistent with the assumption of force redistribution taken for the hand calculation in Chapter 4. Further examination of the reaction forces, however, reveals a redistributed load (ΔN) value of 23.33 kN, which is twice the estimated value from the hand calculation. This discrepancy in redistributed load makes it difficult to correlate the numerical model to one of the hand calculation estimations.

5.1.2 Sensitivity Study (Macro-TSRCM)

A sensitivity study on the Macro-TSRCM model is conducted on variables related to the tensile cracking and crushing behavior of the structure. Those variables are the tensile fracture energy (G_{ft}^{I}), the tensile strength (f_t), the compressive fracture energy (G_{fc}) and the compressive strength (f_c). The sensitivity study is conducted on the model by varying the values of those parameters and performing pushover analysis on the model. An additional analysis with varied values of the concrete floor's Young's Modulus is also carried out to check the effect of different stiffness of concrete floor on the structural capacity.

Tensile Fracture Energy (G_{ft}^{I})

The first structural parameter to be investigated is the tensile fracture energy. The sensitivity study is conducted with the following values.

Table 5.5 G_{ft}^{I} parameters used for the sensitivity study (Macro-TSRCM)

Portion	**G_{ft}^{I} (N/mm)**
100%	0.021
75%	0.0158
60%	0.0126
50%	0.0105

The capacity curves are presented in the following figure.

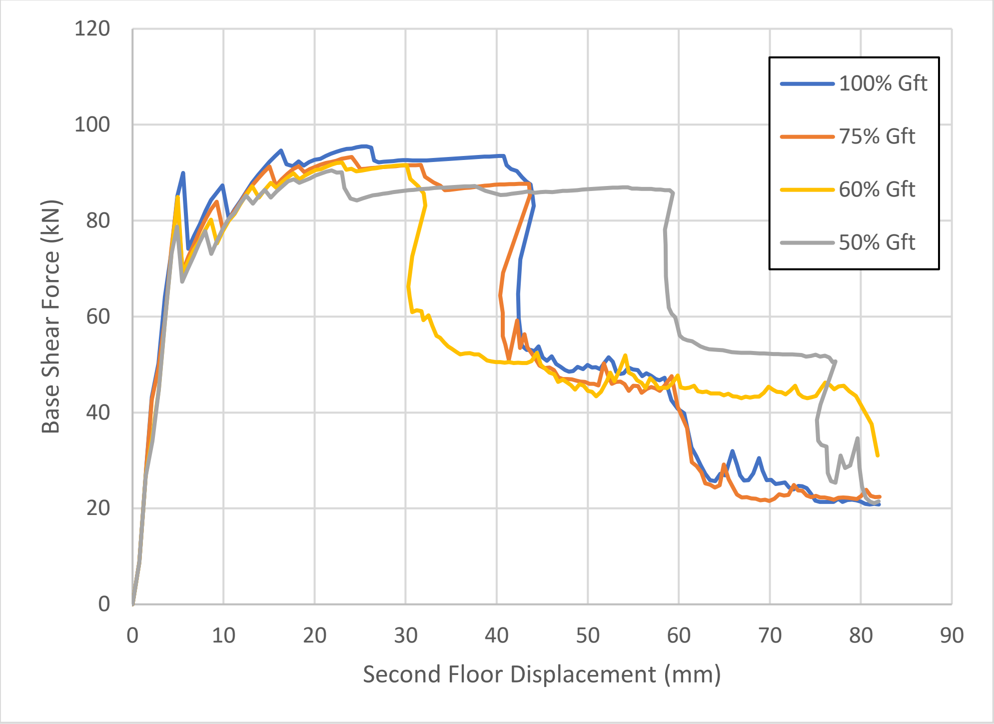

Figure 5.6 Capacity curves from sensitivity study on G_{ft}^{I} parameter (Macro-TSRCM)

As can be seen from the capacity curves, changes in the value of G_{ft}^{I} affect both the pre-peak and post-peak behavior. There is a clear trend in the reduction of the structural capacity and the load required to activate the rocking mechanism. These reductions in the structural capacity and cracking load are caused by the change in tensile cracking behavior, which governs the pre-peak behavior of the structure. As the tensile fracture energy required to open a crack decreases, the load required to activate the rocking mechanism also decreases which in turn decreases the structural capacity. This reduction is, however, not very significant, despite the considerable reduction in G_{ft}^{I}. Considering that tensile fracture energy governs the pre-peak behavior of the structure, this behavior is very unusual for this particular case. A check is conducted on a node at the bottom joint by plotting the stress-relative displacement curves of the model variations in Figure 5.7.

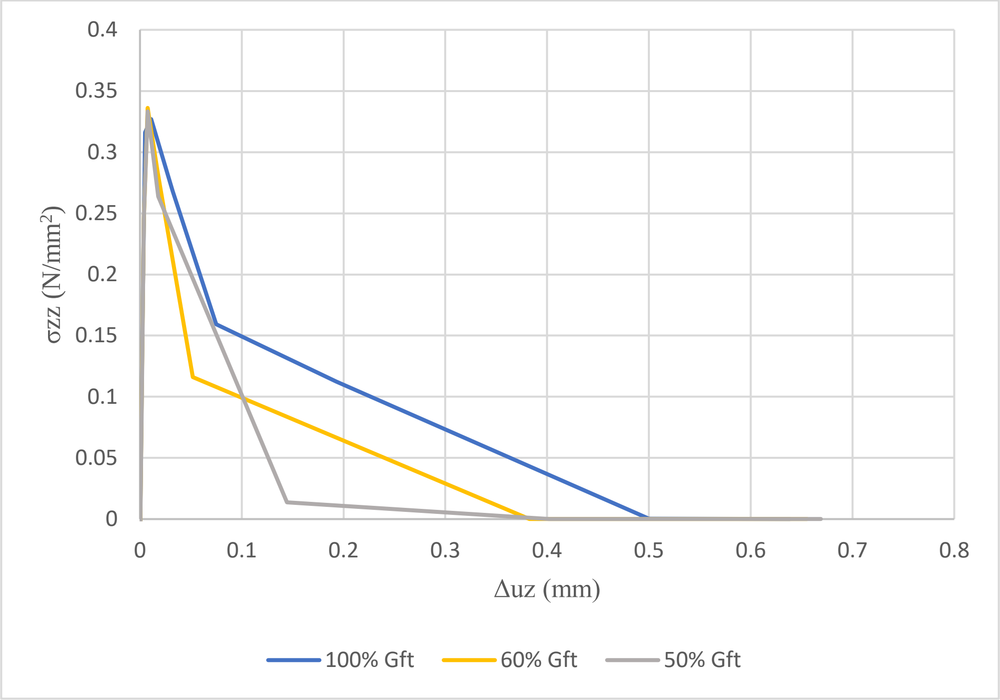

Figure 5.7 Constitutive model check at the bottom joint of the ground floor long pier of Macro-TSRCM model (G_{ft}^{I} parameter)

The model variations curves show that they are consistent with the expected behavior of the Total Strain Crack Model in the tensile region. The tensile strength of the curves remains unchanged and it is evident that each curve has different tensile fracture energy, which is indicated by the different total area under each curve, with a smaller area for curves with lower tensile fracture energy. Overall, the stress-relative displacement curves do not show any sign of abnormality. Considering this, there must be another factor that causes the overestimation of structural capacity.

The post-peak behavior of the structure sees a more significant change from the alteration of G_{ft}^{I} value. The reduction of tensile fracture energy causes the onset of diagonal cracking failure in the long pier to occur at an earlier point, which can be seen on the 75% G_{ft}^{I} and 60% G_{ft}^{I} curve. This trend is, however, not always consistent as demonstrated by the 50% G_{ft}^{I} curve. In the case of the 50% G_{ft}^{I} curve, the failure sequence of the piers is altered and the diagonal cracking failure occurs in the short pier before the long pier. This phenomenon is most likely caused by the interaction between the failure of the long pier and the short pier.

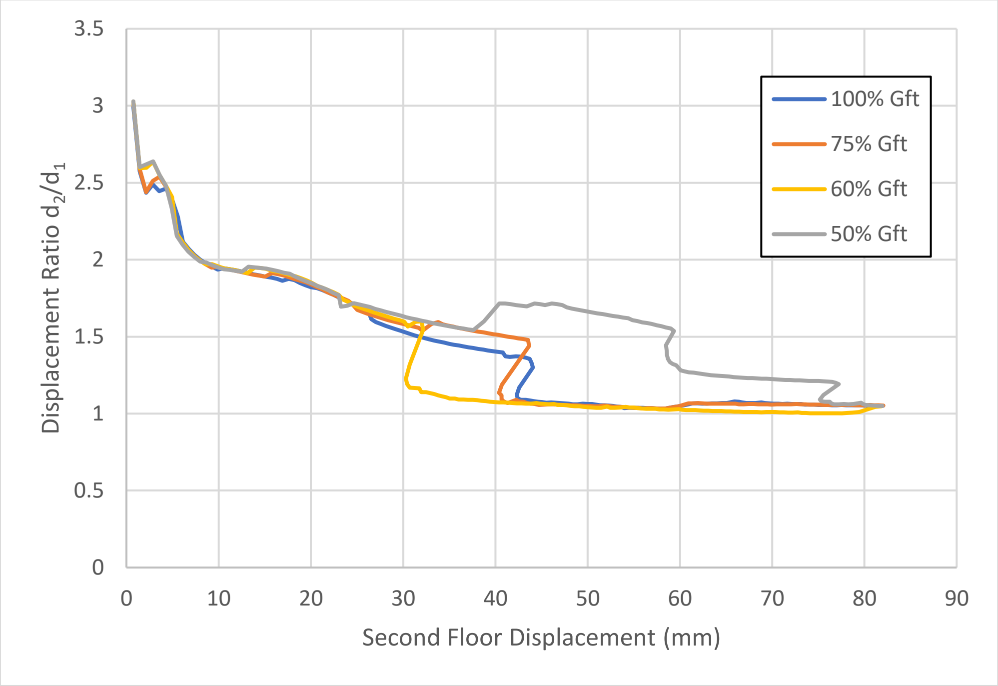

Figure 5.8 Interstory drift curves from the sensitivity study on G_{ft}^{I} parameter (Macro-TSRCM)

The interstory drift curves all show a consistent trend in the decrease of the displacement ratio with increasing horizontal displacement. The post-peak behavior of the numerical models shows a large variation similar to what has been observed in the capacity curves, especially compared to the relatively consistent pre-peak behavior. All interstory drift curves show a sudden decrease in the displacement ratio, which corresponds to the diagonal cracking failure of the piers.

Tensile Strength (f_t)

The following values of f_t are used for the sensitivity study.

Table 5.6 f_t parameters used for the sensitivity study

Portion	**f_t (N/mm^2)**
100%	0.390
75%	0.293
60%	0.234
50%	0.195

The capacity curves are presented as follows.

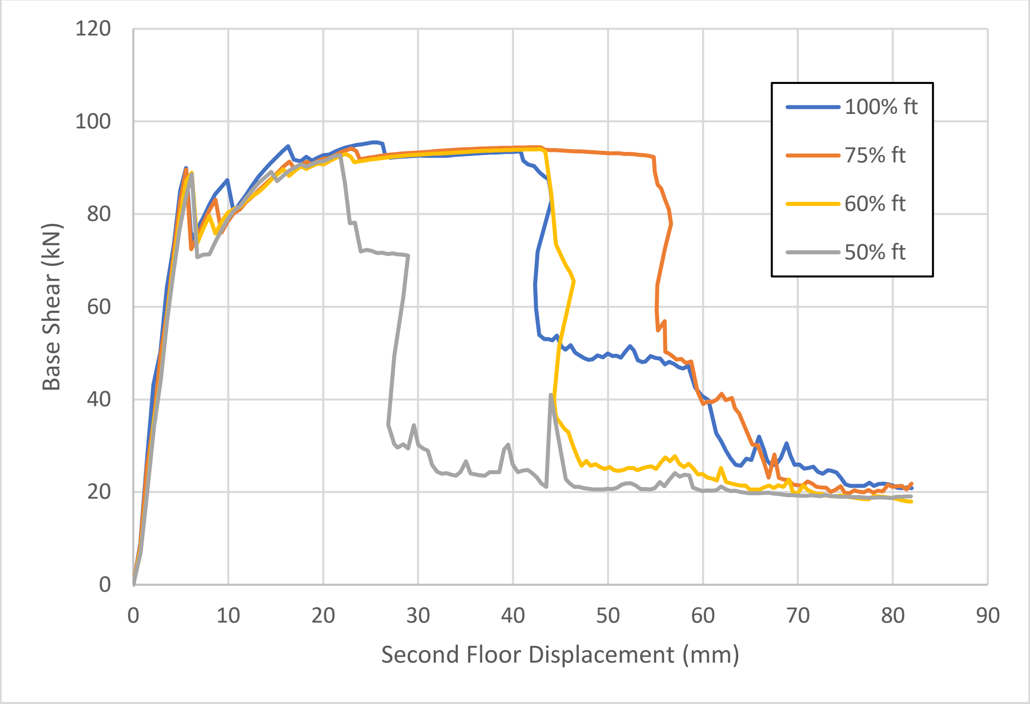

Figure 5.9 Capacity curves from the sensitivity study on f_t parameter (Macro-TSRCM)

Based on the capacity curves, the pre-peak behavior of the model variations is not significantly affected by the changes. The base shear force required to initiate the rocking mechanism remains the same despite the significant reduction in f_t. This behavior is unexpected since the tensile strength is expected to play a significant role in the tensile cracking behavior of the structure. A check on the constitutive model is performed by plotting the traction-relative displacements curves of a node located on the edge of the long pier.

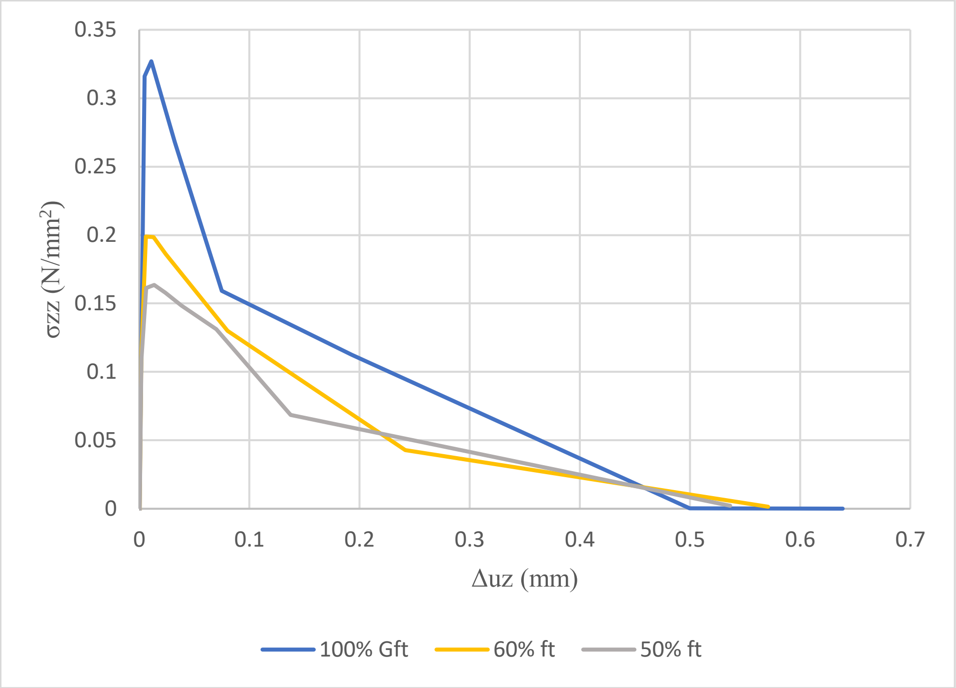

Figure 5.10 Traction-relative displacements curve of a mesh at the bottom joint of the ground floor long pier of Macro-TSRCM model (f_t parameter)

The curves in Figure 5.10 show different values of tensile strength, which is the expected behavior of this particular constitutive model. The 60% f_t and 50% f_t curve, however, show a considerably lower tensile fracture energy than the unmodified model, which is shown by the area under the curve. This does not match with the expected behavior as the tensile fracture energy is expected to remain the same between the curve. The source of this discrepancy is still unclear. Possible causes might include a bug in the software package or a modeling mistake. However, this discrepancy still does not explain the reason for the limited effect the tensile strength has on the pre-peak region. Thus, there is likely another factor influencing the pre-peak behavior of the structure.

Despite the lack of significant changes to the pre-peak behavior of the structure, the post-peak behavior sees a very significant change. The change in the value of f_t seems to significantly affect the onset of the diagonal cracking failure on the model. The reduction of the tensile strength (f_t) tends to cause the onset of the diagonal cracking failure to occur earlier. However, this is not always consistent as can be seen from Figure 5.9. This inconsistency is likely caused by the interaction between the long pier and the short pier, as in some cases the failure sequence of the two piers is switched with the short pier collapsing before the long pier.

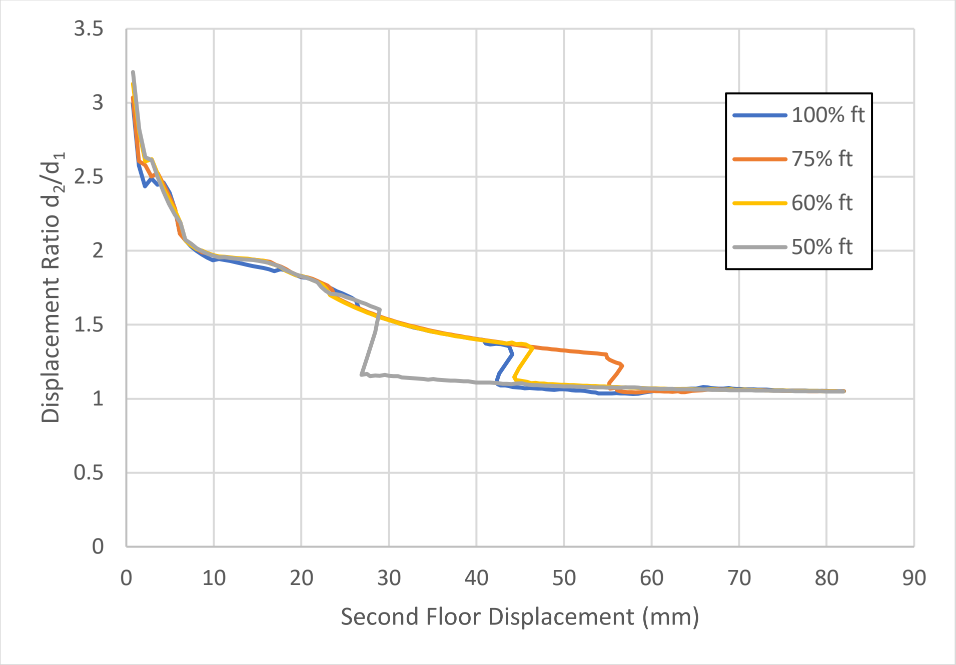

Figure 5.11 Interstory drift curves from sensitivity study on f_t parameter (Macro-TSRCM)

As with the capacity curves, the interstory drift of the model in the pre-peak region is not greatly affected by changes in the value of f_t. The changes affect mostly the post-peak region. All interstory drift curves feature sudden decreases in the displacement ratio, which are related to the diagonal cracking failure seen in Figure 5.9. The displacement ratio of all model variations shows a relatively consistent behavior with the values approaching unity and remains relatively constant after the failure of the piers.

Based on the observations of the results, it can be concluded that the analysis results of the model are very sensitive to the changes in the values of f_t.

Compressive Fracture Energy (G_{fc})

The following G_{fc} values are used for sensitivity study.

Table 5.7 G_{fc} parameters used for the sensitivity study

Portion	**G_{fc} (N/mm)**
100%	20.29
75%	15.22
60%	12.17
50%	10.15

The results of the analysis are presented in the figures below.

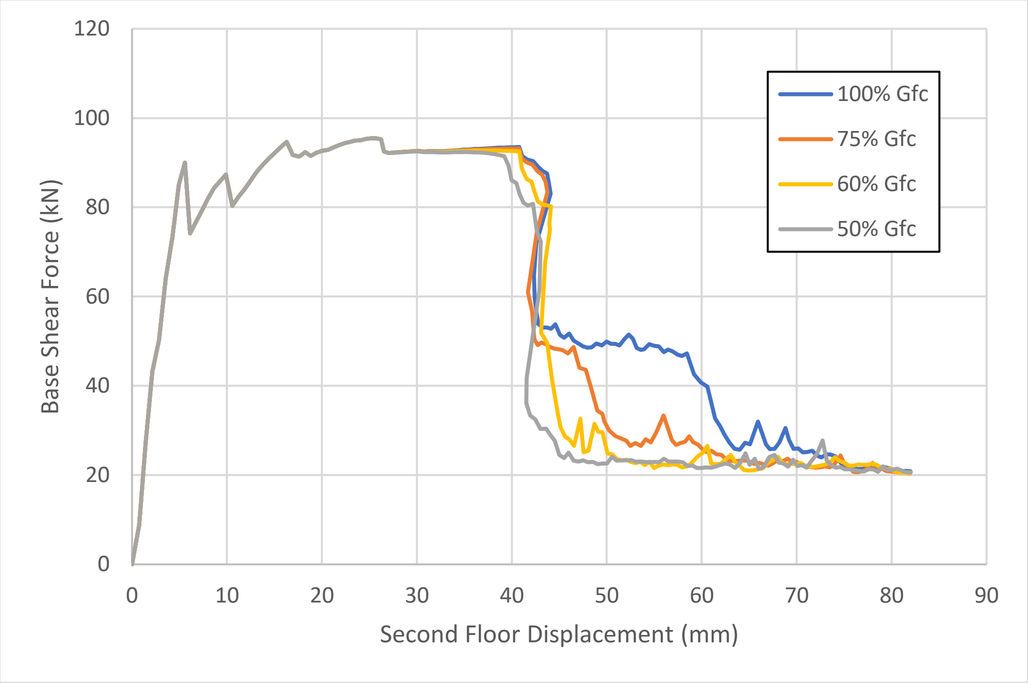

Figure 5.12 Base shear force curves from sensitivity study on G_{fc} parameter (Macro-TSRCM)

The capacity curves from the analyses show no change in the pre-peak behavior, which is consistent with the expectation, since G_{fc} does not govern tensile cracking behavior. Only post-peak behavior is affected by the change in the value of G_{fc}. As can be observed from Figure 5.12, changes in the value of G_{fc} affect the failure behavior of the short pier. Reduction of G_{fc} causes the collapse of the short pier to occur earlier. From the engineering perspective, this development is of little importance, since the structure can already be considered failing after the diagonal cracking failure of the long pier occurs. Therefore, it can be concluded that G_{fc} does not play a crucial role in the structural analysis.

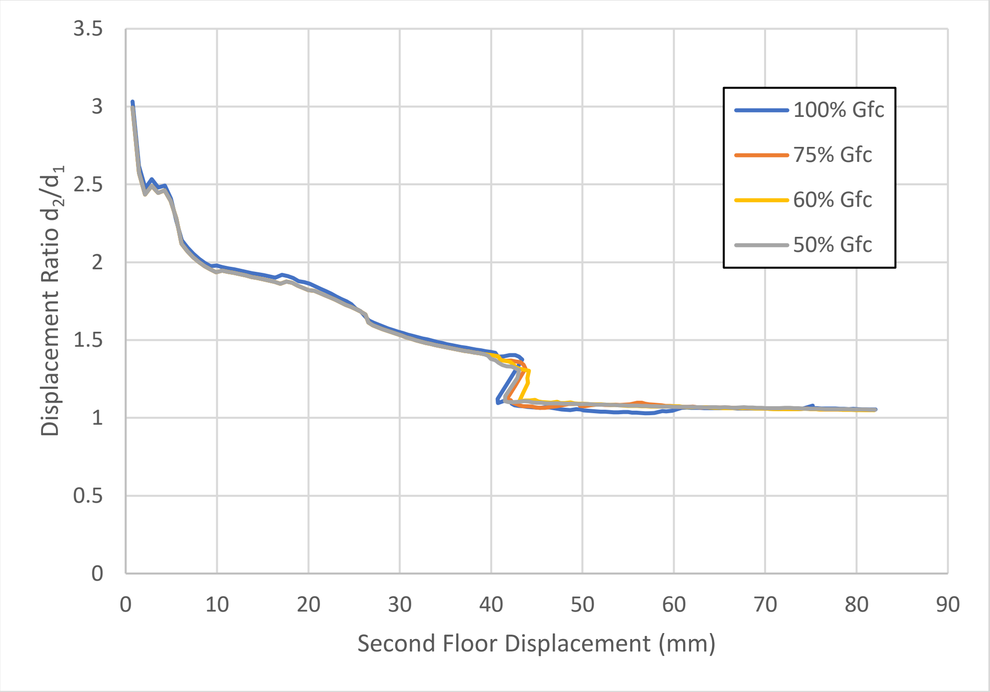

Figure 5.13 Interstory drift curves from sensitivity study on G_{fc} parameter (Macro-TSRCM)

No significant change occurs to the interstory drift from the change in the values of G_{fc}. All interstory drift curves show relatively consistent behavior.

The analysis results show that the pre-peak behavior of the model is insensitive to the change in G_{fc}. The change observed is limited only to the post-peak region, particularly after the first instance of the long pier failure. Considering that the most significant change in the post-peak behavior occurs after the collapse of the long pier, it can be concluded, that the variable G_{fc} does not play a very important role in the analysis.

Compressive Strength (f_c)

The following f_c values are used for the sensitivity study.

Table 5.8 f_c parameters used for the sensitivity study

Portion	**f_c (N/mm)**
100%	13.93
75%	10.45
60%	8.36
50%	6.97

The results of the analysis are presented in the following figure.

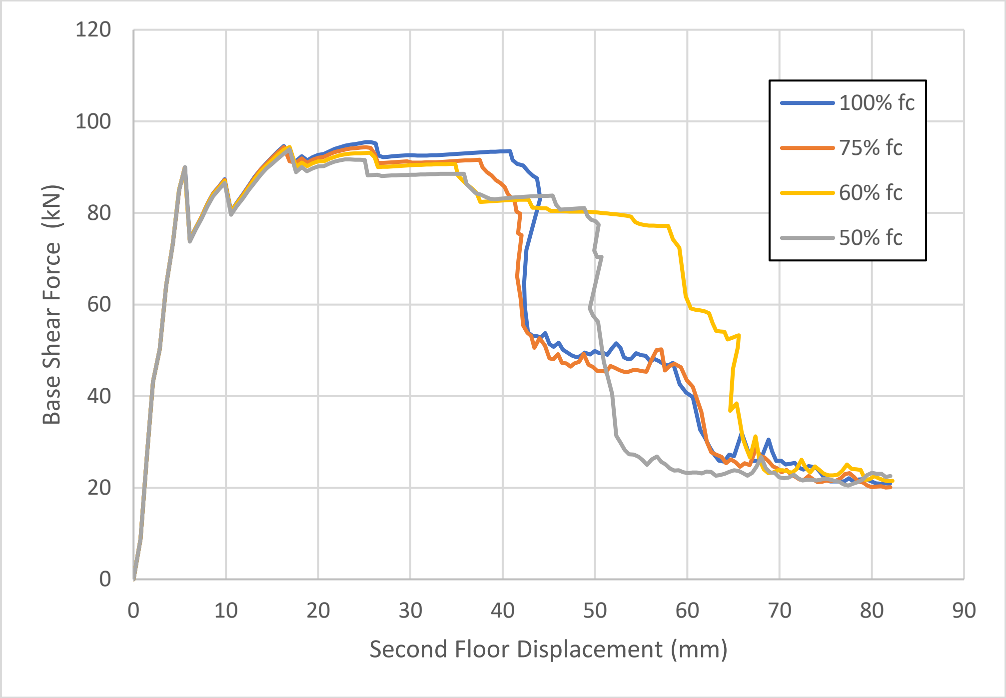

Figure 5.14 Capacity curves from the sensitivity study on f_c parameter (Macro-TSRCM)

The capacity curves show that changing the value of f_c does not significantly affect the pre-peak behavior of the structure as f_c does not govern tensile cracking behavior. Changes in the value of f_c mainly affect the post-peak behavior of the structure, which is mainly related to the collapse of the piers. It is, however, difficult to find a consistent trend from the curves, which is partly caused by the interaction between the long pier and short pier. From the curves, it can be seen that the reduction in the value of f_c generally causes the structure to behave more ductile with increased displacement capacity, although this trend is not entirely consistent as can be seen with the 60% f_c and 50% f_c curve. The interaction between the failure of the long pier and short pier also appears to contribute to the lack of consistent trend in the results, as can be seen with the 60% f_c curve. The failure sequence of the 60% f_c curve is changed drastically with the short pier undergoing failure first instead of the long pier.

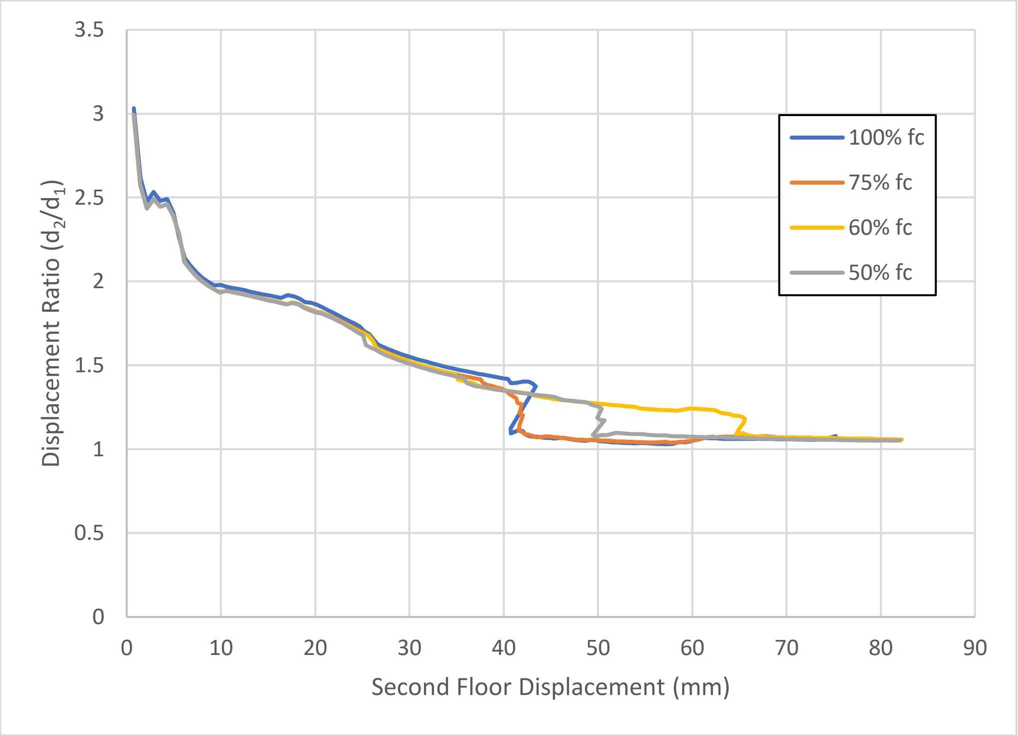

Figure 5.15 Interstory drift curves from sensitivity study on f_c parameter (Macro-TSRCM)

The interstory drift curves show consistent behavior in the pre-peak region. A noticeable difference can be observed in the post-peak region, where the displacement ratios exhibit sudden decreases from diagonal cracking failure. These sudden decreases correlate with the sudden drops in base shear force shown in Figure 5.14.

From the analysis results, it appears that the analysis is relatively sensitive to the change in the value of f_c especially concerning the failure behavior of the piers. A slight change in f_c can change the failure sequence of the model considerably.

Concrete Floor Young's Modulus (E_c)

An additional sensitivity study is carried out by varying the value of Young's modulus of the concrete floor to assess the effect of the change in the stiffness of the concrete floor on the structural behavior of the model. For this particular sensitivity study, an analysis with a concrete Young's modulus value one order of magnitude higher will be performed.

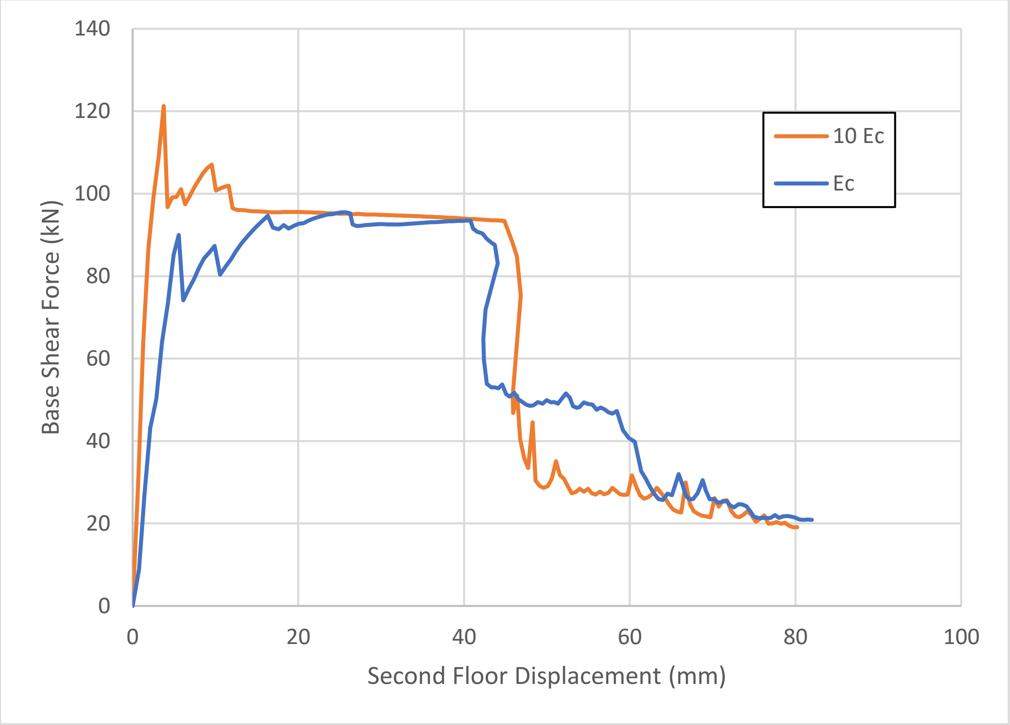

Figure 5.16 Capacity curves from the sensitivity study on E_c parameter (Macro-TSRCM)

The capacity curves of the Macro-TSRCM model with different values of E_c parameter are shown in Figure 5.16. It can be seen that the change in the stiffness of the concrete floor causes significant changes in the structural behavior of the model. The most considerable change to structural behavior is observed in the pre-peak region. It appears that the increase in the stiffness of the concrete floors increases the initial stiffness and the peak base shear force significantly. The peak base shear force also occurs at the point of the activation of the rocking mechanism instead of at the plateau. The stiff concrete floors cause changes in the behavior of the tensile cracks opening in the piers. These changes are shown by the vertical mesh deformation plot in Figure 5.17, where it can be seen that the rocking cracks at the joints open almost simultaneously, instead of gradually as in the case with the unmodified model. It is interesting to note that after the rocking mechanism is initiated, the base shear force drops to a level that is similar to the unmodified model variation. This is most likely related to the fact that tensile cracking parameters (G_{ft}^{I} & f_t) are left unmodified.

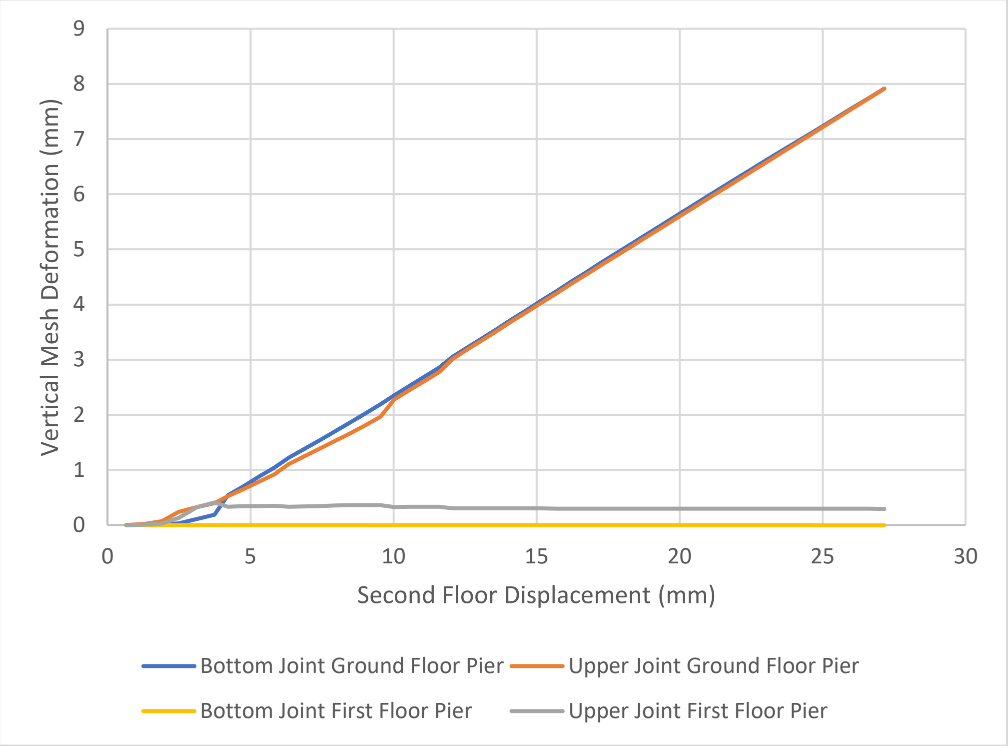

Figure 5.17 The deformation of finite element mesh at the joints of the long pier (Macro-TSRCM with E_c value one order of magnitude higher)

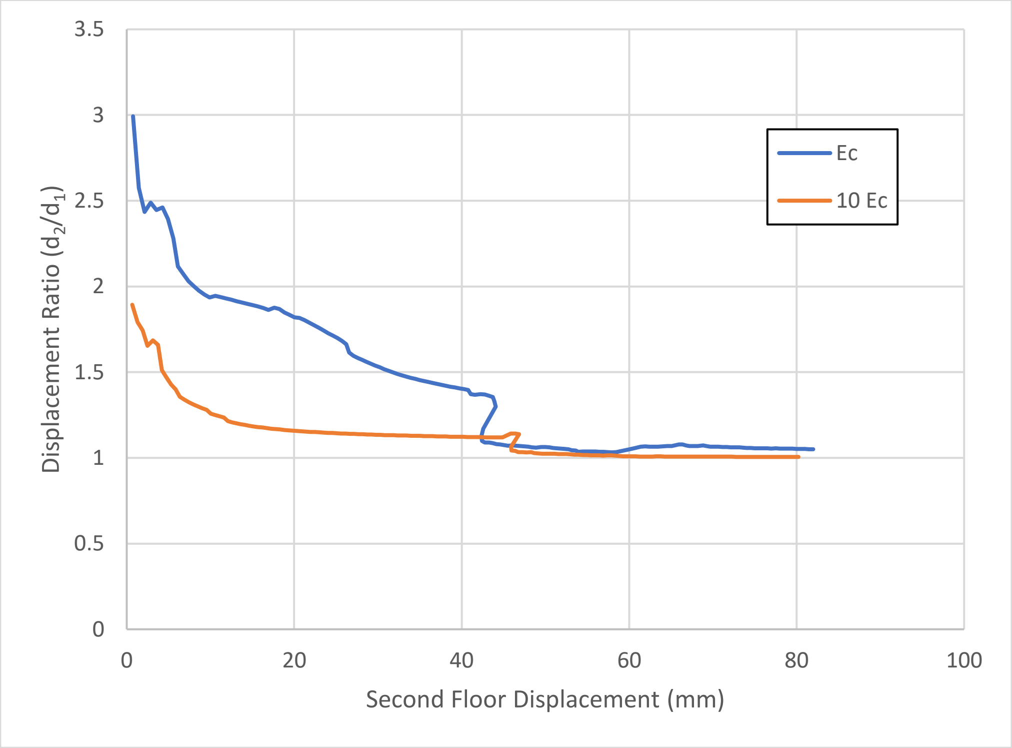

Figure 5.18 Interstory drift curves from sensitivity study on E_c parameter (Macro-TSRCM)

Apart from affecting the capacity of the structure, the change in the stiffness of the concrete floors also affects the interstory drift of the structure. It can be observed from Figure 5.18, that the displacement ratio in the pre-peak region is significantly reduced with the higher concrete floor stiffness. The reduction of the displacement ratio is caused by the increase in the overall structural stiffness from the stiffer concrete floors. The soft-story mechanism at the ground floor also occurs earlier as shown by the low values of the displacement ratio before diagonal cracking failure. The stiffer concrete floors cause the rocking of the piers to be localized on the ground floor.

Summary of Sensitivity Study Results

The results of the sensitivity study conducted on the Macro-TSRCM model are summarized in the table below.

Table 5.9 Qualitative results of the sensitivity study on the Macro-TSRCM model

Variable	**Result**
G_{ft}^{I}	Very sensitive. Small changes in the pre-peak region. Erratic and unpredictable collapse behavior.
f_t	Sensitive. Large changes observed on the post-peak behavior, especially regarding the near-collapse displacement. Failure sequence changes from the alteration in variable.
G_{fc}	Insensitive in the pre-peak region. Relatively sensitive in the post-peak region. Changes are related to the failure of the short pier.
f_c	Sensitive. Change in the value of the variable leads to small changes in the region around the peak. Large changes are observed in the post-peak region related to the failure modes.

Observation of the results indicates that changes to the material parameters above mainly affect the structural behavior in the post-peak region. The structural behavior in the pre-peak region and the structural capacity are not significantly affected, even when the two main variables governing tensile cracking behavior, tensile strength (f_t) and tensile fracture energy (G_{ft}^{I}), are significantly changed. This indicates that there is another factor or parameter not considered in this study, that influences the structural capacity and the structural behavior in the pre-peak region. As for the post-peak region, analysis results have shown that slight change to most of the material parameters can have a very large influence in the displacement capacity and the failure sequence of the structure.

From the results of the sensitivity study on the concrete floor Young's modulus, it appears that the change in the parameter can significantly alter the behavior of the structure in the pre-peak region, especially related to the initiation of the rocking mechanism on the numerical model. A conclusion on the sensitivity of the analysis to the change in the parameter cannot yet be made and requires further investigation. It is, however, clear that careful consideration in the choice in the concrete Young’s modulus value for the analysis is advised.

5.2 Macro-EMM: Macro-Model with Engineering Masonry Model

5.2.1 Nonlinear Pushover Analysis (Macro-EMM)

The nonlinear pushover analysis on the model with the EMM constitutive model is performed in a similar fashion to the analysis of the model with the TSRCM constitutive model. Similar to the analysis of the previous model, the analysis is performed in two phases: the self-weight phase and the lateral loading phase. For this analysis, a prescribed displacement of 200 mm in the global X-direction is applied. The higher value of prescribed displacement is chosen to capture the post-peak behavior of the numerical model clearly. The iteration schemes and the convergence norms used for each loading phase are presented in the table below.

Table 5.10 The analysis details of the nonlinear analysis of Macro-EMM model

Lateral Loads and Nonlinearities Considered		
Prescribed Displacement	200 mm in the global X-direction	
Physical Nonlinearity	Yes	
Geometrical Nonlinearity	No	
Loading Phases and Iteration Schemes		
Self Weight	**Load Steps**	0.1(10)
	Analysis Method	Newton-Raphson (Full)
	Force Norm	0.01
	Displacement Norm	0.01
Lateral Loading	**Load Steps**	0.0025(400)
	Analysis Method	Newton-Raphson (Full)
	Force Norm	0.01
	Displacement Norm	0.01

The head-joint failure type used for these analyses with EMM is the diagonal staircase crack. The appropriate staircase crack angle to be used, however, is not easily determined for masonry structures made from CS Element. The large size of CS Element causes cracks to occur not only in the mortar joints but also through the masonry units making it difficult to determine the appropriate staircase crack angle to use. To assess the effect of choosing different values of the staircase crack angle, analyses will be carried out using two different staircase crack angle values. The staircase crack angle values are assumed to be the angle of the diagonals of the two ground floor piers as illustrated below.

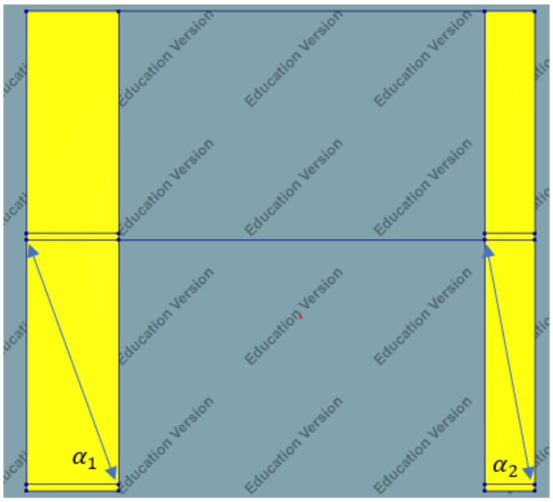

Figure 5.19 The staircase crack angle value chosen for the analysis

$$\alpha_1 = \tan^{-1}\left(\frac{2595}{977}\right) = 69.37^0$$

$$\alpha_2 = \tan^{-1}\left(\frac{2595}{533}\right) = 78.39^0$$

The EMM model variation with the staircase crack angle α_1 will be designated as Macro-EMM(1) and the variation with the staircase crack angle α_2 will be designated Macro-EMM(2).

The results of the analysis are as follows.

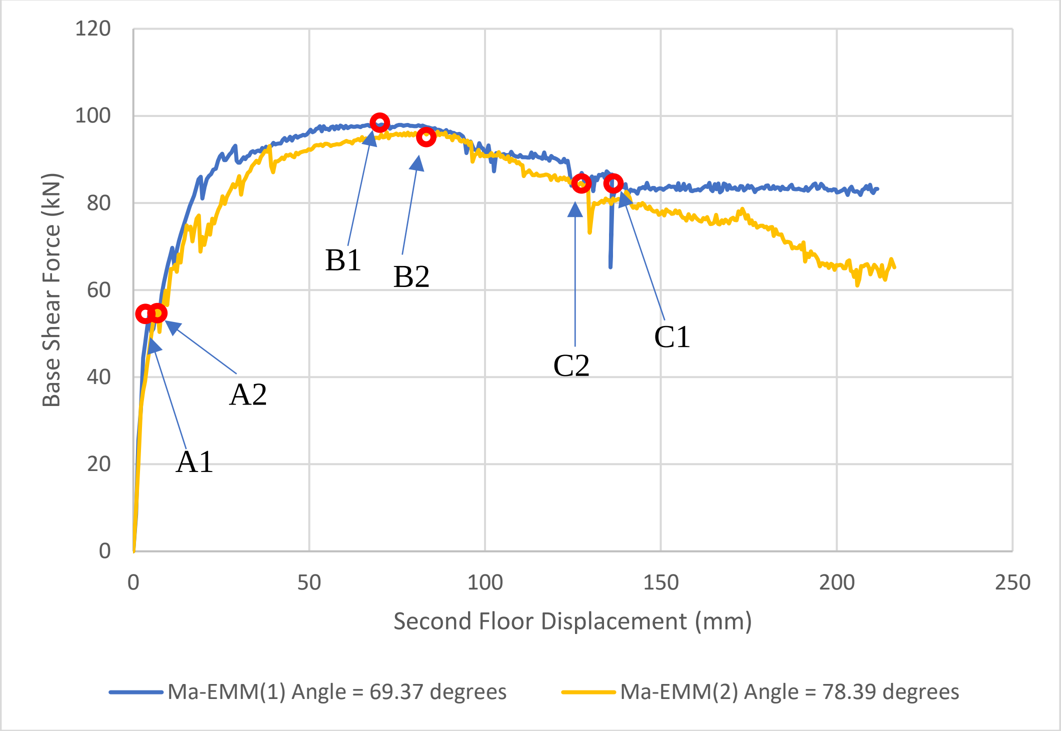

Figure 5.20 Capacity curves of Macro-EMM model

Figure 5.20 shows the capacity curves of Macro-EMM(1) and Macro-EMM(2). Both model variations reach a similar value of structural capacity with 97.99 kN and 96.37 kN for Macro-EMM(1) and Macro-EMM(2) respectively. Initial stiffness values of 16.05 kN/mm and 15.53 kN/mm are obtained from Macro-EMM(1) and Macro-EMM(2) respectively. The near-collapse displacements are not clear from the capacity curves as there is no significant drop in structural capacity, which is found on the Macro-TSRCM model. However, based on engineering judgment, the near-collapse displacement can be taken as the point at which instability in the analysis occurs, which in this case are event C1 and event C2 for the Macro-EMM(1) and Macro-EMM(2) model respectively. As such, the near-collapse displacement is 136 mm for the Macro-EMM(1) model and 129 mm for the Macro-EMM(2) model.

From Figure 5.20, it can be seen that the capacity curves of the Macro-EMM models have different characteristics compared to the capacity curves of the Macro-TSRCM model. The capacity curves of Macro-EMM models feature an initial linear increase in base shear force followed by a slight decrease in structural stiffness which is then accompanied by a gradual transition to the plateau until the peak structural capacity is reached. There is also a noticeable absence of an abrupt decrease in structural capacity, which is found in the Macro-TSRCM model. This is due to the absence of brittle diagonal cracking failure mechanism on the model. Instead of diagonal cracks, the failure of the structure is governed by the rocking mechanism and toe crushing, which cause the models to exhibit a more ductile behavior. Figure 5.20 also shows that the value of the staircase crack angle affects the results of the numerical analysis. The difference is, however, not significant with the Macro-EMM(2) model undergoing a slightly larger reduction in stiffness just after the rocking mechanism is activated. This larger reduction due to the change in the staircase crack angle seems to be related to the fact that the steeper staircase crack angle reduces the horizontal tensile strength (f_{tx}).

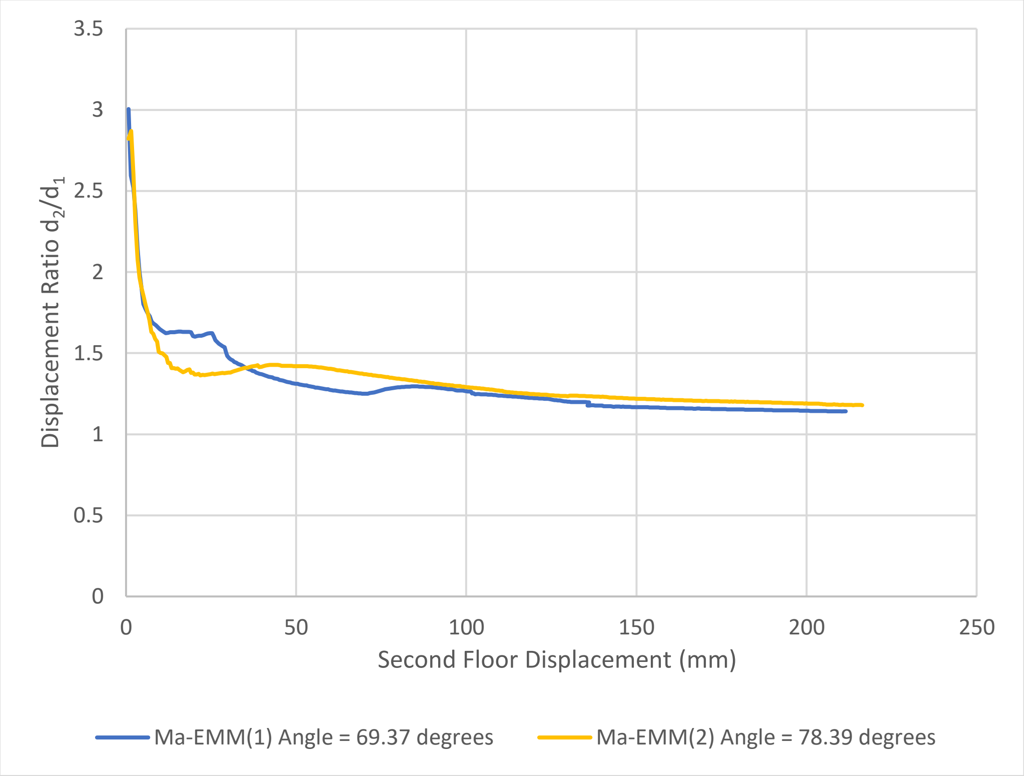

Figure 5.21 Interstory drift curves of Macro-EMM model

The interstory drift curves of the Macro-EMM models show that the displacement ratio of the structure for both values of the staircase crack angle undergoes a significant decrease before leveling off at a relatively constant displacement ratio value. The constant displacement ratio value indicates the existence of a soft story mechanism at the ground floor of the structure. From the interstory drift curve of the analysis of Macro-EMM(1), it is also observed that there is one instance at the horizontal displacement of 25 mm, where the displacement ratio suddenly undergoes another significant decrease. This can be attributed to a new crack opening at the upper part of the ground floor long pier.

Table 5.11 The progression of crack formation and crushing on Macro-EMM(1) model

Macro-EMM(1) Angle = 69.37^0

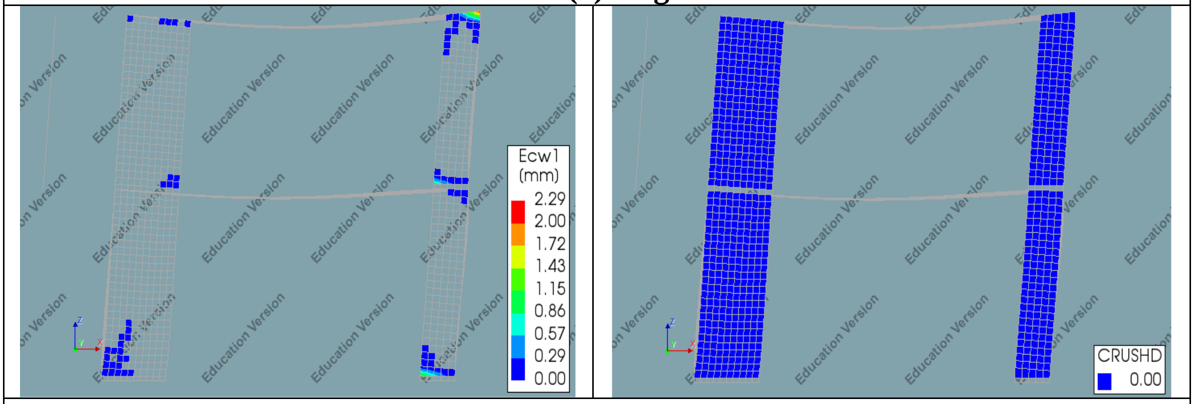

(A1) Rocking mechanism activated

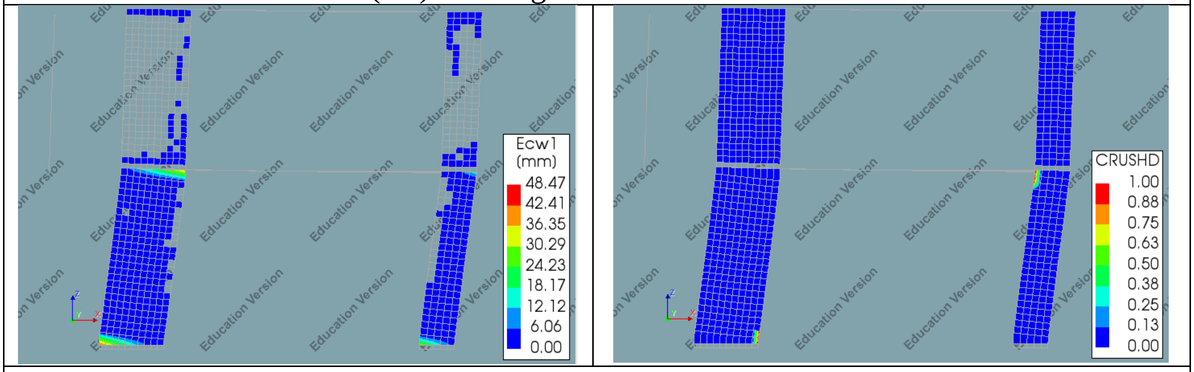

(B1) Peak base shear force reached

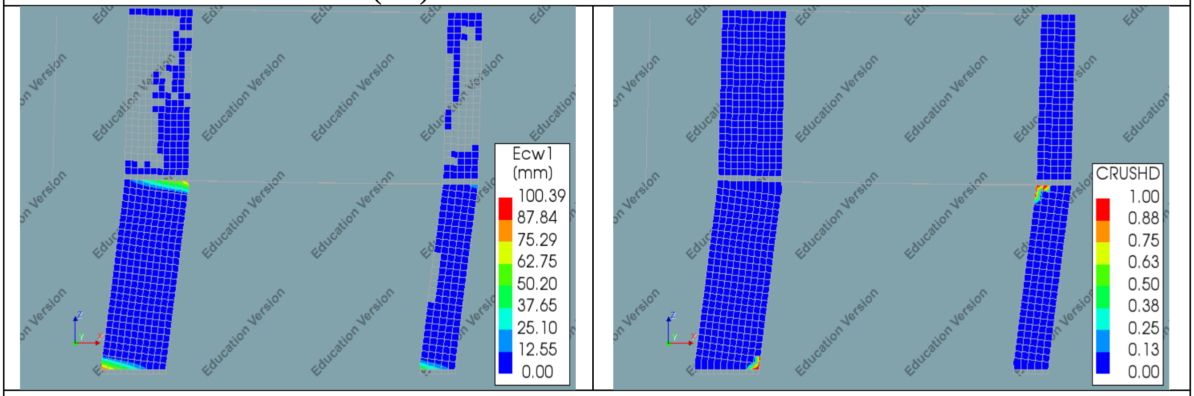

(C1) Near-collapse displacement

Table 5.12 The progression of crack formation and crushing on Macro-EMM(2) model

Macro-EMM(2) Angle = 78.39^0

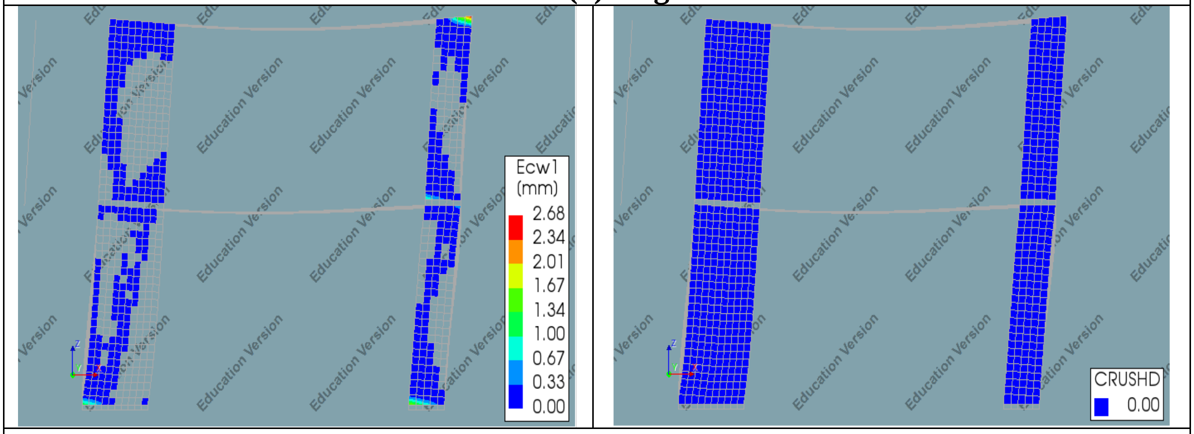

(A2) Rocking mechanism activated

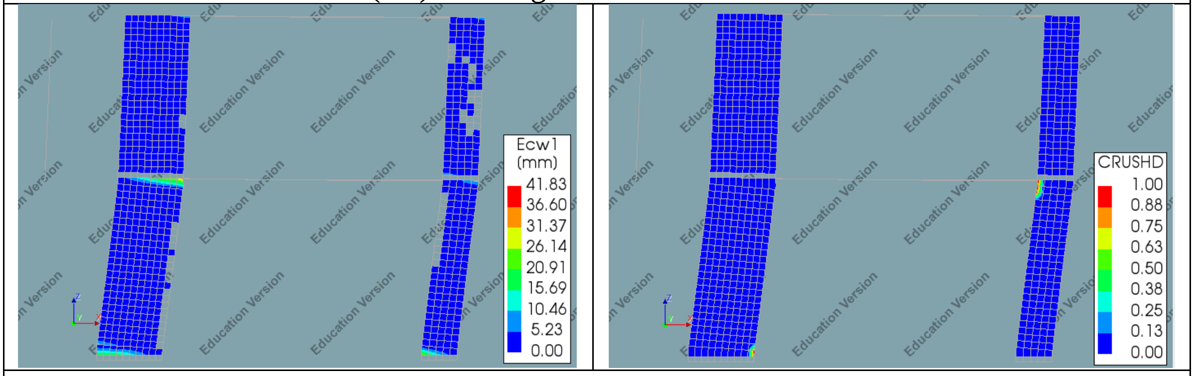

(B2) Peak base shear force reached

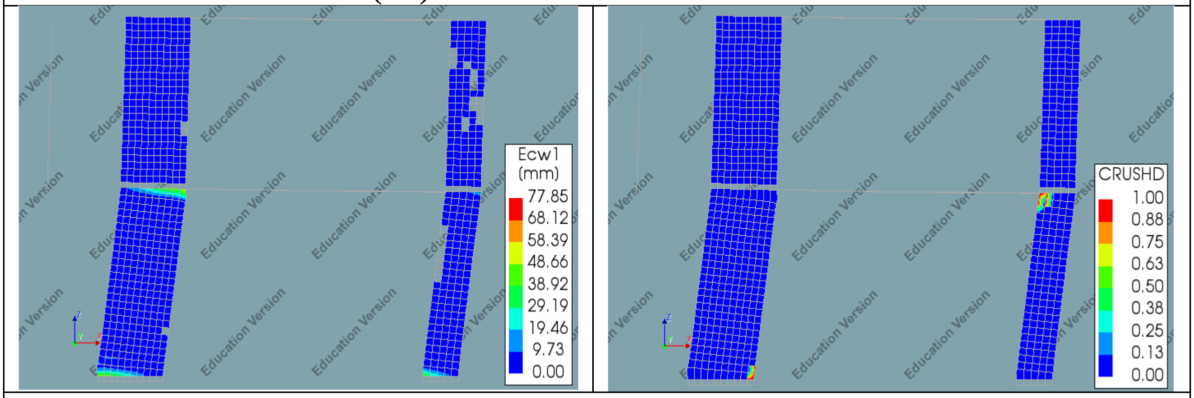

(C2) Near-collapse displacement

Table 5.11 and Table 5.12 show the progression of cracking and crushing on the Macro-EMM(1) and Macro-EMM(2) model respectively. The formation of the rocking mechanism can be observed on both models, which is indicated by the opening of cracks at the extremities of the piers. This is followed by the formation of toe crushing on the ground floor piers due to the flexural behavior of the piers. There is, however, no sign of diagonal cracks forming on the piers. Hence, there is no brittle failure due to diagonal cracking failure observed on the models. This causes the behavior of the models to be more ductile than the Macro-TSRCM model.

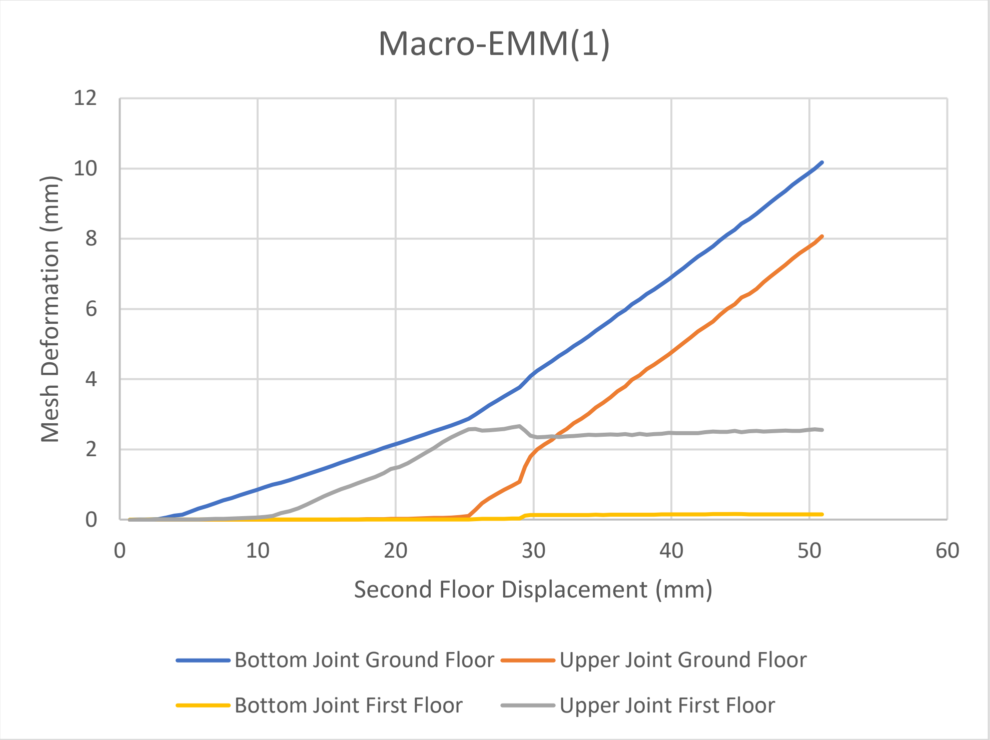

Figure 5.22 The deformation of finite element mesh at the joints of the long pier (Macro-EMM(1))

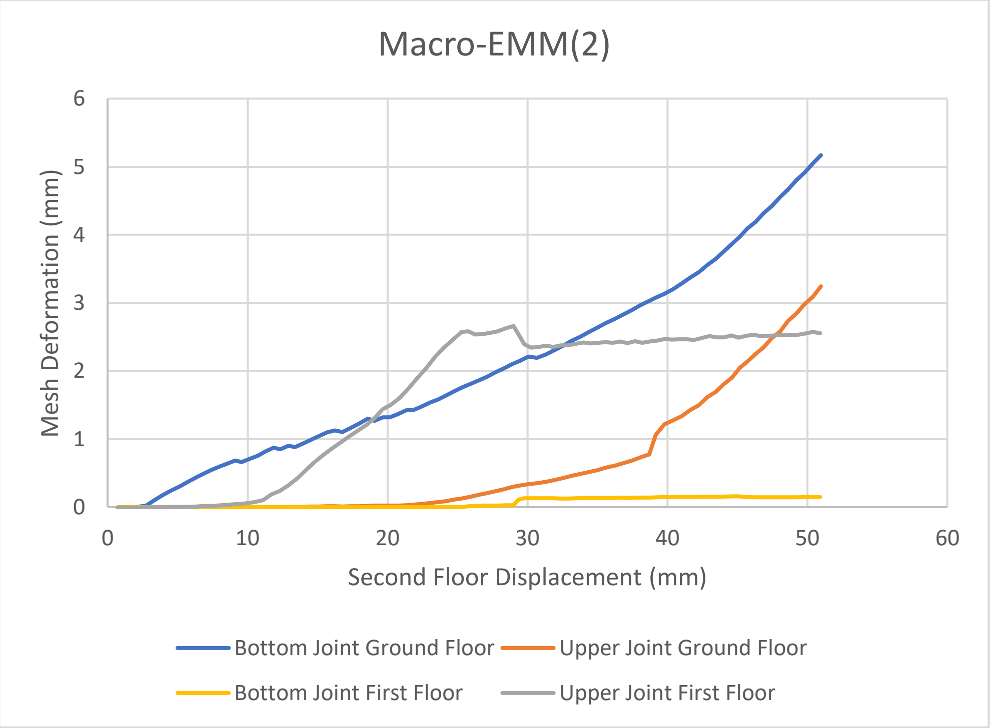

Figure 5.23 The deformation of finite element mesh at the joints of the long pier (Macro-EMM(2))

Figure 5.22 and Figure 5.23 show the deformation of the mesh located at the joints of the long pier, where the cracks open. The opening of cracks at the joints is indicated on the figures with the sudden increase in vertical mesh deformation after the initial zero mesh displacement. Cracks first open at the bottom joint of the ground floor long pier, which starts the rocking mechanism on the structures. As the horizontal displacement increases, cracks start to appear in the other joints starting at the upper joint of the first floor long pier followed by the upper joint of the ground floor long pier. From the figures, it can also be seen that the mesh deformation at the upper joint stops increasing and remains relatively constant after tensile cracks open in the upper joint of the ground floor long pier. This signifies the development of a soft-story mechanism on the ground floor.

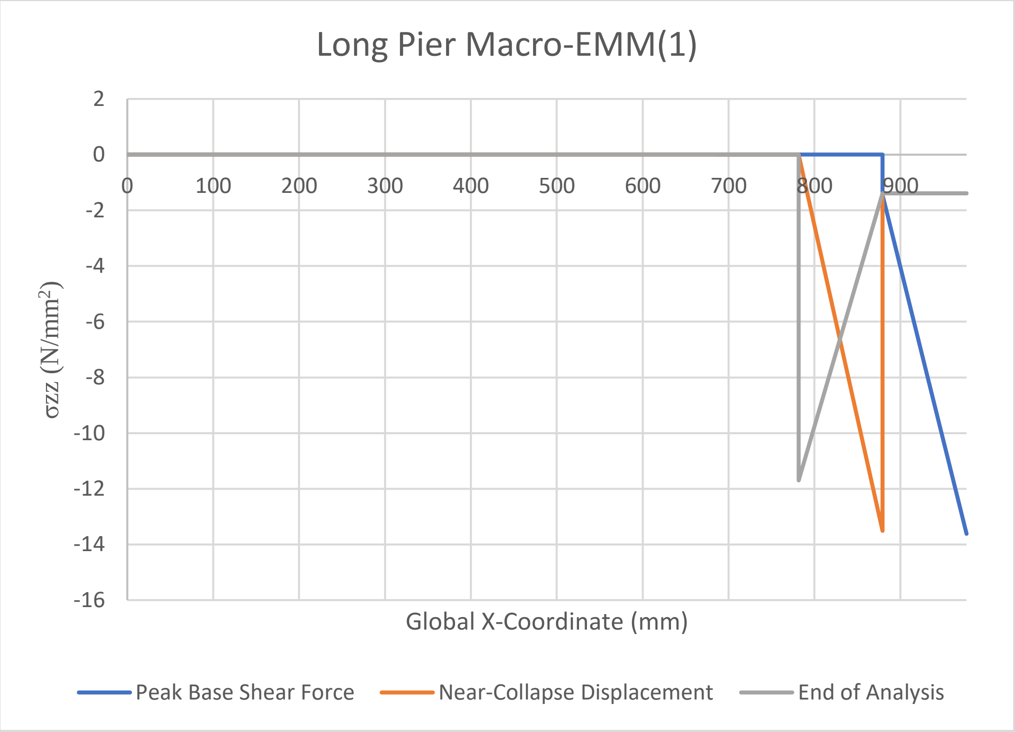

Figure 5.24 Vertical stress distribution of the long pier of the Macro-EMM(1) model

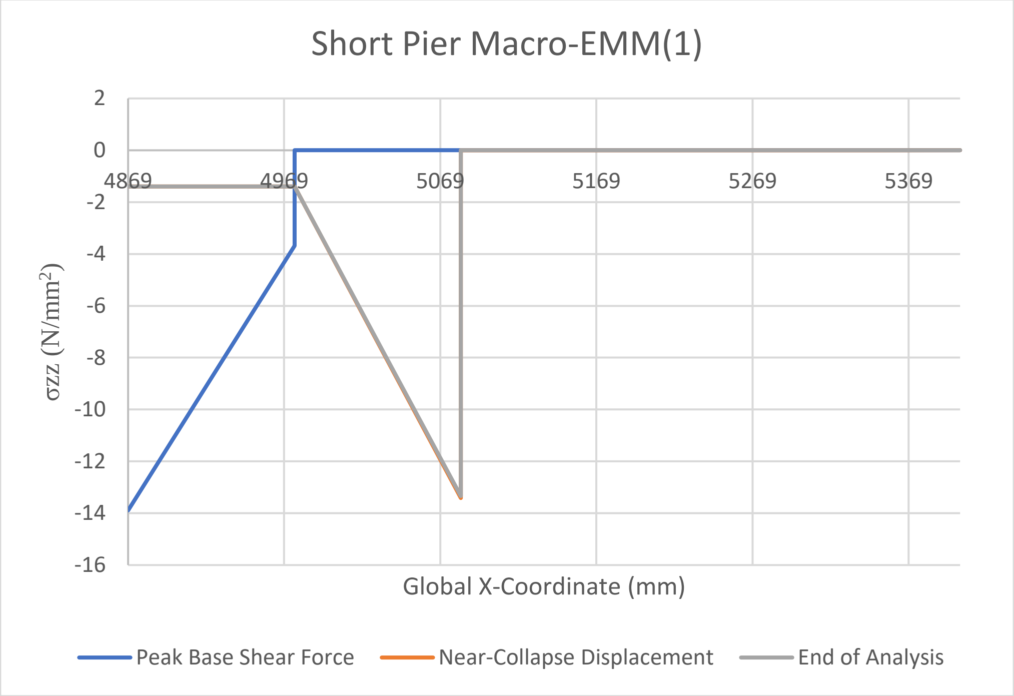

Figure 5.25 Vertical stress distribution of the short pier of the Macro-EMM(1) model

Figure 5.24 and Figure 5.25 show the vertical stress distribution at the bottom of the ground floor long pier and the top of the ground floor short pier for the Macro-EMM(1) model. At the point where the peak base shear force is reached, peak vertical stresses can be observed reaching the compressive strength value at the outermost part of the piers. This corresponds to the crushing of the pier toe, which has been observed from the crushing state contour plots. As the analysis progresses, the toe crushing of the piers continues to progress and the affected areas lose the capacity to sustain loads. The vertical stress in the crushed section decreases to almost zero. With the loss of load capacity, the peak vertical stress moves inward along the width of the piers to the section that can still resist loads. From the figure, it can also be observed that the vertical stresses on the rest of the pier section are zero, which is due to the tensile cracks in the piers.

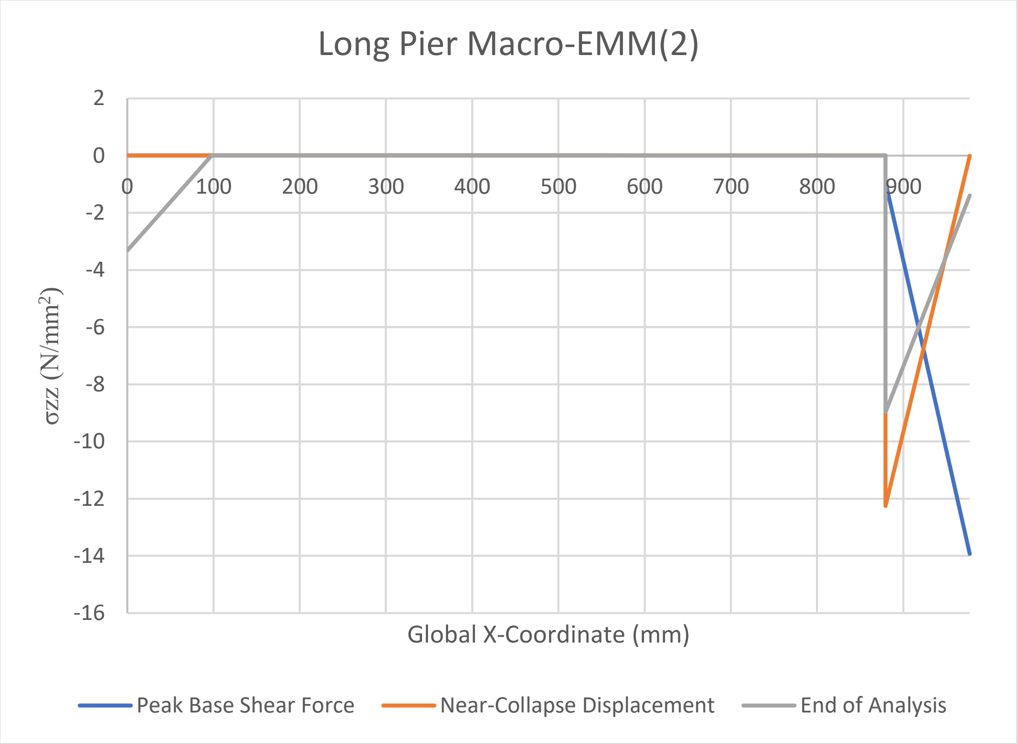

Figure 5.26 Vertical stress distribution of the long pier of the Macro-EMM(2) model

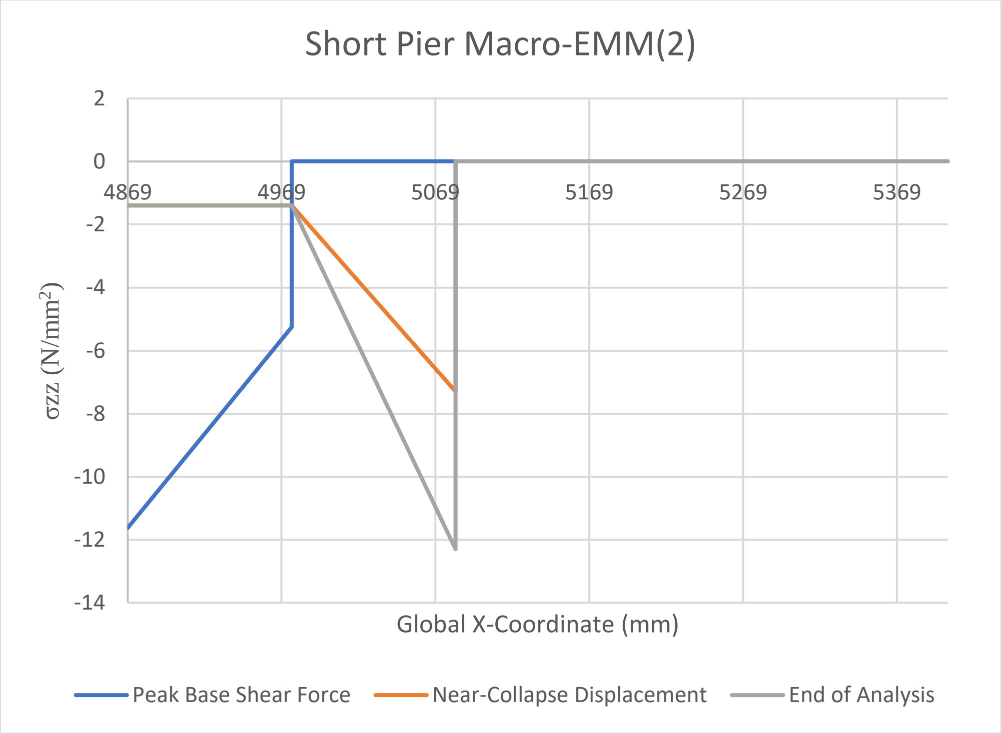

Figure 5.27 Vertical stress distribution of the short pier of the Macro-EMM(2) model

Figure 5.26 and Figure 5.27 shows the vertical stress distribution in the piers of the Macro-EMM(2) model. Just like the Macro-EMM(1) model, the peak vertical stress is initially found at the outermost edge of the pier before moving inwards as the outermost edge of the piers loses its ability to sustain loads. The crushed section of the piers loses its capacity to sustain loads, which is shown by the reduced compressive stress in that section. Figure 5.26 also shows an anomalous behavior at the end of the analysis with compressive stresses in the section that should be under tension. This is likely caused by the instability in the analysis.

Table 5.13 The distribution of vertical reaction force in the half of the Macro-EMM(1) and Macro-EMM(2) model

Structural Element	**Vertical Reaction Force (kN)**			
	Macro-EMM(1)		**Macro-EMM(2)**	
	Static Condition	**Peak Base Shear Force**	**Static Condition**	**Peak Base Shear Force**
Long Pier	20.37	74.85	21.17	84.84
West Wall	74.89	-3.97	74.11	-13.36
Short Pier	11.54	2.74	11.50	-2.76
East Wall	72.49	105.68	72.51	110.58
Total Reaction Force	179.30	179.30	179.30	179.30

The vertical reaction forces across the structural elements in the Macro-EMM(1) and Macro-EMM(2) at the static condition and the peak base shear force are shown in Table 5.13. The total reaction forces for both the Macro-EMM(1) and Macro-EMM(2) models are the same at both events, which satisfy the vertical force equilibrium. A comparison of vertical reaction forces at both events shows considerable redistribution of axial loads between the masonry structural elements. From the table, the redistributed axial loads (ΔN) for the Macro-EMM(1) and Macro-EMM(2) model are 24.39 kN and 23.80 kN respectively. As with the Macro-TSRCM model, these redistributed axial loads are significantly larger than the estimated value from the hand calculation. Due to this, it is also difficult to relate the results of the numerical model to the hand calculation.

5.2.2 Sensitivity Study (Macro-EMM)

A sensitivity study on the Macro-EMM model is carried out to assess to what extent the change in the values of material parameters affects the numerical results of the model. As with the previous sensitivity study with the Macro-TSRCM model, the material parameters chosen are related to the cracking and crushing failure of the structure.

Tensile Fracture Energy (G_{ft}^{I}) and Tensile Strength (f_t)

The following values of G_{ft}^{I} and f_t are used for the sensitivity analysis.

Table 5.14 G_{ft}^{I} and f_t parameters used for the sensitivity study (EMM)

Portion	G_{ft} (N/mm)	f_t (N/mm^2)
100%	0.021	0.39
50%	0.0105	0.195
10%	0.0021	0.039

The sensitivity study is carried out on both Macro-EMM(1) and Macro-EMM(2). The resulting capacity curves of the sensitivity study are as follows.

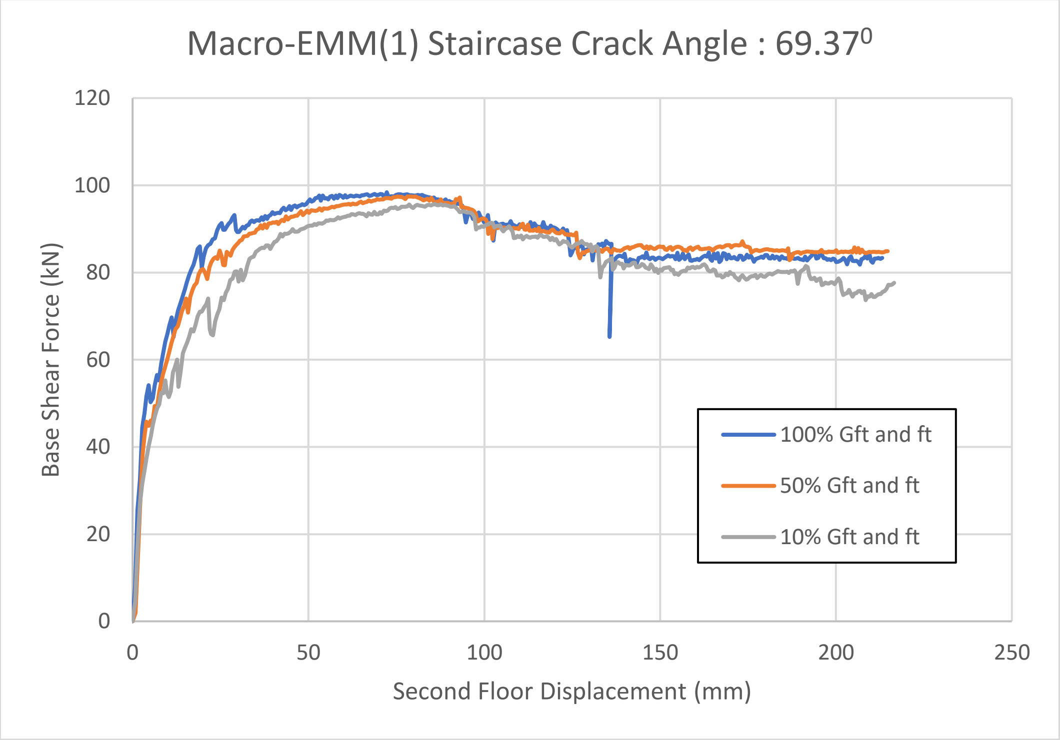

Figure 5.28 Base shear force curves from sensitivity study on G_{ft}^{I} and f_t parameters (Macro-EMM staircase crack angle = 69.37^0)

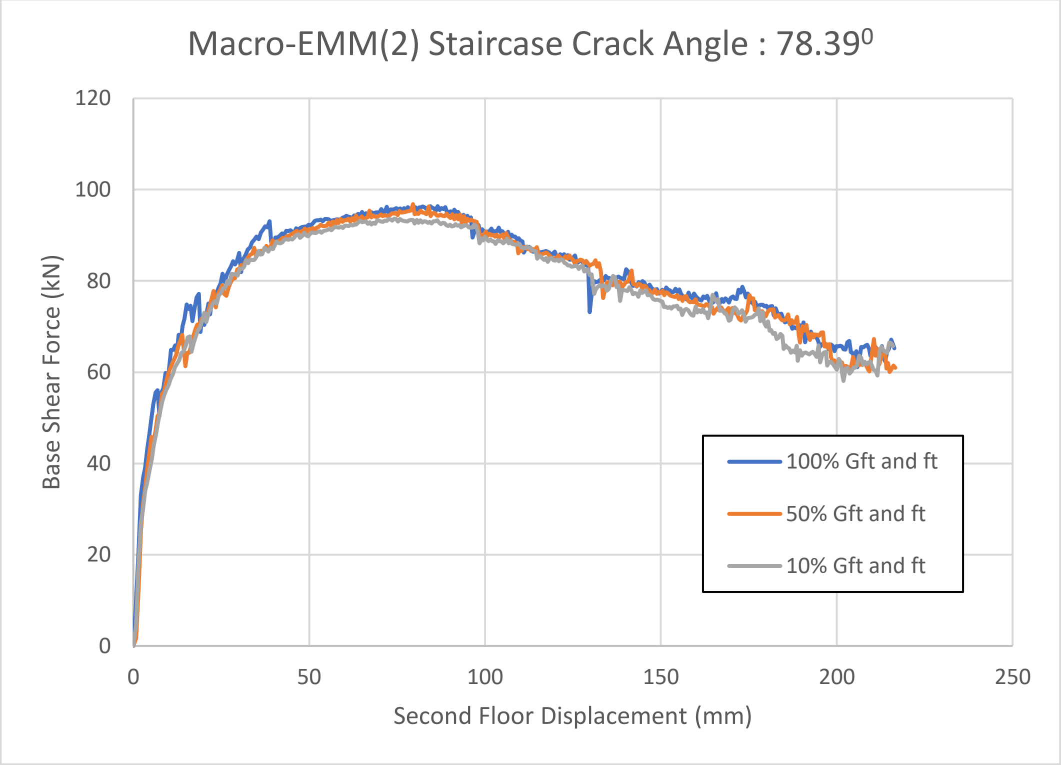

Figure 5.29 Base shear force curves from sensitivity study on G_{ft}^{I} and f_t parameters (Macro-EMM(2) staircase crack angle = 78.39^0)

Figure 5.28 and Figure 5.29 show the capacity curves obtained from the sensitivity study results. The capacity curves of both models show small to no changes in the structural capacity and nonlinear behavior of the models, despite the significant change in the values of G_{ft}^{I} and f_t. All model variations reach similar values of structural capacity. This implies that tensile cracking parameters do not heavily influence the structural capacity. The capacity curves of Macro-EMM(1) show slight changes in the pre-peak region from the reduction of the values of G_{ft}^{I} and f_t. It appears that reducing the values of the two variables slightly decreases the resistance of the model in the pre-peak region. This difference diminishes as the peak base shear force is reached and the analysis transitions into the post-peak region, where toe crushing governs. By comparing the capacity curves of the Macro-EMM(1) and Macro-EMM(2) model, it can be observed that the value of staircase crack angle also influences the sensitivity of the analysis to the change in G_{ft}^{I} and f_t. The capacity curves of Macro-EMM(2) show almost no difference to the change in the value of G_{ft}^{I} and f_t. This is most likely caused by the reduction in the influence of horizontal tensile strength (f_{tx}) due to the steeper staircase crack angle.

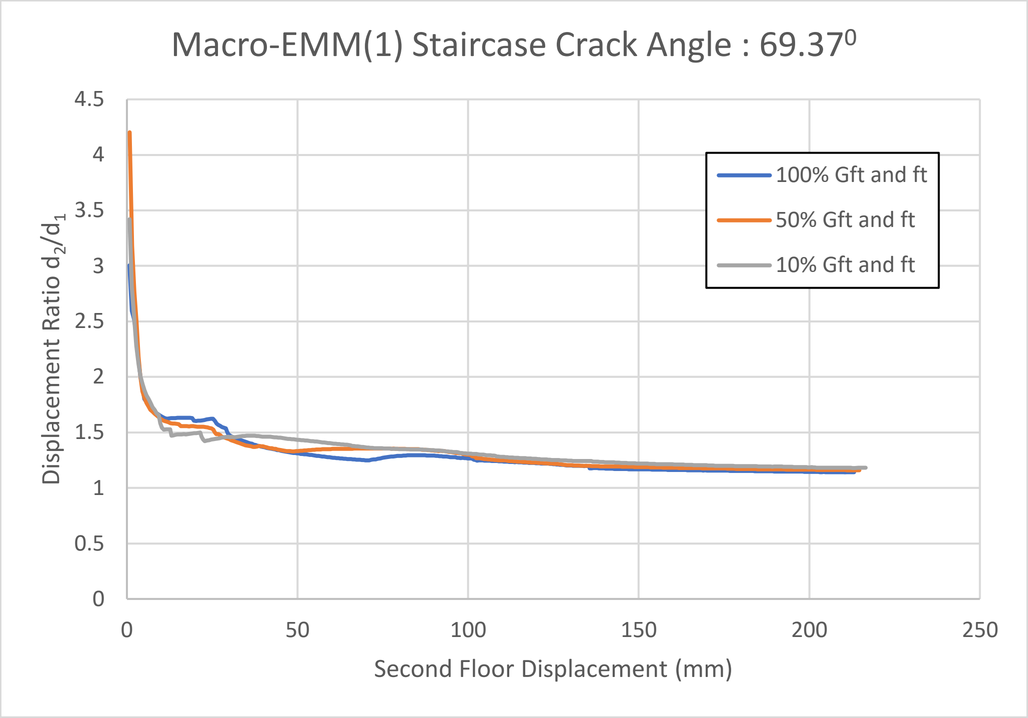

Figure 5.30 Interstory drift curves from sensitivity study on G_{ft}^{I} and f_t parameters (Macro-EMM(1) staircase crack angle = 69.37^0)

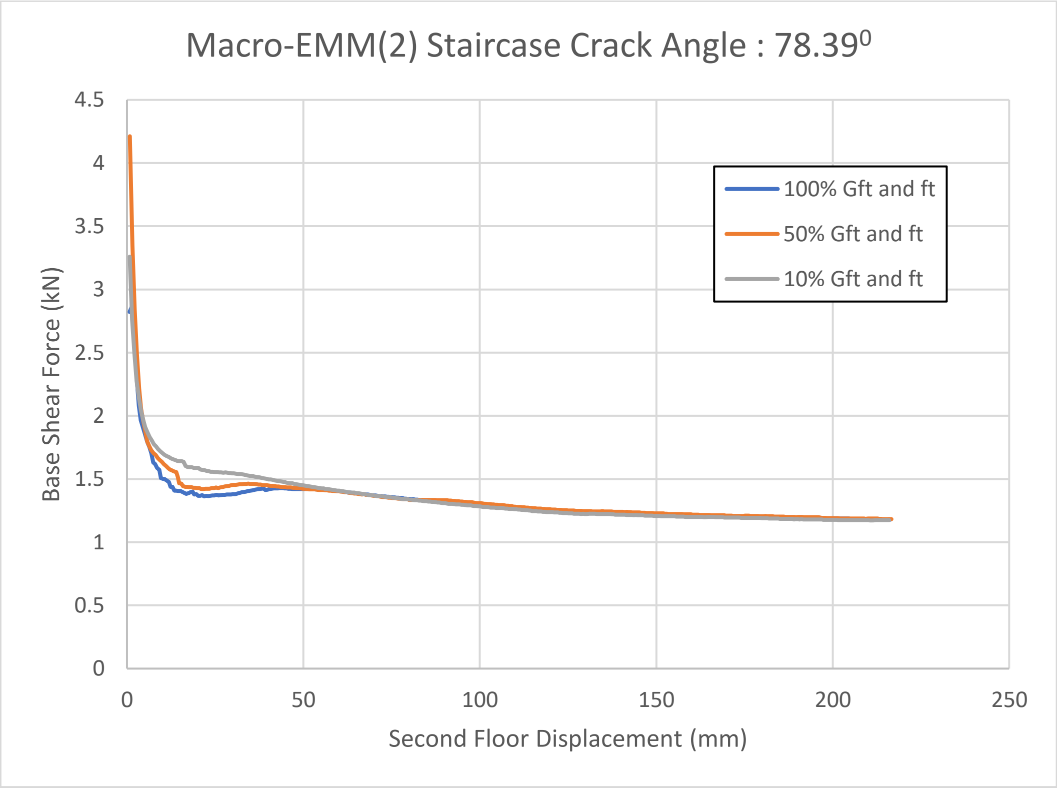

Figure 5.31 Interstory drift curves from sensitivity study on G_{ft}^{I} and f_t parameters (Macro-EMM(2) staircase crack angle = 78.39^0)

The interstory drift curves of both model variations show no significant difference from the change in the values of G_{ft}^{I} and f_t. Only some small changes in the pre-peak region are observed. This indicates that the interstory drift of the model is not sensitive to the changes in G_{ft}^{I} and f_t.

Compressive Fracture Energy (G_{fc}) and Compressive Energy (f_c)

The following values of G_{fc} and f_c are used for the sensitivity study.

Table 5.15 G_{fc} and f_c parameters used for the sensitivity study (EMM)

Portion	G_{fc} **(N/mm)**	f_c **(N/mm^2)**
100%	20.29	13.93
50%	10.15	6.97
10%	2.03	1.39

The resulting capacity curves for the Macro-EMM(1) and Macro-EMM(2) model are plotted below.

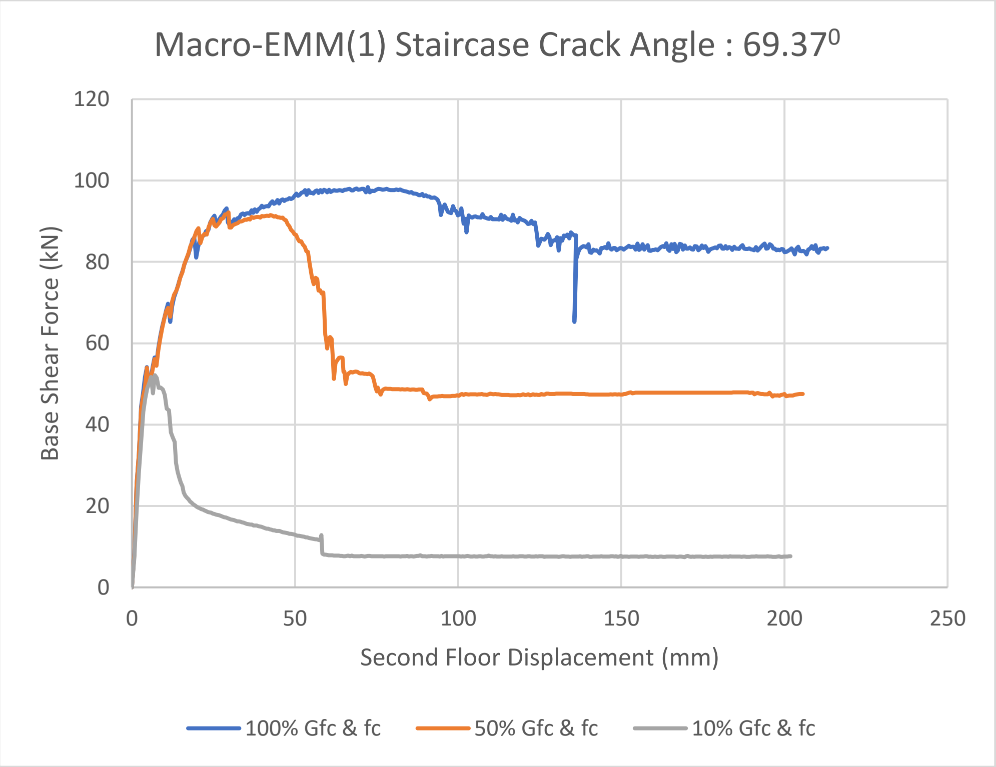

Figure 5.32 Capacity curves from sensitivity study on G_{fc} and f_c parameters (Macro-EMM(1) staircase crack angle = 69.37^0)

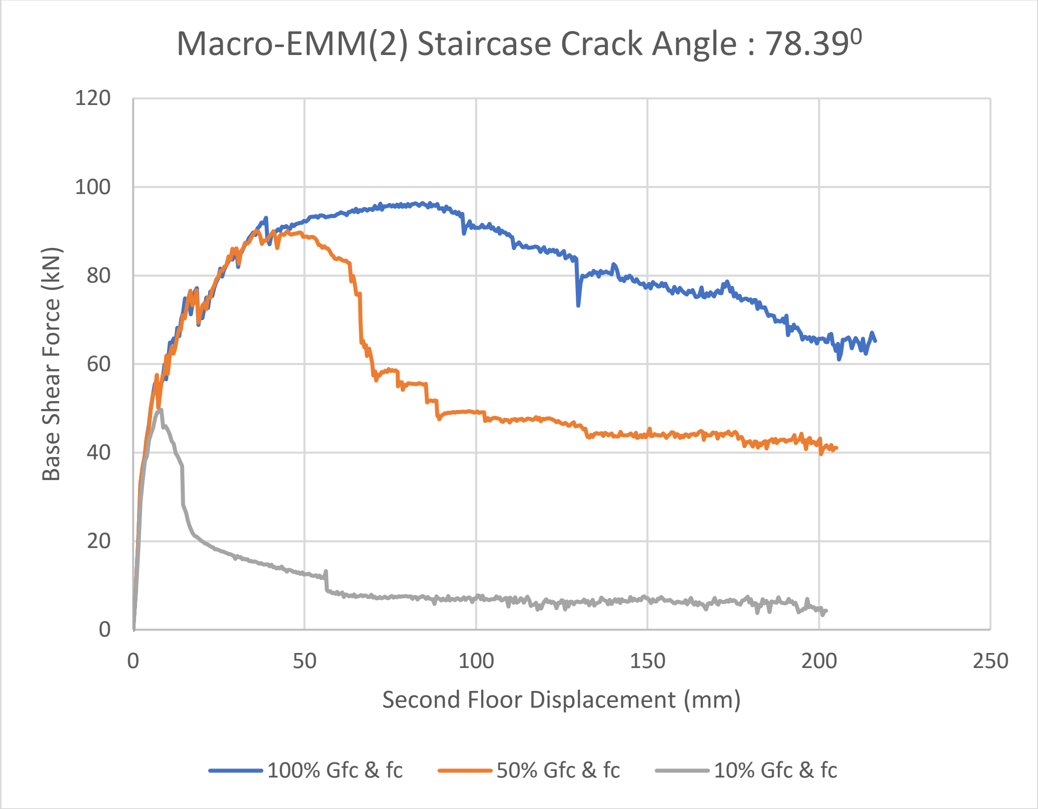

Figure 5.33 Base shear force curves from sensitivity study on G_{fc} and f_c parameters (Macro-EMM(2) staircase crack angle = 78.39^0)

The capacity curves of Macro-EMM(1) and Macro-EMM(2) are plotted in Figure 5.32 and Figure 5.33. From the figures, it can be seen that the analysis is very sensitive to the change in the values of G_{fc} and f_c. Drastic changes to the model behavior in the post-peak region can be observed from both figures. Reduction in G_{fc} and f_c causes reduction in structural capacity and residual base shear force. Residual base shear force, in particular, experiences a very significant reduction. This severe reduction comes as a result of the more widespread toe crushing of the piers on the model. It can be seen from the figures that the reduction of both material parameters causes the onset of failure to occur earlier, which in turn causes the structural capacity to decrease. As can be seen from the figures, the pre-peak behavior of the model is not affected by the changes in the variables. Each capacity curves of the model variations follow the same path as the curve from the original model (100% G_{fc} & f_c) before deviating to reach the peak base shear force. The large influence of the changes in the value of G_{fc} and f_c to the structural behavior signifies that toe crushing is the dominant failure mode of these numerical models.

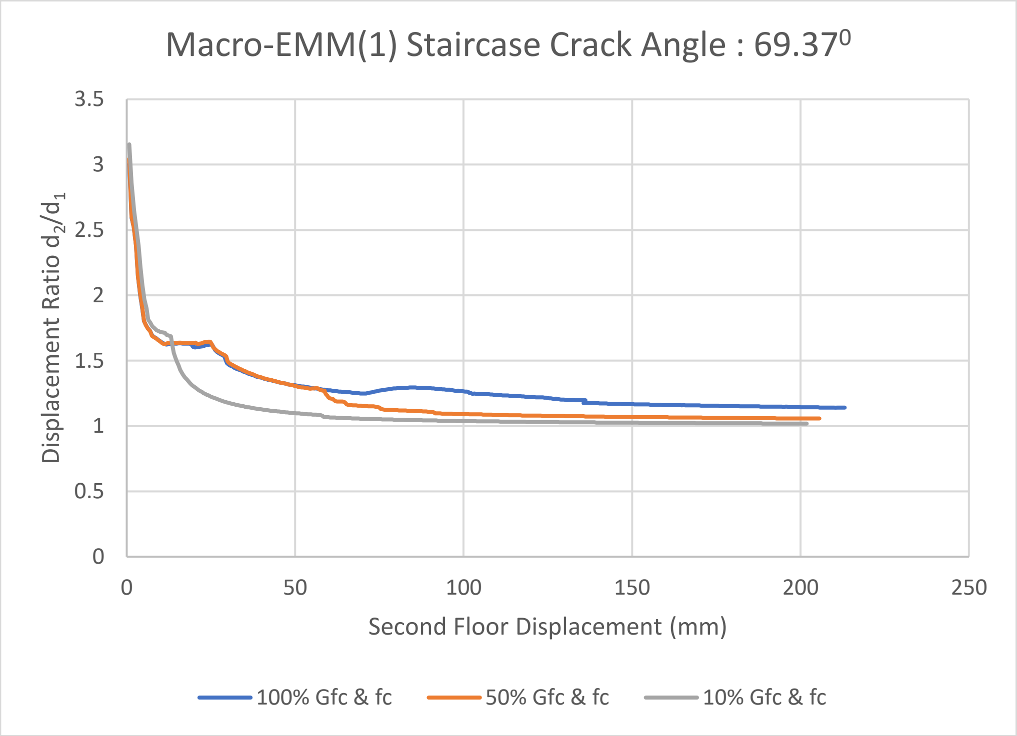

Figure 5.34 Interstory drift curves from sensitivity study on G_{fc} and f_c parameters (Macro-EMM(1) staircase crack angle = 69.37^0)

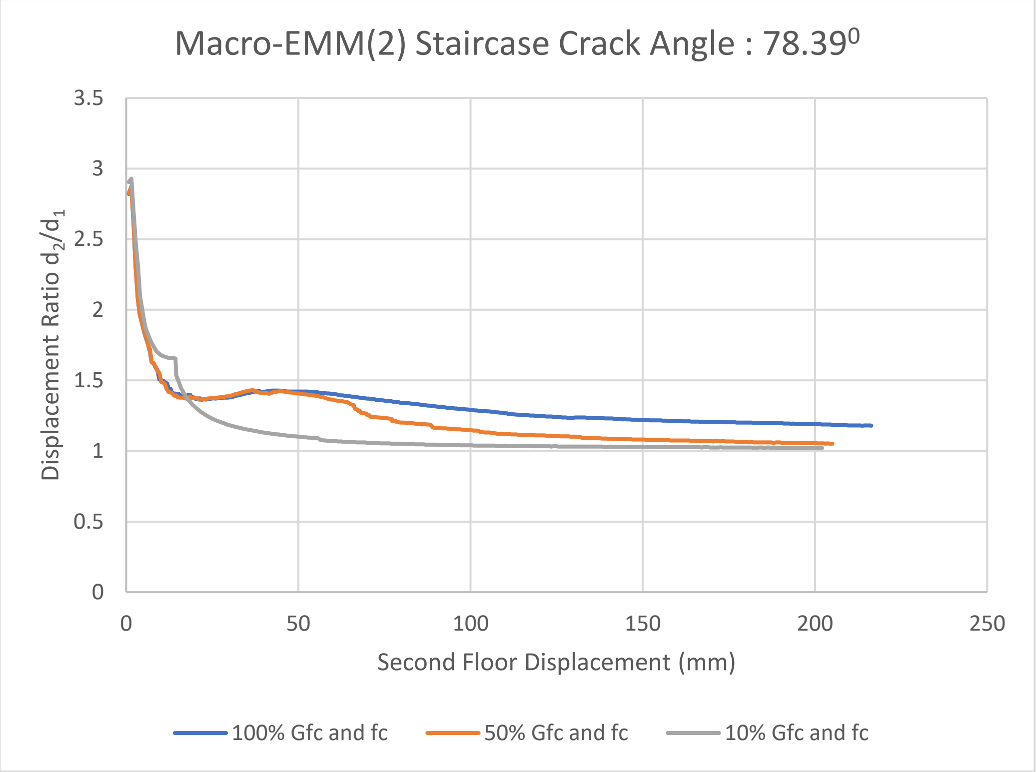

Figure 5.35 Interstory drift curves from sensitivity study on G_{fc} and f_c parameters (Macro-EMM(2) staircase crack angle = 78.39^0)

Figure 5.34 and Figure 5.35 show the interstory drift curves of Macro-EMM(1) and Macro-EMM(2) model respectively. All interstory drift curves show a consistent trend of an initial sharp decrease in displacement ratio followed by a gradual transition to a relatively constant displacement ratio. By observing the interstory drift curves, it can be seen that the curves do not undergo significant change in the pre-peak region and follow the original curve consistently. The interstory drift curves start to deviate from the original curve at the onset of structural failure. After the onset of structural failure, the displacement ratio decreases significantly and approaches unity.

Concrete Floor Young's Modulus (E_c)

An additional sensitivity study on the concrete floor Young's modulus is carried out to assess the effect of the concrete floor stiffness on the analysis results. In the same way as the sensitivity study on the Macro-TSRCM model, a value of concrete floor Young's modulus one order of magnitude higher than the original value will be used. The results of the analyses are as follows.

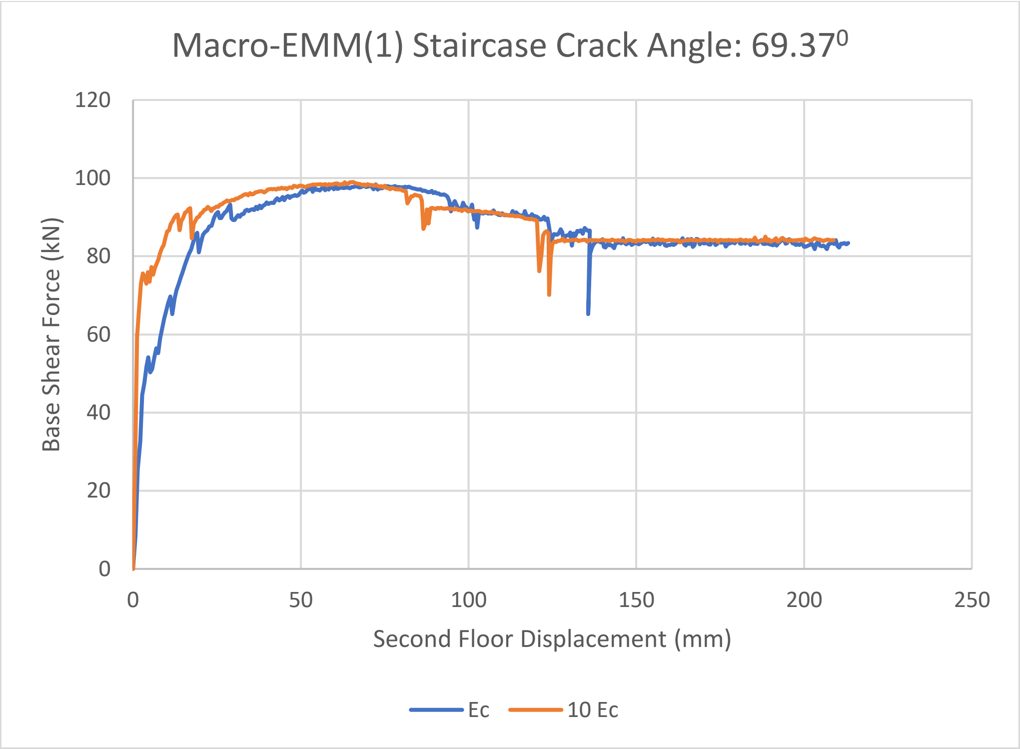

Figure 5.36 Capacity curves from the sensitivity study on E_c parameter (Macro-EMM(1))

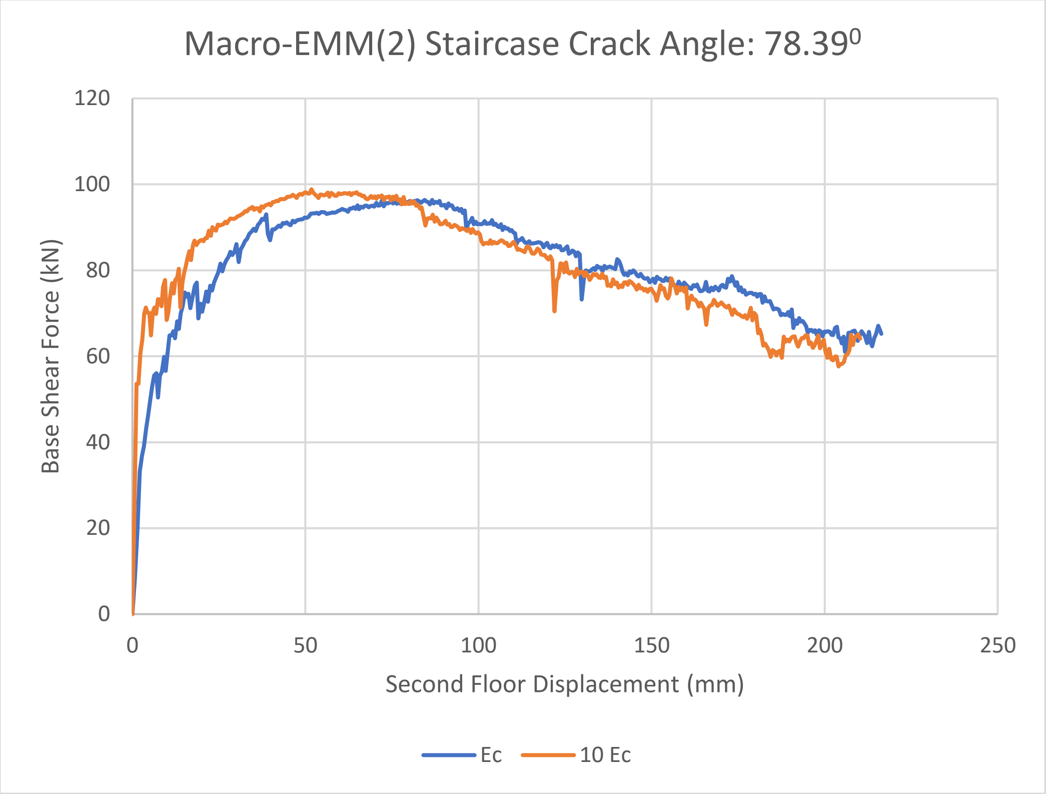

Figure 5.37 Capacity curves from the sensitivity study on E_c parameter (Macro-EMM(2))

The capacity curves of the analyses on the Macro-EMM(1) and Macro-EMM(2) model are shown in Figure 5.36 and Figure 5.37 respectively. The capacity curves show that E_c mainly influences the structural behavior in the pre-peak region, since the stiffness of the concrete floor heavily influences the progression of the rocking mechanism on the structure. The increase in the value of E_c causes the overall increase in the structural stiffness as evidenced by the slight increase in initial stiffness in Figure 5.36 and Figure 5.37. Apart from the initial stiffness increase, the structure also reaches the peak base shear value earlier. The structural behavior in the post-peak region is not significantly influenced by the change in concrete floor stiffness, indicating that the toe crushing mechanism is not affected by the alteration of the parameter.

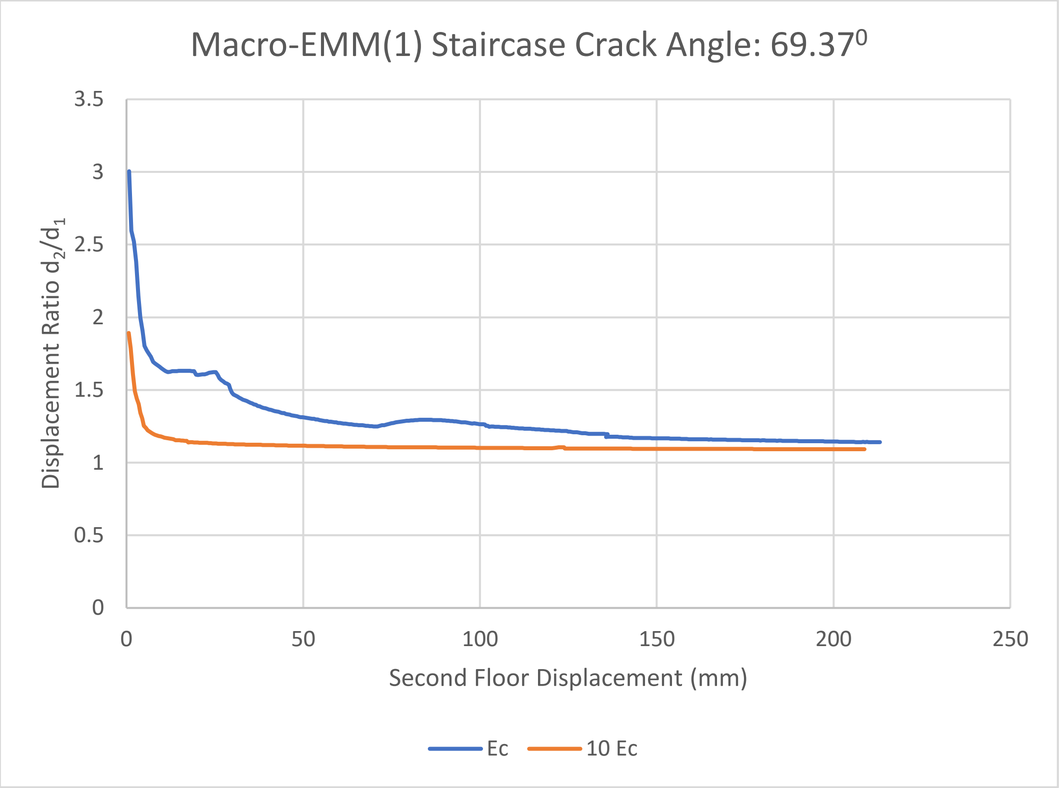

Figure 5.38 Interstory drift curves from sensitivity study on E_c parameter (Macro-EMM(1))

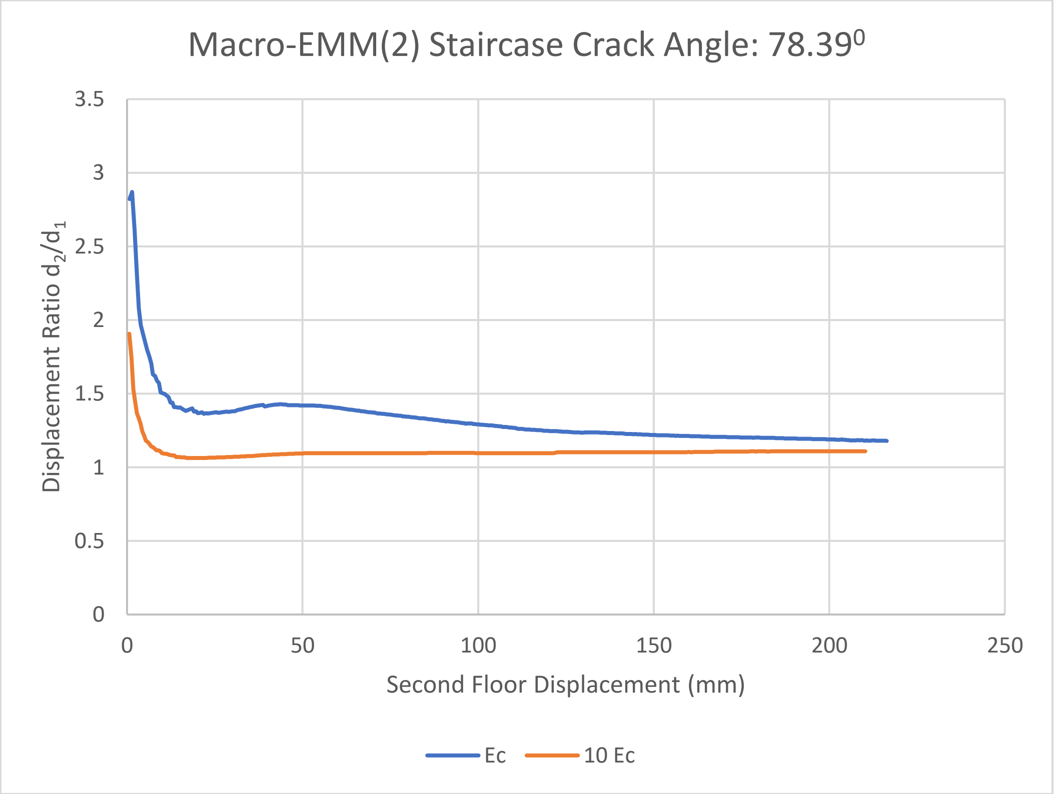

Figure 5.39 Interstory drift curves from sensitivity study on E_c parameter (Macro-EMM(2))

Figure 5.38 and Figure 5.39 shows the interstory drift curves comparison between unmodified models and models with different values of E_c. Comparison between the unmodified models and the modified models shows a significant reduction in displacement ratio with higher E_c value. The soft-story mechanism occurs earlier and is more prominent in the modified numerical model since the stiffer concrete floor at the top of the ground floor causes a more localized failure at the ground floor on the numerical model.

Summary of Sensitivity Study Results

The results of the sensitivity study conducted on the Macro-EMM model are summarized in the table below.

Table 5.16 Qualitative results of the sensitivity study on the Macro-EMM model

Variable	**Result**
$\boldsymbol{G_{ft}^{I}}$ **&** $\boldsymbol{f_t}$	Relatively insensitive. Slight changes in the pre-peak behavior. Effect on the analysis results depends on the staircase crack angle
$\boldsymbol{G_{fc}}$ **&** $\boldsymbol{f_c}$	Sensitive. Significant changes observed on the post-peak behavior.

From the sensitivity study results, it appears that the analysis is very sensitive to the change in compressive behavior parameters (G_{fc} & f_c), while relatively insensitive to the change in tensile behavior parameters (G_{ft}^{I} & f_t). This is likely related to the fact that toe crushing is the dominant failure mode for models with the EMM constitutive model. Despite this, G_{ft}^{I} and f_t still have some influence on the analysis as shown by the capacity curve in Figure 5.28. The staircase crack angle also seems to affect the sensitivity of the analysis with its effect more prominent in the pre-peak region.

The additional sensitivity study on the variable E_c shows the concrete floor stiffness to affect the behavior of the structure in the pre-peak region, which is related to the formation of tensile cracks and activation of the rocking mechanism. The effect is more pronounced in the interstory drift behavior with the occurrence of a soft-story mechanism at an early stage of the analysis. The sensitivity of the analysis to the change in the variable is not entirely clear and more analyses are required before a conclusion can be made. However, given the effect of the variable to the analysis results, it is evident that careful consideration in choosing the value of E_c for the analysis is required.

5.3 Comparison of Shell Elements Macro-Model Variations

The results of the analyses on the shell elements macro-models are summarized in the following tables. Table 5.17 shows the summary of the numerical results obtained from the analyses and Figure 5.40 shows the plot of the capacity curves. The interstory drift curves are plotted in Figure 5.41. Failure mechanisms observed on the numerical models are summarized in Table 5.18.

Table 5.17 Summary of base shear force results of the shell elements macro-models

Analysis	Initial stiffness (kN/mm)	Peak base shear force (kN)	Near collapse displacement (mm)
Experiment	16.67	65.7	54.4
Macro-TSRCM	16.18 (-2.9 %)	95.2 (+44.9 %)	44.08 (-19 %)
Macro-EMM(1)	16.05 (-3.7 %)	97.99 (+49.2 %)	136.00 (+150 %)
Macro-EMM(2)	15.53 (-6.8 %)	96.37 (+46.7 %)	129.00 (+137.1 %)

Table 5.17 shows the initial stiffness, peak base shear force and near-collapse displacement of the model variations. The initial stiffness of the models shows a relatively good agreement with the physical experiment results with only small differences ranging from 3 – 7 %. In terms of peak base shear force, all numerical models greatly overestimate the capacity of the structure. The cause of this overestimation is not entirely clear. In the case of the Macro-TSRCM model, the sensitivity study on the model does not indicate any particular parameter that has a significant effect on the structural capacity and the pre-peak behavior, even when the study is carried out with material parameters related to the development of rocking mechanism (G_{ft}^{I} & f_t). In the case of the Macro-EMM models, material parameters related to the compressive behavior are found to have a significant effect on the capacity curves. However, the change requires a significant reduction of the two parameters, which risks making the analysis not representative of the actual physical condition. The near-collapse displacement data show various degrees of accuracy in approximating the displacement capacity of the physical specimen. The Macro-TSRCM model shows the most accurate approximation to the physical specimen, while the Macro-EMM models behave in a very ductile way and greatly overestimate the displacement capacity of the structure.

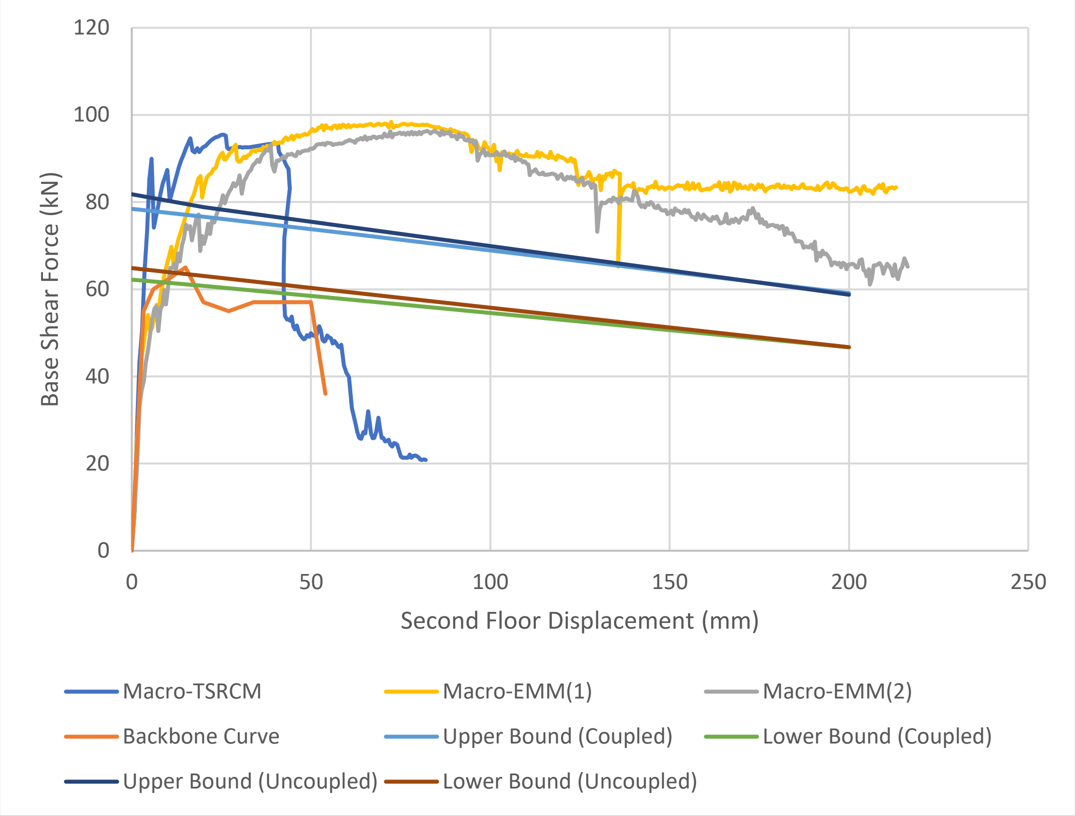

Figure 5.40 Comparison of capacity curves of shell elements macro-model variations

The capacity curves of all model variations and the backbone curve are plotted in Figure 5.40. The Macro-TSRCM model is the most accurate in terms of the approximation of the backbone curve with it exhibiting the plateau and the significant decrease in base shear force found on the backbone curve. The Macro-EMM models show an excessively ductile behavior compared to the Macro-TSRCM model and the backbone curve. In comparison with the approximated curves from hand calculation, all of the numerical models' results exceed the upper bound curves. The cause of this overestimation is still unclear and requires further investigation.

Table 5.18 Summary of observed failure mechanism of the shell elements macro-models

Model Variation	**Failure Mechanisms**			
	Rocking Mechanism	**Diagonal Cracking Failure**	**Toe Crushing**	**Others**
Experiment	Yes	Wide pier	No	Cracks in the transversal walls
Macro-TSRCM	Yes	Wide pier followed by short pier	No	-
Macro-EMM(1)	Yes	No	Yes	-
Macro-EMM(2)	Yes	No	Yes	-

Table 5.18 summarizes the failure mechanisms observed in the models. All model variations exhibit a rocking mechanism on the piers similar to the experimental result. However, out of the three model variations, only the Macro-TSRCM model exhibits diagonal cracking failure on the long pier as observed from the experimental result. Both variations of the model with the EMM constitutive model, Macro-EMM(1) and Macro-EMM(2), only exhibits rocking mechanism and toe crushing. Based on this result, it can be seen that the Macro-TSRCM model is better in simulating the failure mechanisms on the physical specimen. From the table, it can also be seen that no macro-model can accurately simulate the out-of-plane behavior of the structure. This likely stems from the limitations of the shell finite elements in modeling the out-of-plane behavior.

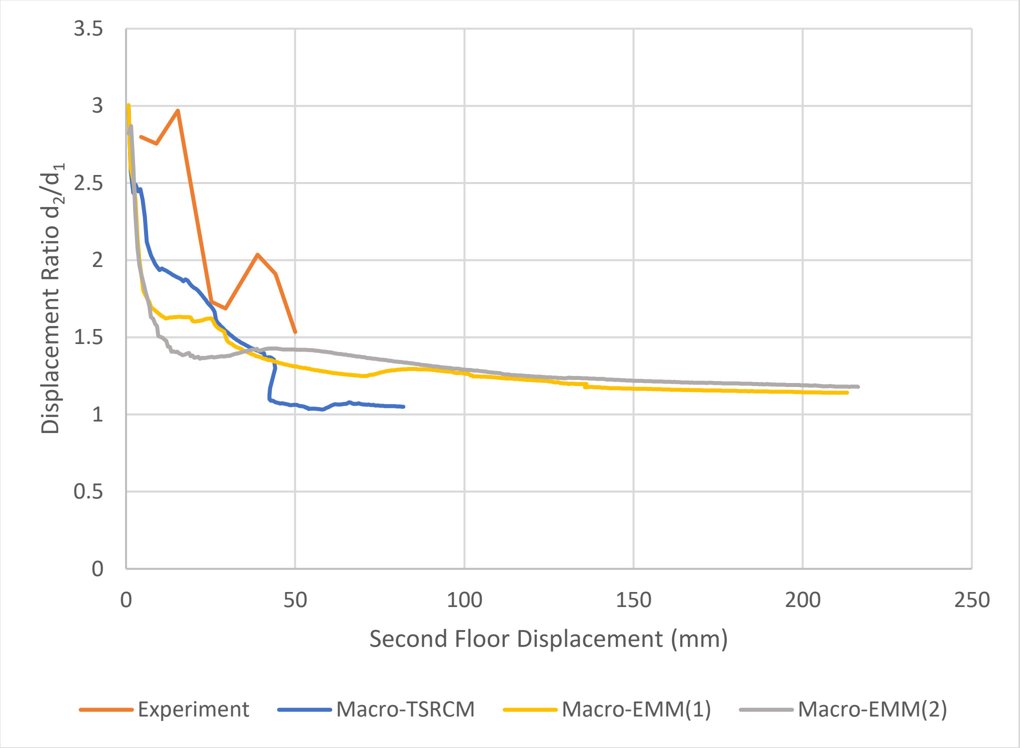

Figure 5.41 Comparison of interstory drift curves of shell macro-model variations

The interstory drift curves of the numerical models and the physical specimen are plotted in Figure 5.41. The interstory drift curves of the numerical models show a consistent trend consisting of an initial significant decrease in displacement ratio followed by the displacement ratio leveling off at a constant value. In the case of the Macro-TSRCM model, an abrupt decrease in the displacement ratio is observed due to diagonal cracking failure. The displacement ratio of the physical specimen also shows similar behavior in the form of a significant decrease at the beginning. The physical specimen behavior, however, does not agree with the numerical models' predictions and shows some discrepancies. These discrepancies between the numerical models and the physical specimen are possibly caused by the simplifying assumptions taken in the modeling process and the limitation of the constitutive models. It can thus be concluded that the numerical models are not ideal in predicting the interstory drift behavior of the physical specimen.

5.4 Concluding Remarks

The analyses of macro-models and the sensitivity study results have been discussed in this chapter. After examining the structural analysis and the sensitivity study results, the following conclusions can be made:

- A sensitivity study on the Macro-TSRCM model shows that the model is sensitive to the change in most of the material parameters that govern the failure mechanism of the structure. The change in the value of the parameters mainly affects the post-peak behavior of the structure, while the pre-peak behavior only sees limited change. Considering that no parameters significantly affect the pre-peak behavior and the structural capacity, there is probably an unknown factor that governs the structural behavior in that region. An additional sensitivity study on the stiffness of the concrete floor shows that the change in the concrete floor stiffness affects the pre-peak behavior significantly. The change in this particular material parameter leads to an even larger overestimate of the peak lateral capacity of the structure.

- A sensitivity study on both Macro-EMM models indicates that the material parameters governing the compressive behavior of the structure (G_{fc} & f_c) play a more dominant role in the models than the ones related to tensile cracking (G_{ft}^{I} & f_t). Despite the significant effect of the two variables on the structure, a significant reduction in material parameters is required to achieve the desired effect. This risks making the analysis not representative of the real physical specimen condition. From the study, it can also be seen that the value of the staircase crack angle can affect the sensitivity of the analysis to the change of the material parameters to some degree.

- Based on the comparison between the macro-models and the physical specimen structural behavior, it appears that Macro-TSRCM model offers the most accurate approximation of the physical specimen structural behavior. The Macro-EMM models prove to be too ductile and do not accurately simulate the failure mechanisms present in the specimen. However, based on the numerical data, it is evident that the Macro-TSRCM model still has considerable limitations. The model cannot accurately simulate the out-of-plane behavior of the masonry elements, due to the limitations of shell finite elements. There is also an issue of the model overestimating the structural capacity. Taking these into account, the author does not recommend the use of the considered models for simulations of such structure until these issues are addressed.

Chapter 6
Application of Vertical Interfaces to The Finite Element Model

As has been discussed in section 3.1, the wall-pier connections in a CS element structure are usually not constructed by interlocking the masonry units. Instead, the walls and the piers are joined by a thin layer of mortar along the height of the structural elements with steel anchors placed on the bed joints of the CS elements as has been shown in Figure 3.1. Therefore, it is more appropriate to model the wall-pier connections on the structure with interface elements than with shared nodes. This section will discuss the effect of the inclusion of vertical interfaces on the analysis of models with the TSRCM and the EMM constitutive model.

6.1 Application of Vertical Interfaces

Vertical interfaces are applied at the corner connections of the transversal walls and the piers as shown in the figure below.

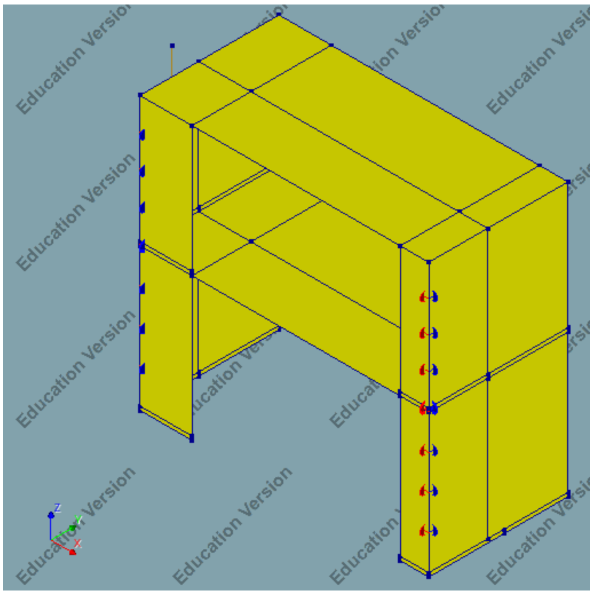

Figure 6.1 Application of vertical interfaces on shell elements macro-model to model the behavior of the wall-pier connections

The wall-pier connections are placed from the top of the kim-layer on the ground floor. The mortar joints along the kim-layer at the bottom of the ground floor are assumed to not crack due to its short height and its bottom being clamped.

The 3+3 nodes interface to shell elements, CL24I, that is described in section 2.5 is used for the vertical interfaces. The interface element has three local axes with one axis corresponds to the axial behavior and the other two axes correspond to the shear behavior. The local y-axis of the interface elements that correspond to the axial behavior is oriented in the direction of the global X-axis. The local x-axis and z-axis that correspond to the shear behavior of the interfaces are oriented to the global Z-axis and the global Y-axis respectively. The orientation of the interface element local axes is shown in the figure below.

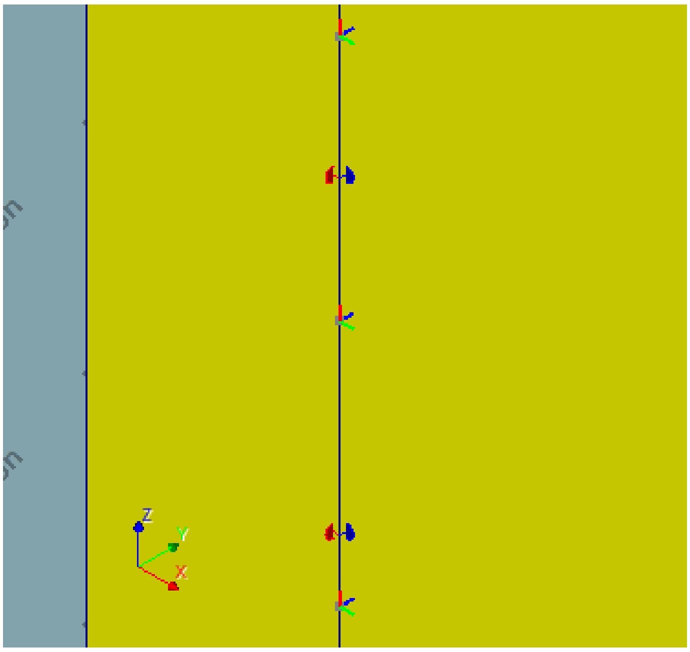

Figure 6.2 The orientation of the interface element local axes showing the local y-axis (green), the local x-axis (red) and the local z-axis (blue)

Nonlinear elasticity is chosen as the constitutive model of the interface elements due to the vertical joints behavior being a combination of the shear behavior of the mortar joints and the axial behavior of the steel anchors. The nonlinear elasticity model is defined in the software package by specifying traction-relative displacement diagrams for the axial and the shear behavior. The axial behavior diagram is shown in the figure below.

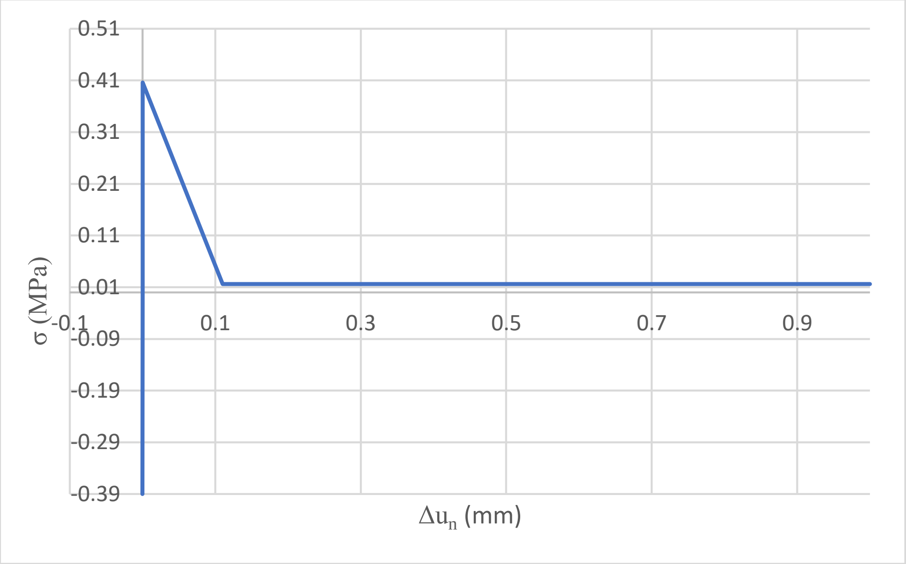

Figure 6.3 The axial traction-relative displacement of the vertical interfaces on shell elements macro-model

The shear behavior of the interface elements is influenced by the maximum shear stress τ_{max}. This variable is influenced by the axial stress on the interface and changes as the axial stress changes. However, due to the limitation of the nonlinear elasticity model, this variable is assumed to be constant. To compensate for this, a value of τ_{max}, which results in the most accurate representation of the structural responses, needs to be chosen. A sensitivity study will be performed with the τ_{max} variable to gauge its effect on the analysis results.

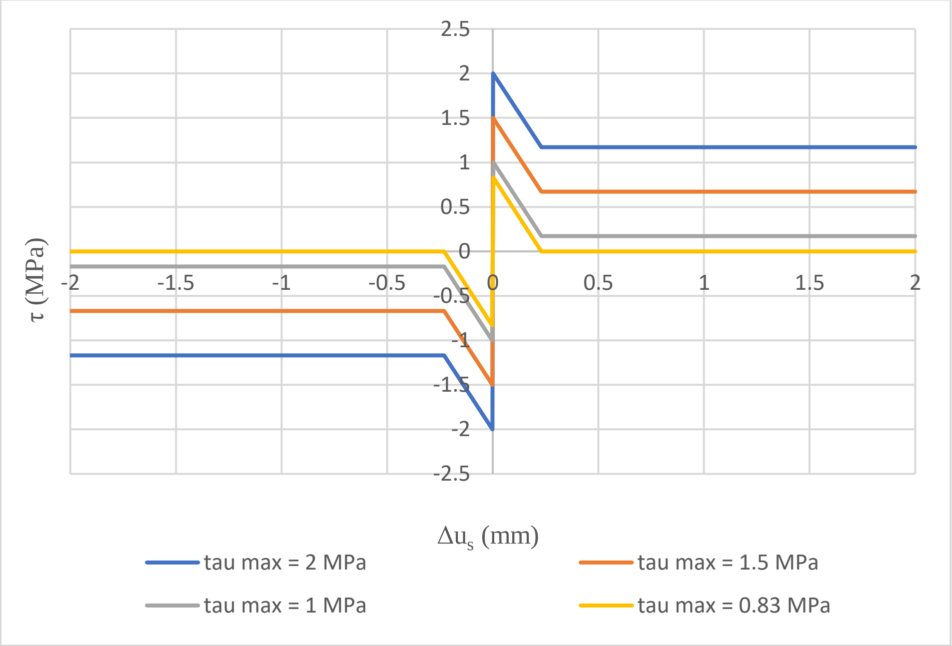

Figure 6.4 The shear traction-relative displacement diagrams of the vertical interfaces on shell elements macro-model

Other than the vertical interface elements, horizontal interface elements can also be added on the model to simulate the horizontal tensile cracks on the joints between the masonry structural elements and the concrete floors or the kim-layers. The analysis of the effect of these interface elements, however, will not be pursued in this project. Horizontal cracks in the extremities of the piers are assumed to be simulated by the cracks in the integration points inside the masonry unit finite elements.

6.2 Macro-TSRCM-Int: TSRCM Macro-Model with Vertical Interfaces

For this sensitivity study with the TSRCM model, a prescribed displacement of 80 mm in the direction of the global X-axis is applied to the model. The iteration schemes and the load steps for the analysis are summarized in the following table.

Table 6.1 The iteration scheme used for the sensitivity study on the application of the vertical interfaces (Macro-TSRCM-Int)

Lateral Loads and Nonlinearities Considered		
Prescribed Displacement	80 mm in the global X-direction	
Physical Nonlinearity	Yes	
Geometrical Nonlinearity	No	
Loading Phases and Iteration Schemes		
Self Weight	**Load Steps**	0.1(10)
	Analysis Method	Newton-Raphson (Full)
	Force Norm	0.01
	Displacement Norm	0.01
Lateral Loading	**Load Steps**	0.00625(160)
	Analysis Method	Newton-Raphson (Full)
	Force Norm	0.01
	Displacement Norm	0.01

The capacity curves from the sensitivity study analyses are presented in the following figure.

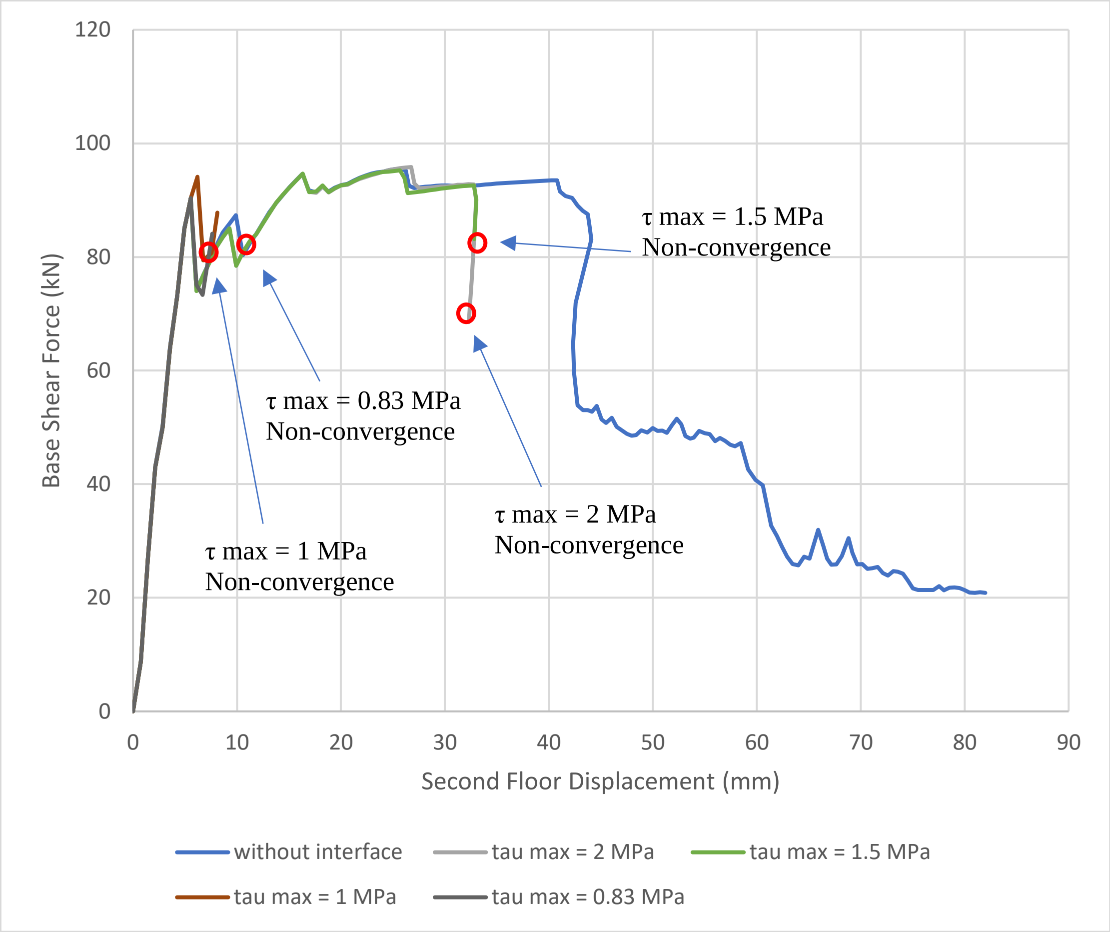

Figure 6.5 The capacity curves from the vertical interfaces sensitivity study (Macro-TSRCM-Int)

The application of vertical interface elements on the model alters the failure behavior of the model quite significantly, especially in the post-peak region. The reduction in the strength of the wall-pier connections causes the diagonal cracking failure to occur earlier and makes the structural model to be less ductile. This phenomenon seems to be caused by the change in the formation of compression struts, which affects the progression of the diagonal cracking failure. The compression struts in the numerical models with interface elements appear to form earlier causing a more abrupt collapse of the long pier. This is demonstrated in Figure 6.6 with the comparison between the principal stresses vector contour plots of the Macro-TSRCM model and the Macro-TSRCM-Int model at the same horizontal displacement. The interaction between the interface elements of the wall-pier connection and the shell elements can be seen in the figure altering the flow of the stresses across the long pier considerably.

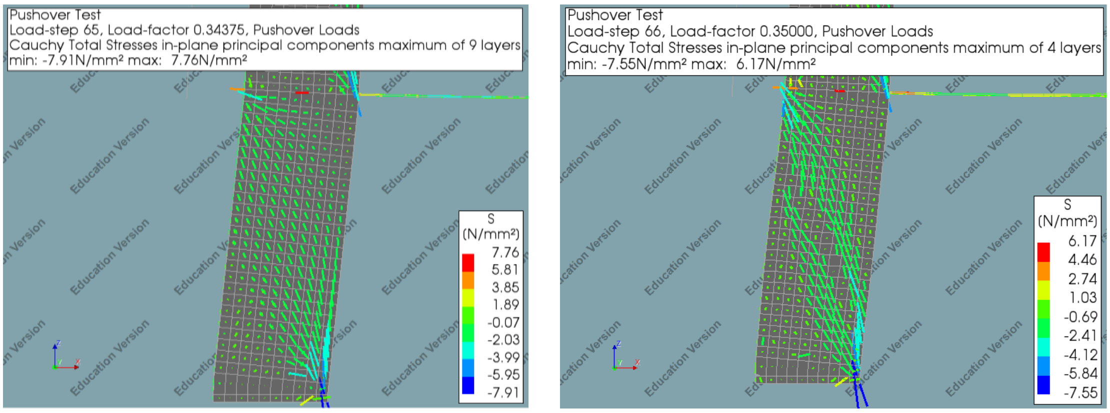

(a) (b)

Figure 6.6 The principal stresses vector contour plot at horizontal displacement = 32 mm for (a) Macro-TSRCM (without interface) and (b) Macro-TSRCM-Int ($\tau_{max} = 2\ MPa$)

The capacity curves in Figure 6.5 also clearly show that the inclusion of vertical interfaces introduces large instability to the analysis, which is indicated by the non-convergences of the analyses. These non-convergences are caused by the failure of the vertical interfaces, which occurs as soon as cracks open in the vertical joints. Reduction in the value of the maximum shear stress (τ_{max}) and the residual shear stress results in the failure of the interface elements to occur earlier. Further reduction results in the change of the governing failure mode as shown by the capacity curves with $\tau_{max} = 1\ MPa$ and $\tau_{max} = 0.83\ MPa$. Due to these non-convergences, however, it is impossible to properly assess the consequences of the vertical joints failure to the failure behavior of the structure as a whole.

Figure 6.7 and Figure 6.8 depict the crack patterns of the Macro-TSRCM model (without interface elements) and one of the Macro-TSRCM-Int model variations ($\tau_{max} = 2\ MPa$) shortly before and after the diagonal cracking failure occurs. The cracking pattern of these particular Macro-TSRCM-Int variations in the pre-peak region follows a similar pattern as the Macro-TSRCM model. However, as shown by the figures, the cracking patterns of the two models differ significantly in the post-peak region.

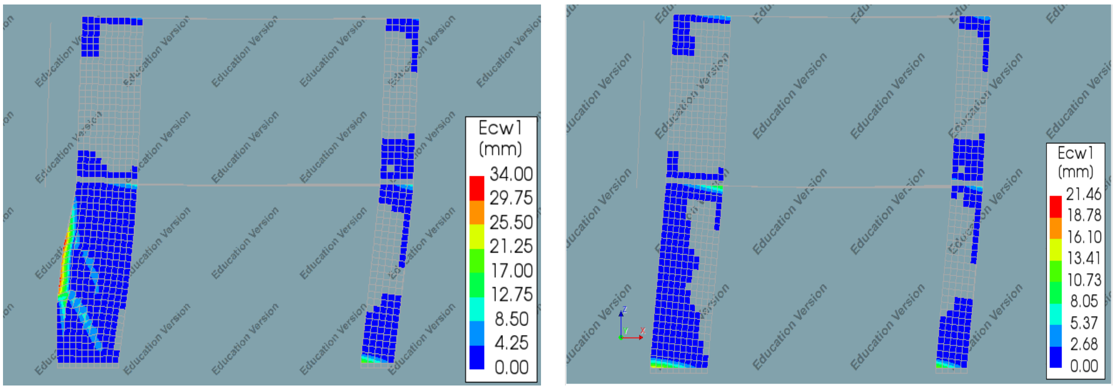

(a) (b)

Figure 6.7 The cracking pattern of the numerical models when the near-collapse displacement is reached for (a) Macro-TSRCM and (b) Macro-TSRCM-Int ($\tau_{max} = 2\ MPa$)

The cracking patterns of the two numerical models at near-collapse displacement are shown in Figure 6.7. There is a significant difference between the two models with the Macro-TSRCM model exhibiting tensile crack openings along the vertical joint between the transversal wall and the long pier. It can also be seen that the Macro-TSRCM-Int model undergoes early instance of diagonal cracking failure with little to no warning, which is indicated by the absence of crack openings along the vertical joint just before the diagonal cracks open.

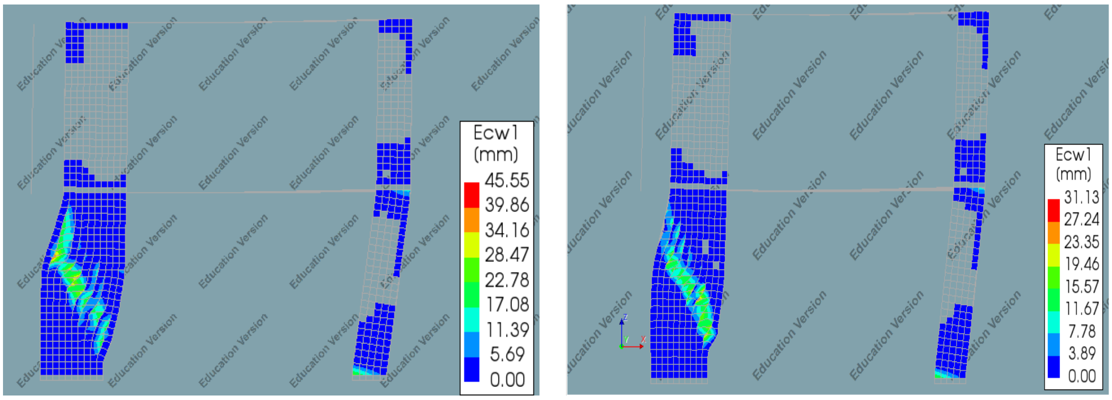

(a) (b)

Figure 6.8 The cracking pattern of the numerical models after diagonal cracking failure for (a) Macro-TSRCM and (b) Macro-TSRCM-Int ($\tau_{max} = 2\ MPa$)

Figure 6.8 shows the cracking patterns on the numerical model after the diagonal cracking failure occurs. Both models show similar cracking patterns with diagonal cracks propagating across the long pier from the wall-pier connection to the toe of the long pier. There is, however, a slight difference between the two. Vertical splitting cracks can be seen along the wall-pier connection of the Macro-TSRCM model, while these vertical cracks are not present in the Macro-TSRCM-Int model. This difference reflects the change in the flow of the stresses due to the change in the wall-pier vertical joints constitutive model.

Table 6.2 The relative displacements of Macro-TSRCM-Int ($\tau_{max} = 2\ MPa$) showing the axial relative displacements (Δu_{ny}) and the longitudinal shear relative displacements (Δu_{sx})

<table>
<tr><td colspan="2">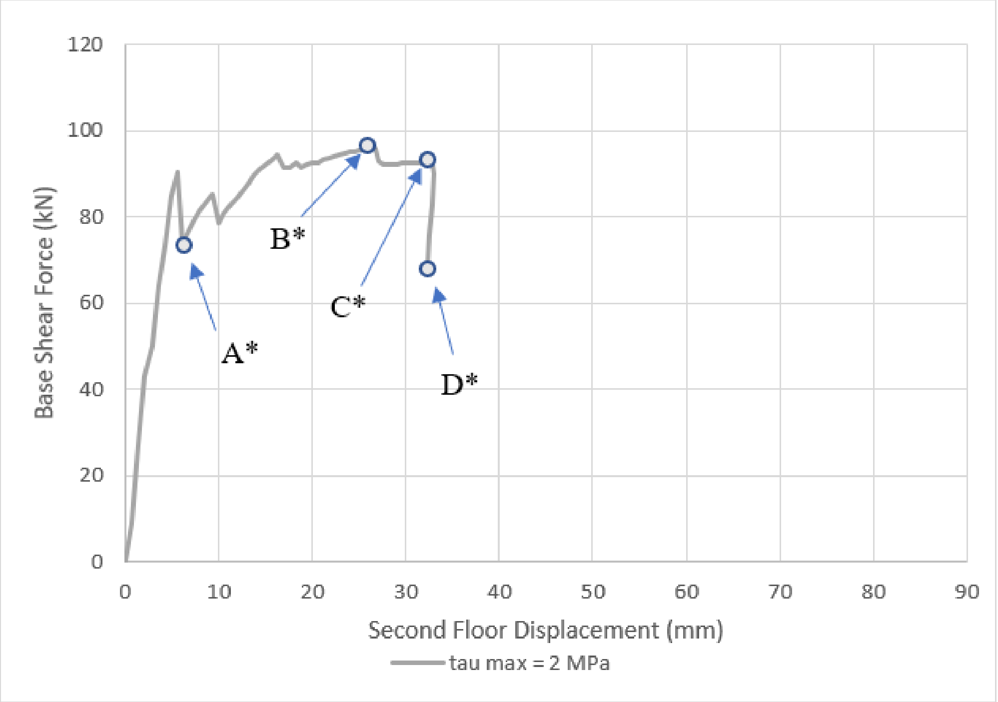
</td></tr>
<tr><td>$\boldsymbol{\Delta u_{ny}}\ (\boldsymbol{mm})$</td><td>$\boldsymbol{\Delta u_{sx}}\ (\boldsymbol{mm})$</td></tr>
<tr><td>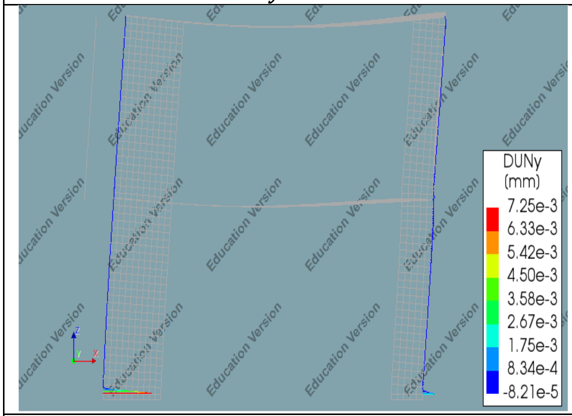
</td><td>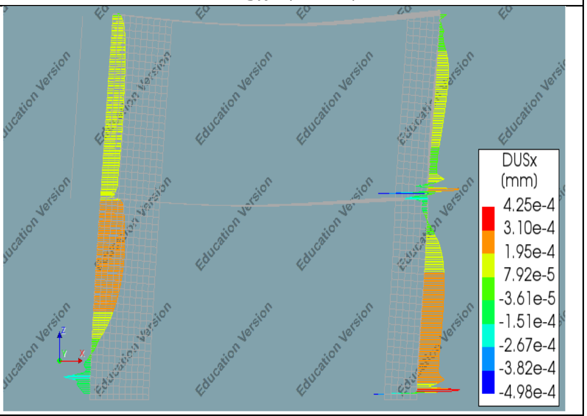
</td></tr>
<tr><td colspan="2">(A*) Activation of rocking mechanism</td></tr>
</table>

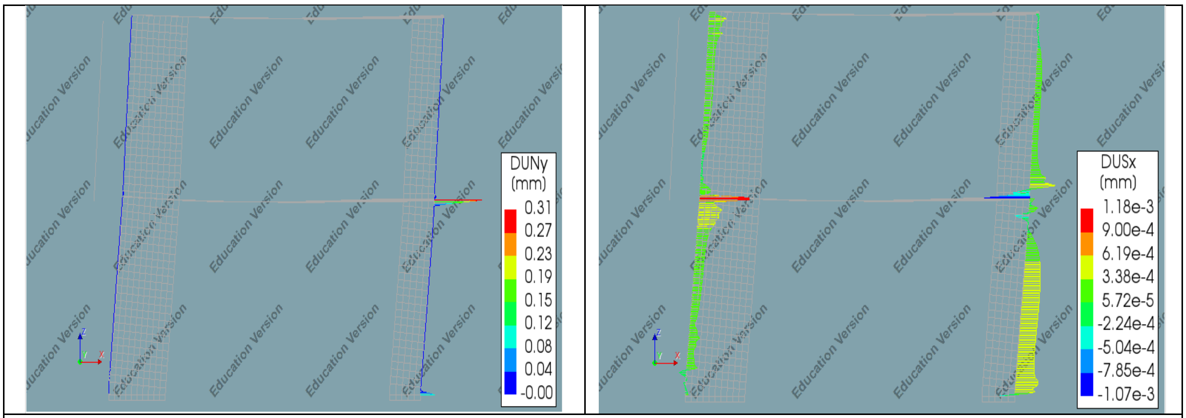

(B*) Peak base shear force reached

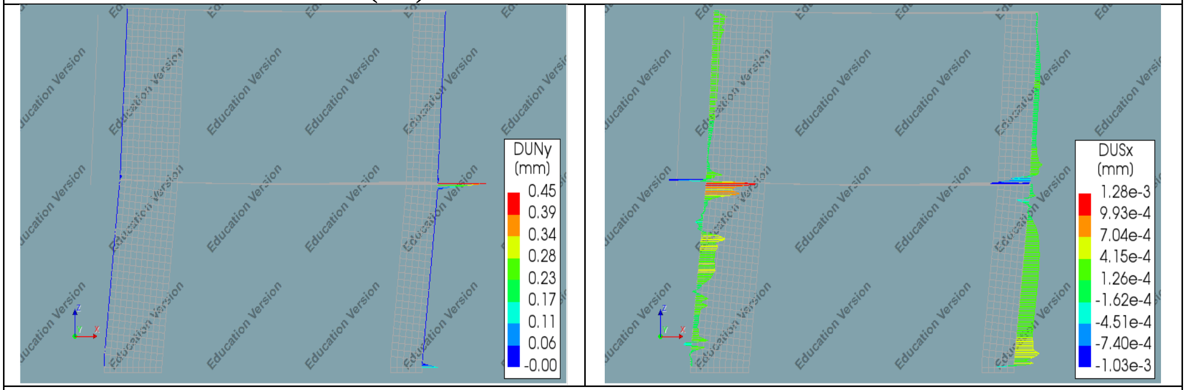

(C*) Near-collapse displacement reached

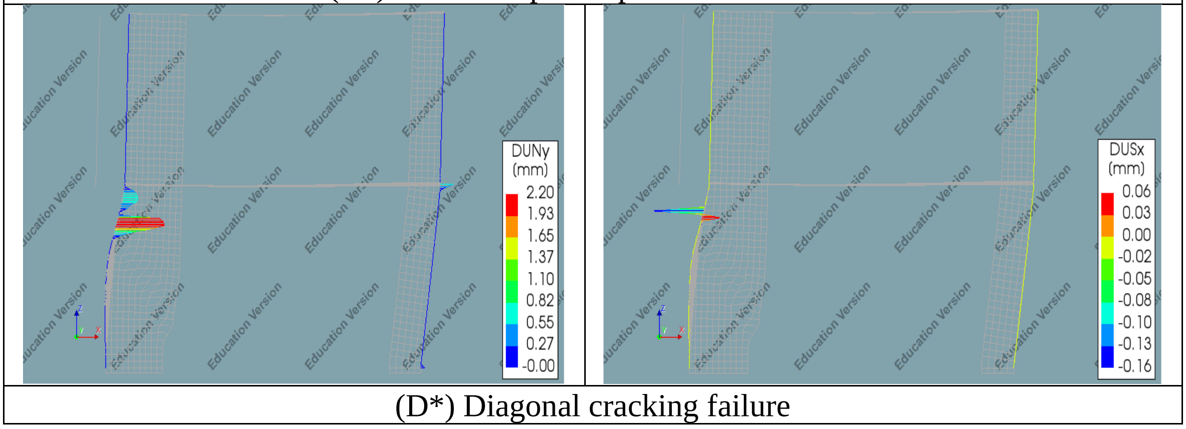

(D*) Diagonal cracking failure

Table 6.2 shows the interface element relative displacement of Macro-TSRCM-Int model variation with $\tau_{max} = 2\ MPa$. The relative displacement line diagrams show that the interface elements mostly undergo shear in the longitudinal direction. The shear relative displacement initially shows a smooth and continuous distribution at the beginning as can be seen at event A*. As the analysis progresses, the shear relative displacement distribution becomes more erratic. It is unclear why this phenomenon occurs, but it is probably related to the formation of cracks in the shell elements. After the diagonal cracking failure occurs at event D*, large relative displacements in the axial direction are spotted in the vertical joint between the westside transversal wall and the long pier. These large relative displacements are caused by the diagonal cracking failure of the long pier.

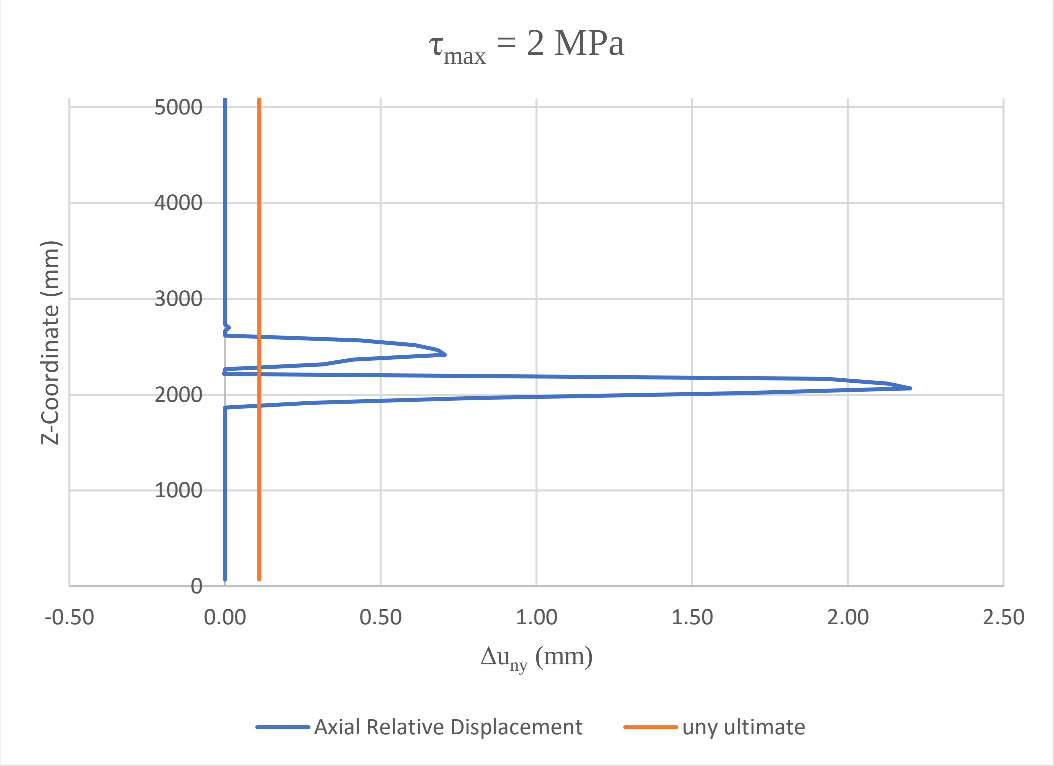

Figure 6.9 Axial interface relative displacement of the long pier connection of the Macro-TSRCM-Int ($\tau_{max} = 2\ MPa$) at failure

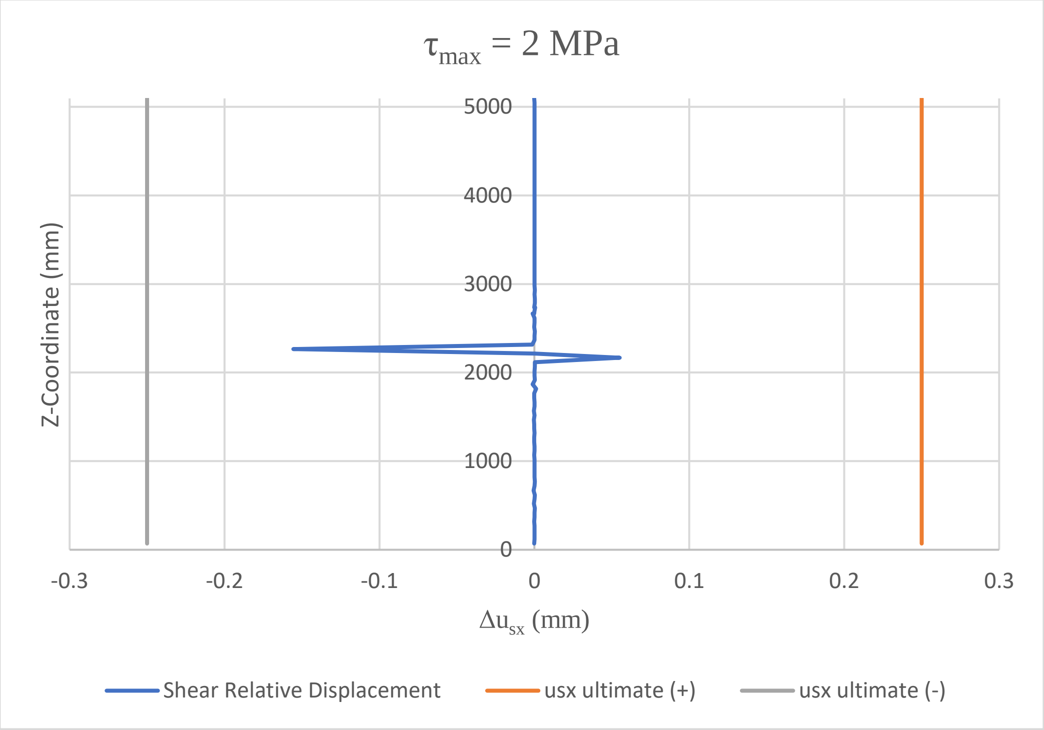

Figure 6.10 Shear interface relative displacement of the long pier connection of the Macro-TSRCM-Int ($\tau_{max} = 2\ MPa$) at failure

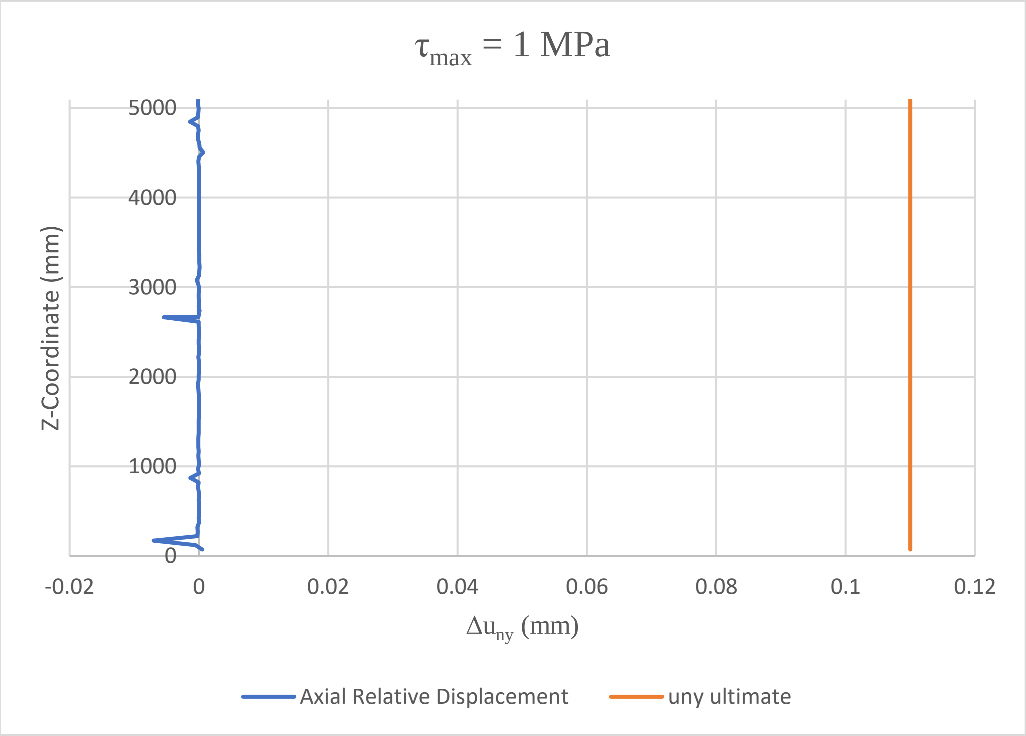

Figure 6.11 Axial interface relative displacement of the long pier connection of the Macro-TSRCM-Int ($\tau_{max} = 1\ MPa$) at failure

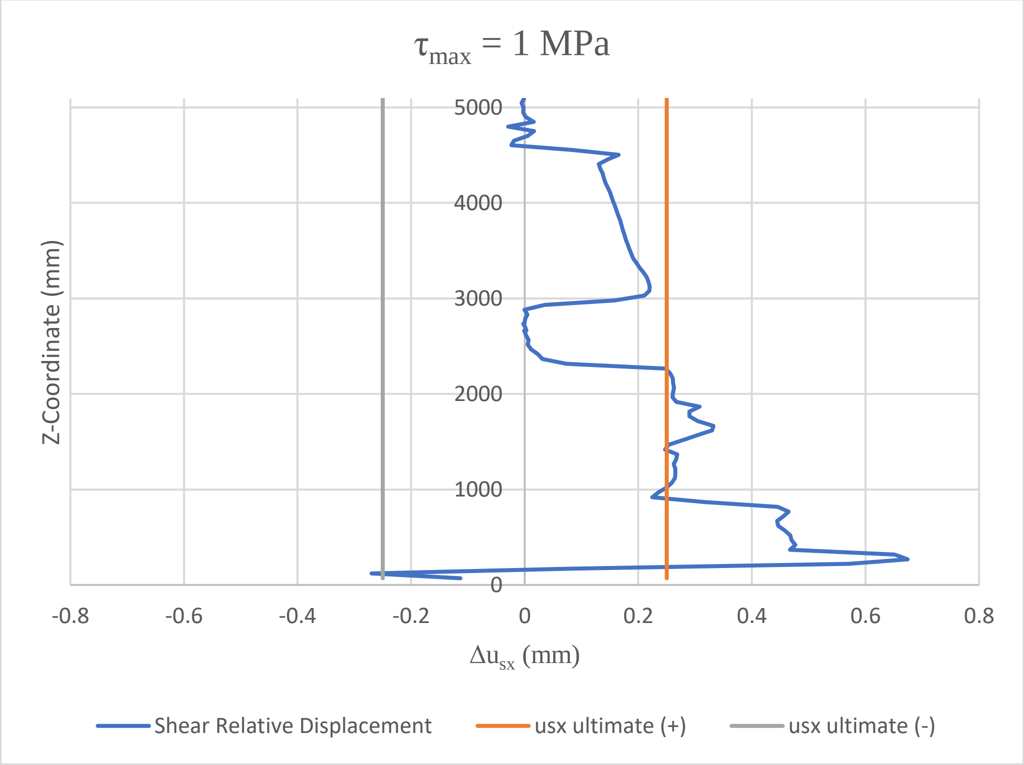

Figure 6.12 Shear interface relative displacement of the long pier connection of the Macro-TSRCM-Int ($\tau_{max} = 1\ MPa$) at failure

The relative displacement diagrams of the long pier show the change in the failure behavior of the vertical joints. Figure 6.9 and Figure 6.10 show the relative displacement diagrams of the wall-pier connection at the long pier of the numerical model with $\tau_{max} = 2\ MPa$. The axial interface relative displacement of the model variation shows large axial displacements that exceed the ultimate tensile crack displacement indicating the opening of tensile cracks in the wall-pier connection, which is the consequence of the diagonal cracking failure of the pier. On the other hand, the shear relative displacement shows that it does not exceed the ultimate shear displacement even after the failure of the pier. This indicates that the interface elements do not undergo the opening of the shear cracks signifying the absence of the Mode-II mechanism on the connection. This shows that the wall-pier connection fails due to the failure of the piers by splitting cracks.

On the other hand, the relative displacement of the numerical model with $\tau_{max} = 1\ MPa$ in Figure 6.11 and Figure 6.12 show different behavior. Figure 6.11 shows that the axial relative displacement of the wall-pier connection does not exceed the ultimate tensile relative displacement at failure, while it can be seen that the shear relative displacement in Figure 6.12 exceeds the ultimate shear relative displacement. This behavior indicates that the wall-pier connection undergoes a pure Mode-II mechanism. In other words, the connection fails due to the transversal wall undergoes a sliding movement relative to the pier instead of the failure of the piers.

6.3 Macro-EMM-Int: EMM Macro-Model with Vertical Interfaces

The sensitivity study on the Macro-EMM-Int model is carried out in a similar fashion with the one on the Macro-TSRCM-Int model. A prescribed displacement of 200 mm in the global X-direction is applied to the model similar to the EMM model without any interface element, Macro-EMM. The analyses will be conducted on the model with two different values of the staircase crack angle similar to the analysis conducted in section 5.2.1. The iteration schemes and load steps used for the analysis are summarized in the table below.

Table 6.3 The iteration scheme used for the sensitivity study on the application of the vertical interfaces (Macro-EMM-Int)

Lateral Loads and Nonlinearities Considered		
Prescribed Displacement	200 mm in the global X-direction	
Physical Nonlinearity	Yes	
Geometrical Nonlinearity	No	
Loading Phases and Iteration Schemes		
Self Weight	Load Steps	0.1(10)
	Analysis Method	Newton-Raphson (Full)
	Force Norm	0.01
	Displacement Norm	0.01
Lateral Loading	Load Steps	0.0025(400)

	Analysis Method	Newton-Raphson (Full)
	Force Norm	0.01
	Displacement Norm	0.01

The capacity curves from the sensitivity study on Macro-EMM-Int are presented as follows.

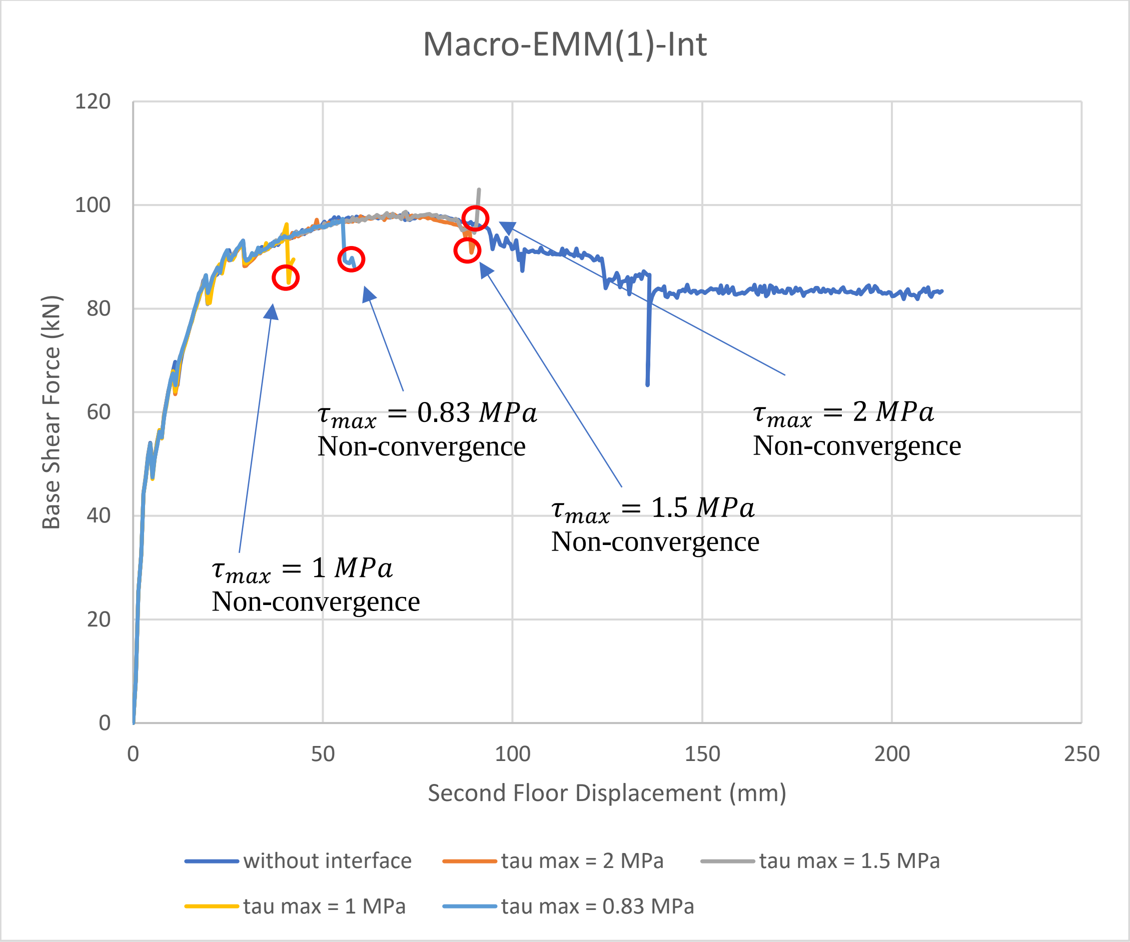

$\tau_{max} = 0.83\ MPa$ Non-convergence

$\tau_{max} = 2\ MPa$ Non-convergence

$\tau_{max} = 1.5\ MPa$ Non-convergence

$\tau_{max} = 1\ MPa$ Non-convergence

Figure 6.13 The capacity curves from the sensitivity study (Macro-EMM(1)-Int staircase crack angle = 69.37^0)

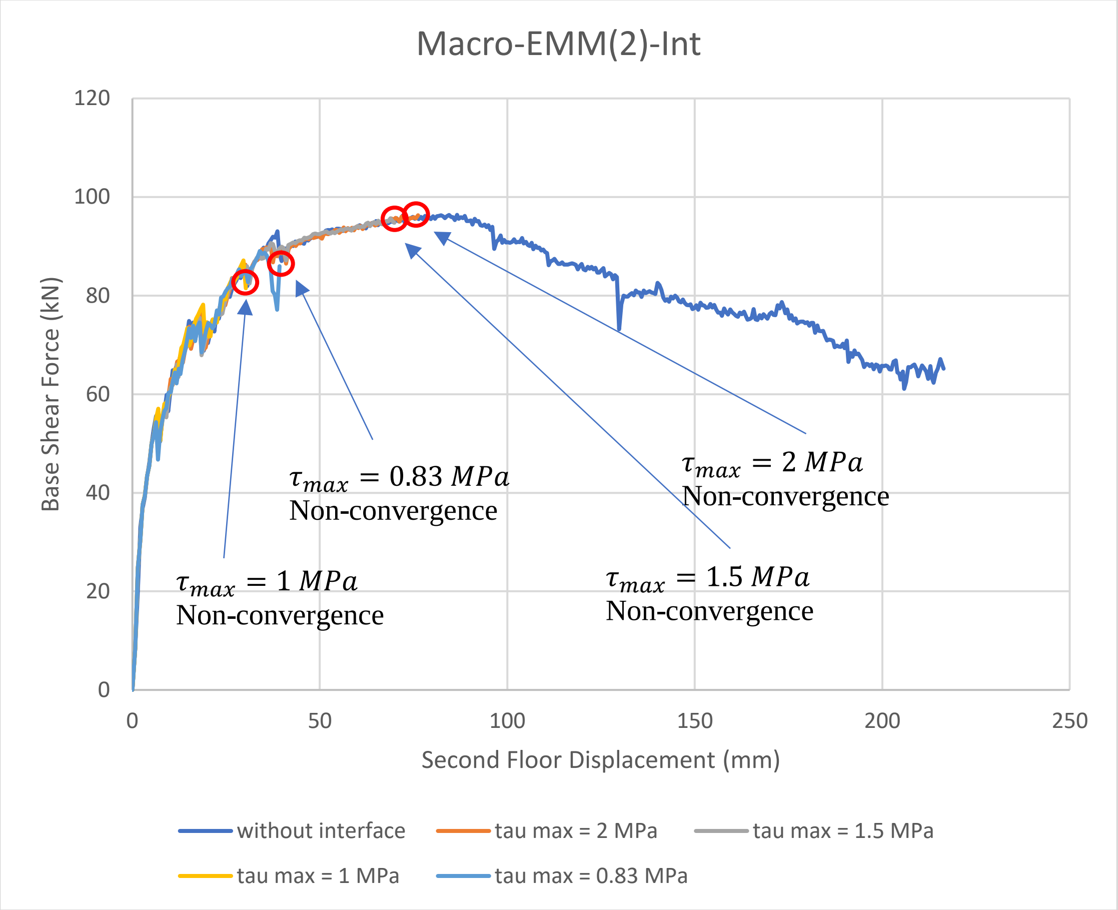

Figure 6.14 The capacity curves from the sensitivity study (Macro-EMM(2)-Int staircase crack angle = 78.39^0)

The capacity curves of the sensitivity study on the Macro-EMM(1)-Int and Macro-EMM(2)-Int model variations show that the inclusion of vertical interface elements introduces large instability to the analysis. This is shown by the non-convergences of the analyses indicated on the plot. These non-convergences are caused by the failure of the interface elements. The figure shows that the reduction of τ_{max} and residual shear stress results in the failure of the interface elements to occur earlier. Apart from introducing instability to the analysis, the inclusion of vertical interface elements does not significantly alter the properties of the capacity curves. In terms of initial stiffness and structural capacity, no significant change is observed. The lack of noticeable change in the capacity curves might be due to the model exhibiting tensile cracking and crushing, which are the results of flexural behavior that is not influenced by the vertical interface elements. The combination of different values of the staircase crack angle and the vertical interfaces does not seem to affect the capacity curves behavior either as evidenced by the capacity curve of Macro-EMM(2)-Int in Figure 6.14. It is of note, however, that this observation is made based on the structural behavior before the failure of the vertical joints. The failure of the vertical joints might have a more significant effect on the structural behavior at a later stage. However, due to the non-convergences on the model, it is currently impossible to properly assess the full extent of the effect the vertical joints failure has on the structural behavior.

The following table shows the evolution of crack patterns on the piers and the crushing damage of the piers represented by Ecw1 contour plots respectively.

Table 6.4 Comparison of cracking pattern on model Macro-EMM(1) (staircase crack angle = 69.37^0 & no interface) and Macro-EMM(1)-Int (staircase crack angle = 69.37^0 & $\tau_{max} = 2\ MPa$)

<table>
<tr><th>Macro-EMM(1)</th><th>Macro-EMM(1)-Int</th></tr>
<tr><td>
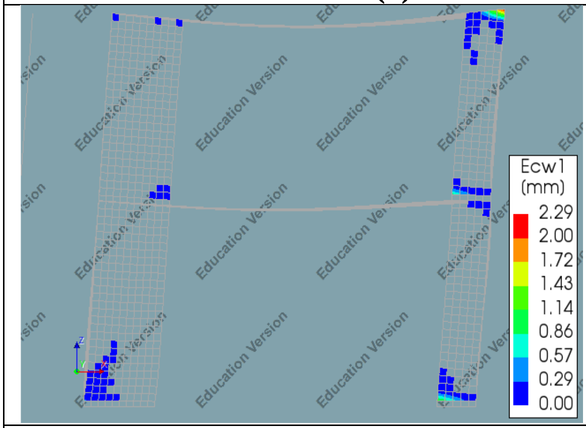

</td><td>
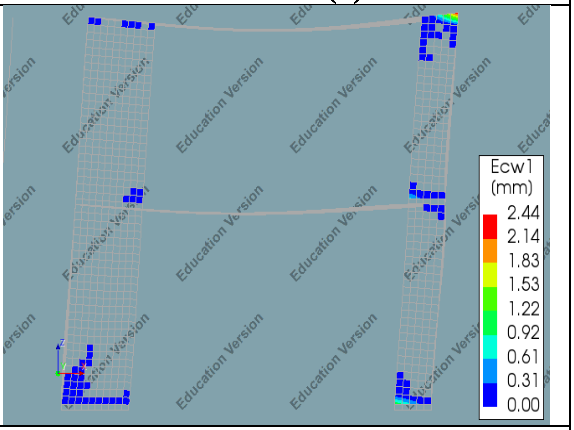

</td></tr>
<tr><td colspan="2">(A) Activation of rocking mechanism</td></tr>
<tr><td>
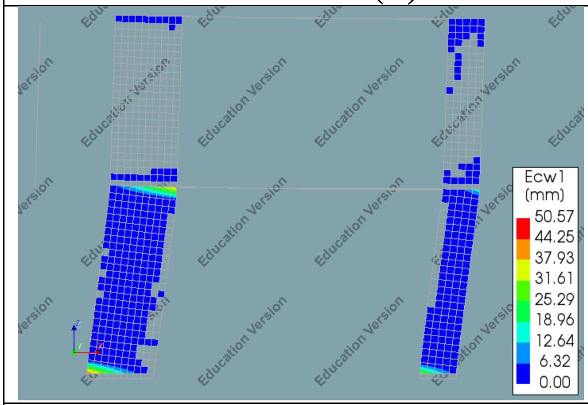

</td><td>
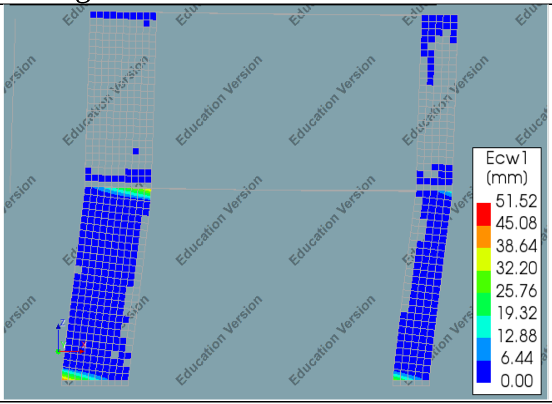

</td></tr>
<tr><td colspan="2">(B) Peak base shear force reached</td></tr>
<tr><td>
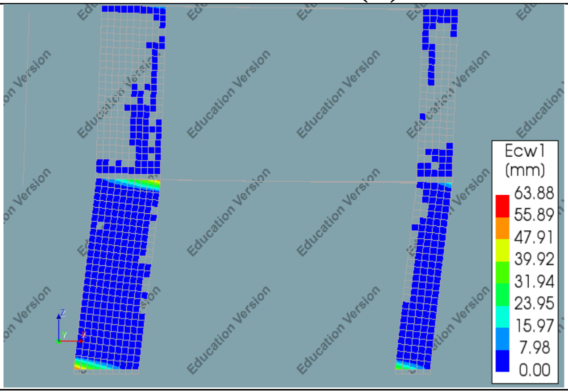

</td><td>
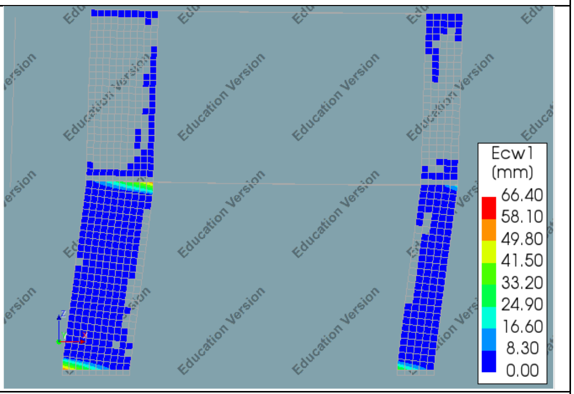

</td></tr>
<tr><td colspan="2">(C) Maximum horizontal displacement of Macro-EMM(1)-Int model</td></tr>
</table>

Table 6.5 Comparison of crushing damage on model Macro-EMM(1) (staircase crack angle = 69.37^0 & no interface) and Macro-EMM(1)-Int (staircase crack angle = 69.37^0 & $\tau_{max} = 2\ MPa$)

<table>
<tr><th>Macro-EMM(1)</th><th>Macro-EMM(1)-Int</th></tr>
<tr><td>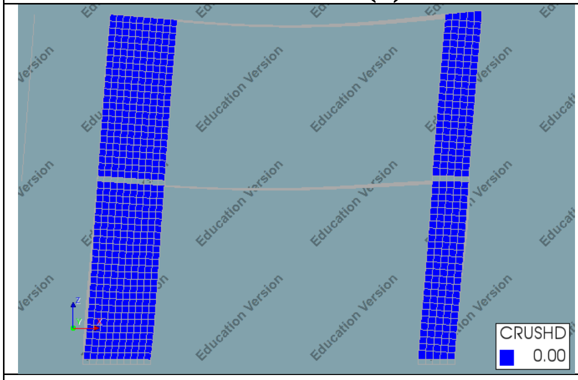
</td><td>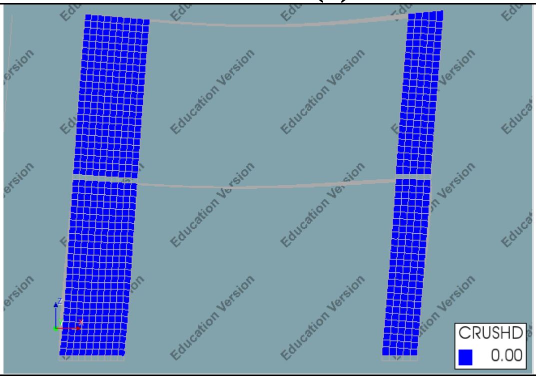
</td></tr>
<tr><td colspan="2">(A) Activation of rocking mechanism</td></tr>
<tr><td>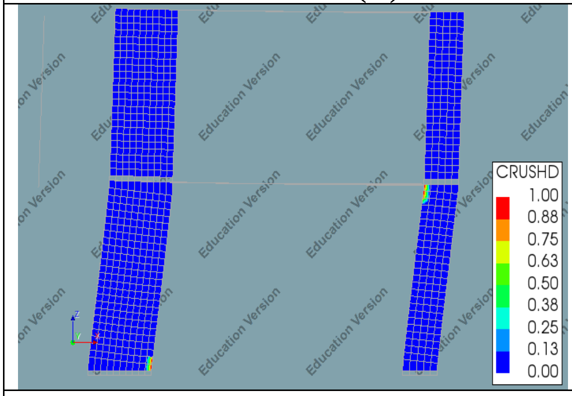
</td><td>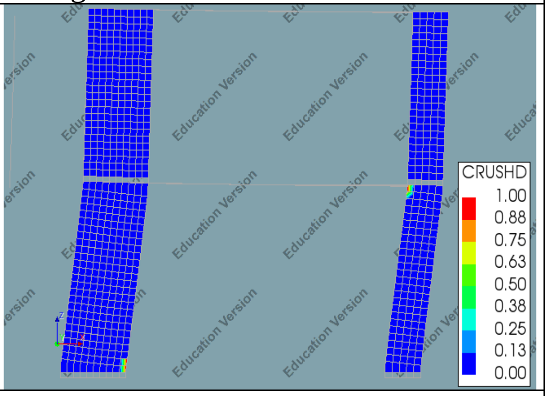
</td></tr>
<tr><td colspan="2">(B) Peak base shear force is reached</td></tr>
<tr><td>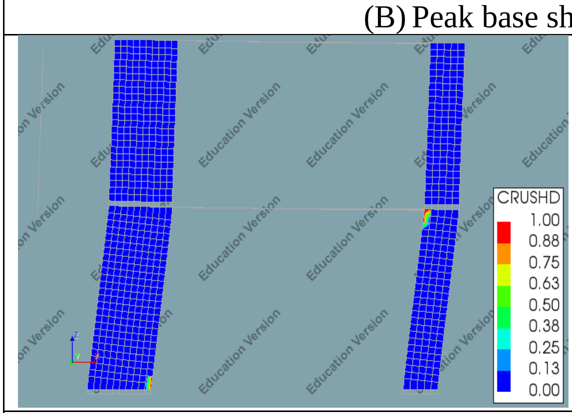
</td><td>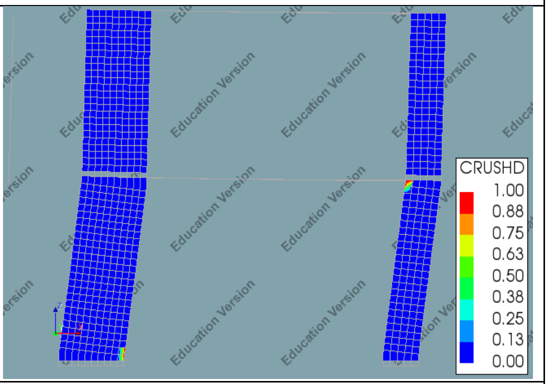
</td></tr>
<tr><td colspan="2">(C) Maximum horizontal displacement by Macro-EMM(1)-Int model</td></tr>
</table>

Table 6.4 and Table 6.5 show the comparison of damages sustained by the Macro-EMM(1) and Macro-EMM(1)-Int model. As can be seen from the two tables, there is no significant difference in terms of cracking patterns and crushing between the two numerical models. This supports the observation of the capacity curves, that the inclusion of vertical interfaces does not affect the formation of failure mechanisms in the piers and

transversal walls. The other model variation with a different value of staircase crack angle, Macro-EMM(2)-Int, also shows a similar trend as Macro-EMM(1)-Int, where there is no significant change in the structural behavior and the extent of structural damages when compared to the model with no vertical interface.

Table 6.6 The relative displacements of Macro-EMM(1)-Int ($\tau_{max} = 2\ MPa$) showing the axial relative displacements (Δu_{ny}) and the longitudinal shear relative displacements (Δu_{sx})

<table>
<tr><td colspan="2">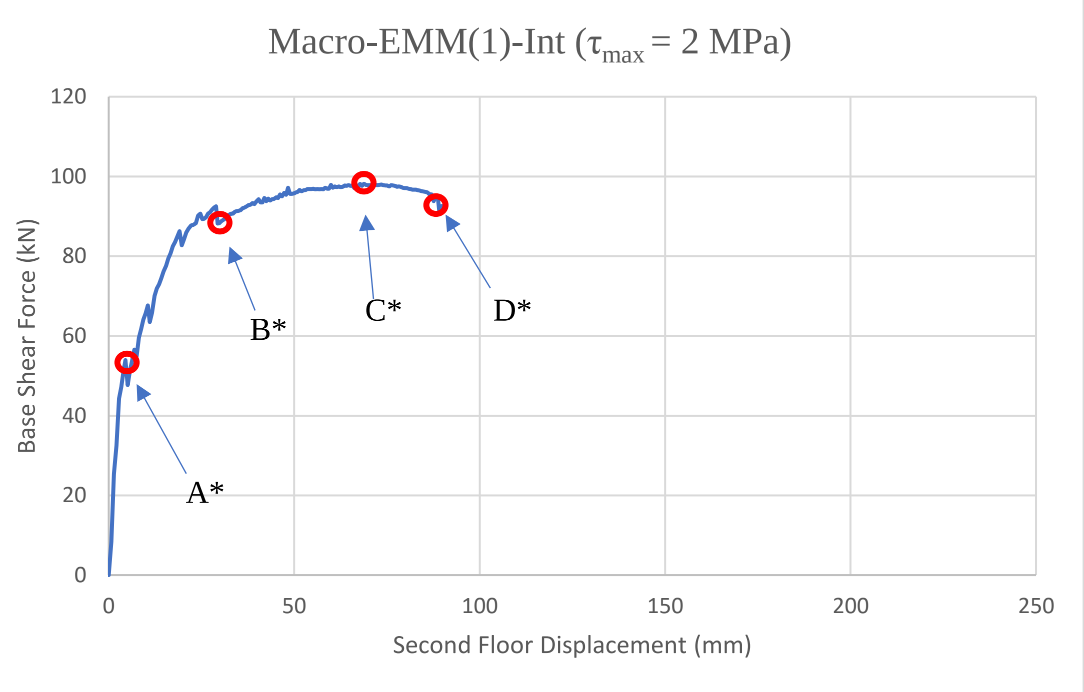
</td></tr>
<tr><td>$\Delta u_{ny}\ (mm)$</td><td>$\Delta u_{sx}\ (mm)$</td></tr>
<tr><td>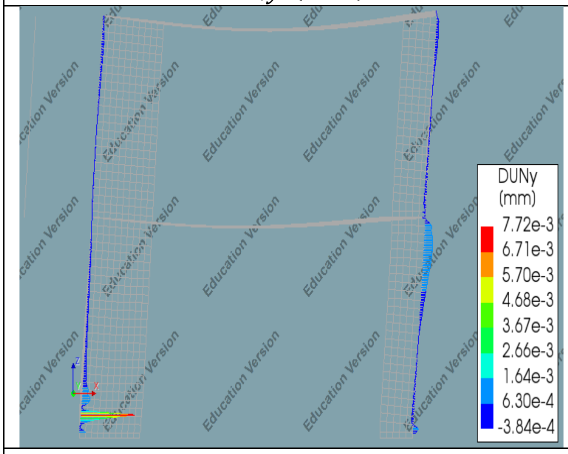
</td><td>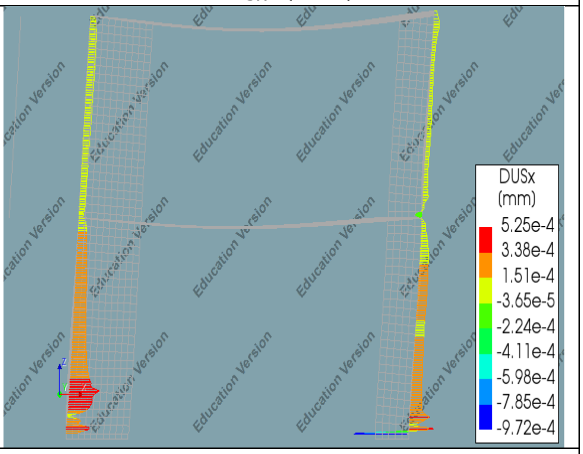
</td></tr>
<tr><td colspan="2">(A*) Activation of rocking mechanism</td></tr>
</table>

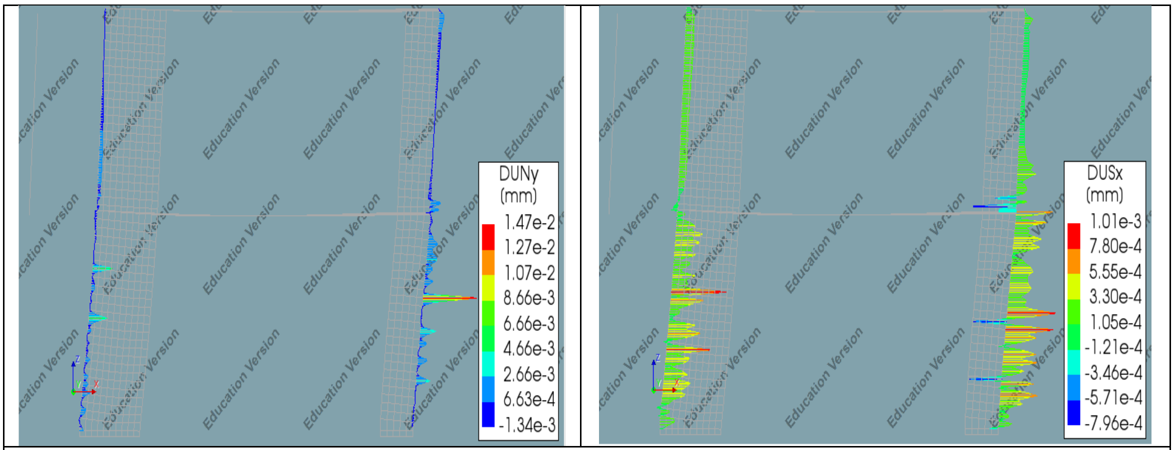

(B*) Beginning of the plateau

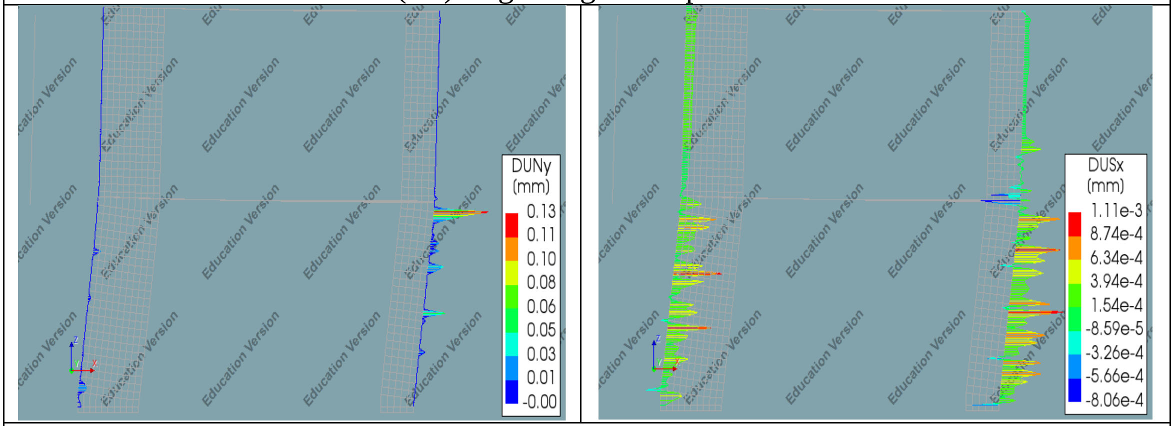

(C*) Peak base shear force reached

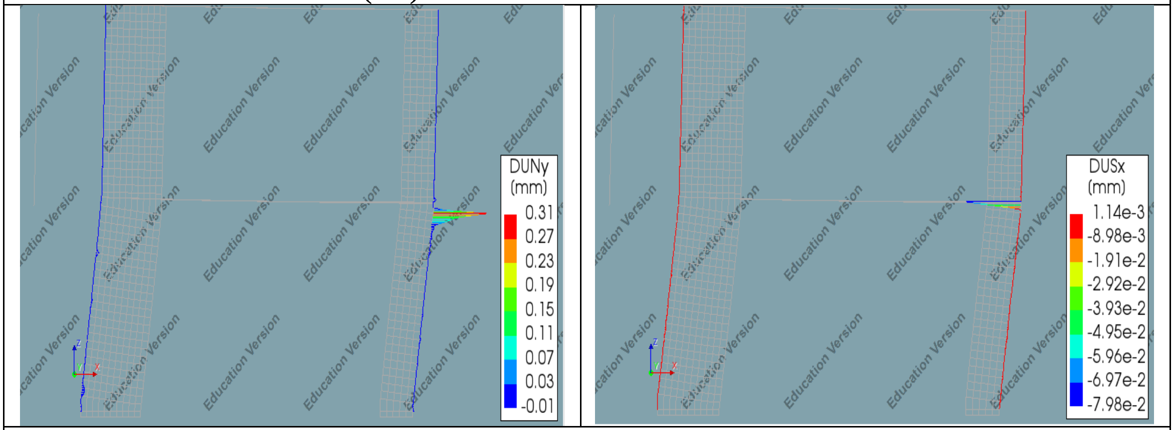

(D*) Maximum horizontal displacement of the numerical model

Table 6.4 and Table 6.5 show the comparison of damages sustained by the Macro-EMM(1) and Macro-EMM(1)-Int model. As can be seen from the two tables, there is no significant difference in terms of cracking patterns and crushing between the two numerical models. This supports the observation of the capacity curves, that the inclusion of vertical interfaces does not affect the formation of failure mechanisms in the piers and transversal walls. The other model variation with a different value of staircase crack angle, Macro-EMM(2)-Int, also shows a similar trend as Macro-EMM(1)-Int, where there is no significant change in the structural behavior and the extent of structural damages when compared to the model with no vertical interface.

Table 6.6 shows the relative displacement of Macro-EMM(1)-Int, which represents the opening of cracks in the vertical interfaces. The relative displacement line diagrams show very erratic behavior, especially in the longitudinal shear direction. It is interesting to note that this erratic behavior is mainly observed on the ground floor. By comparing the shear relative displacement diagram to the crack width contour plot, it can be seen that the locations, where this erratic relative displacement is found, correspond to the locations where the pier shell elements undergo cracking. It is, however, still not clear how the relative displacement is affected by the formation of cracks in the shell elements.

Table 6.7 The relative displacements of Macro-EMM(2)-Int ($\tau_{max} = 2\ MPa$) showing the axial relative displacements (Δu_{ny}) and the longitudinal shear relative displacements (Δu_{sx})

<table>
<tr><td colspan="2">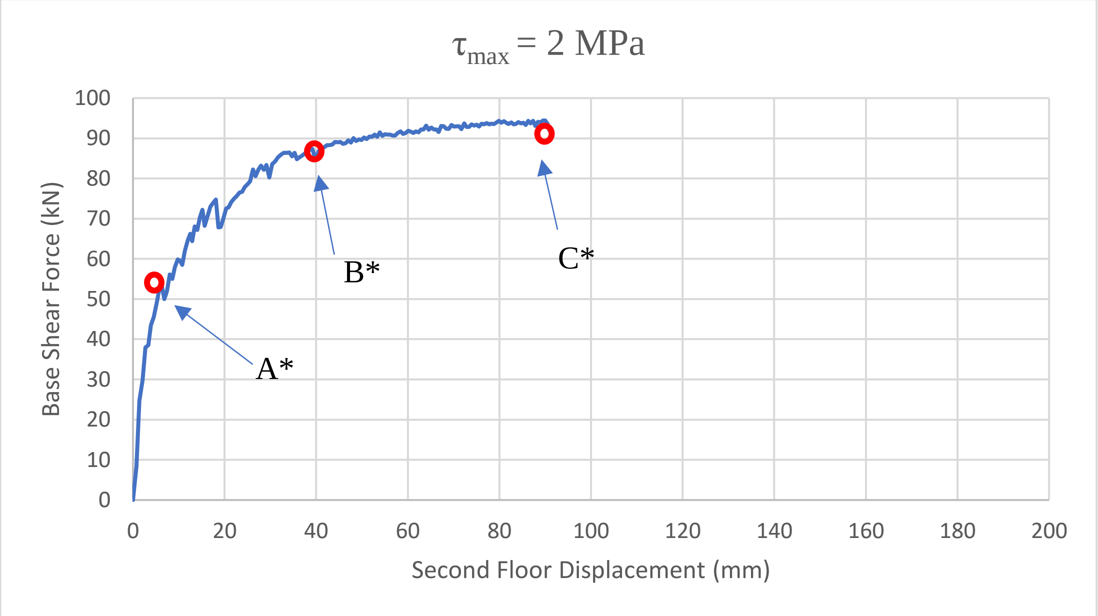 </td></tr>
<tr><td>$\Delta u_{ny}\ (mm)$</td><td>$\Delta u_{sx}\ (mm)$</td></tr>
<tr><td>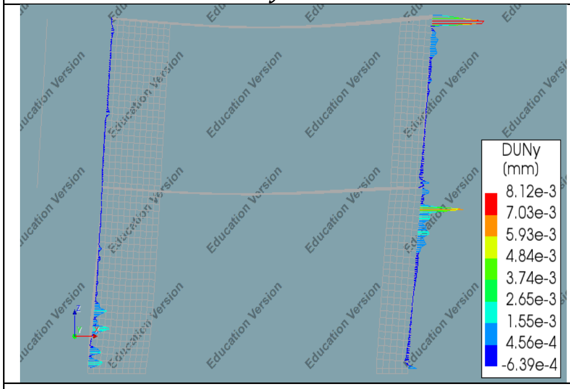 </td><td>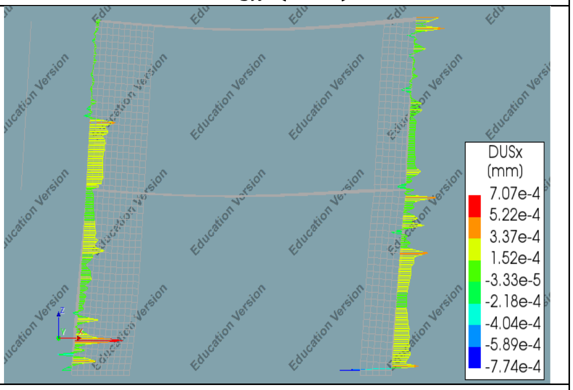 </td></tr>
<tr><td colspan="2">(A*) Activation of rocking mechanism</td></tr>
</table>

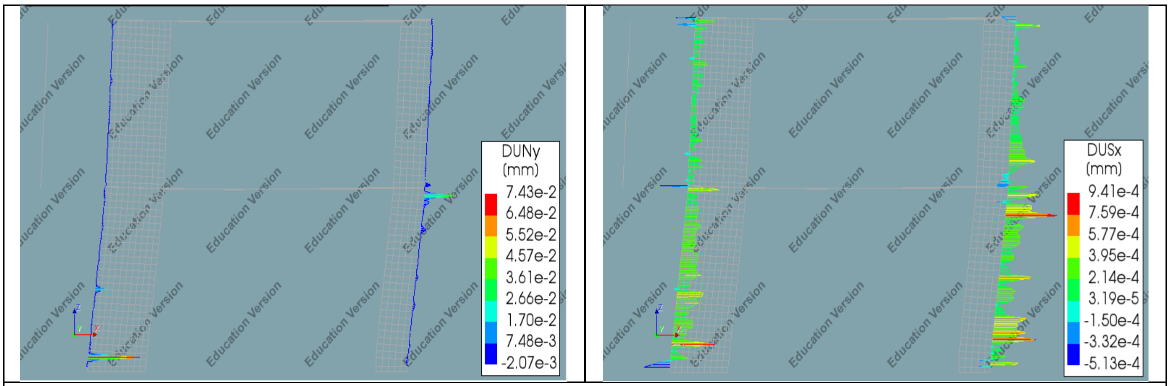

(B*) Beginning of the plateau

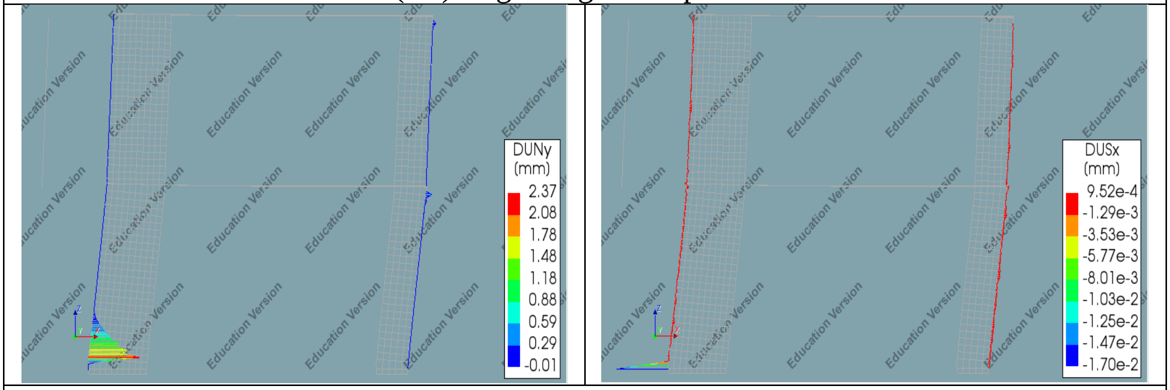

(C*) Maximum horizontal displacement reached by the numerical model

The relative displacement of the Macro-EMM(2)-Int model is shown in Table 6.7. The vertical interfaces of the model also show similar behavior as the ones on the Macro-EMM(1)-Int model. As with Macro-EMM(1)-Int, the erratic distribution of shear relative displacement also corresponds to the location where the shell elements undergo cracking. The reason behind this irregular distribution of relative displacement is still unclear. But it is likely related to the formation of cracks in the shell elements. Large axial relative displacement is spotted at the area around the bottom pier joint, where the pier undergoes the largest flexural deformation. Large shear relative displacement shown at event C* indicates the presence of dry friction mechanism in the vertical joints. However, as with the previous model, this dry friction mechanism also does not last long as the model undergoes divergence due to out of bound shear relative displacement shortly after.

6.4 Concluding Remarks

The analysis of shell macro-models with the inclusion of vertical interfaces at corners has been discussed in this chapter. From the analyses that have been carried out, the following conclusions can be made:

- The inclusion of interface elements to the Macro-TSRCM model affects the post-peak behavior of the model significantly. The diagonal cracking failure of the model occurs at an earlier point with the change in the vertical joint behavior. The sensitivity study on the shear traction-relative displacement diagram shows that the change in the traction diagram can drastically change the governing failure mechanism of the structure as evidenced by the change in the governing mechanism from diagonal cracking failure to the failure of the vertical joint with the reduction in the interface elements shear strength.

- The effect of the interface elements on the Macro-EMM models is less significant compared to the Macro-TSRCM model. Apart from changing the governing failure mode on the structure, there is no significant change to the capacity curve and the cracking patterns on the structure. The inclusion of the interface elements introduces large instability to the analysis, which is shown in the capacity curves as non-convergences. These non-convergences in the analyses are caused by the failure of the vertical joint. The presence of these non-convergences causes a comprehensive study on the post-peak behavior of the structure to be impossible to be carried out.

Chapter 7

Finite Element Analysis of Shell Elements Micro-Model

This chapter will discuss the nonlinear pushover analysis of shell elements micro-model. Shell elements micro-model is constructed with the simplified micro-model approach. Several different types of constitutive models for the interface elements will be used for the analysis. The material parameters used for the constitutive models of the interface elements have been defined in section 3.3.3. Each model with different interface constitutive models will also be analyzed using different types of continuum element constitutive models. Two variations of constitutive models for the shell elements will be used for shell elements micro-model; the linear elastic constitutive model and the TSRCM constitutive model. The TSRCM constitutive model is used to simulate cracking inside the masonry units. For all analyses, geometrical nonlinearity is not considered. All micro-model variations considered in the analysis are summarized in the following table.

Table 7.1 Shell micro-model variations considered for the analysis

Modeling Approach	**Model Designation**	**Constitutive Model (Interface Element)**	**Constitutive Model (Continuum Element)**
Block-based micro-model (monotonic)	Micro-Coulomb-Linear	Coulomb Friction	Linear Elastic
	Micro-Coulomb-TSRCM	Coulomb Friction	TSRCM
	Micro-Discrete-Linear	Discrete Cracking	Linear Elastic
	Micro-Discrete-TSRCM	Discrete Cracking	TSRCM
	Micro-Discrete-TSRCM(Cmp)	Discrete Cracking	TSRCM (Compression-Only)
	Micro-NL_Elastic-Linear	Nonlinear Elasticity	Linear Elastic
	Micro-NL_Elastic-TSRCM	Nonlinear Elasticity	TSRCM

7.1 Structural Analysis Schemes

Similar to shell elements macro-model from the previous chapter, shell elements micro-model will also be subjected to lateral loading in the form of a prescribed deformation. A prescribed deformation of 80 mm in the global X-axis direction is applied to the models.

The models will initially be loaded with the self-weight of the model followed by the applied prescribed deformation. The load steps and the iteration schemes used for the analyses are summarized in the following table.

Table 7.2 The analysis details of the nonlinear analysis of shell micro-models

Lateral Loads and Nonlinearities Considered		
Prescribed Displacement	80 mm in the global X-direction	
Physical Nonlinearity	Yes	
Geometrical Nonlinearity	No	
Loading Phases and Iteration Schemes		
Self Weight	**Load Steps**	0.1(10)
	Analysis Method	Newton-Raphson (Full)
	Force Norm	0.01
	Displacement Norm	0.01
Lateral Loading	**Load Steps**	0.00625(160)
	Analysis Method	Newton-Raphson (Full)
	Force Norm	0.01
	Displacement Norm	0.01

Shell elements micro-model will be analyzed using three different variations of interface element constitutive models with each model using two alternative shell element constitutive models; the linear-elastic and the TSRCM model.

7.2 Micro-Coulomb: Micro-Model with Coulomb Friction Interface Model

7.2.1 Micro-Coulomb-Linear: Coulomb Friction Interface Elements and Linear Elastic Shell Elements

The results of the analysis of the model with the Coulomb friction interface elements and the linear elastic shell elements are presented as follows.

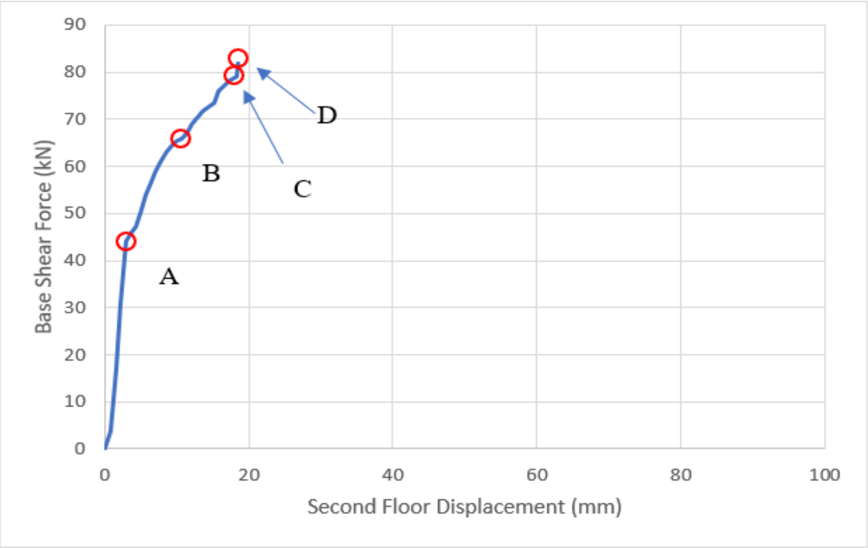

Figure 7.1 The capacity curve result from the nonlinear pushover analysis of Micro-Coulomb-Linear model variation

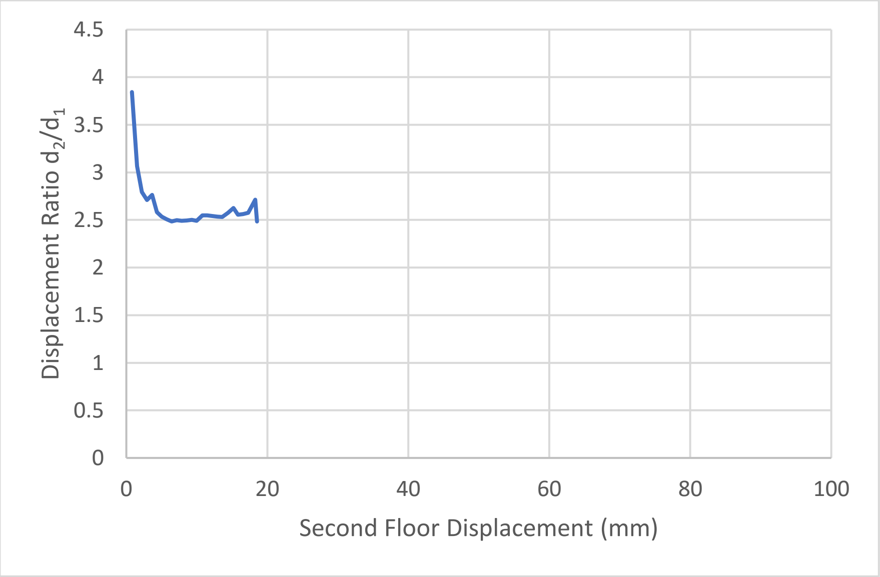

Figure 7.2 The interstory drift curve from the nonlinear pushover analysis of Micro-Coulomb-Linear model variation

The analysis of Micro-Coulomb-Linear results in the highest value of the base shear force of 79.14 kN, an initial stiffness of 15.09 kN/mm and the highest value of horizontal displacement of 18.27 mm. The capacity curve in Figure 7.1 shows a gradual transition from the linear region to the peak, instead of the slight decrease that occurs when the rocking mechanism is activated like in the Macro-TSRCM model. This behavior is most likely caused by the presence of the shear behavior in the interface elements constitutive model. It can be seen from the figure, that the analysis is unstable with it encountering non-convergence in the pre-peak region. The interstory drift curve is plotted in Figure 7.2. The curve shows an initial sharp decrease, which is then followed by a transition to a relatively constant displacement ratio value. However, judging from the deformation of the structure, this constant displacement ratio does not indicate the development of a soft-story mechanism on the ground floor.

Table 7.3 The mortar joints cracks of Micro-Coulomb-Linear model represented by interface relative displacements Δu_{ny} and Δu_{sz} for events depicted in Figure 7.1

<table>
<tr><th>$\boldsymbol{\Delta u_{ny}}$</th><th>$\boldsymbol{\Delta u_{sz}}$</th></tr>
<tr><td>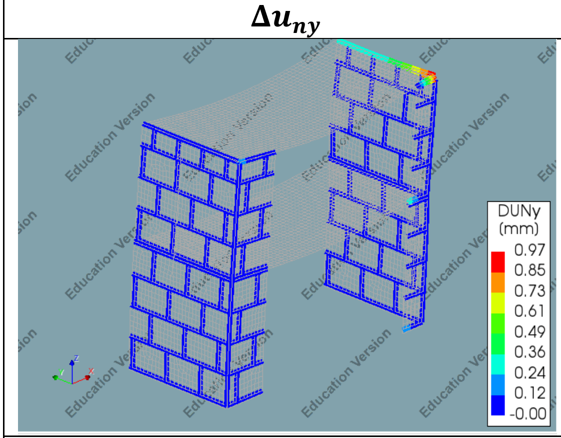
</td><td>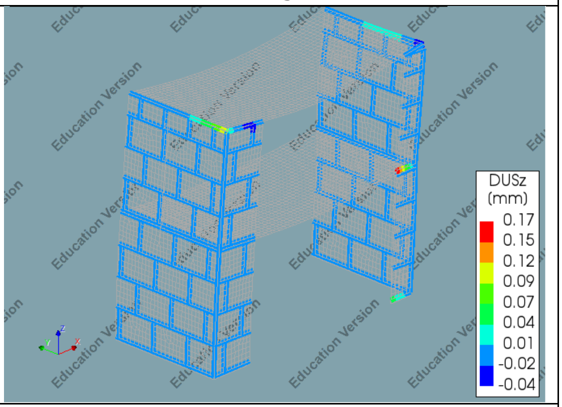
</td></tr>
<tr><td colspan="2">(A) Rocking mechanism activated</td></tr>
<tr><td>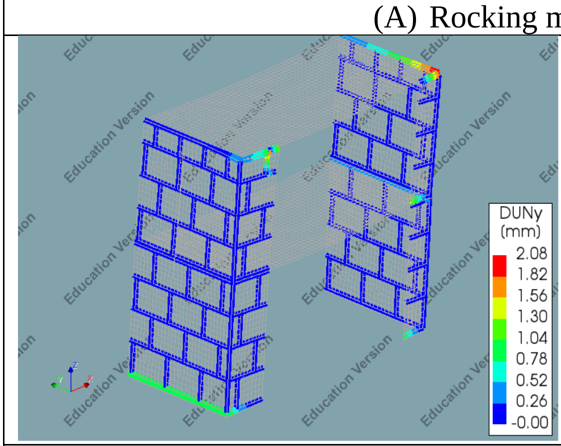
</td><td>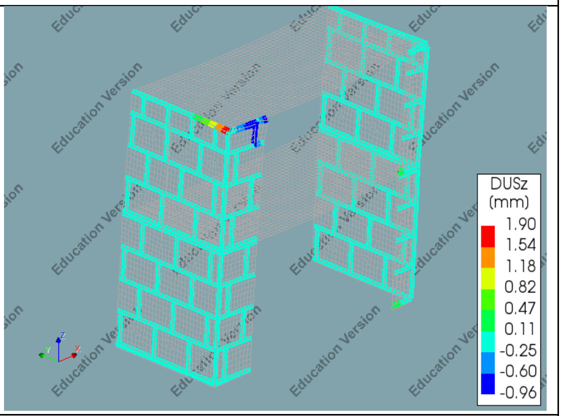
</td></tr>
<tr><td colspan="2">(B) Transition to the peak</td></tr>
</table>

<table>
<tr>
<td>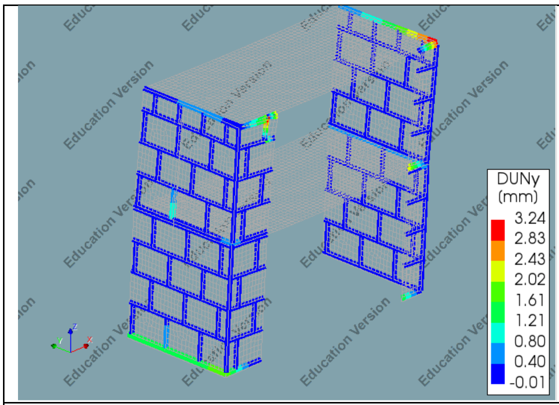 </td>
<td>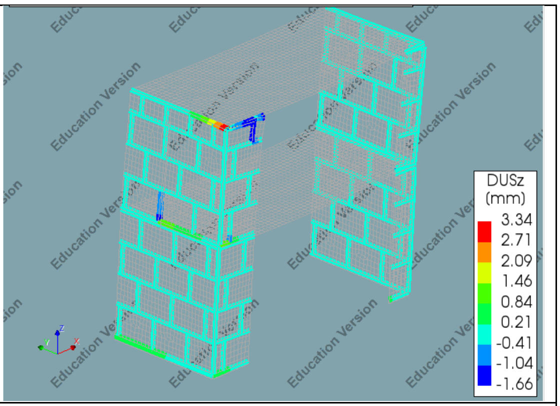 </td>
</tr>
<tr>
<td colspan="2">(C) Highest value of base shear force reached</td>
</tr>
<tr>
<td>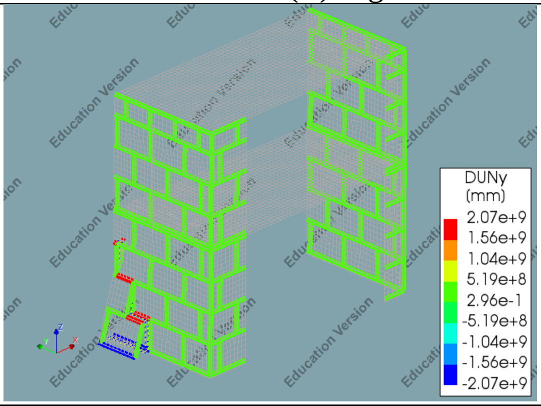 </td>
<td>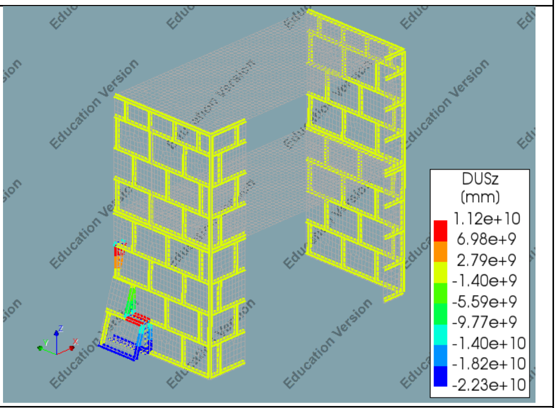 </td>
</tr>
<tr>
<td colspan="2">(D) Non-convergence of the analysis</td>
</tr>
</table>

Table 7.3 shows the evolution of crack patterns on the model, which are represented by the relative displacement of the interfaces. The initiation and development of the rocking mechanism can be seen from the table with the opening of tensile cracks in the interface elements at the top and bottom joints of the structure. Apart from the opening of tensile cracks on the structure, the second concrete floor also undergoes sliding, as can be seen from the shear relative displacement contour plots at event B and event C. This sliding behavior is caused by the inclusion of shear behavior to the interface element constitutive model. The sliding of the concrete slab also causes a masonry unit to detach from the structure. This type of behavior was not observed from the physical specimen. In the transversal walls, there are some cracks observed in the interface elements. However, the cracking pattern in the transversal walls still does not match with the cracking pattern of the physical specimen.

7.2.2 Micro-Coulomb-TSRCM: Coulomb Friction Interface Elements and TSRCM Shell Elements

The results of the analysis of the model with Coulomb friction interface elements and TSRCM shell elements are presented as follows.

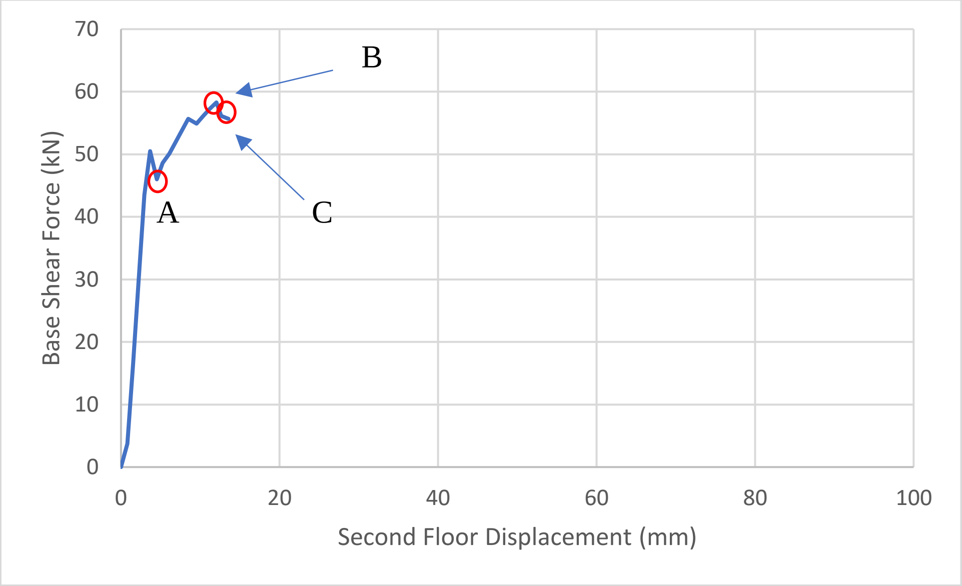

Figure 7.3 The capacity curve result from the nonlinear pushover analysis of Micro-Coulomb-TSRCM model

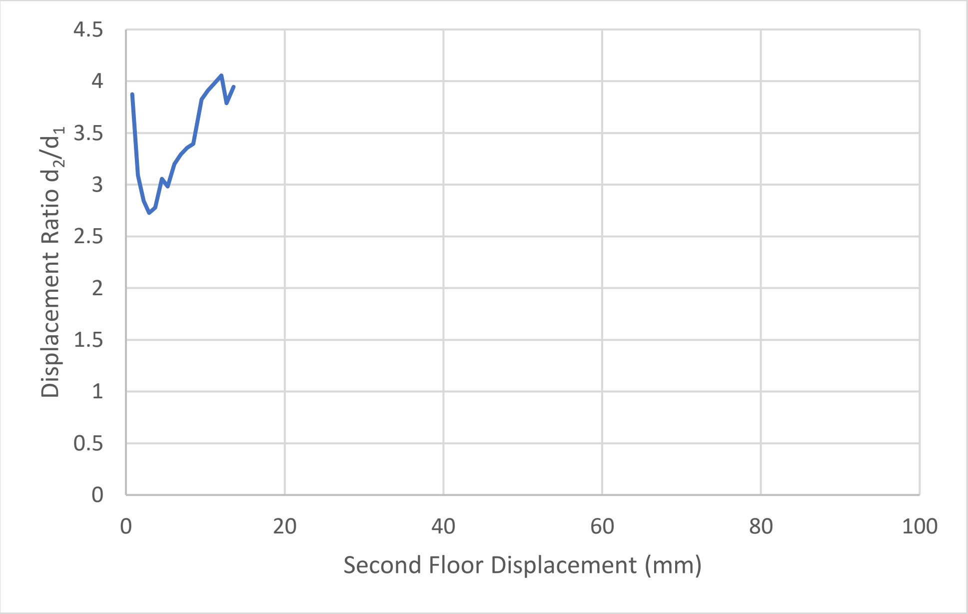

Figure 7.4 The interstory drift curve from the nonlinear pushover analysis of Micro-Coulomb-TSRCM model

The capacity curve of the Micro-Coulomb-TSRCM model is shown in Figure 7.3. The analysis results in the highest base shear force value of 58.28 kN and an initial stiffness value of 12.5 kN/mm. As with the previous variation with the linear-elastic shell elements, the analysis of this model is also unstable. Divergence is encountered at the horizontal displacement of 14.33 mm. The capacity curve of this model variation deviates from the capacity curve of Micro-Coulomb-Linear with a more abrupt transition to the post-peak region instead of the more gradual transition of the previous model. The change in the shell elements constitutive model appears to introduce a significant change to the structural behavior of the physical specimen. From event A, the capacity curve undergoes a significant reduction in stiffness, which results in the base shear force of the Micro-Coulomb-TSRCM model being much lower than the Micro-Coulomb-Linear model.

Figure 7.4 shows the interstory drift curve of the analysis in terms of displacement ratio. The displacement ratio obtained from the analysis initially shows a decreasing trend. However, after the horizontal displacement of 2.92 mm is reached, the value of the displacement ratio increases significantly. This significant increase in displacement ratio is caused by the sliding of the concrete floor on the first floor and the detachment of one of the transversal walls as shown in event C, as shown in Table 7.4.

Table 7.4 The mortar joints cracks of Micro-Coulomb-TSRCM model represented by interface relative displacements Δu_{ny} and Δu_{sz} for events depicted in Figure 7.3

Δu_{ny}	Δu_{sz}
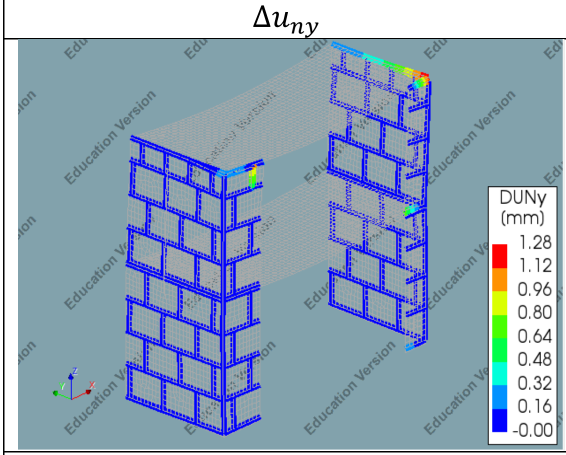	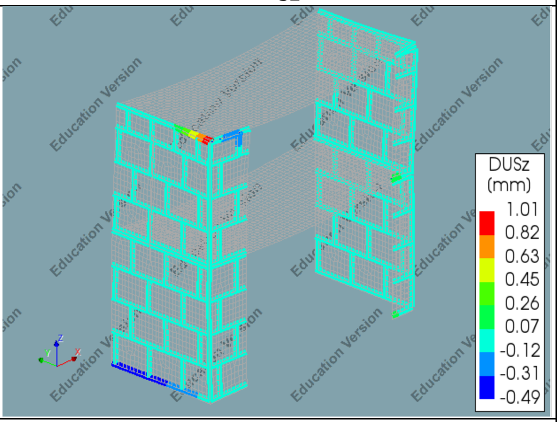
(A) Stiffness reduction	
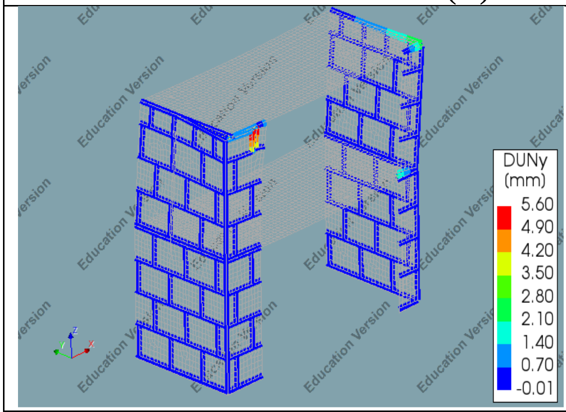	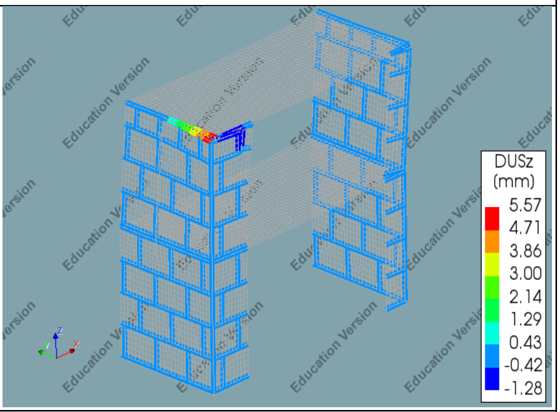
(B) Peak base shear force	

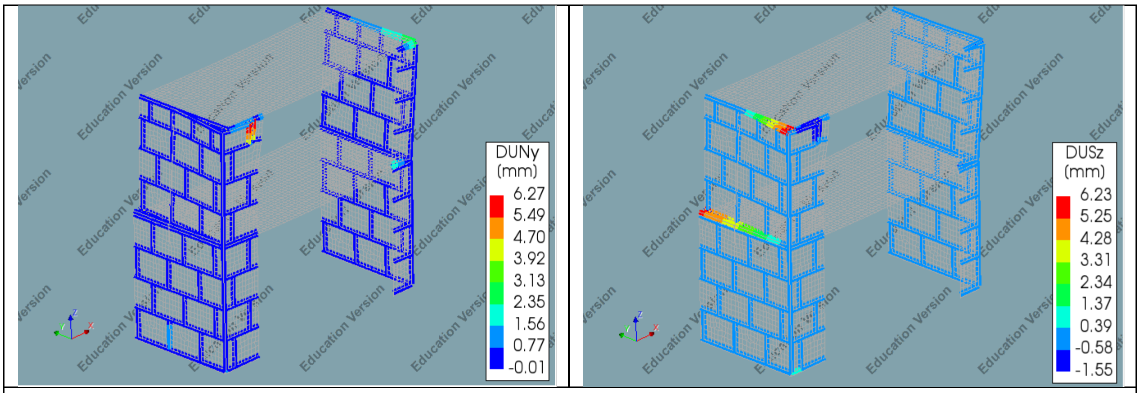

(C) Detachment of the transversal wall on the first floor

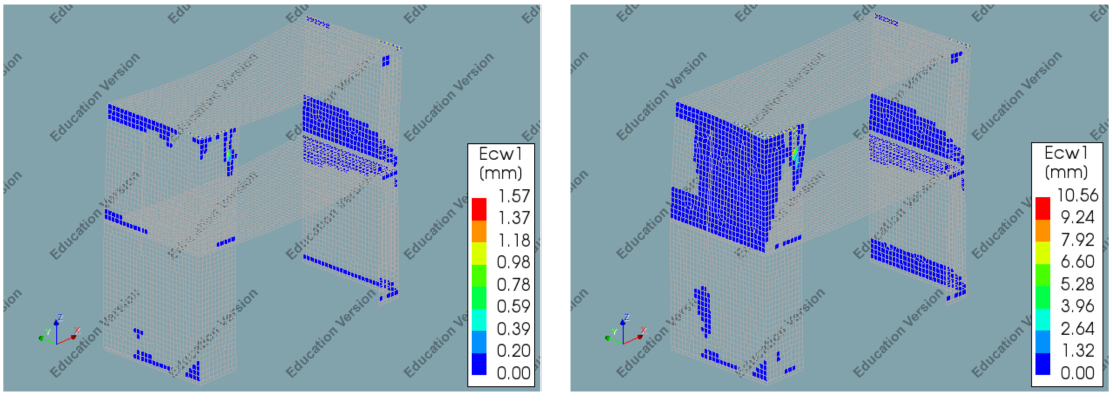

(A) Stiffness reduction (B) Peak base shear force is reached

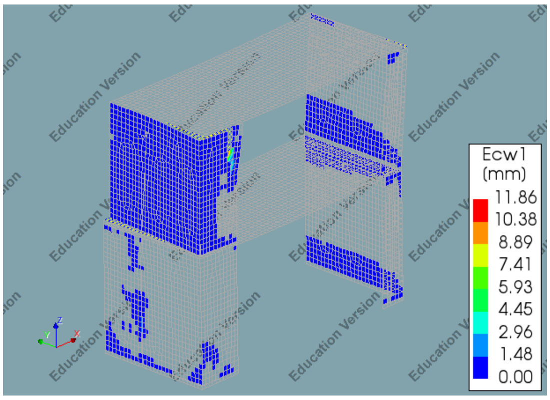

(C) The detachment of the transversal wall on the first floor

Figure 7.5 The cracks in the shell elements of Micro-Coulomb-TSRCM model corresponding to the events depicted in Figure 7.3

The damages on the model in the form of cracks are represented in Table 7.4 as the interface element relative displacements and in Figure 7.5 as cracks in the shell elements. From both figures, it is evident that there are large differences from the Micro-Coulomb-Linear model. The first notable difference compared to the previous model is the absence of rocking mechanism on the model. As shown in Table 7.4, there is no sign of activation of the rocking mechanism on the model. Allowing the shell elements to crack seems to alter the failure mechanism considerably. Crack is observed opening at the base of the ground floor transversal wall, but there is no tensile crack opening at the base of the pier which indicates the initiation of the rocking mechanism. The shell elements crack contour plot in Figure 7.5 shows that the damage is concentrated on the first floor, which does not match the results of the observation on the physical specimen. The cause of these discrepancies is still unclear.

7.3 Micro-Discrete: Micro-Model with Discrete Cracking Interface Model

7.3.1 Micro-Discrete-Linear: Discrete Cracking Interface Elements and Linear Elastic Shell Elements

The results of the nonlinear pushover analysis of the Micro-Discrete-Linear model are presented as follows.

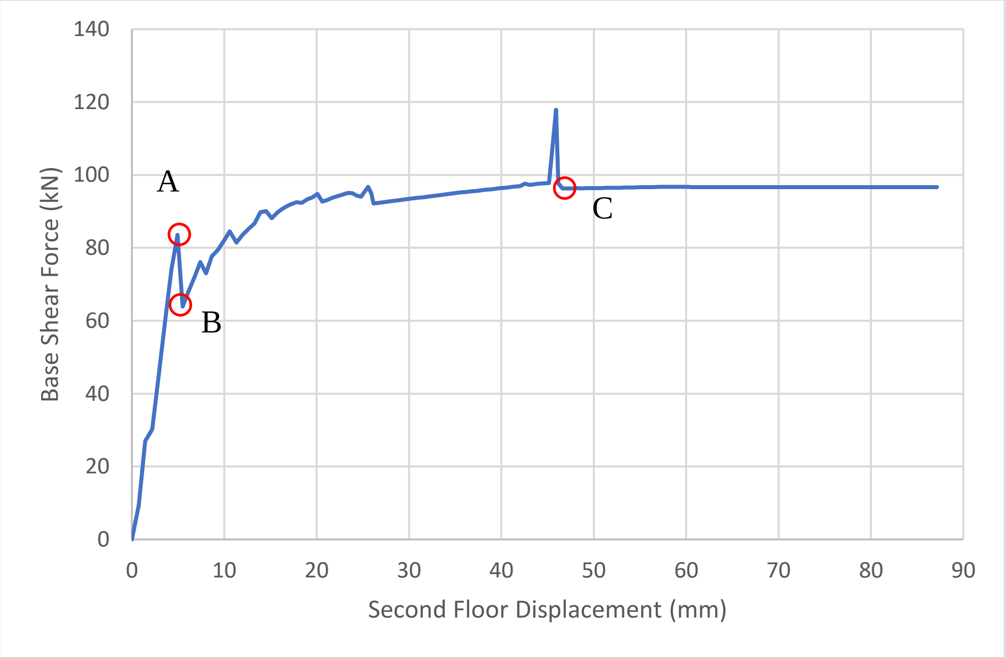

Figure 7.6 The capacity curve result from the nonlinear pushover analysis of Micro-Discrete-Linear model

Figure 7.6 shows the capacity curve of the Micro-Discrete-Linear model. The numerical analysis of this model results in the peak base shear force of 96.26 kN and the initial stiffness of 16.94 kN/mm. The behavior of the structure in the pre-peak region resembles that of the Macro-TSRCM model. A slight decrease in base shear force can be seen on the capacity curve as the rocking mechanism on the structure is activated, which is then followed by the gradual increase of the structural capacity until a plateau of relatively constant base shear force is reached. The transition phase between the rocking mechanism activation and the plateau also features similar behavior with cracks gradually opening at other joints of the piers as the horizontal displacement is increased. The structure can be seen entering a state of tilting equilibrium at event C, which is indicated by a constant base shear force with continuously increasing horizontal displacement. From the figure, it can be seen that tensile cracking is the dominant and sole failure mechanism present on the structural model as there is no significant decrease in base shear force in the post-peak region. An anomalous spike in base shear force on the capacity curve is observed on the capacity curve just before event C. The cause of this anomaly is not entirely clear, but it seems to be influenced by the wall-pier connections. The particular definition of the material parameters for the wall-pier connections for this case probably causes instability in the numerical analysis.

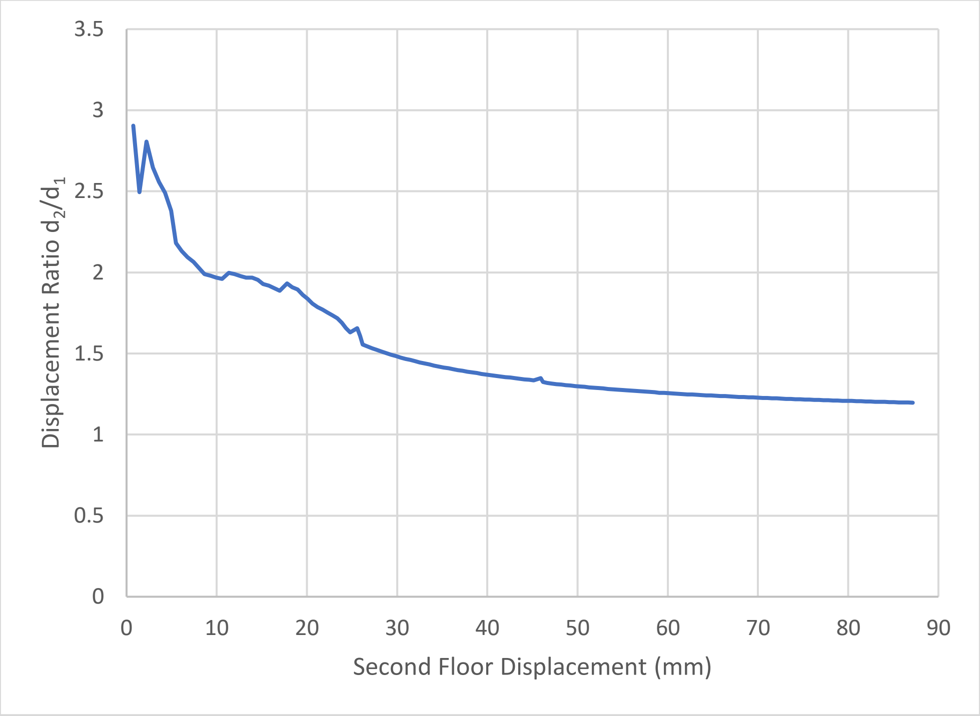

Figure 7.7 The interstory drift curve from the nonlinear pushover analysis of Micro-Discrete-Linear model

The interstory drift curve from the analysis shows a steady decrease in the displacement ratio. The displacement ratio decreases significantly at the beginning and slowly approaches a constant value with increasing horizontal displacement. A displacement ratio value of 1.2 is reached at the end of the analysis. This low value of displacement ratio and the relatively constant value of displacement ratio on the curve indicate the existence of a soft-story mechanism on the model.

Table 7.5 The mortar joints cracks of Micro-Discrete-Linear model represented by interface relative displacements Δu_{ny} and Δu_{sz} for events depicted in Figure 7.3

<table>
<tr><th>$\boldsymbol{\Delta u_{ny}}$</th><th>$\boldsymbol{\Delta u_{sz}}$</th></tr>
<tr><td>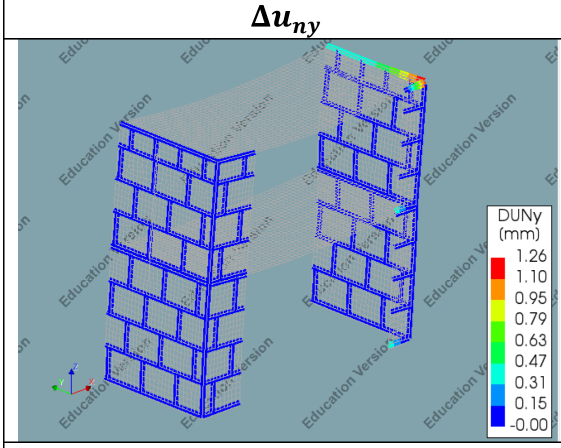
</td><td>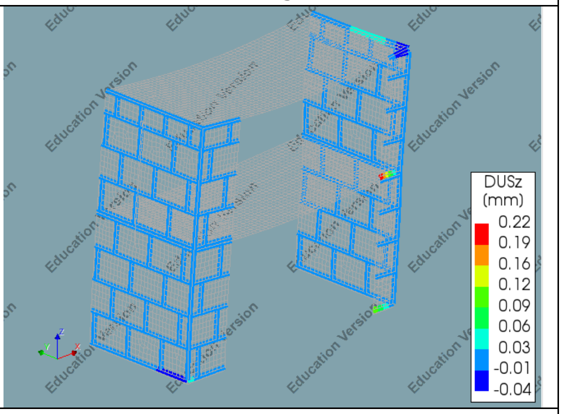
</td></tr>
<tr><td colspan="2">(A) Activation of rocking mechanism</td></tr>
<tr><td>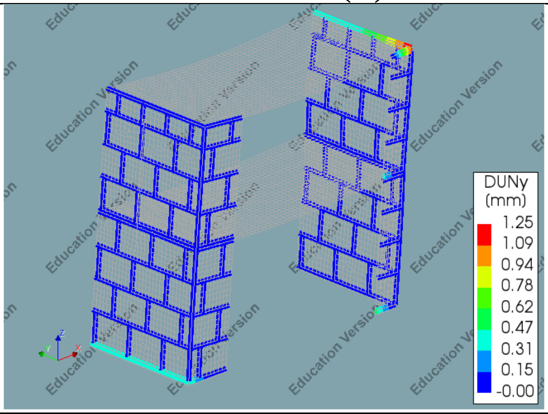
</td><td>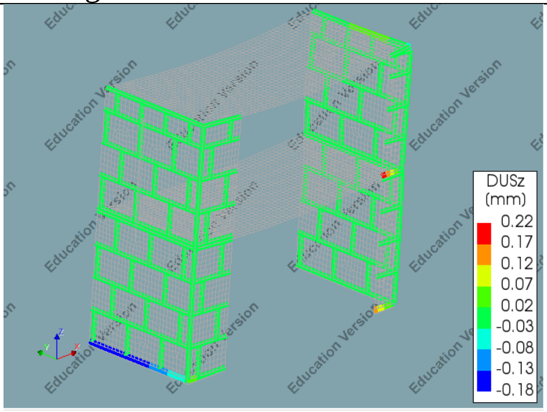
</td></tr>
<tr><td colspan="2">(B) Slight loss of structural capacity after the opening of cracks</td></tr>
<tr><td>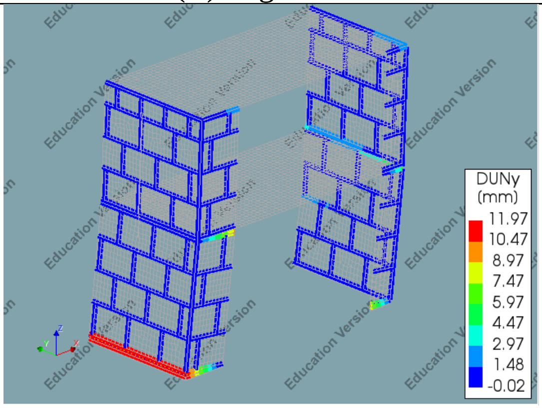
</td><td>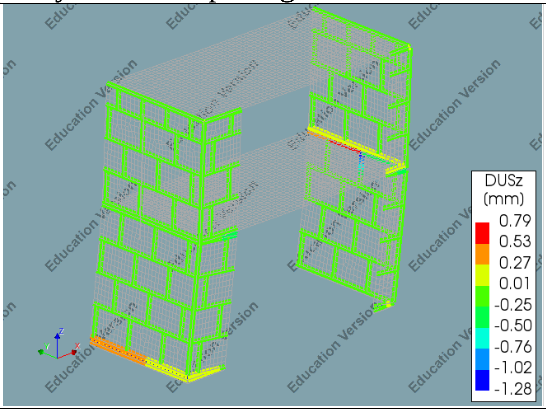
</td></tr>
<tr><td colspan="2">(C) Peak base shear force is reached</td></tr>
</table>

Table 7.5 shows the evolution of cracking patterns on the model, which are represented here as the interface elements relative displacements. It can be observed from the table, that the rocking mechanism of the model is activated at event B with the opening of the interface elements at the joint located at the bottom of the long pier. The soft-story mechanism at the ground floor can also be observed on the model at event C, with tensile

cracks opening on the ground floor and closing on the first floor. Despite the relatively accurate depiction of the initiation of the rocking mechanism, the model fails to replicate other failure mechanisms such as diagonal cracking failure and the formation of cracks in the transversal walls. Diagonal cracking failure does not form on the model since it requires the formation and collapse of diagonal struts in the shell elements. On the other hand, the lack of cracks in the transversal walls is possibly caused by the limitation of the shell finite elements in modeling the out-of-plane behavior.

7.3.2 Micro-Discrete-TSRCM: Discrete Cracking Interface Elements and TSRCM Shell Elements

The results of the nonlinear pushover analysis of shell elements micro-model with TSRCM shell elements and discrete cracking interface elements are presented as follows.

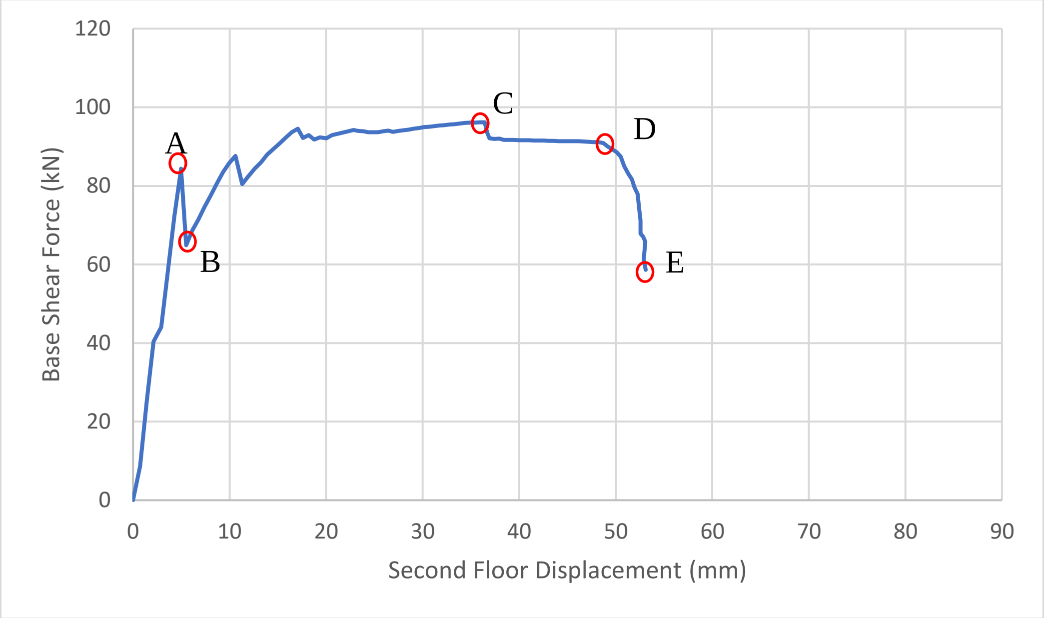

Figure 7.8 The capacity curve result from the nonlinear pushover analysis of Micro-Discrete-TSRCM model

Figure 7.8 shows the capacity curve of the model. The analysis results in a peak base shear force value of 96.18 kN, an initial stiffness value of 17 kN/mm and a near-collapse displacement value of 49.19 mm. The capacity curve follows a similar pattern as the Macro-TSRCM model with the activation of the rocking mechanism, which is then followed by a gradual increase of base shear force to the maximum structural capacity and the diagonal cracking failure. As with the Macro-TSRCM model, the pre-peak behavior of the numerical model is dominated by the formation of tensile cracks at the joints of the masonry piers and transversal walls. The diagonal cracking failure of the numerical model occurs in the shell elements as will be shown later in Table 7.7. Shortly after the diagonal cracking failure occurs, the analysis encounters non-convergence due to the failure of the wall-pier connections.

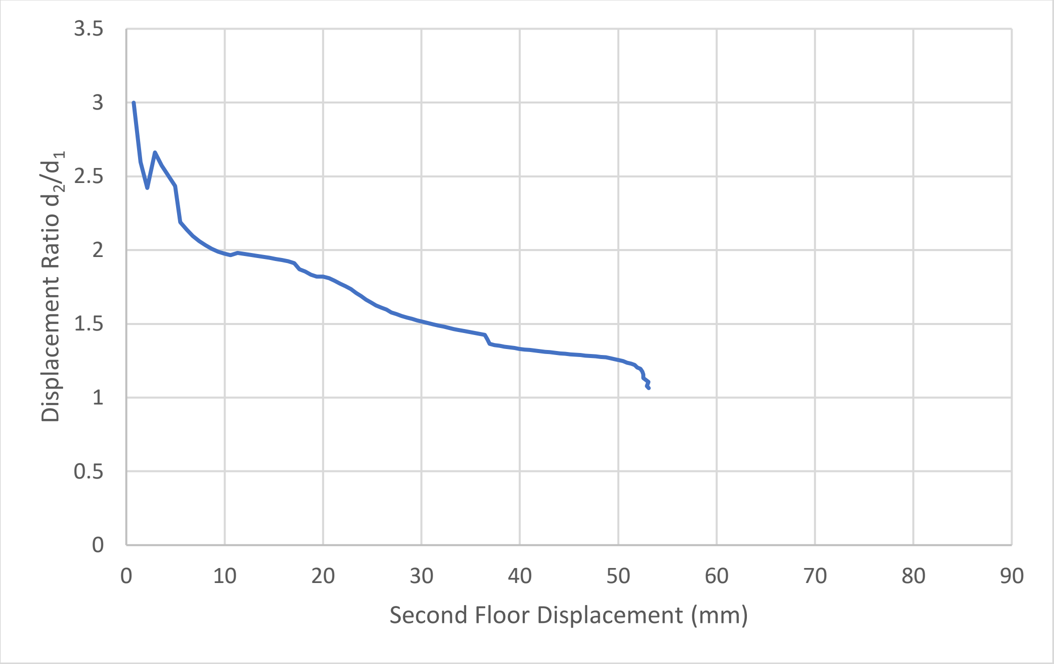

Figure 7.9 The interstory drift curve from the nonlinear pushover analysis of Micro-Discrete-TSRCM model

The interstory drift curve shows a similar trend to the Micro-Discrete-Linear model with the displacement ratio steadily decreasing as the horizontal displacement increases. The displacement ratio gradually levels off indicating the development of a soft-story mechanism on the ground floor. An abrupt decrease in displacement ratio can be observed at the horizontal displacement of 52.43 mm, which corresponds to the diagonal cracking failure of the long pier.

Table 7.6 The mortar joints cracks of Micro-Discrete-TSRCM model represented by interface relative displacements Δu_{ny} and Δu_{sz} for events depicted in Figure 7.8

$\boldsymbol{\Delta u_{ny}}$	$\boldsymbol{\Delta u_{sz}}$
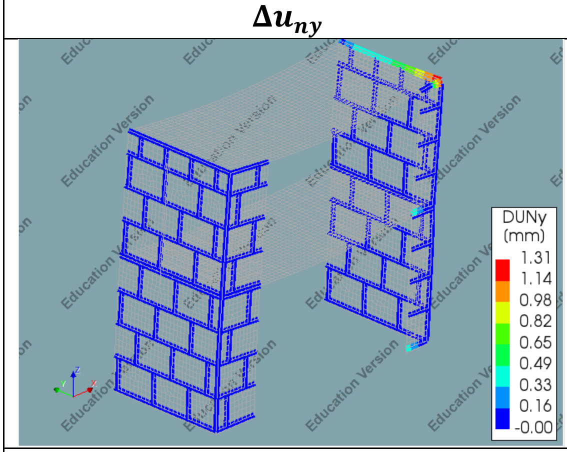	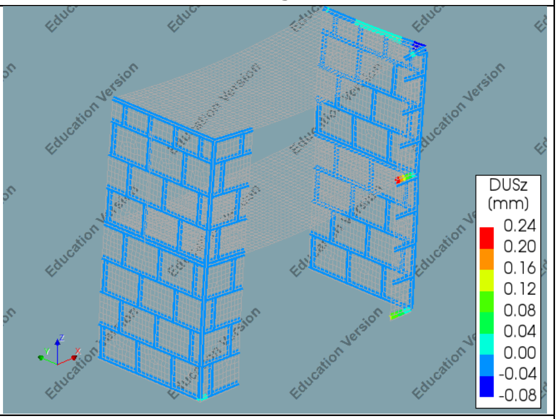
(A) Activation of rocking mechanism	

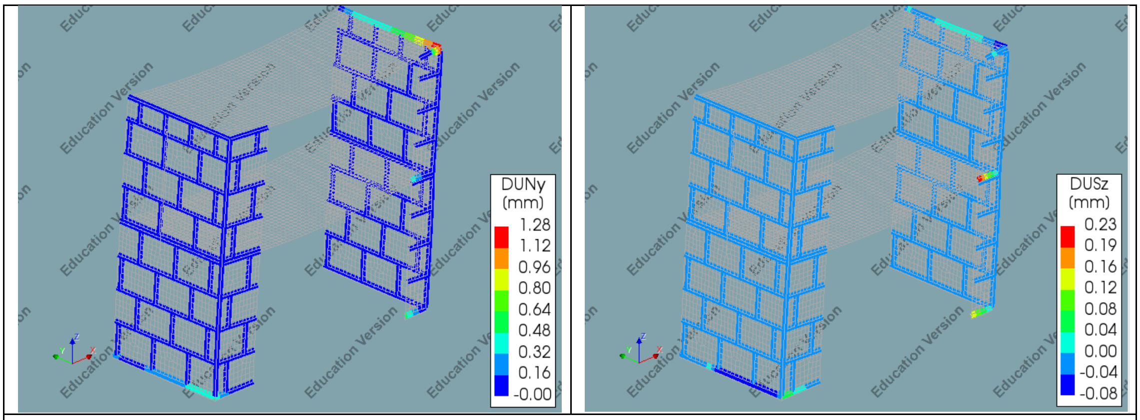

(B) Slight loss of structural capacity after the opening of cracks

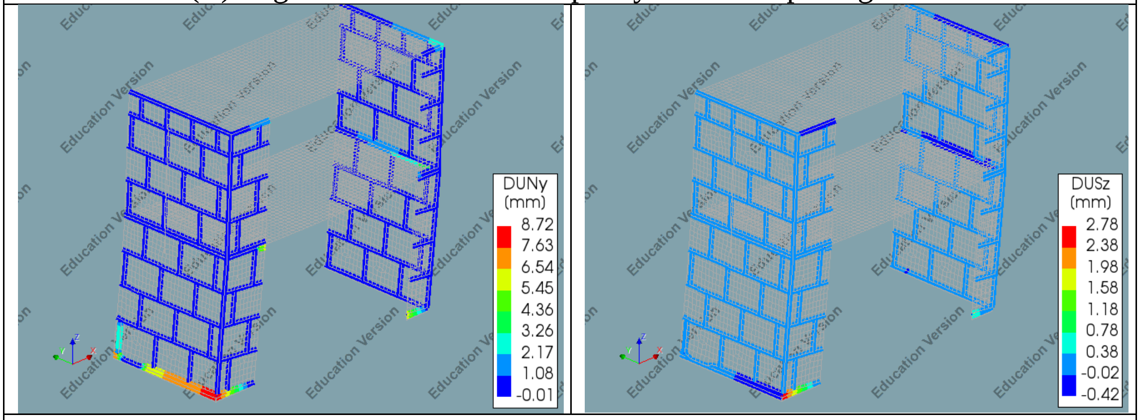

(C) Peak base shear force reached

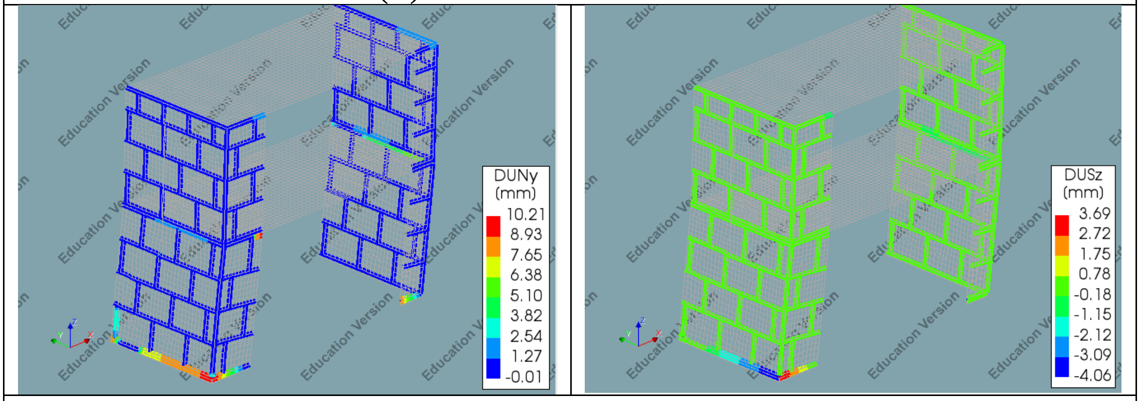

(D) Near-collapse displacement reached

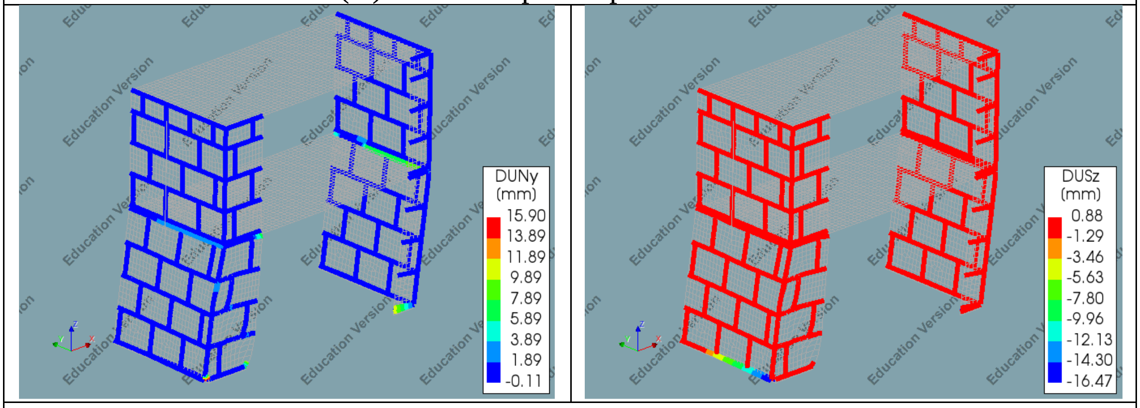

(E) Diagonal cracking failure

The interstory drift curve shows a similar trend to the Micro-Discrete-Linear model with the displacement ratio steadily decreasing as the horizontal displacement increases. The displacement ratio gradually levels off indicating the development of a soft-story mechanism on the ground floor. An abrupt decrease in displacement ratio can be observed at the horizontal displacement of 52.43 mm, which corresponds to the diagonal cracking failure of the long pier.

Table 7.6 shows the formation of cracks in the mortar joints, which is represented in the table by the interface elements relative displacements. The openings of the interface elements at the joints are observed on the model, which indicates the activation of the rocking mechanism. Almost no crack is observed in the interface elements on the transversal walls. This is likely to be caused by the tilting of the piers and transversal walls. The transversal walls do not have a significant contribution to resisting the lateral load. The resistance of the lateral load is mainly offered by the interface elements at the extremities of the structure and the in-plane masonry structural elements. Despite the diagonal cracking failure in the piers, there is almost no crack in the interface elements located in the long pier. It appears that the diagonal cracking failure only affects the shell elements.

Table 7.7 The cracks on TSRCM shell elements of Micro-Discrete-TSRCM model corresponding to the events depicted in Figure 7.8

<table>
<tr>
<td>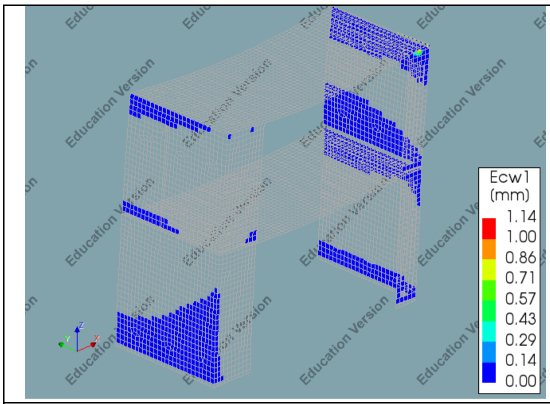 </td>
<td>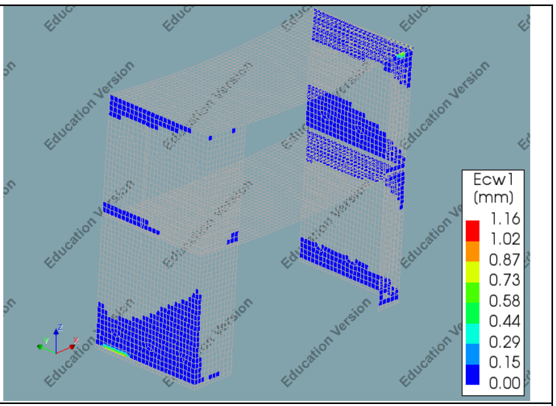 </td>
</tr>
<tr>
<td>(A) Activation of rocking mechanism</td>
<td>(B) Slight loss of structural capacity after the opening of cracks</td>
</tr>
<tr>
<td>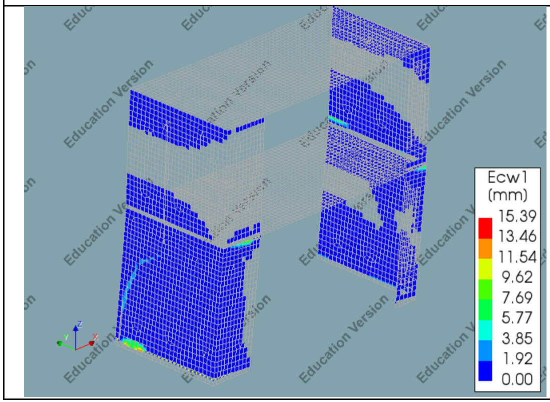 </td>
<td>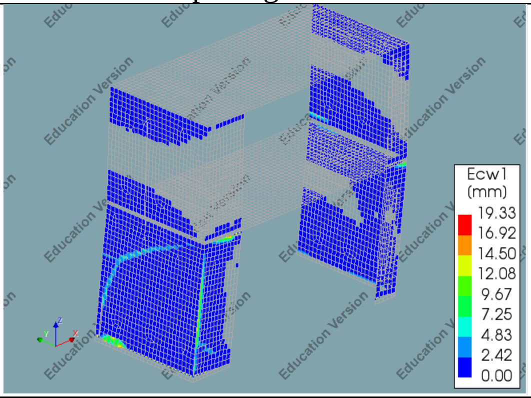 </td>
</tr>
</table>

(C) Peak base shear force reached	(D) Near-collapse displacement reached
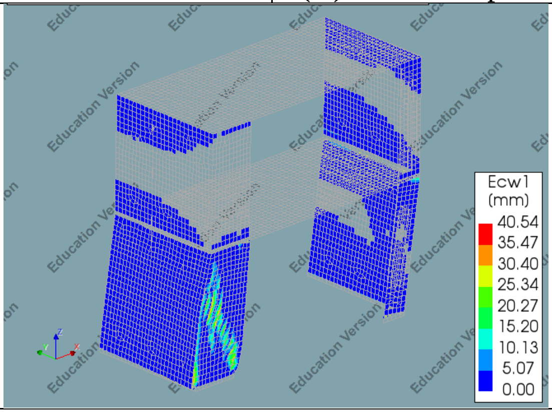	
(E) Diagonal cracking failure	

The progression of the cracking patterns in the shell elements is shown in Table 7.7. Cracks in the shell elements first appear at the base of the ground floor transversal wall as tensile cracks due to the rocking mechanism of the structure. It is of note, that this tensile crack occurs in the shell elements around that area, instead of in the interface elements. This is likely caused by the fact that both shell elements and interface elements have similar material parameters and are allowed to undergo cracking in the tensile region. The diagonal cracks can be seen forming in the long pier at event D, where the cracks propagate along the wall-pier connection to the toe of the pier. The cracks propagate through the masonry units and are not significantly affected by the interface elements in the pier. The lack of influence by the interface elements is caused by the nature of the diagonal cracking failure. For the diagonal cracking failure to occur, compression struts need to form in the pier. The interface elements can only simulate tensile cracking, thus the cracks are limited in the shell elements.

7.3.3 Micro-Discrete-TSRCM(Cmp) : Discrete Cracking Interface Elements and TSRCM Shell Elements (Compression-Only)

An additional model variation of the discrete cracking micro-models is constructed with a modified TSRCM constitutive model of the shell elements that only takes into account the compressive behavior while assuming the shell elements to behave linear elastically in the tensile direction. Therefore, tensile cracking is assumed to only be taken by the mortar joints while masonry units only undergo compressive failure. This model is constructed to investigate the effect of such changes on the results.

The capacity curve of the analysis is shown below.

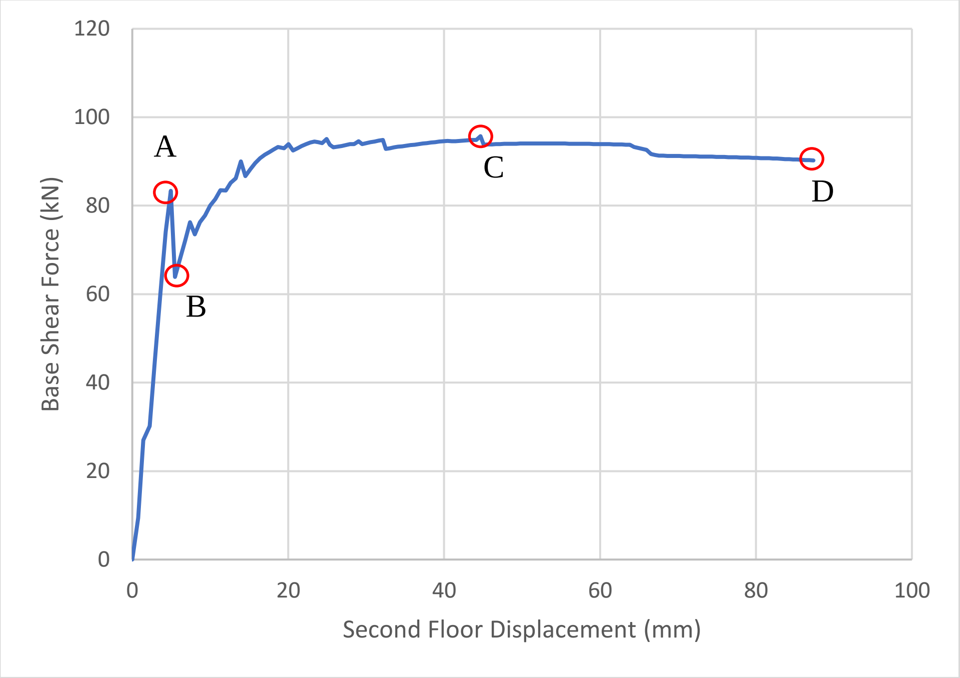

Figure 7.10 The capacity curve result from the nonlinear pushover analysis of Micro-Discrete-TSRCM(Cmp) model

The capacity curve of the analysis is shown in Figure 7.10. The analysis results in the peak base shear force of 95.72 kN and the initial stiffness of 16.91 kN/mm. The change in the tensile behavior of the shell elements constitutive model causes the numerical model to behave more like the model with the linear-elastic constitutive model than the model with the TSRCM constitutive model. Diagonal cracking failure, which is indicated by the sudden drop in base shear force, is absent in the model behavior even though the TSRCM constitutive model is used. It appears that the tensile parameters of the constitutive model have a big influence on the formation of diagonal cracks in the shell elements. The behavior of the numerical model in the pre-peak region remains unchanged, due to the tensile cracking behavior in the pre-peak region occurring in the interface elements rather than in the shell elements.

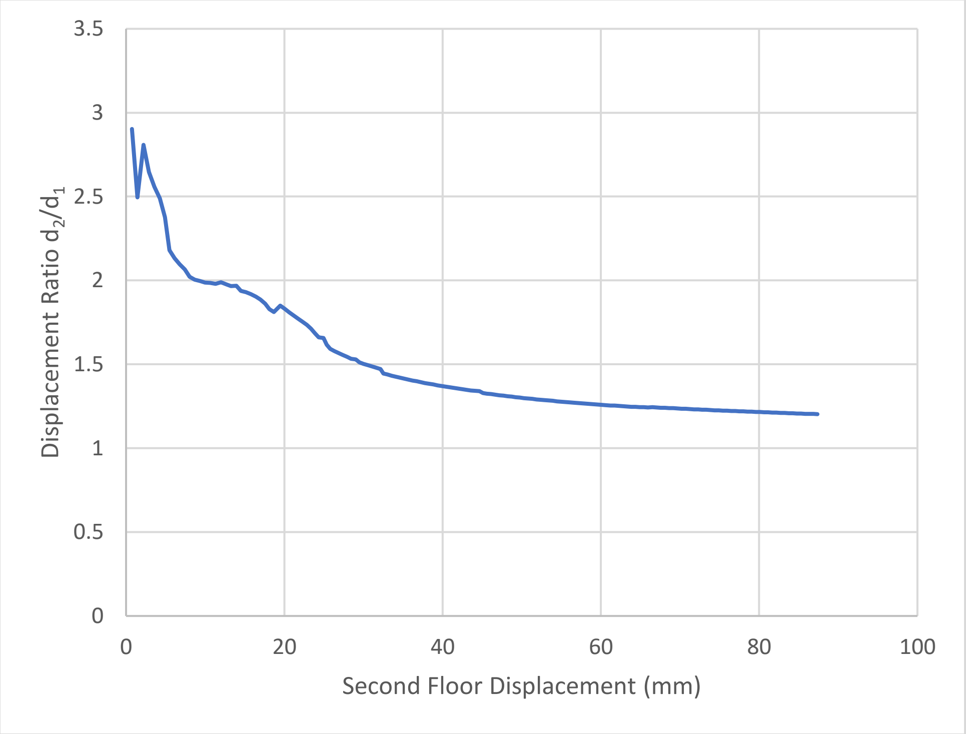

Figure 7.11 The interstory drift curve from the nonlinear pushover analysis of Micro-Discrete-TSRCM(Cmp) model

The interstory drift curve of the model in terms of displacement ratio is shown in Figure 7.11. The curve shows a steady decrease in the displacement ratio with increasing horizontal displacement. The displacement ratio slowly transitions to a constant value of displacement ratio. This relatively constant value of displacement ratio indicates the presence of a soft-story mechanism at the ground floor on the model. It can be seen from the figure, that the interstory drift curve bears a closer resemblance to the Micro-Discrete-Linear model than the Micro-Discrete-TSRCM model due to the absence of diagonal cracking failure on the model. It appears that changing the tensile behavior to linear elastic behavior affects the formation of diagonal cracking failure considerably. The assumption of linear-elastic tensile behavior on the model prevents cracks from forming in the shell elements, which in turn also prevents the formation of diagonal cracking failure in the elements. This causes the numerical model to behave in a similar fashion as the Micro-Discrete-Linear model variation, where failure occurs through the opening of tensile cracks in the interface elements.

Table 7.8 The mortar joints cracks of Micro-Discrete-TSRCM model represented by interface relative displacements Δu_{ny} and Δu_{sz} for events depicted in Figure 7.10

<table>
<tr><th>$\boldsymbol{\Delta u_{ny}}$</th><th>$\boldsymbol{\Delta u_{sz}}$</th></tr>
<tr><td>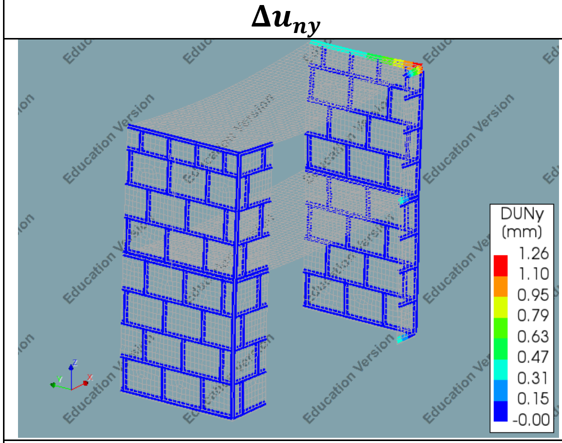 </td><td>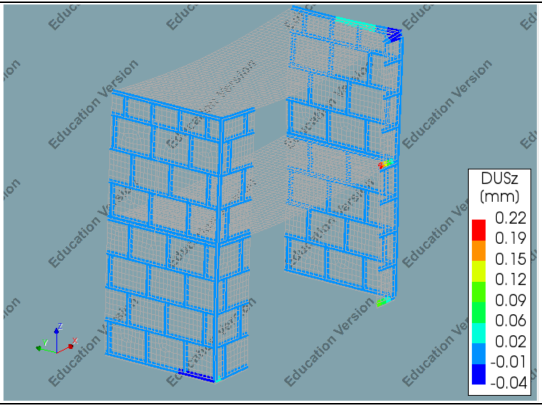 </td></tr>
<tr><td colspan="2">(A) Activation of rocking mechanism</td></tr>
<tr><td>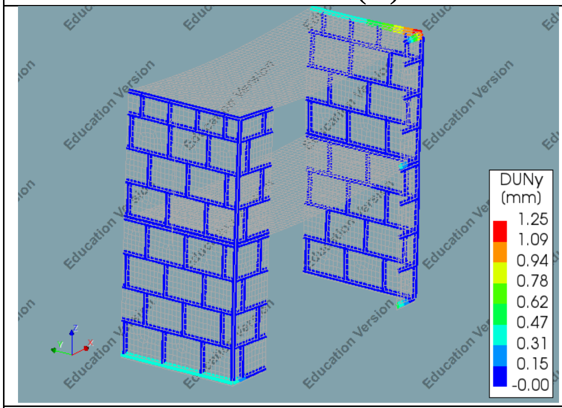 </td><td>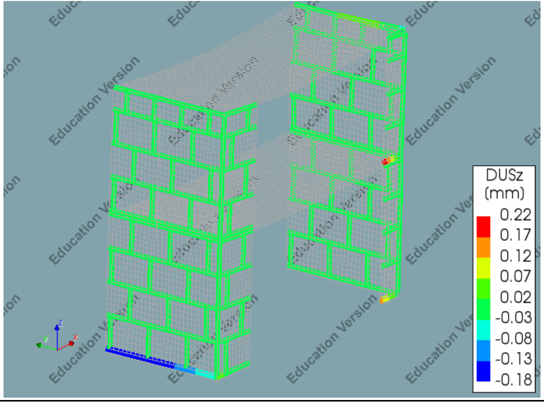 </td></tr>
<tr><td colspan="2">(B) Slight loss of structural capacity ofter the opening of cracks</td></tr>
<tr><td>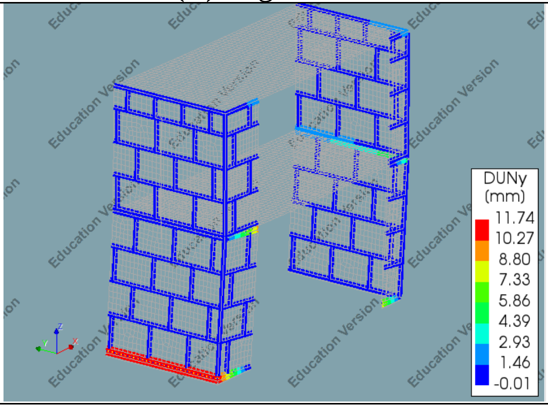 </td><td> </td></tr>
<tr><td colspan="2">(C) Peak base shear force reached</td></tr>
</table>

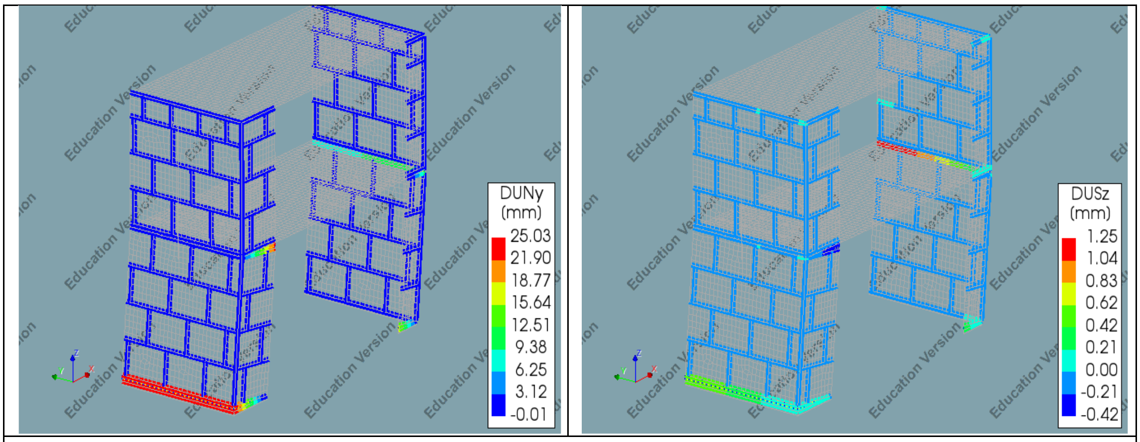

(D) End of analysis

Table 7.8 shows the progression of the formation of the cracks in the mortar joints of the Micro-Discrete-TSRCM(Cmp) model. The initiation of the rocking mechanism can be observed on the model at event B, which is indicated by the opening of the horizontal interface elements at the joints of the masonry structural elements. The development of a soft-story mechanism at the ground floor can also be observed on the model with tensile cracks opening at both joints of the ground floor piers and the tilting of the ground floor structural elements. Like the previous numerical models with the discrete cracking constitutive model, there is also a noticeable lack of cracks in the transversal walls due to the limitation of the shell finite elements.

No data is available on the formation of cracks inside the shell elements. As has been discussed before, the assumption of linear elastic behavior of the model in the tensile region prevents the formation of cracks in the shell elements, which in turn prevents the formation of diagonal cracking failure. Due to this, there is no significant difference between this model and the Micro-Discrete-Linear model and it can thus be concluded that this model offers no significant improvement in terms of results over the other two models with the same type of interface element constitutive model.

7.4 Micro-NL_Elastic: Micro-Model with Nonlinear Elasticity Interface Model

7.4.1 Micro-NL_Elastic-Linear: Nonlinear Elasticity Interface Elements and Linear Elastic Shell Elements

The results of the analysis of the Micro-NL_Elastic-Linear model are presented as follows.

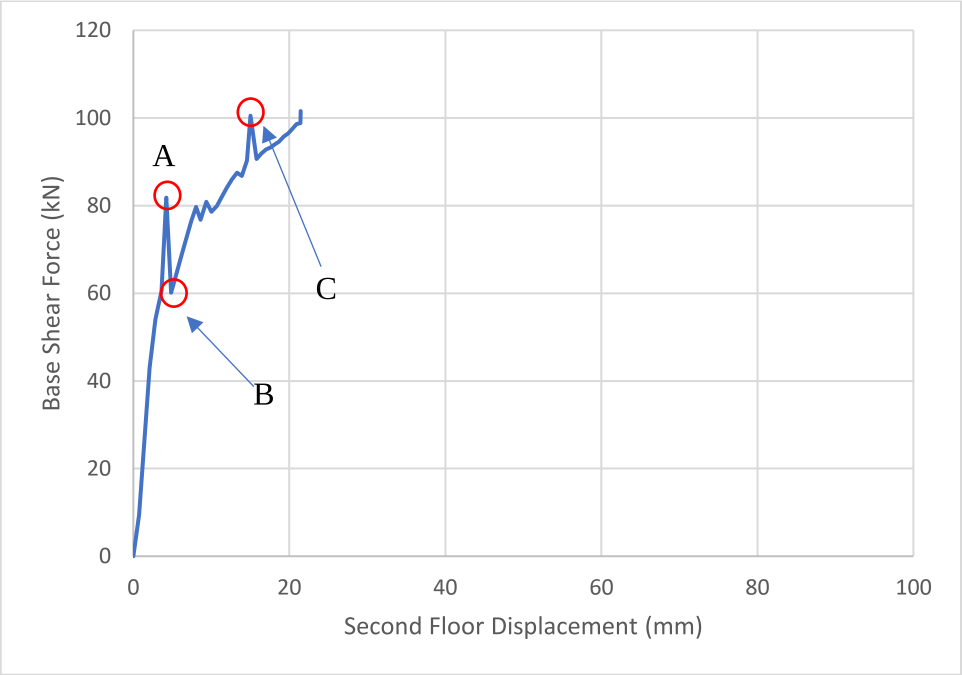

Figure 7.12 The capacity curve result from the nonlinear pushover analysis of Micro-NL_Elastic-Linear model

The capacity curve of Micro-NL_Elastic-Linear is plotted in Figure 7.12. The analysis of the numerical model results in an initial stiffness of 18.73 kN/mm. From the curve, it is evident that the analysis is not stable as it encounters divergence at the early stage of the analysis. The highest value of base shear force reached is 101.56 kN before the analysis is stopped due to divergence. Considering that the divergence seems to occur in the pre-peak region, this base shear force value is likely not the structural capacity of the model. The pre-peak behavior of the structural model follows the same pattern as models with the discrete cracking constitutive model with the rocking mechanism being the dominant failure mechanism. The activation of the rocking mechanism occurs at event B, which is indicated by a slight drop in base shear force similar to what occurs in the discrete cracking micro-models. This similarity with models that use discrete cracking interface constitutive model is due to the fact that the tensile behavior of the interface elements is based on the discrete cracking model. After the activation of the rocking mechanism, the base shear force undergoes a slight increase before encountering divergence at the horizontal displacement of 21.45 mm. The cause of divergence is the failure of one of the interface elements between the masonry units.

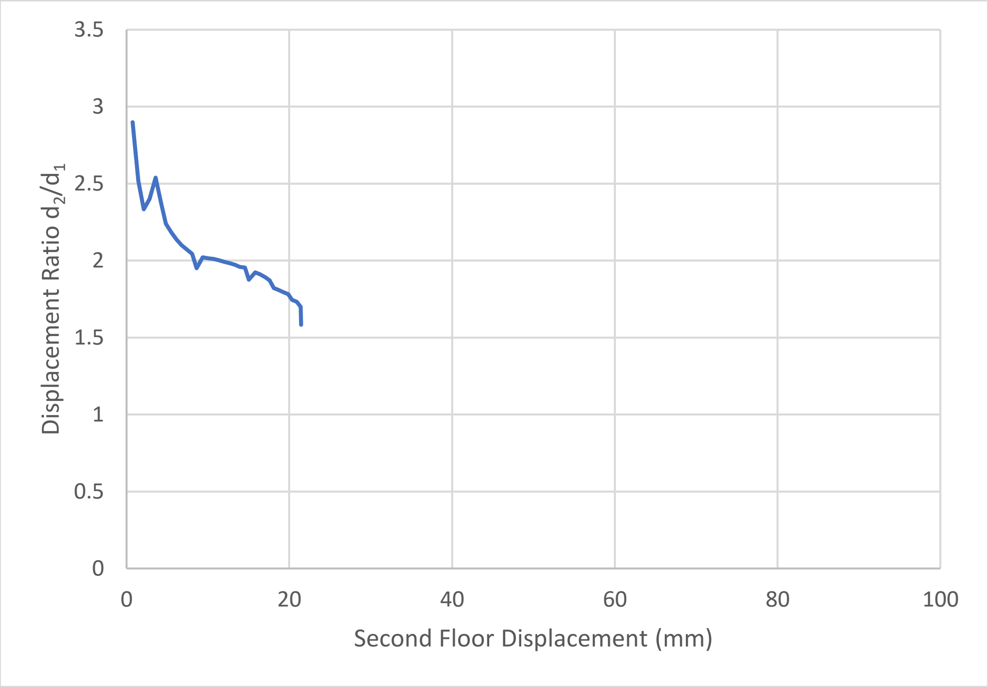

Figure 7.13 The interstory drift curve from the nonlinear pushover analysis of Micro-NL_Elastic-Linear model

The interstory drift shows a decrease in the displacement ratio, which is similar to the behavior observed from previous numerical models. This indicates the tendency of a soft-story mechanism to occur on the ground floor. However, due to the analysis encountering divergence before the post-peak region is reached, a full assessment of the post-peak behavior of the structural model cannot be made.

Table 7.9 The mortar joints cracks of Micro-NL_Elastic-Linear model represented by interface relative displacements Δu_{ny} and Δu_{sz} for events depicted in Figure 7.12

$\boldsymbol{\Delta u_{ny}}$	$\boldsymbol{\Delta u_{sz}}$
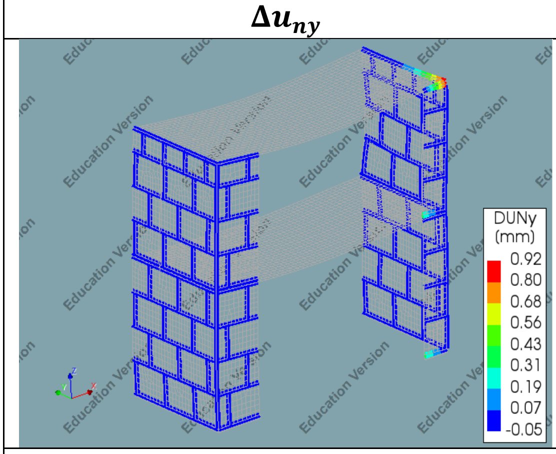	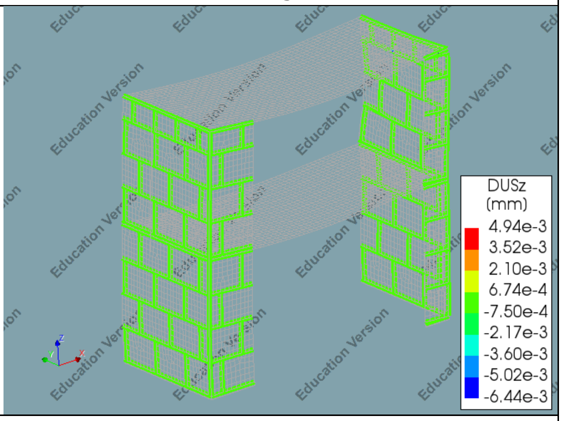
(A) Activation of rocking mechanism	

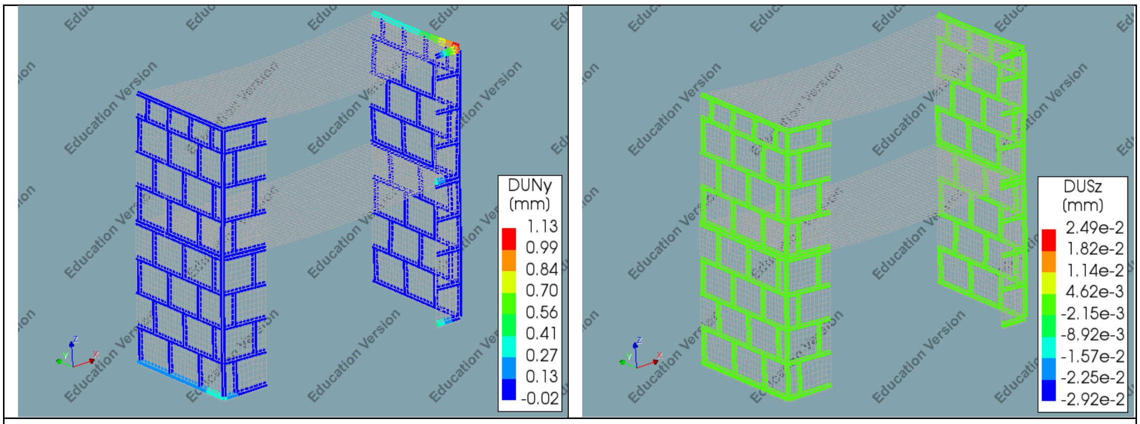

(B) Slight loss of structural capacity after the opening of cracks

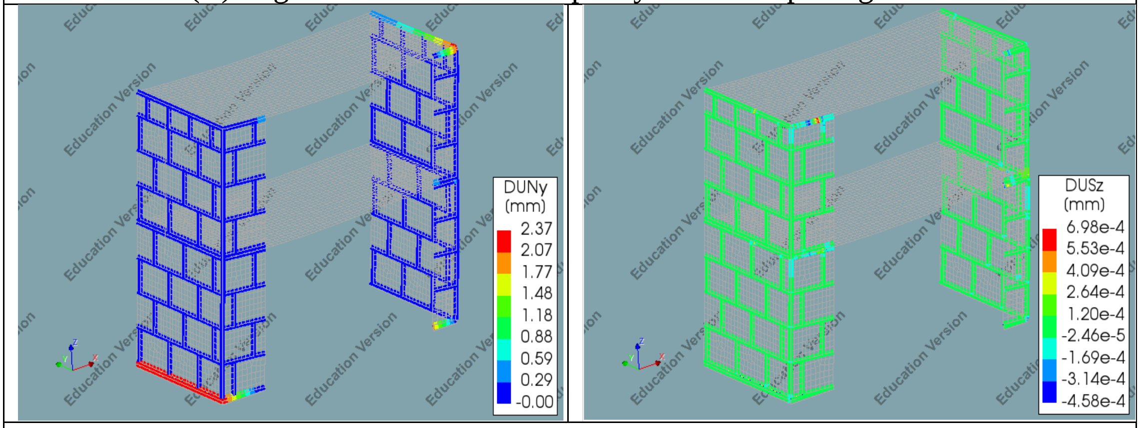

(C) Peak base shear force is reached

The evolution of cracks in the mortar joints of the model is shown in Table 7.9. Cracks can be observed forming at the joints of the masonry walls and piers. This indicates the activation of the rocking mechanism on the model similar to the model with the discrete cracking constitutive model. Crack openings are concentrated at the upper and bottom joints. There is, however, no crack in the mortar joints at any other parts of the masonry walls and piers. The absence of crack in the transversal walls is possibly caused by the tilting of the whole masonry structural elements as shown in Table 7.9 above.

7.4.2 Micro-NL_Elastic-TSRCM: Nonlinear Elasticity Interface Elements and TSRCM Shell Elements

The results of the analysis on the model with TSRCM shell element and nonlinear elasticity interface elements are presented as follows.

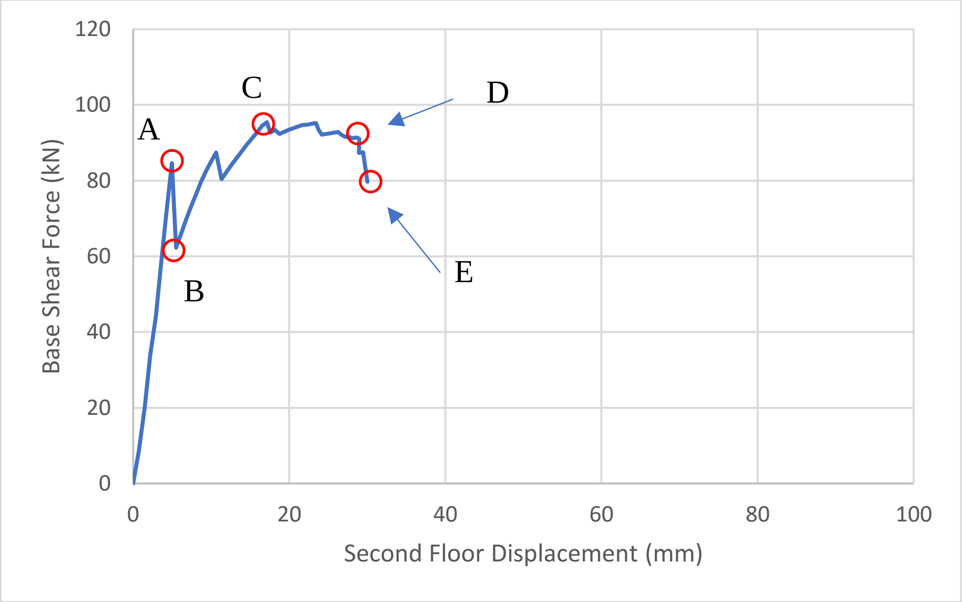

Figure 7.14 The capacity curve result from the nonlinear pushover analysis of Micro-NL_Elastic-TSRCM model

The numerical analysis of this model is slightly more stable compared to the Micro-NL_Elastic-Linear model. The capacity curve follows a similar pattern to the TSRCM macro-model, Macro-TSRCM, with the activation of the rocking mechanism shown at event B. The structural capacity of 95.43 kN and initial stiffness of 17.05 kN/mm are obtained from the analysis. The capacity curve shows the near-collapse displacement of 28.96 mm. This is then followed by diagonal cracking failure of the short pier. Shortly after, the structural analysis encounters a divergence, which is caused by the failure of the wall-pier joint. The diagonal cracking failure of the piers in this model occurs earlier compared to the previous numerical models with the TSRCM constitutive model. Observation on the longitudinal shear relative displacement of the interface elements suggests that this is likely caused by the sliding of the long pier from its position at the base of the structure as shown in Figure 7.15. This causes the change in the tilting behavior of the long pier, which in turn affects the load path of the lateral load in the long pier causing significant changes to the diagonal cracking failure behavior.

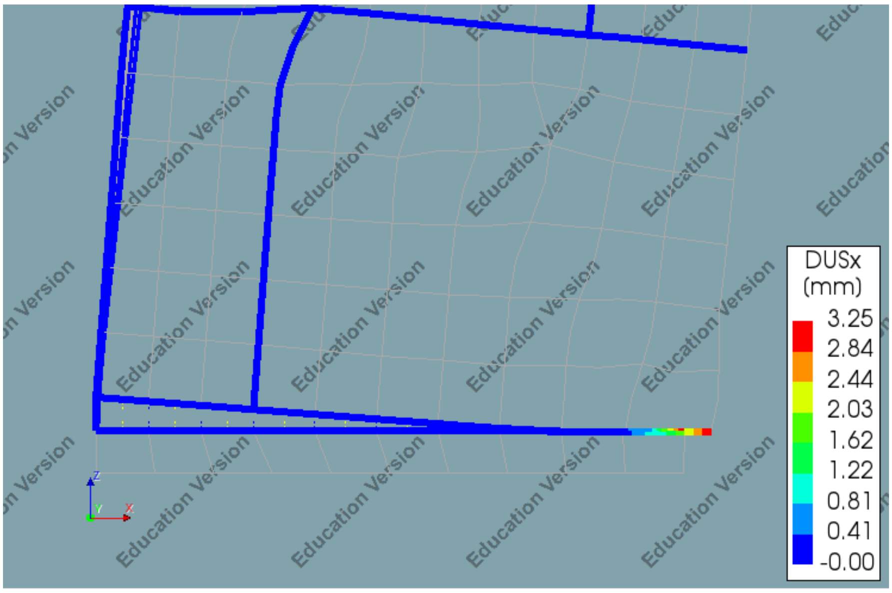

Figure 7.15 Longitudinal shear relative displacement of the long pier after the occurrence of diagonal cracking failure

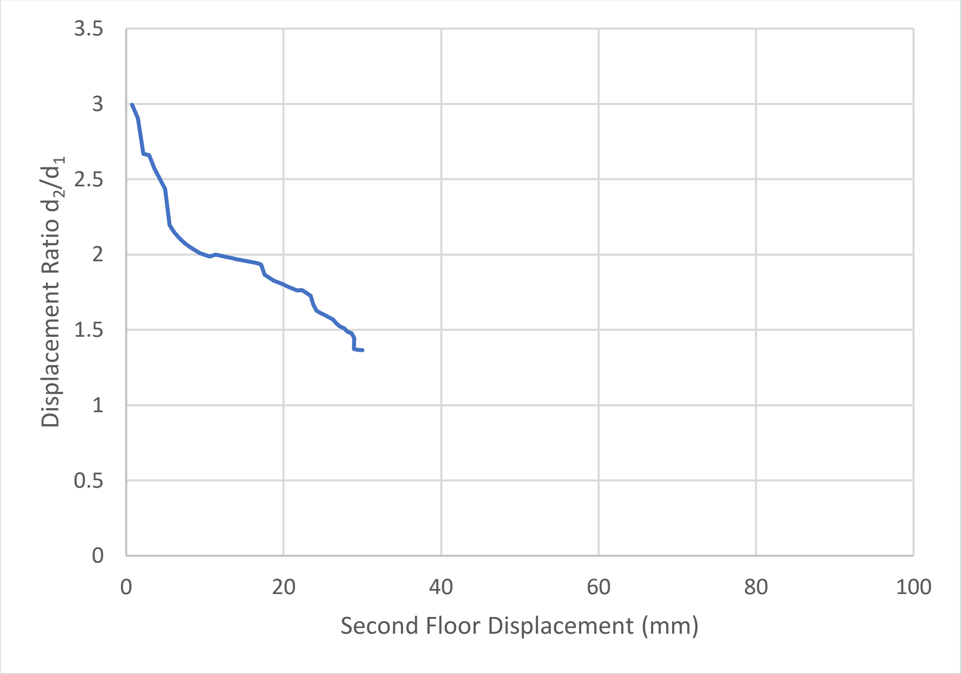

Figure 7.16 The interstory drift curve from the nonlinear pushover analysis of Micro-NL_Elastic-TSRCM model

The interstory drift curve shows a steady decrease in the displacement ratio as the horizontal displacement progresses as shown in Figure 7.16. This indicates the formation of a soft story mechanism on the ground floor. This can be seen in the displaced form of the numerical model and the interface relative displacement contour plots in Table 7.10.

Table 7.10 The mortar joints cracks of Micro-NL_Elastic-TSRCM represented by interface relative displacements Δu_{ny} and Δu_{sz} for events depicted in Figure 7.14

<table>
<tr><th>$\boldsymbol{\Delta u_{ny}}$</th><th>$\boldsymbol{\Delta u_{sz}}$</th></tr>
<tr><td>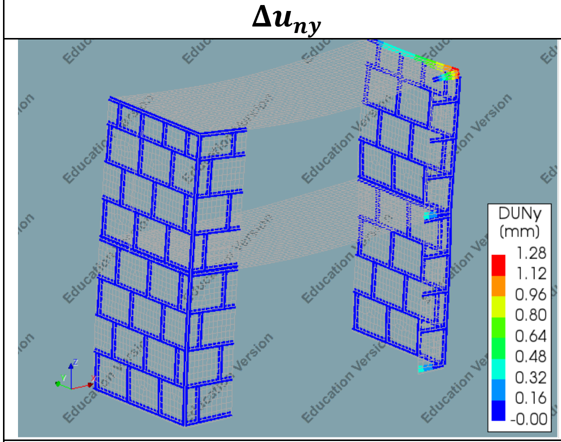
</td><td>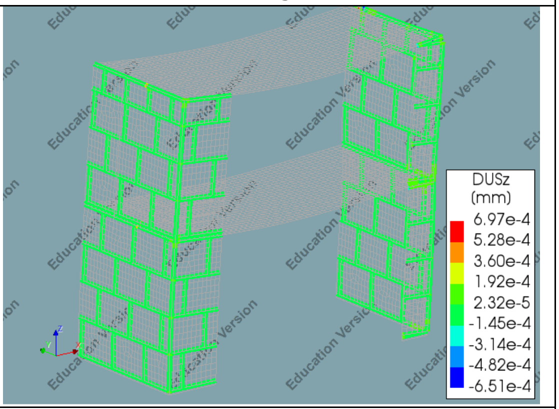
</td></tr>
<tr><td colspan="2">(A) Activation of rocking mechanism</td></tr>
<tr><td>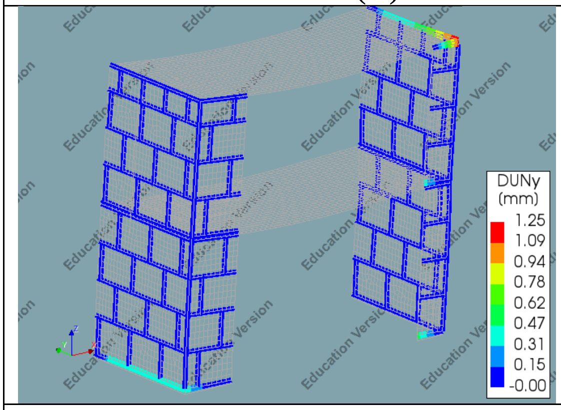
</td><td>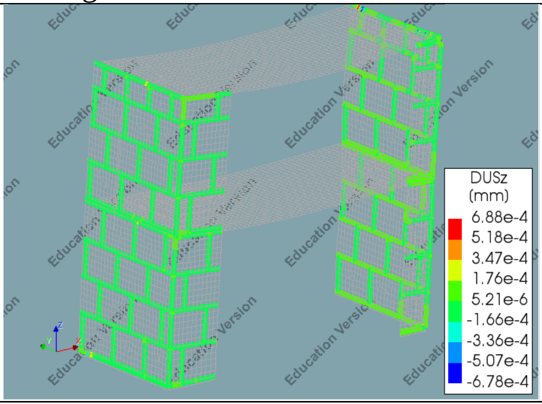
</td></tr>
<tr><td colspan="2">(B) Slight loss of structural capacity after the opening of tensile cracks</td></tr>
<tr><td>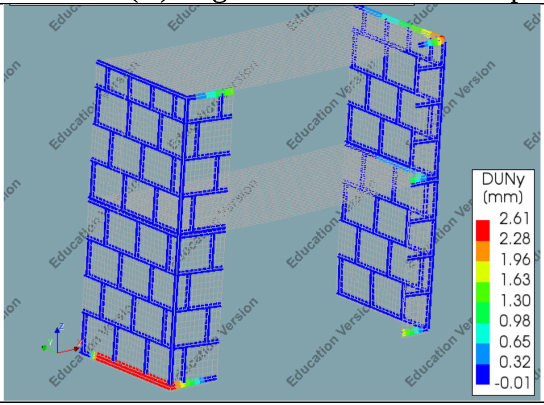
</td><td>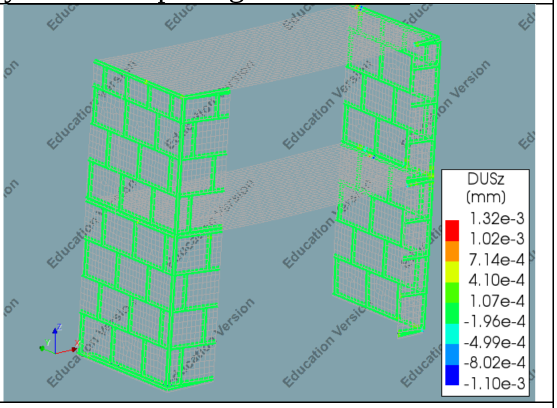
</td></tr>
<tr><td colspan="2">(C) Peak base shear force reached</td></tr>
</table>

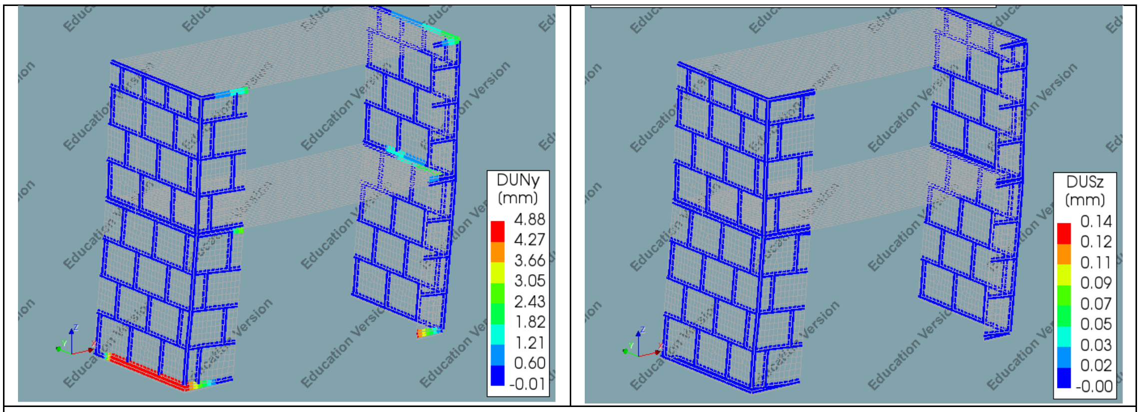

(D) Near-collapse displacement

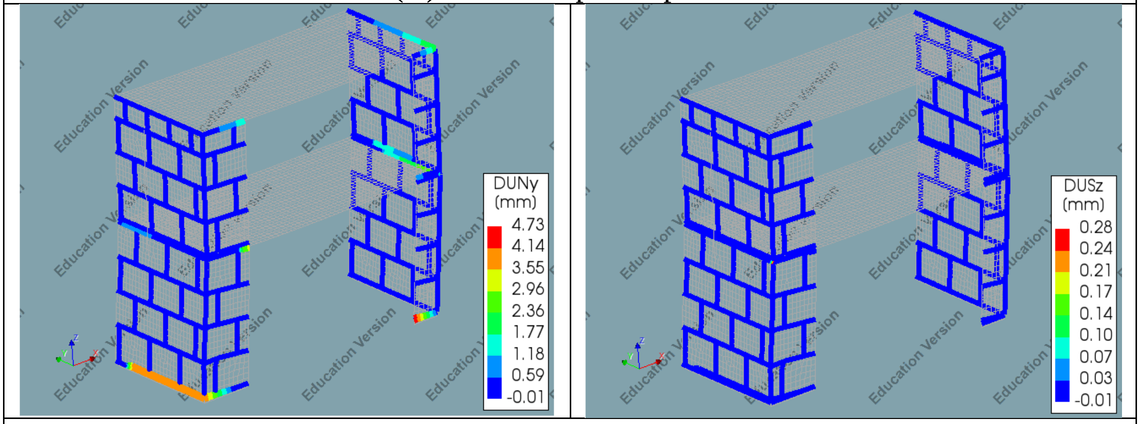

(E) Diagonal cracking failure

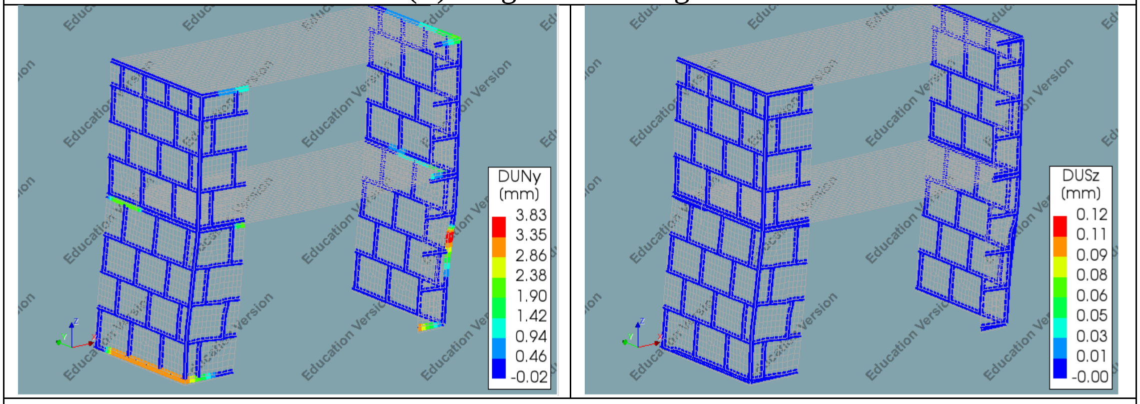

(F) End of the analysis

Table 7.11 The cracks on TSRCM shell elements of Micro-NL_Elastic-TSRCM model corresponding to the events depicted in Figure 7.14

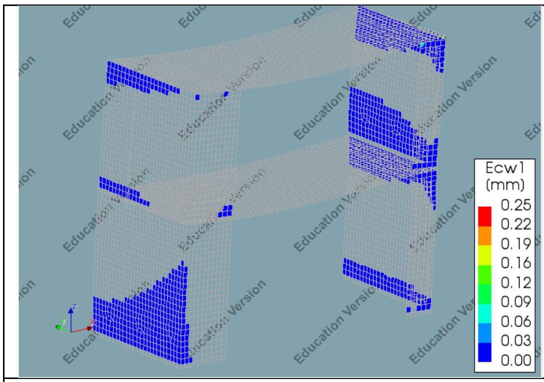

(A) Activation of rocking mechanism

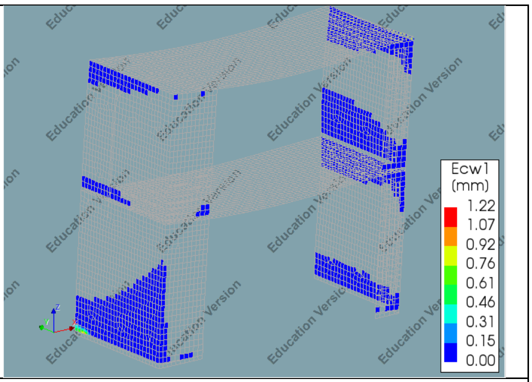

(B) Slight loss of structural capacity after the opening of tensile cracks

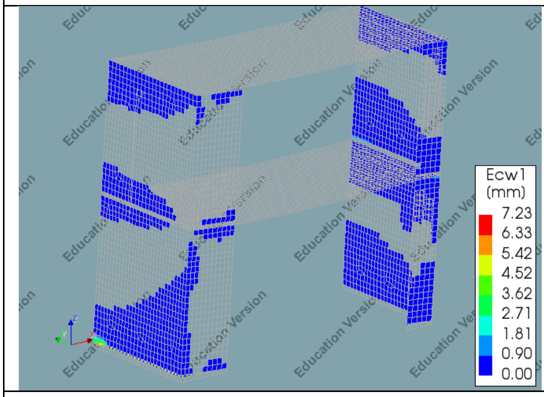

(C) Peak base shear force is reached

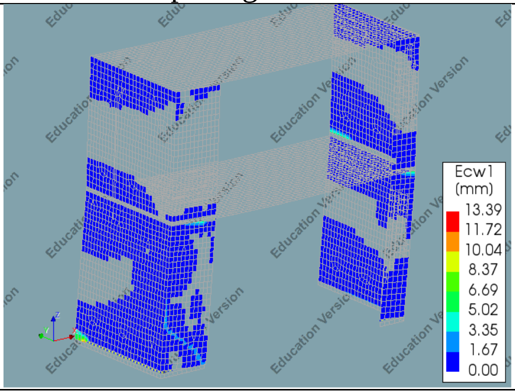

(D) Near-collapse displacement

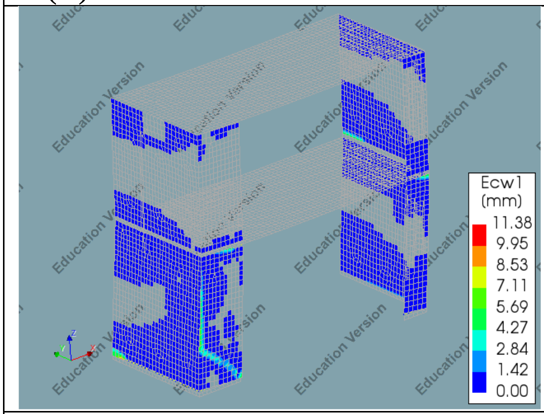

(E) Diagonal cracking failure

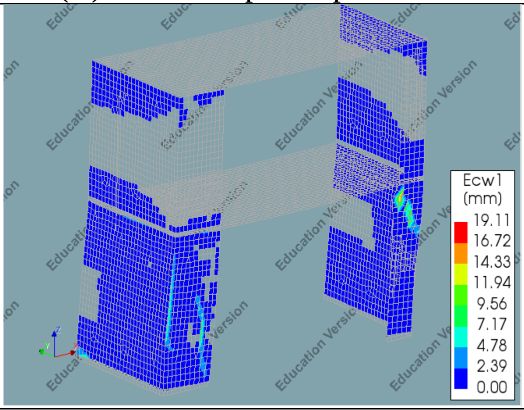

(F) End of the analysis

The progression of cracks and damages on the model are shown in Table 7.10 and Table 7.11. The activation of the rocking mechanism on the model is signified by the opening of the interface elements at the extremities of the masonry structural elements as seen on the relative displacement contour plot of event B in Table 7.10. There is, however, no crack observed in the mortar joints located on other parts of the structure, particularly in the transversal walls, despite of the inclusion of shear behavior to the constitutive model. The lack of cracks in the interface elements located at the transversal walls indicates the dominant failure modes to be the rocking of the piers and the formation of diagonal cracks in the piers. At event E, a large interface relative displacement can be observed on the model. This large relative displacement indicates the failure of the vertical joint, which causes the divergence of the analysis.

Table 7.11 shows the progression of cracks formation in the shell elements. Cracks initially form at the base of the ground floor transversal wall, which follows the initiation of the rocking mechanism on the structural model. Diagonal cracks appear both in the long pier and the short pier with the long pier undergoing diagonal cracking failure first followed by the short pier as shown by event E and event F. The shape of the cracks in the long pier resembles the diagonal cracks in the Macro-TSRCM model with vertical cracks opening along the wall-pier connection before changing the orientation to diagonal cracks that propagate to the toe of the pier. The angle of these diagonal cracks is, however, considerably shallower. This difference is most likely the result of the sliding of the long pier, which changes how the load is transferred through the long pier. Shortly after the long pier undergoes diagonal cracking failure, the short pier also experiences diagonal cracking failure which is accompanied by the failure of the wall-pier connection.

7.5 Comparison of Shell Micro-Model Variations

The numerical results of the analyses are summarized in Table 7.12. The plot of capacity curves and interstory drift curves are shown in Figure 7.17 and Figure 7.20 respectively. A summary of the failure mechanisms observed on the numerical models is presented in Table 7.13.

Table 7.12 Summary of base shear force results of the shell micro-models (shell elements micro-model)

Analysis	Initial stiffness (kN/mm)	Peak base shear force (kN)	Near collapse displacement (mm)
Experiment	16.67	65.7	54.4
Micro-Coulomb-Linear	15.09 (-9.48%)	79.14 (+20.46%)	18.27 (-66.42%)
Micro-Coulomb-TSRCM	12.50 (-25.02%)	58.28 (-11.29%)	14.33 (-73.66%)
Micro-Discrete-Linear	16.94 (+1.62%)	96.26 (+46.51%)	not reached
Micro-Discrete-TSRCM	17.00 (+1.98%)	96.18 (+46.39%)	49.19 (-9.58%)
Micro-Discrete-TSRCM(Cmp)	16.91 (+1.43%)	95.72 (+45.69%)	not reached

Micro-NL_Elastic-Linear	18.73 (+12.36%)	101.57 (+54.59%)	21.45 (-60.57%)
Micro-NL_Elastic-TSRCM	17.05 (+2.28%)	95.43 (+45.25%)	28.96 (-46.76%)

Table 7.12 shows the initial stiffness values, peak base shear force and near-collapse displacement. The initial stiffness values of most of the micro-models do not differ significantly from the value obtained from the physical experiment. The largest difference is found on Micro-Coulomb-TSRCM with a difference of 25% compared to the experiment. The small difference between the numerical models and the physical specimen shows that the choice of the linear-elastic parameters values are appropriate for the analysis of the physical specimen. In terms of peak base shear force, it is evident that the majority of the numerical models significantly overestimate the structural capacity of the physical specimen. The discrete cracking models (Micro-Discrete-Linear, Micro-Discrete-TSRCM & Micro-Discrete-TSRCM(Cmp)), the nonlinear elasticity models (Micro-NL_Elastic-Linear & Micro-NL_Elastic-TSRCM) and the Coulomb friction model with the linear elastic shell constitutive model (Micro-Coulomb-Linear) overestimate the structural capacity greatly with a difference ranging from 20-54 % compared to the physical specimen. The cause of this overestimation of the structural capacity is still unclear and a sensitivity study will need to be conducted on the models. Out of the seven numerical models, the Micro-Coulomb-TSRCM model is the only one that underestimates the capacity of the structure. However, as has been discussed in section 7.2.2, this result is most likely not valid, considering the abnormal structural behavior on the numerical model.

From Table 7.12, it can also be seen that many of the model variations underestimate the deformation capacity of the structure. Most of them are caused by instability issues, which lead to non-convergence. The Coulomb friction variations (Micro-Coulomb-Linear & Micro-Coulomb-TSRCM) and the nonlinear elasticity model variations (Micro-NL_Elastic-Linear & Micro-NL_Elastic-TSRCM) seem to suffer from this problem. The discrete cracking models, on the other hand, are relatively stable. The Micro-Discrete-Linear and Micro-Discrete-TSRCM(Cmp) model reaches the target displacement without encountering divergence in the analyses. In the case of both models, there is no point at which the near-collapse displacement occurs due to the governing failure mechanism of the two models being tensile cracking. In the case of the Micro-Discrete-TSRCM model, non-convergence is encountered in the analysis. However, this occurs after the diagonal cracking failure and does not affect the analysis results negatively.

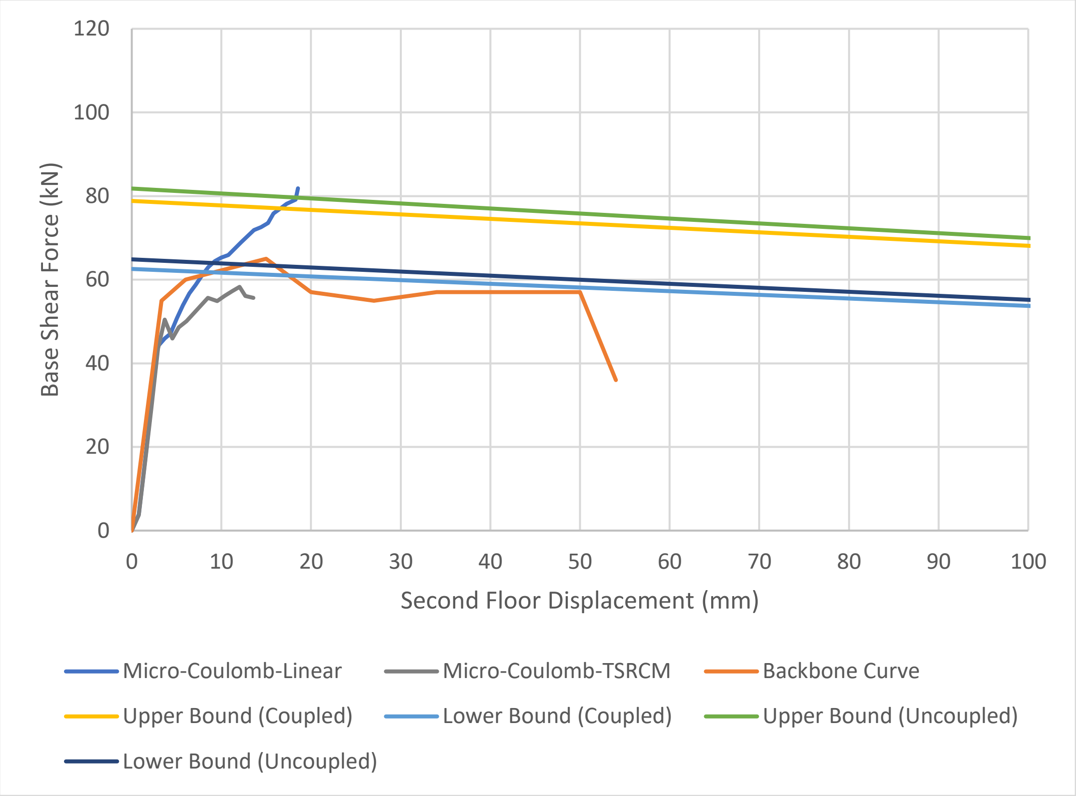

Figure 7.17 Comparison of capacity curves of Coulomb friction micro-model variations

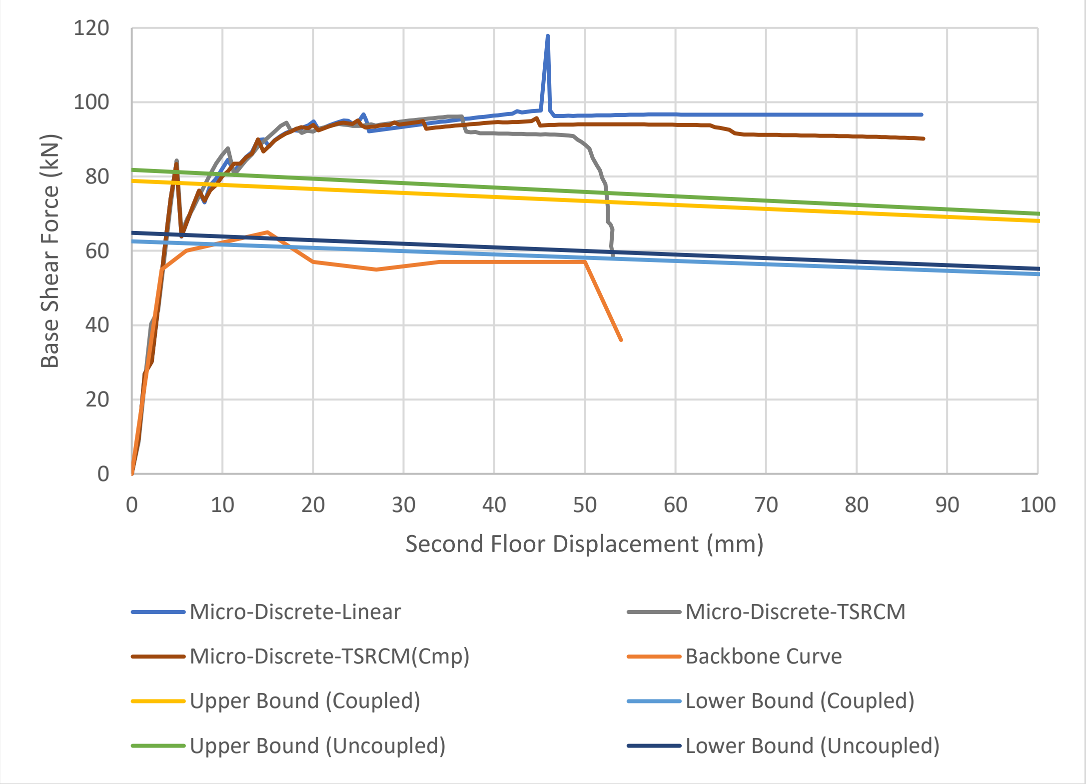

Figure 7.18 Comparison of capacity curves of discrete cracking micro-model variations

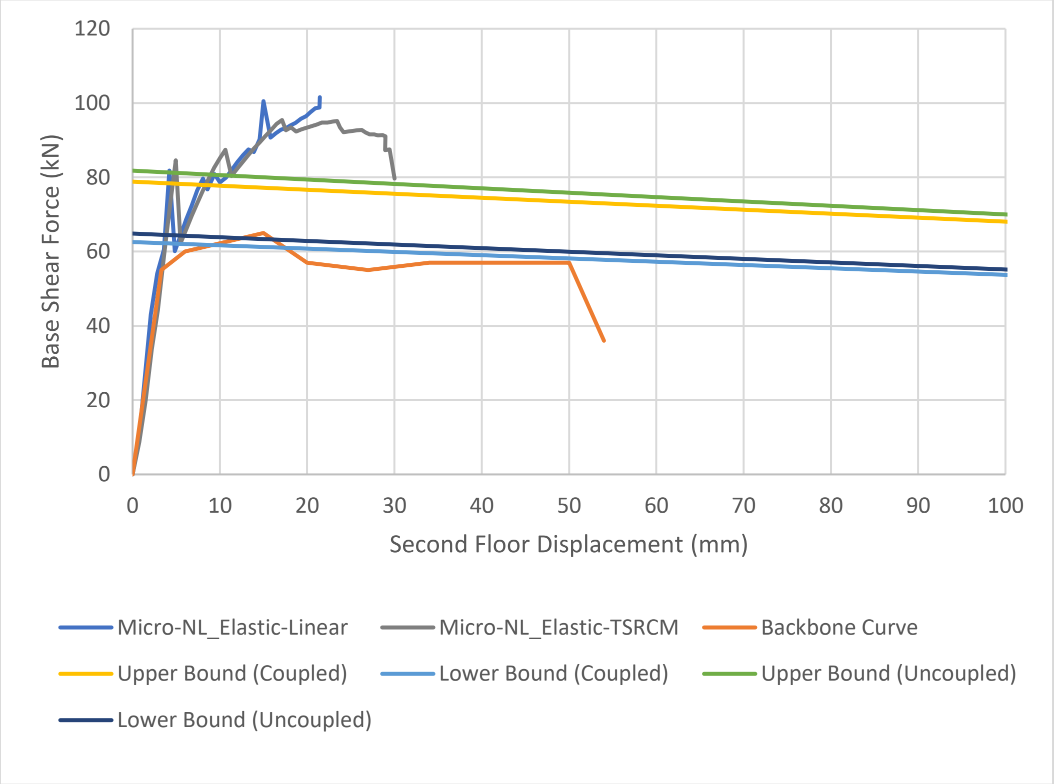

Figure 7.19 Comparison of capacity curves of nonlinear elasticity micro-model variations

Figure 7.17, Figure 7.18 and Figure 7.19 show the comparisons between the capacity curves from shell elements micro-models and the backbone curve. Figure 7.18 shows that the discrete cracking model variation with TSRCM shell elements (Micro-Discrete-TSRCM) offers the best approximation of the structural behavior of the physical specimen in terms of the shape of the capacity curve. The other two variations (Micro-Discrete-Linear & Micro-Discrete-TSRCM(Cmp)) also show similar behavior to Micro-Discrete-TSRCM. However, both models lack the abrupt base shear force decrease that was observed from the experimental results. Figure 7.19 shows that the nonlinear elasticity models (Micro-NL_Elastic-Linear & Micro-NL_Elastic-TSRCM) follow a similar pattern to the capacity curves of the discrete cracking models. This similarity comes from the fact that the definition of the nonlinear elasticity is partly based on the discrete cracking constitutive model. However, both variations are not stable, since both numerical models encounter divergence. Figure 7.17 shows that the Coulomb friction models feature significantly different results compared to the other micro-models. These differences are caused by the significantly different behavior of the interface constitutive model when compared to the other micro-models. Both models suffer from instability issue, that causes them to undergo early failure.

Apart from the capacity curves of the numerical models, the figures also show the upper and lower limit values from the hand calculation. Comparison between the capacity curves and the hand calculation results show that most of the micro-models exceed the upper limit expected from the structure. The cause of this is still unclear and further investigation is required.

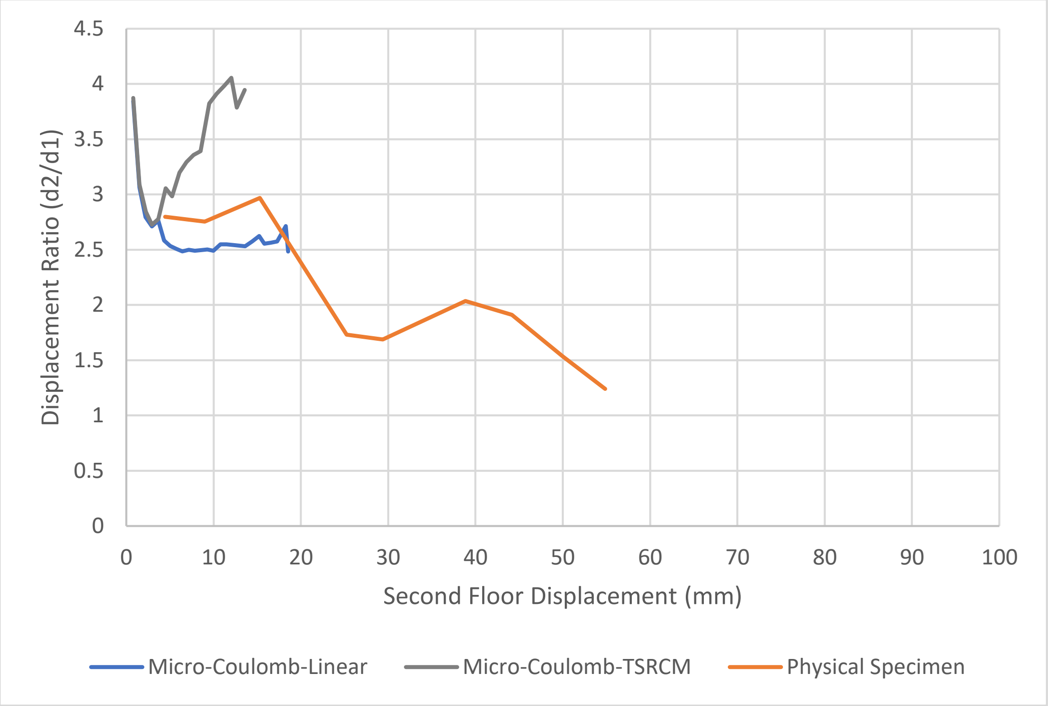

Figure 7.20 Comparison of interstory drift curves of Coulomb friction micro-model variations

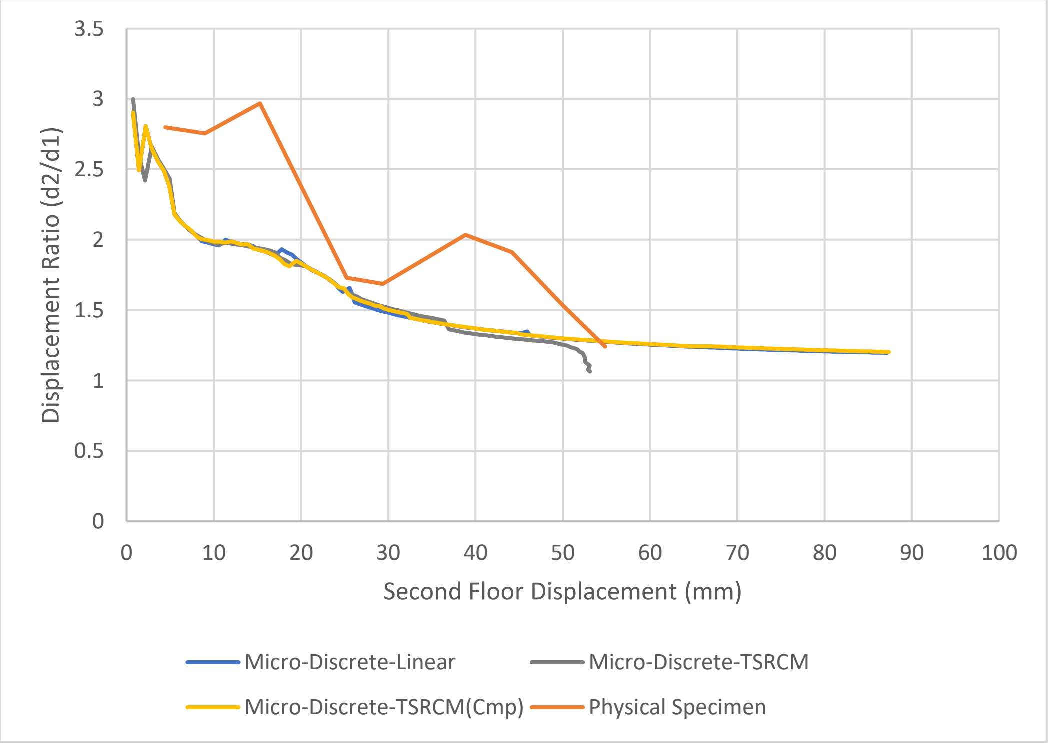

Figure 7.21 Comparison of interstory drift curves of discrete cracking micro-model variations

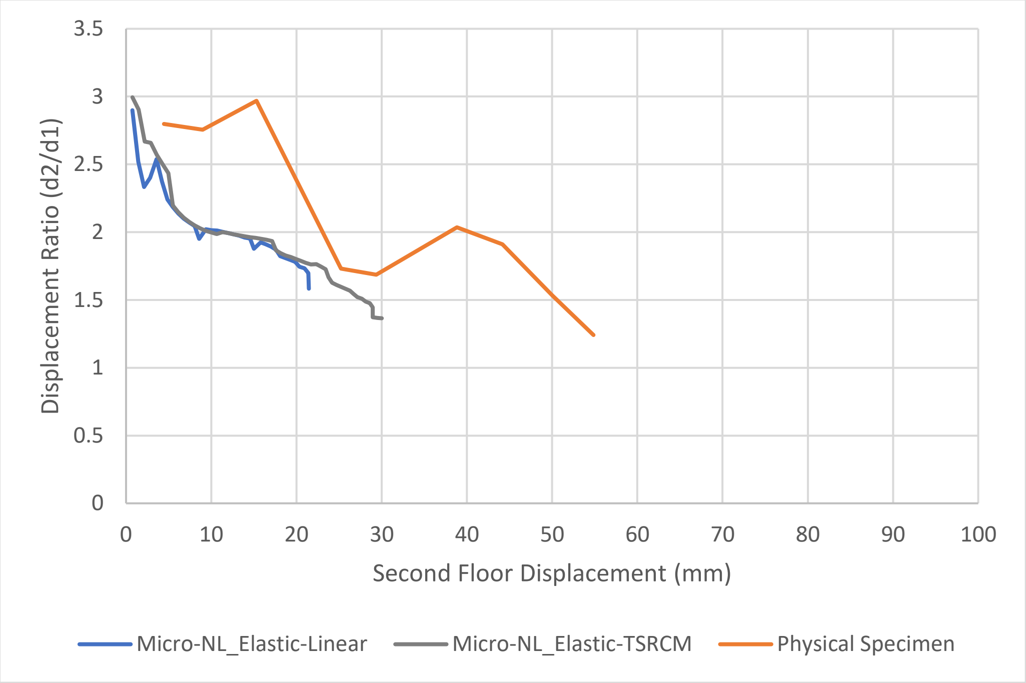

Figure 7.22 Comparison of interstory drift curves of nonlinear elasticity micro-model variations

Figure 7.20, Figure 7.21 and Figure 7.22 show the interstory drift curves of the physical specimen and the numerical models. The figures show that almost all numerical models curves follow a similar behavior, which is characterized by a steady decrease of displacement ratio followed by a region of relatively constant displacement ratio. Two numerical model variations deviate from this trend, the Micro-Coulomb-Linear and Micro-Coulomb-TSRCM model. The interstory drift curves of the two Coulomb friction models exhibit behaviors that are significantly different when compared to the other numerical models. This discrepancy is caused by the difference in the behavior of the Coulomb friction constitutive model when compared to the discrete cracking model and the nonlinear elasticity model. Looking at the interstory drift curve of the physical experiment, it can be seen that the curve follows a similar trend as the numerical models' curves with decreasing displacement ratio value and a soft-story mechanism forming at the ground floor. However, by comparing the numerical model curves with the curves extracted from the experimental results, it is evident that no micro-model variation considered in this chapter offers a reasonably accurate prediction of the physical specimen interstory drift.

Table 7.13 Summary of observed failure mechanism of the shell micro-models

Model Variation	**Failure Mechanisms**			
	Rocking Mechanism	**Diagonal Cracking Failure**	**Cracks in the Transversal Walls**	**Others**
Experiment	Yes	Wide pier	Yes	
Micro-Coulomb-Linear	Yes	No	Yes	Sliding of the second floor concrete slab
Micro-Coulomb-TSRCM	No	No	Yes	Sliding of the second floor concrete slab; Detachment of one of the first floor transversal wall
Micro-Discrete-Linear	Yes	No	No	-
Micro-Discrete-TSRCM	Yes	Wide pier	No	-
Micro-Discrete-TSRCM(Cmp)	Yes	No	No	-
Micro-NL_Elastic-Linear	Yes	No	No	Failure of one of the interface elements in one of the transversal wall
Micro-NL_Elastic-TSRCM	Yes	Both piers simultaneously	No	Failure of the wall-pier connection

Table 7.13 shows the summary of failure mechanisms on the models, which are observed on the micro-models. There is no micro-model that perfectly simulates the failure mechanisms of the physical specimen. In terms of rocking mechanism, almost all micro-models except the Micro-Coulomb-TSRCM model exhibit rocking behavior. Diagonal cracking failure is also present in the models that utilize the TSRCM model. However, the Micro-Discrete-TSRCM model is the only numerical model that comes close to properly simulate the diagonal cracking behavior of the physical specimen. In terms of cracks in the transversal walls, only the Coulomb friction models manage to exhibit cracking behavior in the transversal walls. The cracking patterns in the transversal walls on those models, however, do not accurately simulate the cracking patterns on the physical specimen. The lack of cracks in the transversal walls on other numerical models can be attributed to the limitation of the shell finite elements in modeling the out-of-plane masonry behavior. From the table, it can also be seen that the nonlinear models (Micro-

NL_Elastic-Linear & Micro-NL_Elastic-TSRCM) exhibit unusual failure behavior that was not observed on the physical specimen. Based on the observations of the failure mechanisms, it can be concluded that the Micro-Discrete-TSRCM model provides the most promising result out of the micro-models.

7.6 Concluding Remarks

In this chapter, seven different model variations have been analyzed and compared with the physical experiment results and to each other. Based on the results, the following conclusions can be made:

- The Coulomb friction micro-models suffer from instability issues, as both models encounter divergence during the analyses. Apart from the instability issues, the models also suffer from other problems. Micro-Coulomb-TSRCM model, in particular, exhibits some strange failure behavior that does not match the physical specimen behavior. As such, the Coulomb friction models are currently not recommended for practical use.

- The discrete cracking models are the most stable out of all micro-models. Micro-Discrete-TSRCM model, in particular, simulates the structural behavior of the physical specimen adequately from a qualitative point of view and in terms of displacement capacity. All discrete cracking models, however, greatly overestimate the structural capacity of the structure. Further investigation of the parameters that cause the overestimation is needed. The analysis of the additional model variation with the compression-only TSRCM shell element constitutive model (Micro-Discrete-TSRCM(Cmp)) also reveals that said model does not bring any significant improvement compared to the Micro-Discrete-Linear model. Thus, there is no benefit in modeling the nonlinear behavior of the CS units using this modified TSRCM constitutive model.

- The nonlinear elasticity model variations exhibit similar pre-peak behavior as the discrete cracking models due to the similarity in the defined constitutive model. The two models are, however, very unstable as have been demonstrated by the capacity curves of both models in section 7.4.1 and 7.4.2. Like the discrete cracking models, the nonlinear elasticity models also grossly overestimate the capacity of the structure. Considering the instability issue and the lack of significant improvement in the results compared to the discrete cracking models, both model variations cannot be recommended for practical use.

Chapter 8
Conclusion & Recommendation

8.1 Conclusions

In this thesis, several different approaches used to model a masonry CS element masonry structure have been investigated. Two main modeling methods, macro-model and micro-model, are used in this thesis with different constitutive models combination. Each model is assessed in terms of structural capacity, capacity curve, interstory drift and failure mechanisms. These analysis results are then compared with the other numerical models and with a tested structure.

The first modeling approach examined is the macro-model approach. Two different shell element constitutive models are used: Total Strain Rotating Crack Model and Engineering Masonry Model. Sensitivity studies are also carried out to assess the effect of the material parameters on each model. Furthermore, the models were modified with the inclusion of vertical interface elements for the wall-pier connections. Analyses of these modified models were performed to examine the effect of the interface elements.

The other modeling approach examined in this thesis is the micro-model approach. Three different types of interface elements constitutive models are used for the analyses; Coulomb friction; discrete cracking; nonlinear elasticity. Each model is then constructed with two different types of shell elements constitutive model: linear elastic or Total Strain Rotating Crack Model. An additional variation is considered for the discrete cracking model variation with the modified version of the TSRCM model.

From the analyses that have been conducted on every numerical model, the following conclusions are derived:

- Based on the results of the analyses of the macro-models, it appears that the Total Strain Crack Model can simulate the structural behavior of the physical specimen better than the Engineering Masonry Model. The Macro-TSRCM model is able to model the failure mechanisms of the tested specimen accurately, which includes rocking of the piers and the diagonal cracking failure of the piers. On the other hand, the Macro-EMM models show an exceedingly ductile behavior, that does not match the behavior of the physical specimen. Despite of the promising results obtained from the analysis on the Macro-TSRCM model, the numerical model still has considerable limitations. The numerical model cannot simulate the out-of-plane behavior of the transversal walls accurately, which is likely caused by the limitation of the shell finite elements used to model the CS elements. Apart from that, the model also still overestimates the structural capacity of the specimen significantly. The cause of this significant overestimation is still unclear even after the sensitivity studies conducted on the model. Given the limitations of the model and other issues pertaining to this model, this model is not recommended by the author for practical use.

- The sensitivity study on the Macro-TSRCM model shows that changes in the material parameters mainly affect the post-peak behavior of the structure, which is related to the diagonal cracking failure of the piers. The pre-peak behavior and the structural capacity are not sensitive to the changes, even when the material parameters related to tensile cracking (G_{ft}^{I} & f_t) are varied. This result is unexpected since the pre-peak behavior is governed by tensile cracking and changes in the parameters are expected to have a more significant impact on the pre-peak region and the peak capacity. Given this unusual behavior, the author assumes that there is another factor that influences the pre-peak behavior of the model, but this study was not able to identify it.

- The sensitivity study on the Macro-EMM models suggests that the dominant material parameters governing the behavior of the structure are parameters related to the crushing behavior of the structure (G_{fc} & f_c). This result indicates that toe crushing is the dominant failure mechanism for the EMM models.

- The inclusion of interface elements to the numerical models changes the behavior of the numerical models considerably. In the case of the Macro-TSRCM model, the inclusion of interface elements causes the diagonal cracking failure to occur earlier. The interface elements in the model also introduce another failure mechanism to the model behavior: the vertical joint failure. A sensitivity study on the shear traction-relative displacement diagram indicates that the reduction of vertical joint strength causes the structure to suffer from early failure due to the vertical joint failure. The effect of the change in the shear traction-relative displacement is less pronounced in the case of Macro-EMM models. The reduction in the vertical joint shear strength only introduces instability to the model and causes the model to undergo early failure due to the failure of the vertical joint.

- The analyses on the micro-models show instability issues with some models exhibiting non-convergences at the early stage of the analysis. This problem is more evident for the Coulomb friction models and the nonlinear elasticity models. The discrete cracking models are more stable compared to the other models showing the most promising results. However, similar to the macro-models, the discrete cracking models also greatly overestimate the structural capacity of the structure. Due to these issues, the author does not recommend any micro-model for analyzing the structure. A sensitivity study on the discrete cracking models is recommended to find the most significant parameters governing the failure behavior of the structure.

8.2 Recommendations

Based on the previous conclusions, The recommendations for future research are as follows:

- Further sensitivity studies are recommended to be performed on the TSRCM macro-model with other parameters that possibly have an influence on the pre-peak behavior and the structural capacity.

- The modeling strategy of the models considered in this thesis might have played a role in the overestimation of the structural capacity. It is highly recommended to consider reanalyzing the physical structure using other modeling strategies to provide a comparison and find factors that possibly cause this overestimation.

- Further numerical analyses are recommended to be carried out on the TSRCM macro-model with the inclusion of geometrical nonlinearity and a higher number of integration points, especially to study the out-of-plane behavior of the transversal walls.

- As the numerical analyses only examine the behavior of the structure when loaded in the positive x-axis direction, it is recommended to conduct another numerical analysis on both the macro-models and the micro-models with lateral loads in the negative x-axis direction.

- To properly assess the effects of the vertical joints on the post-peak behavior of the macro-models, it is advisable to run another analysis on the models using a more stable interface elements constitutive model.

- In regards to the instability issue in the micro-models, it is of interest to investigate the cause of this instability by analyzing a smaller scale micro-model.

- Given that no numerical model considered in this thesis are able to replicate the out-of-plane behavior of the tested specimen accurately, the development of a new constitutive law for the interface element that may be able to represent adequately and with a stable behavior the Coulomb friction failure is advised. It is also of interest to consider numerical studies with another more detailed modeling approach (e.g. 3D brick elements with combined cracking-shearing-crushing constitutive model).

Bibliography

Abrams, Daniel P., Omar AlShawa, Paulo B. Lourenço, and Luigi Sorrentino. 2017. "Out-of-Plane Seismic Response of Unreinforced Masonry Walls: Conceptual Discussion, Research Needs, and Modeling Issues." *International Journal of Architectural Heritage* 11(1): 22–30.

Backes, H.-P. 1985. "On the Behavior of Masonry under Tension in the Direction of the Bed Joints." Aachen University of Technology.

Barbagallo, F. et al. 2019. "Seismic Assessment of Steel MRFs by Cyclic Pushover Analysis." *The Open Construction and Building Technology Journal* 13(1): 12–26.

Binda, L., A. Fontana, and G. Frigerio. 1988. "Mechanical Behavior of Brick Masonries Taken from Bed Joints." In *8th Int. Brick and Block Masonry Conf.*, ed. J.W. de Courcy. London, UK: Elsevier Applied Science, 205–16.

Calderini, Chiara, Serena Cattari, and Sergio Lagomarsino. 2009. "In-Plane Strength of Unreinforced Masonry Piers." *Earthquake Engineering and Structural Dynamics* 38(2): 243–67.

CBS. 2016. "Vier Op de Tien Huishoudens Wonen in Een Rijtjeshuis." *CBS*: 1. https://www.cbs.nl/nl-nl/nieuws/2016/14/vier-op-de-tien-huishoudens-wonen-in-een-rijtjeshuis.

CEN. 2013. *Eurocode 6 - Design of Masonry Structures - Part 1-1: General Rules for Reinforced and Unreinforced Masonry Structures*.

D'Altri, Antonio Maria et al. 2019. "Modeling Strategies for the Computational Analysis of Unreinforced Masonry Structures: Review and Classification." *Archives of Computational Methods in Engineering*.

Dhanasekar, M., and A.W. Page. 1985. "The Failure of Brick Masonry under Biaxial Stresses." *Proceedings of the Institution of Civil Engineers* 79: 295–313.

DIANA FEA 10.3 User Manual. 2019. Delft, The Netherlands.

Esposito, R. et al. 2018. "Influence of the Behavior of Calcium Silicate Brick and Element Masonry on the Lateral Capacity of Structures." In *10th Australasian Masonry Conference*, Sydney, Australia.

de Felice, Gianmarco, and Renato Giannini. 2001. "Out-of-Plane Seismic Resistance of Masonry Walls." *Journal of Earthquake Engineering* 5(2): 253–71.

Giaretton, Marta, Dmytro Dizhur, Francesca da Porto, and Jason M. Ingham. 2016. "Construction Details and Observed Earthquake Performance of Unreinforced Clay Brick Masonry Cavity-Walls." *Structures* 6: 159–69.

Griffith, M, and Jaroslav Vaculik. 2007. 25 TMS Journal *Out-of-Plane Flexural Strength of Unreinforced Clay Brick Masonry Walls*.

Lourenço, Paulo B., and J.G. Rots. 1997. "Multisurface Interface Model for Analysis of Masonry Structures." *Journal of Engineering Mechanics* 123(7).

Lourenço, Paulo B. 1996. 70 PhD Thesis "Computational Strategies for Masonry Structures." Delft University of Technology.

Magenes, Guido, and Gian Michele Calvi. 1997. "In-Plane Seismic Response of Brick Masonry Walls." *Earthquake Engineering & Structural Dynamics* 26: 1091–1112.

Messali, F. et al. 2018. "Blind Predictions of a Cyclic Pushover Test on a Two-Storey Masonry Assemblage: A Comparative Study." In *16th European Conference on Earthquake Engineering*, Thessaloniki.

Messali, F, and M Pari. 2017. *Structural Behaviour of a Calcium Silicate Element Masonry Assemblage: Comparison of Blind Predictions*. Delft.

Moon, Franklin L., Tianyi Yi, Roberto T. Leon, and Lawrence F. Kahn. 2006. "Recommendations for Seismic Evaluation and Retrofit of Low-Rise URM Structures." *Journal of Structural Engineering* 132(5): 663–72.

NEN. 2017. *NPR 9998:2017 - Beoordeling van de Constructieve Veiligheid van Een Gebouw Bij Nieuwbow, Verbouw En Afkeuren - Geïnduceerde Aardbevingen - Grondslagen, Belastingen En Weerstanden*.

Pari, M (author) et al. 2017. "Computational Modeling of the Cyclic Pushover Test on a Calcium Silicate Element Masonry Assemblage." In *4th WTA International PhD Symposium*, Delft, The Netherlands: 4th WTA Nederland - Vlaanderen.

van der Pluijm, R. 1992. "Material Properties of Masonry and Its Components under Tension and Shear." In *6th Canadian Masonry Symposium*, ed. V.V. Neis. Saskatoon, Saskatchewan, Canada, 675–86.

———. 1993. "Shear Behavior of Bed Joints." In *6th North American Masonry Conf.*, eds. A.A. Hamid and H.G. Harris. Philadephia, Pennsylvania, USA: Drexel University, 125–36.

Rots, J.G. 1997. "Case Study Pier-Main Wall Conections." In *Structural Masonry*, ed. J.G. Rots. Rotterdam: A.A. Balkema, 132–42.

Rots, J.G., R. van der Pluijm, A.Th. Vermeltfoort, and H.J.M. Janssen. 1997. *Structural Masonry*. ed. J.G. Rots. Rotterdam: A.A. Balkema.

RTV Noord. 2019. "Vanaf Nu Mogelijk Om Eigen Aannemer Aardbevingsschade Te Laten Vastleggen." *RTV Noord*. https://www.rtvnoord.nl/nieuws/212424/Vanaf-nu-mogelijk-om-eigen-aannemer-aardbevingsschade-te-laten-vastleggen (January 29, 2020).

Schipper, H.R., G.J.P. Ravenshorst, and Pieter Ham. 2017. *Proposal of Quasi-Static Cyclic Pushover Test on an Assembled Structure in CS Elements*.

Schreppers, G.M.A., A. Garofano, F. Messali, and J.G. Rots. 2017. *DIANA Validation Report for Masonry Modeling*. Delft.

Schubert, P. 1988. “The Influence of Mortar on the Strength of Masonry.” In *8th Int. Brick and Block Masonry Conf.*, ed. J.W. de Courcy. London, UK: Elsevier Applied Science, 162–74.

Schubert, P., and Hoffmann. 1994. “Compressive Strength of Mortar in Masonry: Significance, Influences, Test Methods, Requirements.” In *10th Int. Brick and Block Masonry Conf.*, eds. N.G. Shrive and A. Huizer. Calgary, Alberta, Canada, 1335–44.

Tso, W.K., and A.S. Moghadam. 1998. “Pushover Procedure for Seismic Analysis of Buildings.” *Progress in Structural Engineering and Materials* 1(3): 337–44.